Assembling an array of polar molecules with full quantum-state control

Citation
Zhang, Jessie T. 2021. Assembling an array of polar molecules with full quantum-state control. Doctoral dissertation, Harvard University Graduate School of Arts and Sciences.

HARVARD UNIVERSITY
Graduate School of Arts and Sciences

DISSERTATION ACCEPTANCE CERTIFICATE

The undersigned, appointed by the

Department of Physics

have examined a dissertation entitled

Assembling an array of polar molecules with full quantum-state control

presented by Jessie Zhang

candidate for the degree of Doctor of Philosophy and hereby
certify that it is worthy of acceptance.

Signature ____

Typed name: Professor Kang-Kuen Ni, Chair

Signature John Doyle

Typed name: Professor John Doyle

Signature ____

Typed name: Professor Mikhail Lukin

Date: August 24, 2021

Assembling an array of polar molecules with full quantum-state control

a dissertation presented
by
Jessie Zhang
to
The Department of Physics

in partial fulfillment of the requirements
for the degree of
Doctor of Philosophy
in the subject of
Physics

Harvard University
Cambridge, Massachusetts
August 2021

Thesis advisor: Professor Kang-Kuen Ni Jessie Zhang

Assembling an array of polar molecules with full quantum-state control

Abstract

The ability to control particles in the quantum regime at the individual particle level is a challenge at the frontier of quantum science and engineering. Of the many quantum objects developed in pursuit of this goal, ultracold molecules host rich internal states and unique interparticle interactions that could lend themselves useful to a broad range of applications including quantum computing and simulation, precision measurements and quantum chemistry. In this thesis we present a bottom-up approach to creating single molecules in individual optical tweezers. In particular, single atoms of two different species are first trapped and cooled in individual optical tweezers then brought together to form a single molecule coherently. Using this approach, we have successfully created an array of fully quantum-state-controlled polar molecules. The quantum state –including both internal and external states –of the resulting molecules are known to us, and is the first time single neutral molecules have been under full quantum state control. This platform offers exciting new opportunities to harness the rich properties of molecules in many quantum science applications.

Contents

Citations to previously published work

Parts of this thesis cover research reported previously in the following publications:

- Forming a single molecule by magnetoassociation in an optical tweezer

  Jessie T. Zhang, Yichao Yu, William B. Cairncross, Kenneth Wang, Lewis R. B. Picard, Jonathan D. Hood, Yen-wei Lin, Jeremy M. Hutson, Kang-Kuen Ni

  Phys. Rev. Lett. 124, 253401 (2020)

- Assembly of a rovibrational ground state molecule in an optical tweezer

  William B. Cairncross*, Jessie T. Zhang*, Lewis R. B. Picard, Yichao Yu, Kenneth Wang, Kang-Kuen Ni

  Phys. Rev. Lett. 126, 123402 (2021)

Listing of figures

To all my heroes

Adapted from the Ph.D thesis of the one and only Dr. Cathy Zhang.

Acknowledgments

This is probably the most important section of this entire thesis, for (a) it might easily be the most-read section, and (b) this thesis would not have been possible without the help of many.

First, I would like to thank my advisor, Prof. Kang-Kuen Ni, who took me in as a student despite the fact that I had never set foot in an optics lab and instilled confidence in me. I appreciated her support, understanding, and patient guidance throughout the ups and downs of my Ph.D. She led the lab forward with such a tenacious spirit that has been truly inspirational. From her, I learned how to set sight on a scientific goal and go into the lab to make it happen. I also learned how to conquer problems that may arise along the way with a curious heart.

I would also like to thank Prof. John Doyle and Prof. Misha Lukin for serving on my committee, and engaging in helpful conversations over the years. I am indebted to my undergraduate advisor Prof. Jenny Hoffman, who was my first mentor in experimental physics, and encouraged me to pursue a Ph.D. in the first place. I enjoyed teaching with her and I still turn to her for advice in life.

Over the past few years, I have had the privilege of working with some very talented people in the lab in a welcoming and supportive environment. When I joined the lab, the NaCs project was in its early stages of trapping single atoms. I was fortunate to have Yichao Yu as my first mentor, who taught me the in and outs of working in an AMO lab, and who later provided much selfless help after I started NaCs 1.5 – sharing his experience and wealth of knowledge to get us off the ground. During this time I also overlapped with Lee Liu on the 1.0 apparatus, with whom I shared many late nights (or was it early mornings?) in the lab. As the first and most senior graduate student in the lab at the time, he was always generous to provide sage advice along the way. I also learned from postdoc Nick Hutzler many experimental physics tips; I still hear his voice in my head when it comes to good lab practices.

After I started building NaCs 1.5, then postdoc Jon Hood joined for a while before focusing on the 1.0 efforts. His positive spirit in the lab was infectious, and helped kick the 1.5 project into being. Later on, I was joined by postdoc Yen-wei Lin, who was crucial to getting things running smoothly and obtaining the Feshbach resonance spectroscopy data presented in this thesis. He always had a way of thinking outside the box, and his many creative ideas inspired the last page of this thesis. The experiment was later joined by postdoc Will Cairncross, who somehow managed to tear down and improve every single part of the experiment in the first month of his time here, and whose expertise on molecules helped us immensely in getting to rovibrational ground state molecules efficiently. Right before the pandemic, graduate student Lewis Picard joined our efforts and quickly picked up the experiment despite the social distancing rules in place, and who together with new graduate student Gabriel Patenotte, helped proofread my thesis. I am sure the experiment is in good hands and that they will bring the NaCs molecule experiment to ever greater heights.

In addition, I would like to thank Eliot Fenton, Rémy Vatre, Frederic Condin and Yu Wang, who all contributed to various parts of the experiment; Kenneth Wang on NaCs 1.0, who was always willing to lend a hand with servo troubles; KRb folks Yu Liu and Ming-guang Hu, who provided much advice during the early building phase of our experiment; and Andrei Gheorghe, Matt Nichols, David Grimes, Lingbang Zhu, Hyungmok Son, and Yu-Ting Chen, all of whom I overlapped with and learned from at various points while I was in the lab. I would also like to thank Yi-Xiang Liu for reminding me to complete Crimson Clear, and who, together with Fang Fang, imparted much wisdom on me, and made the last stretch of my Ph.D. so much fun for me.

And it is not only the scientific discussions and collaboration in the lab that I enjoyed over the years. It was our experiences outside as well – our epic Rhino cup run (go Bus Drivers!), food excursions at conferences, and hotpot and dumpling parties, to name just a few, are some of my fondest memories of the Ni lab.

I would also like to thank all the support from the department, both physics and CCB, that have made our lives in the lab easier. Stan Cotreau, whose help in the machine shop was crucial to the early phases of apparatus building; Lisa Cacciabaudo, who always had an open door and made graduate school so much easier to navigate; Susan Kinsella and Felix Negron, for, among many other things, helping with our lab purchases; and all the facilities, security and custodial personnel in the department, who always tried their best to support the needs of our experiments, and cheerfully greeted me in the mornings while I was on either side of the night.

Beyond the lab, I would like to thank the Center for Ultracold Atoms for providing a collaborative and intellectually stimulating environment – joint group meetings with the Greiner, Lukin, and Doyle groups were always enlightening. Thanks also to the Women in Physics community and the entire 2015 physics cohort, for all the support and fun over the years.

Finally I would like to thank my family and friends. Bella Wu, Winnie Yeung, Joyce Kwan, Anne Hébert, Anna Shneidman, and all members of the various table tennis communities I have been fortunate to be a part of during my time through graduate school – the MIT and Harvard table tennis clubs, Boston Table Tennis Club, and the Chinatown club – thank you all for keeping me sane. And last, but certainly not least, I am grateful for my family. Thanks to my parents, who instilled a love for science in me from an early age, and for their unwavering support every step of the way. And thanks to my sister Cathy Zhang, for always being there for me. Together with her boyfriend Stephen Giandomenico, we had many fun times over the years. Looking back, it is funny to think that she convinced me to stick around in Cambridge for graduate school together; I am glad she did. It has been quite a ride.

1

Introduction

1.1 The quest for quantum control

The ability to control particles in the quantum regime at the individual particle level has been a long-sought goal in the realm of quantum science and engineering in the past few decades . Such individually controlled entities could then be scaled-up to build many-body quantum systems in a way that allows quantum phenomena such as quantum superposition and entanglement to be utilized. In particular, one desires a system consisting of individual quantum objects simultaneously satisfying the following properties[1]:

- *Fully controllable* - all the quantum degrees of freedom of the particles of interest, including internal and external states where applicable, as well as interparticle interactions, are controllable.
- *Scalable* - able to build larger and more complex quantum systems from the individual quantum particles without compromising on individual control and performance.
- *Exhibits quantum behavior* - able to exploit quantum effects such as quantum superposition and entanglement.

Systems satisfying these properties could lead to many applications in areas such as quantum simulation[2,3,4] and quantum computing[5,6]. In quantum simulation, many-body quantum systems can be simulated directly using well-controlled quantum systems built from the individually controlled quantum particles, which could provide insight into models in condensed matter such as high Tc superconductivity and quantum magnetism, create new forms of matter, and guide the design of new materials[7]. In quantum computation, the individual quantum particles could serve as quantum bits and quantum phenomena be used to perform gate operations to achieve computation intractable to even the best classical computers as we know them now[8].

Towards this goal, many platforms using different quantum objects and techniques have been developed, including ultracold neutral atoms[9,10,11,12,13], atomic and molecular ions[5,6,14,15,3], color centers in diamonds[16,17,18], superconducting circuits[19,20,21], and photonic circuits[22,23,24], among many others. Each have their own advantages, and have all achieved varying levels of success in a diverse range of applications[25]. The goal of the present work lies within this broad motivation of developing a system of quantum particles that can be well-controlled at the individual particle level. Here, our particles of interest are ultracold molecules – molecules cooled down to temperatures where they behave and interact quantum mechanically (typically ~μK or lower).

1.2 The case for ultracold molecules

The advent of laser cooling has allowed for an unprecendented level of control over atoms[26], and the field of atomic physics has evolved towards ever finer control over atoms at ultracold temperatures. This control of atoms in the quantum regime has led to a plethora of breakthroughs in precision measurement, quantum sensing, quantum simulation and computation, and more[27,28,29,30].

In the past decade, there has been growing interest in expanding these techniques developed on atoms to molecules[31,32]. On top of the many features atoms possess, such as being identical and indistinguishable from on another of the same species, neutral molecules have drawn attention for many of its unique features not offered by their atomic counterparts. Polar molecules – molecules which have a net dipole moment due to uneven charge distribution within the neutral molecule – inherently exhibit strong electric dipole-dipole interactions that are long-range, anisotropic and tunable[33]. Furthermore, while atoms typically have only electronic, fine and hyperfine internal degrees of freedom, molecules also have vibrational and rotational degrees of freedom arising from the motion of the atoms within the molecule[34]. These interparticle interactions and additional degrees of freedom lend themselves useful to many quantum science applications.

For instance, it has been proposed that single molecules can act as qubits for quantum computation[35]. In some proposed schemes, pairs of states that interact with each other by the dipole-dipole interaction can be used for performing quantum gates, while non-interacting states can be used as storage qubits to allow for longer coherence times[36]. In the context of quantum simulation, there have been a plethora of proposals utilizing the rich degrees of freedom of molecules to simulate spin Hamiltonians in lattices, such as the XYZ Heisenberg model, and investigate collective phenomena such as quantum magnetism[37,38,39]. In a complementary approach, there have been proposals to utilize the internal states of molecules to form "synthetic dimensions" in addition to the real space dimensions of an array of molecules, which are predicted to host rich physics[40].

Some of the key ingredients for many of these applications are:

- Molecules that are pinned in sites, with the ability to prepare and address the molecules at the individual molecule level.
- Large electric dipole moment. This is required to generate the dipole-dipole interactions between the molecules.
- Long coherence times. Because the dipole-dipole interactions are sensitive to interparticle distance, they are in turn susceptible to decoherence from their relative motion which necessitates the molecules being as cold as possible.

Towards realizing many of these proposals, as well as many other exciting applications in precision measurement, quantum chemistry and more[31], the recent decade has seen great developments in our ability to obtain and control ultracold molecules.

One method of obtaining ultracold molecules is to associate them from quantum degenerate gases of atoms in a coherent manner. First achieved on the bi-alkali molecule ^{40}K^{87}Rb[41], similar techniques have since been expanded to many of the bi-alkalis in labs around the world[42,43,44,45,46]. This approach has thus far produced ultracold molecule gases with the highest phase-space density[47] and has among others allowed the study of quantum chemistry[48,49,50]. Using a similar approach, molecules have also been created in optical lattices to study spin dynamics[51,52].

A separate approach to obtaining ultracold molecules is to directly cool molecules, for example by using lasers or DC electric/magnetic fields[31]. Of these, laser cooling has achieved the coldest molecule temperatures to-date. Due to the rich internal structure of molecules, molecules typically lack optical cycling transitions and thus present challenges to cycle enough photons for direct laser cooling. Nevertheless, careful selection of molecules and transitions has enabled molecular MOTs[53,54,55], sub-Doppler cooling[56,57,58], and trapping arrays of ultracold molecules in optical tweezers[59].

In addition, much work has been done in controlling the internal state control of molecules. The hyperfine and rotational internal states of molecules can typically be manipulated by microwave and electric fields[60]. Using these, coherence times at the second-scale for nuclear states[61] and milli-second scale for rotational states with magic trapping[62] have been achieved. Electric fields can be used to polarize the molecules in the lab frame, and can also be used to tune the local interactions[63].

On a separate front, molecular ions have also seen great success in achieving full quantum state control. While typical molecular ions similarly lack convenient closed transitions for direct laser cooling, ions can interact with other charged particles and can therefore be sympathetically cooled with motional ground state cooled atomic ions[64]. Moreover, by utilizing the motional coupling between a molecular ion and an atomic ion, quantum logic spectroscopy has been used to prepare the ions in specific internal states[15], and to entangle a single molecular ion with an atomic ion[14].

While much of these previous works have realized many of the key ingredients necessary mentioned above, a scalable platform capable of individual particle control is yet to be realized. Bulk gas molecule approaches inherently fail to achieve individual particle control, while work towards motional ground state cooling for directly cooled molecules in optical tweezers has been concurrent with the work in this thesis. In the mean time, ions typically suffer from decoherence arising from their interactions with the environment and other ions, limiting their scalability with current technology. Thus, in the present work, we develop a platform consisting of associating single molecules in optical tweezers.

1.3 Optical tweezers

Optical tweezer arrays of neutral atoms have emerged as a powerful and versatile platform for quantum simulation and quantum computing in recent years. In these systems, laser beams are focused down to diffraction limited spot sizes that are capable of trapping single atoms. Notably, these traps can be steered and arranged in configurable geometries, and arranged *in situ* to near-unity filling[65,66,67,68,69]. This setup naturally offers site-resolved imaging, and the ability to address and control individual sites. For example, in a pioneering work, exactly two atoms were brought close together and entangled with unprecedented control using optical tweezers[70]. More recently, optical tweezer arrays have been used to trap neutral atoms that can be excited to Rydberg states that can interact with each other by electric dipole-dipole interactions[71,72]. These have led to exciting work in simulating and probing new states of matter[73,74,75], among others.

Seeing the advantages that optical tweezer arrays offer, the goal of the present work was to bring the single particle control that optical tweezers offer to ultracold molecules. In particular, we envision a system of single molecules trapped in individual optical tweezers and where the molecules are capable of long-range interactions. Moreover, each of the individual molecules can be independently addressed and controlled, and their dipole-dipole interactions can also be tuned.

1.4 Molecule assembly

In the approach presented in this thesis, we set out to achieve full quantum state control of individual molecules by a bottom-up approach of assembling single molecules in optical tweezers starting from individually trapped atoms. Compared to directly cooling and loading molecules into optical tweezers[59], this approach utilizes the mature quantum state control machinery already developed for atoms. The challenge is in (a) applying these techniques to gain full quantum state control over two different species in the same system and (b) converting the atoms to molecules in a way that our quantum state control of the atoms map over to the resulting molecules. In our solution to this, we draw on the approach of associating molecules previously developed in bulk gases, and employ a method consisting of fully coherent transfer processes.

A schematic of the assembly process is shown in Fig. 1.1. In the present work we choose the bi-alkali molecule ^{23}Na^{133}Cs, which is chemically non-reactive* and has one of the largest electric dipole moments among the bi-alkali's in the lab frame when polarized (4.6 Debye)[76,77]. The electric field required to polarize the molecule in the lab frame is ~10 kV/cm. In order to achieve and utilize these electric dipole moments, the NaCs molecules need to be in their rotational and vibrational (rovibrational) ground state, which is bound by ~4500 cm^{-1}, or ~7000 K[76]. This state has a large electric dipole moment and is stable from relaxation.

More specifically, the assembly process consists of the following steps:

- *1. Load single atoms*. Atoms are loaded into individual optical tweezers directly from a dual species magneto-optical trap. This process relies on light-assisted collisions between pairs of atoms, which ultimately ensures either one or no atoms are loaded into

---

*This may not be strictly true in the presence of optical trapping light as has been observed in a number of other bi-alkali species[49]. However, since we form single molecules in individual traps in our approach, we are not susceptible to such chemical reactions leading to molecule loss.

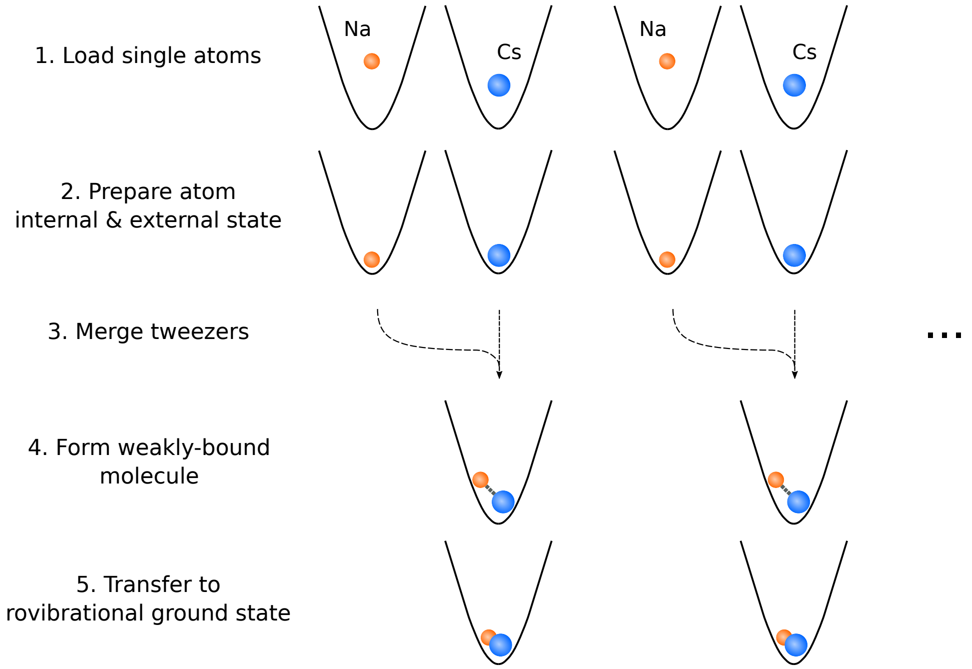

Figure 1.1: Scheme for associating single molecules in optical tweezer arrays. (1) Individual single atoms of different species are loaded into separate optical tweezers. (2) The internal and external states of the atoms are prepared in the individual optical tweezers. (3) The tweezers for the different species are merged so that a single atom pair occupies the ground state of an optical tweezer. (4) A weakly-bound molecule is formed from the atom pair. (5) The internal state of the molecule is transferred from the weakly-bound state to the rovibrational ground state. All these steps can be performed in parallel in an array for the creation of an optical tweezer array of molecules.

each optical tweezer.

- *2. Prepare atom internal and external state*. For the molecule formation step, it is crucial that the atoms occupy the lowest motional state of the optical tweezers. The atoms loaded into the trap are thermal at 10s of uK which is too hot for further molecule formation. Therefore, we must cool the optically-trapped atoms to their individual motional ground states, which we accomplish with Raman sideband cooling. In addition, the atoms are prepared in the proper internal states for molecule formation.
- *3. Merge tweezers*. Once the atoms are prepared in their individual tweezers, the tweezers are merged so that a single atom pair occupies a single optical tweezer. This needs to be completed adiabatically, such that the internal and external states of the atoms are preserved in the process.
- *4. Form weakly-bound molecule*. The rovibrational ground state is typically difficult to access directly from unbound atoms. Therefore, the molecule formation process consists of two steps. The first is to form a weakly-bound molecule to serve as a bridge to the rovibrational ground state. In the present work this is achieved by magnetoassociation through a Feshbach resonance.
- *5. Transfer to rovibrational ground state*. In the final step of molecule assembly, the internal state of the molecule is transferred to the rovibrational ground state. This is performed by a coherent two-photon optical transfer that preserves the internal and external state of molecule.

The assembly process can be performed in parallel in an array of optical tweezers to achieve an array of molecules. Furthermore, this bottom-up assembly approach can be scaled up in parallel and combined with rearrangement schemes[68,69] to achieve arrays with a high filling fraction of molecules to serve as a starting point for molecule entanglement and quantum science applications.

Prior to the present work, rovibrational ground state NaCs molecules had not been created coherently, whether in bulk gases or optical lattices. In this work, we mapped out a pathway from unbound atoms to rovibrational ground state molecules, including Feshbach resonance spectroscopy and excited state and ground state optical spectroscopy. Furthermore, this is the first time this approach has been completed for any molecule in optical tweezers with single atoms, a new parameter regime compared to previous work. The high intensity of optical tweezers at the trap center presents additional challenges in the molecule formation process that were unforeseen prior to our attempts. A feature of the present approach is that by performing the association process in optical tweezers, the molecule conversion efficiency does not suffer from collisions and reactions in the trap, which as we shall see leads to high conversion efficiencies that are not fundamentally limited.

1.5 Outline of thesis

In this thesis, we present the first fully-quantum-controlled rovibrational ground state molecules capable of generating entangling interactions trapped in optical tweezers arrays, where all the internal and external states of the molecules are well-controlled. This is the first step towards a large scale quantum simulation and quantum computation platform with ultracold molecules in optical tweezers with our molecular assembly approach.

This project evolved in parallel with an all-optical approach of forming molecules. That apparatus, which was a separate and slightly earlier generation and was referred to internally as version 1.0, laid much of the groundwork[78,79,80,81,82] in the efforts towards assembling rovibrational ground state molecules in optical tweezers in the present work, which was dubbed version 1.5. In this thesis we will focus on the creation of single rovibrational ground state molecules in an optical tweezer array, and discuss the key features and improvements of the version 1.5 apparatus. For the work that overlapped with version 1.0, we refer the reader to the theses that have covered them previously[83,84].

In Chapter 2 we discuss the main hardware components of the experimental apparatus that enabled the experiments presented in this thesis, including the vacuum chamber, electromagnetic coils, laser systems, and main optical beampaths.

In Chapter 3, we go over the steps to achieve dual species single atoms trapped in optical tweezers and quantum state control over the individual atoms, with a focus on the key features and improvements compared to version 1.0 of the apparatus.

In Chapter 4 we present the first results of Feshbach spectroscopy on Na+Cs atoms, where we detect multiple Feshbach resonances in multiple hyperfine channels. Using a particular s-wave resonance, we coherently magnetoassociate a single pair of atoms to a Feshbach molecule, and characterize its properties.

In Chapter 5 we present the creation and characterization of a rovibrational ground state NaCs molecule in an optical tweezer. This is achieved by a coherent two-photon transfer process, which involved first performing spectroscopy on the excited and ground state potentials to identify a suitable pathway to the rovibrational ground state.

After having completed the formation of a single rovibrational ground state molecule, in Chapter 6 we will discuss initial attempts in the experiment to scale the system up to multiple molecules in an array of optical tweezers.

Finally, in Chapter 7, we will conclude and provide an outlook for future directions.

2

Experimental apparatus

In this chapter we detail the crucial parts of the experimental apparatus that enabled the science presented in this thesis. These include the vacuum chamber, electromagnetic coils, electronics, and the lasers and optics for the trapping and control of all the atoms and molecules. Some parts that are common to the previous generation of experiment are detailed in previous theses[84,83] and are omitted here.

An overview of the mechanical parts of the apparatus are shown in a CAD schematic in

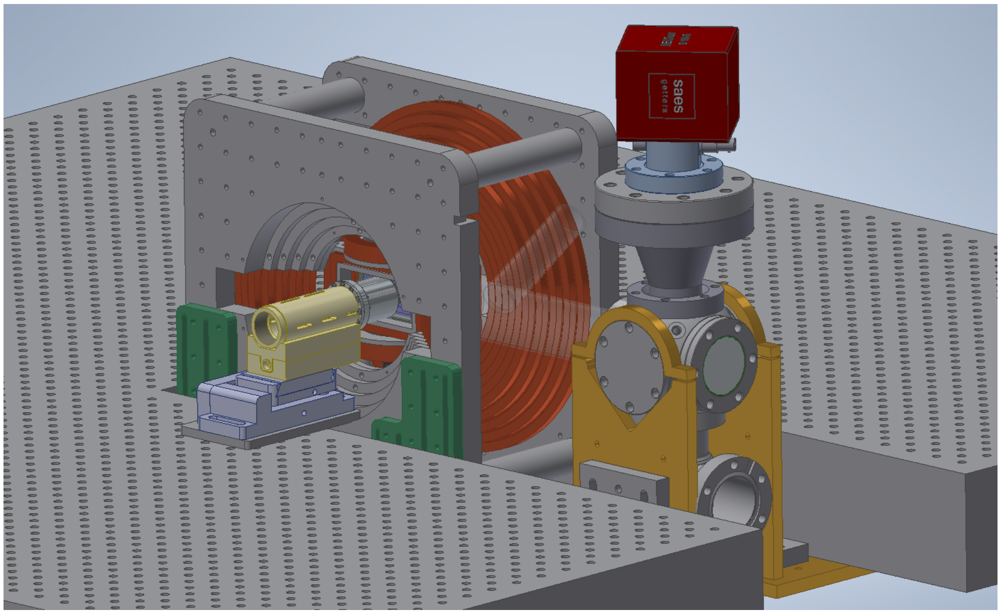

Figure 2.1: CAD drawing of chamber and breadboard.

Fig. 2.1. The entirety of the apparatus lies on a custom-built double-sided honeycomb breadboard (TMC), which is mounted on an optics table with numerous lead-shot filled 80-20 aluminum structures to reduce vibrations. All the relevant optics lie on the top and bottom side of the breadboard and are independent of the lower optics table.

2.1 Vacuum chamber

All of the actual experiment happens in a single glass cell maintained at ultra-high vacuum (UHV, $< 10^{-11}$Torr) conditions. In our experiment, atoms are loaded into optical tweezers directly from a magneto-optical trap (MOT). This relaxes some of the vacuum requirements to achieve bulk quantum degenerate gases, which typically involve multiple chambers and pumping stages. However, since background collision rates scale proportionally to background gas density[85], and equivalently pressure, better vacuum conditions would allow for

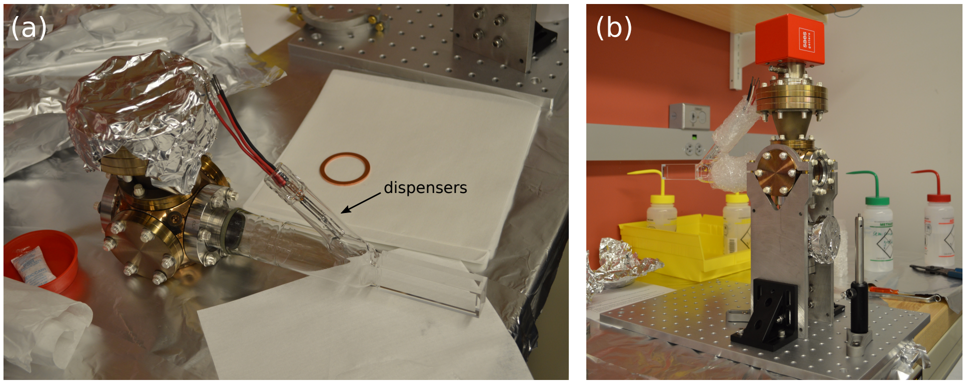

Figure 2.2: Chamber assembly. (a) Close-up of glass chamber and atom dispensers inside the glass tube. (b) Assembled and mounted vacuum chamber.

longer lifetimes and coherence times, which is important for many of our applications. Therefore, careful care was taken to ensure the best UHV conditions possible. In general, the small volume and form factor of the glass cell allows for good optical access, less pumping volume, and a compact apparatus overall.

2.1.1 Glass cell

The glass cell was manufactured by Japan Cell Co. and consists of five 4mm thick non-AR coated glass plates bound together by optical contact. The inner dimensions are 10 mm × 20 mm × 89 mm. The remaining side is connected to a glass blown tube ~1.65″ in diameter, that is then fused onto a 2.75″ ConFlat flange. Another small tube that contains the atom dispensers protrudes from this portion, as shown in Fig. 2.2(a).

The flange is attached to a vacuum spherical cube from Kimball physics (MCF275-SphCube-C6). On the opposite side is an AR-coated vacuum viewport (MPF A8004-1-CF) to allow for optical access from this direction. An ion/getter pump from SAES (NEXTORR D 100-5 with NIOPS-03 controller) is attached to the top for pumping during operation, and the bottom is closed off with a gate valve (VAT 54132-GE02). The remaining two sides of the spherical cube are closed off with blank ConFlat flanges and used to mount the chamber on the breadboard.

2.1.2 Alkali dispensers

The source for our Na and Cs atoms in our experiment is individual linear alkali dispensers that release Na and Cs in atom form when current is run through them. Four linear alkali dispensers (2 for Na and 2 for Cs, all from SAES) along with their electrical connections were sealed into an arm off the glass cell during glass blowing, as shown in Fig. 2.2(a). The wires for the electrical connection are color-coded, with Na red and Cs black; white is common return. When new, their resistances were 0.1 Ohm. During normal operation, Na was operated around 3-4A, while Cs was around 2A. We found that the Na dispensers give off a sufficient amount of Cs atoms for normal operation of the experiment as well. The resistances increased to 0.5 Ohm after operation, likely due to the increased temperature.

2.1.3 Vacuum chamber assembly

Before the assembly of the vacuum chamber, all the parts excluding ion pump, viewport, and glass cell were first cleaned in turn with soap water (Alconox), acetone, isopropanol, ethanol and methanol in turn in an ultrasonic bath. They were then air-baked in an oven at 410°C for four days. After air-baking the parts have a brown finish due to oxidization. During assembly, each part, including all flanges and gaskets, were wiped with acetone and methanol in turn again. All screws were fastened in a star-shaped pattern to evenly distribute the pressure with a torque limiting wrench. A photo of the freshly assembled chamber is shown in Fig. 2.2(a).

Pumping down

The vacuum chamber was first connected to a turbo pump (Agilent Varian TPS-Compact) with the gate valve open for rough pumping at room temperature. This brought the pressure down to 10^{-7} Torr. To achieve the ultra-high vacuum required of the experiment, the vacuum chamber was further baked in an oven to degas any residual gases adsorbed on the surfaces inside the chamber.

The vacuum chamber assembly was placed in a temperature-controlled oven, connected through a gate valve and bellow to the turbo pump (Agilent Varian TPS-Compact) and residual gas analyzer (RGA) (Stanford Research Systems 200amu system). Inside the oven, temperature probes were placed on various parts of the chamber for monitoring. We baked to a maximum temperature of 140°C. This was limited by the magnets in the ion pump, which could stand up to 150°C. In addition, to avoid subjecting the metal-to-glass transition portion of the chamber to large thermal stress, care was taken to maintain a reasonable ramp rate. Outside the oven heat tapes were attached to the bellows to create an additional thermal gradient from the chamber side to the pump. Fig. 2.3 shows the baking setup and temperature ramp curves.

The dispensers were conditioned three separate times while the oven was at high temperature to remove any junk on them. Each time, each of the four dispensers was turned on at 2.5A for ~5 minutes. The pressure typically spiked briefly by an order of magnitude during this time. During the first conditioning, we also took spectra from the RGA before and after the firing of dispensers, shown in the inset of Fig. 2.3(c). Curiously, we did not find any identifying features for Na or Cs. On the third round of conditioning the dispensers, the pressure did not spike again, indicating junk had been eliminated from the dispensers. In addition, the ion pump was flashed in a similar manner for degassing once at high temperature. The

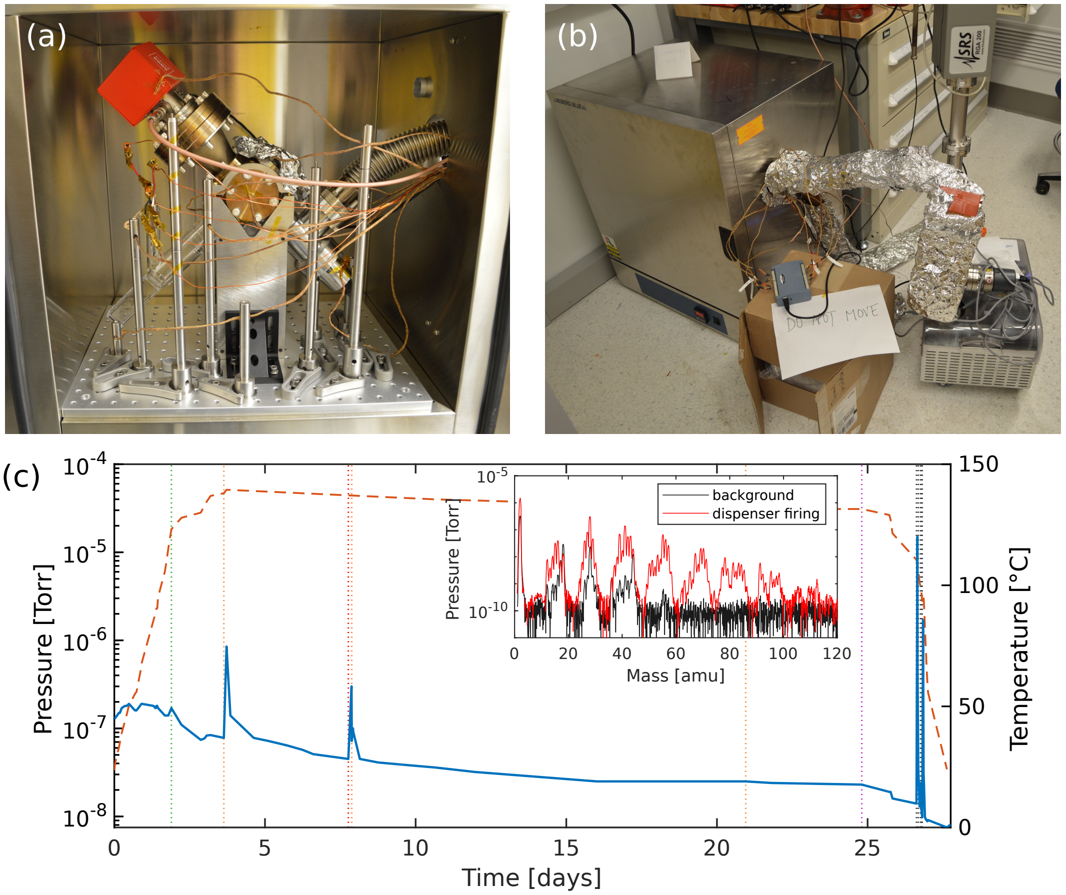

Figure 2.3: Chamber bakeout. (a) and (b) Photos of the baking setup. The chamber and ion/getter pump assembly was placed in an oven and connected via a valve and bellow to a turbo pump outside the oven. (c) Pressure (blue solid line, left axis) and temperature (red dashed line, right axis) curves monitored throughout the bakeout process. Pressure values were read from the turbo pump. Temperature value shown is that of the metal-to-glass interface on the chamber assembly. The temperature values between the different probes were all within 5°C of each other. Inset: RGA mass spectra obtained right before and after firing the dispensers for the first time.

sequence of these steps are detailed in Fig. 2.3(c).

The chamber was cooled down after the pressure had reached equilibrium around ~2×10^{-8} Torr. During cool down, the ion pump was flashed again for degassing, and the non-evaporable getter (NEG) element was conditioned for ~2 hours to remove water and hydrogen physisorbed on the getter surface with the ion pump off. The NEG was then activated after the temperature was below 100°C. Finally, after cooling back down to room temperature, the gate valve was closed, after which the ion pump gauge gave a reading of $< 10^{-11}$ Torr, indicating a pressure value at the gauge location below the detection limit.

2.1.4 Flooding the cell

The dispensers were turned on at a high current of ~4.5A for ~$3 - 4$ hours during the initial run to flood the cell with Na and Cs atoms. We used lasers tuned on resonance to detect the presence of atoms by fluorescence in the cell, as shown for Na in Fig. 2.4(a).

On the initial flooding attempt of Na, a small explosion occurred with the Na dispenser when the dispensers were turned up to ~5A for ~1 minute, causing a small burst of Na to evaporate in a small amount of time and be coated on the tube containing the dispensers (see Fig. 2.4(b)). Fortunately, this did not affect the vacuum conditions, and this particular dispenser has not run out of Na after running for more than four years. Later on, UV light pulses were shined on the Na coated patch in an attempt to desorb the Na atoms using light-induced atom-desoprtion (LIAD) and allow us to run without the dispensers on[86]. In this process, atoms on the walls of the glass chamber are desorbed by the light. The UV light visibly desorbs the Na coating after numerous pulses. In the long run however, UV LIAD did not provide a stable source of Na atoms in the cell and we opted to leave the dispensers constantly on.

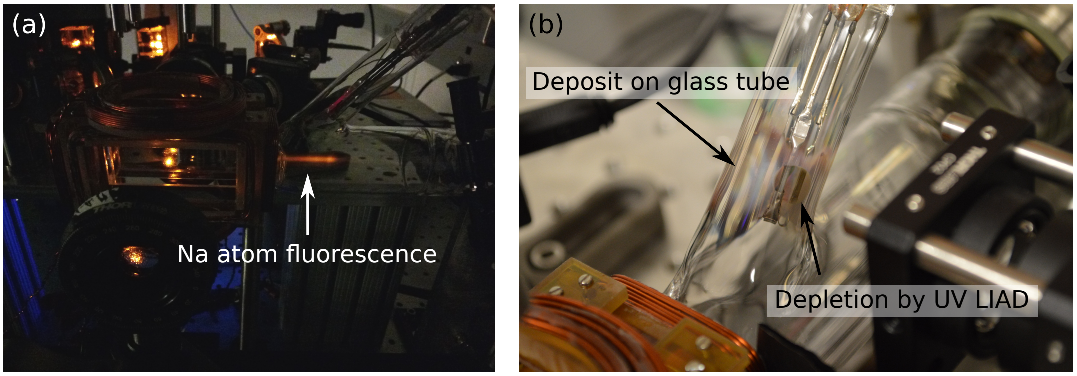

Figure 2.4: Flooding cell with Na. (a) Na atoms are detected by fluorescence from resonant $F = 2 \rightarrow F' = 3$ light. (b) Na evaporation onto glass tube and depletion by UV LIAD.

2.1.5 Vacuum quality

The vacuum quality can be reflected in the lifetime of the single atoms in the chamber. In Sec. 3.2.1 we present a characterization of the single atom lifetimes. In particular, the lifetime of a single Cs trapped in the optical tweezers was initially found to be 80 s. For the lifetime of Cs atoms, we rule out parametric heating from intensity noise on the trap light, and attribute the lifetime to background collisions. This puts an upper limit on the background pressure in our chamber. In the case that the lifetime is limited by background collisions, the lifetime of the single atoms τ is related to the background gas number density by[87]

$$n = \frac{1}{\tau \langle \sigma v \rangle_T} \tag{2.1}$$

where σ is the collisional cross section between the alkali atom and background gas, and v is the relative velocity of the colliding atoms. The expected value is taken over a thermal distribution at room temperature for the background gas. Here, due to the relatively low trap depth ($<$ 1 mK), we estimate the expected value as $\langle \sigma v \rangle_T \approx \sigma \langle v \rangle_T$. From this, we can estimate a

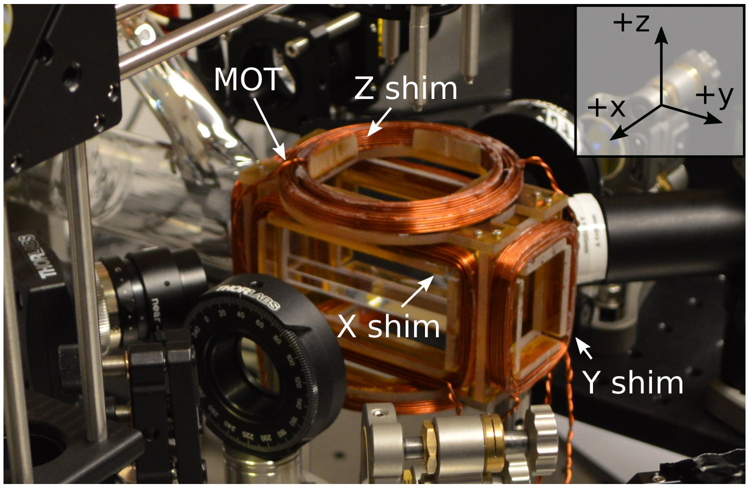

Figure 2.5: Photo of MOT and shim coils and mount. One coil in each pair of coils is labelled. Inset: Axis convention used in the experiment. For reference, the optical tweezer beam propagates in the +x direction.

background pressure by $p = nk_BT$. The value we find is 2×10^{-10} Torr, which is slightly higher than the reading from the ion pump, which is placed away from the glass cell.

We note that the lifetimes we observe are a factor of ~10 longer than that observed in the previous generation apparatus , where the lifetimes were typically a few seconds. We attribute this to the higher level of vacuum achieved with our non-AR coated and optical contacted glass cell. The glass cell in the previous apparatus was AR-coated and epoxied instead (also from Japan Cell); AR-coating precluded the possibility of optical contact bonding with the industry technology at the time of acquirement.

Coil	Shape	Dimensions [in]	Distance [in]	Turns	Magnetic field [G/V]
X shim	Rectangular	H: 1.6, W: 3.12	1.62	33	3.57
Y shim	Rectangular	H: 1.6, W: 1.3	3.81	45	0.85
Z shim	Circular	ID: 1.2	2.36	11	1.0
MOT	Circular	ID: 1.4	2.36	60	7.0 [1/cm]

Table 2.1: MOT and shim coil specifications. Dimensions are given by inner height and width for rectangular shapes and inner diameter for circular. The coils are controlled by separate servos that each drive 0.5A/V.

2.2 Electromagnetic coils

2.2.1 MOT and shim coil

In the apparatus, three pairs of electromagnetic shim coils provide the ability to apply a homogeneous magnetic field in an arbitrary direction at the location of the atoms/molecules, while an additional pair of coils provides the magnetic field gradient necessary to create a magneto-optical trap (MOT). These coils were hand-wound and mounted on a monolithic structure constructed out of Ultem. The shim coils are run in Helmholz configuration, while the MOT coil is in anti-Helmholz configuration. All the coils were wound with AWG #20 wires (Magnet Wire Company) and Krazy Glue. During actual operation however, the Krazy Glue slowly evaporated and the coil was patched up with Huntsman Alraldite 2011 epoxy *in situ*. In addition, the MOT coils tended to heat up (up to 70°C in MOT idle state) in operation, which caused thermal fluctuations of the apparatus depending on the experimental cycle time and experiment idling times. Better heat sinking could be considered in the future. A photo of the coils and mount is shown in Fig. 2.5 along with the axis convention used in the experiment. The geometry specifications and control voltage of the coils are given in Table 2.1. The maximum field magnitude achievable is limited by a combination of the heating of the coils and the maximum current of the power supply; in the y-direction (optical pumping bias field direction) this is ~6G, and in the x-direction (Feshbach field direction) this is ~30G.

2.2.2 Feshbach coil

To reach the high magnetic fields necessary for the Na+Cs Feshbach resonances in the experiment (~870G, see Chapter 4), a separate pair of water-cooled coils in Helmholtz configuration was designed. These coils were designed in a staggered pancake structure to leave sufficient optical access around the objective for the diagonal MOT beams as shown in Fig. 2.6(a). The specifications of the geometry are shown in Fig. 2.6(b).

Hollow magnetic copper square wire ($0.25'' \times 0.25''$) wrapped in Kapton tape (S and W Company) was used and epoxy (Huntsman Alraldite 2011) was applied during the winding process. The mount was made from Ultem due to its lack of Eddy currents, material strength and low thermal expansion. The details of the winding process are included in Appendix D. The coils are mounted to the optical breadboard from below using mounts made from 316 stainless steel. Non magnetic titanium screws were used to prevent magnetic field fluctuations during operation. The coils are cooled with building water, which is maintained at 20°C, and a pressure of 40 PSI. The flow rate during operation is ~12 Gallons/hr.

The pair of coils were wound in mirror images of each other to minimize the effect of imperfections in the winding process causing inhomogeneities of the field. The resulting geometry of the coils is slightly prolated due to the crossing of pancake structures. A simulated field from this geometry by integrating discretized lines using Biot-Savart's law[88] is shown in Fig. 2.6(d). In particular, despite the odd geometry, the homogeneity across 1 mm at the center is expected to be better than .01%. Since the atom arrays are typically within a ~100 μm range, and the width of the Feshbach resonance we use to create Feshbach molecules is ~2 G, this is more than sufficient. The absolute B field value based on current input agrees to theory within ~1%.

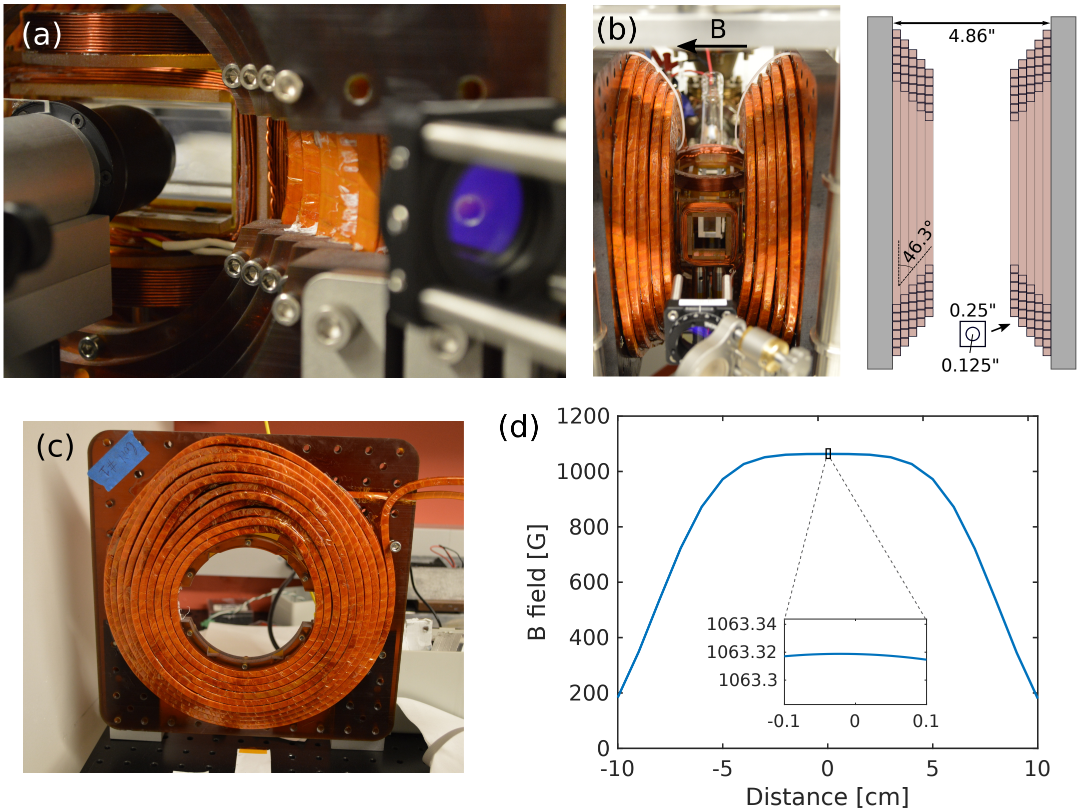

Figure 2.6: Feshbach coil. (a) Image showing optical access of MOT/imaging light around microscope objective. (b) Coil dimensions and magnetic field direction. (c) (d) Simulation of magnetic field x-component cut along the x-axis direction at 400 A current. Inset: Zoomed into ± 1mm from the center. The homogeneity is ~5 mG over 1 mm. The atom array size we expect in the experiment is ~100 um, and therefore expected to be even better over the array.

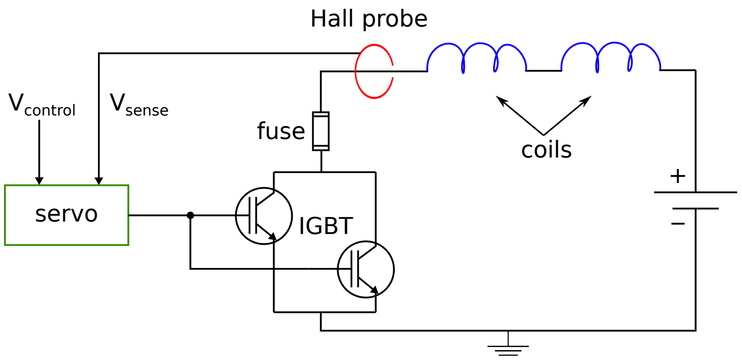

Figure 2.7: Schematic of Feshbach coil control circuit.

Electronics

The coils were powered by a high current power supply (TDK Lambda, GEN 20-500) which provided up to 20 V of voltage and 500 A of current. The current through the coils was measured out-of-loop using a Hall probe (Ultrastab 866-600) and actively stabilized with a PID servo that controlled a pair of insulated-gate bipolar transistor (IGBT) switches. IGBT switches allow for fast switching in high current applications. Two IGBT's were connected in parallel to divide the current to prevent overheating of the IGBT's. In addition, for interlock purposes, a time delay fuse (Littelfuse Mega 150A) was placed in series with the coils. These fuses trip after varying delay times depending on the operating current; at our operating current of ~350 A, the delay time is ~3 s. In practice, we found that the fuse blowing typically caused the IGBT's to die due to large back-EMF's but was nonetheless still useful in preventing overheating the coils.

Field calibration

For the Feshbach resonance spectroscopy data shown in this thesis, a combination of Feshbach field coil and X shim coils were used. The magnetic fields of these coils were calibrated by

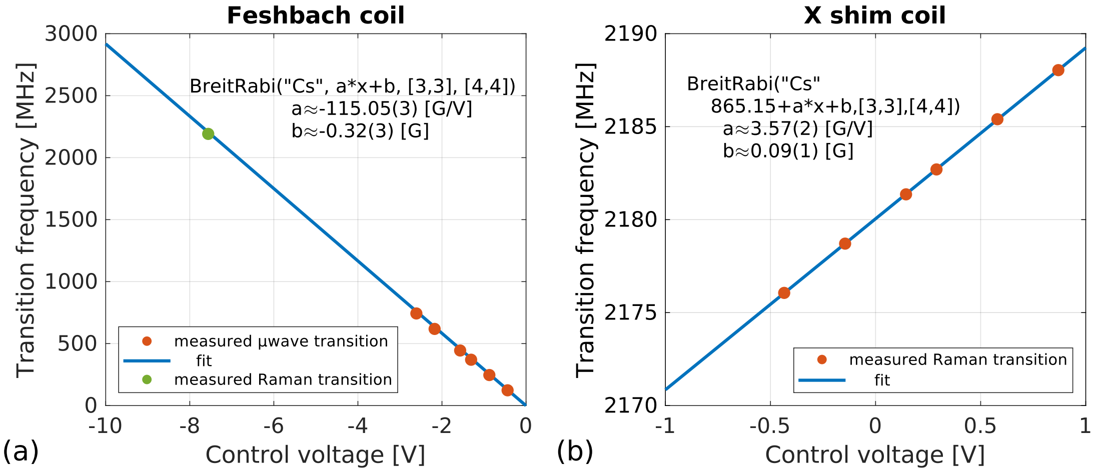

Figure 2.8: Magnetic field calibration (X direction). (a) Feshbach coil calibration. (b) X shim coil calibration. The Zeeman transition frequency $|F = 4, m_F = 4\rangle \rightarrow |F = 3, m_F = 3\rangle$ of Cs atoms is measured using either microwave or optical Raman transition. The fits assume a linear conversion from control voltage to actual magnetic field, and are fit to the Breit-Rabi formula for the expected transition frequencies.

driving the hyperfine transition $|F = 4, m_F = 4\rangle \rightarrow |F = 3, m_F = 3\rangle$ of Cs atoms, either by microwave or optical Raman transition (see section 3.3.2). The transition frequency is measured at multiple control voltage values and fit against the Breit-Rabi formula for Zeeman energy levels[89], as shown in Fig. 2.8. We find a conversion of -115.05(3) G/V for the Feshbach coil and 3.57(2) G/V for the X shim coil.

Eddy current compensation

During operation, we found that ramping the large Feshbach field coils created Eddy currents that caused a slow response ($>$ a few ms) of the actual magnetic field at the location of the atoms. This was despite having used non-metallic mounts wherever possible and cutting slits in cases otherwise. The likely culprits are the casing for the objective, and the shim coils in the x-direction, both of which are concentric with the Feshbach field coils. In order to achieve the faster ramp rates necessary for Feshbach molecule formation (1-10 G/ms), we opted to use the smaller shim coils in the x-direction. Furthermore, we implemented a compensation for the Eddy currents in the control signal following the approach in Ref.[90]. In essence, we ramp the field faster and slightly overshoot to account for the slow response in the presence of Eddy currents. The analytical form of the time varying control signal that gives a linear ramp which compensates for Eddy currents is

$$B(t) = \frac{B_i(t - t_f - \eta\tau) + B_f(-t + t_i + \eta\tau) + e^{-(t-t_i)/(\tau+\eta\tau)}((B_0 - B_i)(t_i - t_f) + \eta\tau(B_i - B_f))}{t_i - t_f} \tag{2.2}$$

t_i, t_f are the initial and final times of the ramp, B_i, B_f are the desired initial and final magnetic field values, and B_0 is the initial actual magnetic field. η and τ are Eddy current coupling constants[90], which we measure in our system to be $\eta \approx 0.4425$ and $\tau \approx -0.2201$ ms.

In Fig. 2.9 we show plots of the measured field with and without the compensation. As in the case of the field calibration, we use the atoms to measure the magnetic field response by driving a Raman transition from $|F = 4, m_F = 4\rangle$ to $|F = 3, m_F = 3\rangle$ on Cs atoms. This compensation ramp allowed us to achieve ramp rates up to 20 G/ms using the shim coils.

2.3 Laser systems

Some of the laser systems were shared between the two apparatuses. For completeness, details on all the lasers relevant to work completed in the present thesis are provided here.

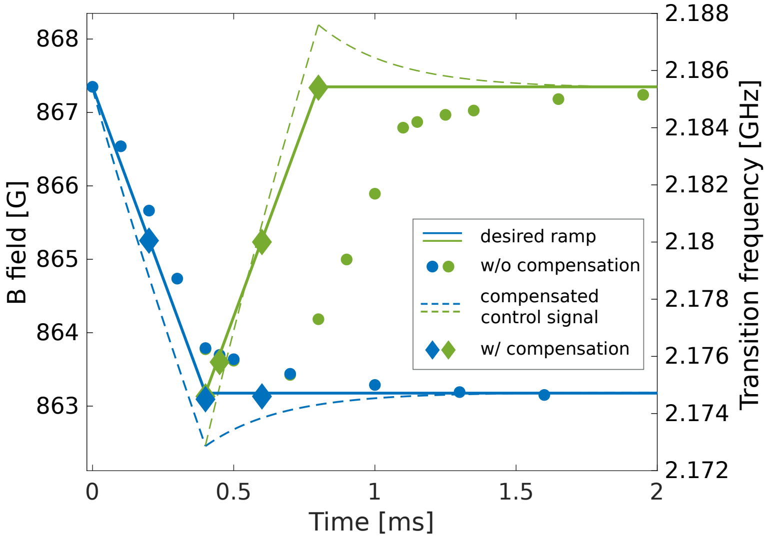

Figure 2.9: Compensation of Eddy currents. Eddy currents are compensated by driving the control signal faster and overshooting the desired value compared to that actually desired. The solid lines indicate the desired ramps. The circle data points show the actual magnetic field at various time points if ramped merely following the desired solid line. The dashed lines show the compensated magnetic field ramps, and the diamond points show the resulting magnetic field with these compensated ramps. The diamond points follow the solid curves as desired.

2.3.1 Na

MOT/imaging and optical pumping lasers

The MOT/imaging light for Na is produced by a commercial ECDL (Time-base, EC-QDL 1178nm) seeded into a Raman fiber amplifier giving up to 2W at 589nm (MPB Communications, VRFA-P-2000-589-SF) and is locked to the crossover peak $F = 1 \rightarrow F' = 1/F' = 2$. The beam is split into two paths and double-passed up and down respectively by 365×2 MHz and 382×2 MHz using AOM's to provide the F1 and F2 light respectively. These AOM's do not have a large tuning range, so a separate double-pass ~120 MHz is placed in the F2 beam path to provide frequency tunability of the F2 light. The F1 and F2 light are then combined and sent through a switching AOM before being fiber coupled to experiment. This light needs to be AC switched at ~few MHz level for Na loading and imaging (see section 3.2). The switching is achieved by focusing the beam into an AOM to provide faster rise times (see Fig. 2.11).

Light from the 0-th order of the switching AOM was picked-off to provide repump F1 light and resonant F2 light for optical pumping and pushout state detection. A separate F2 laser locked to the D1 line of Na is used for D1 optical pumping (see section 3.3.2). This is also frequency doubled from an ECDL (Time-base, EC-QDL 1178nm) with a second harmonic generation crystal (NTT electronics, WH-0589-000-A-B-C 589NM SHG). The laser is locked to the $F = 2 \rightarrow F' = 1/2$ crossover peak in the D1 manifold. This beam is then fiber-coupled and combined with the D2 F1/F2 light in free space again, before being fiber-coupled again to the experiment.

(a) MOT/imaging & OP

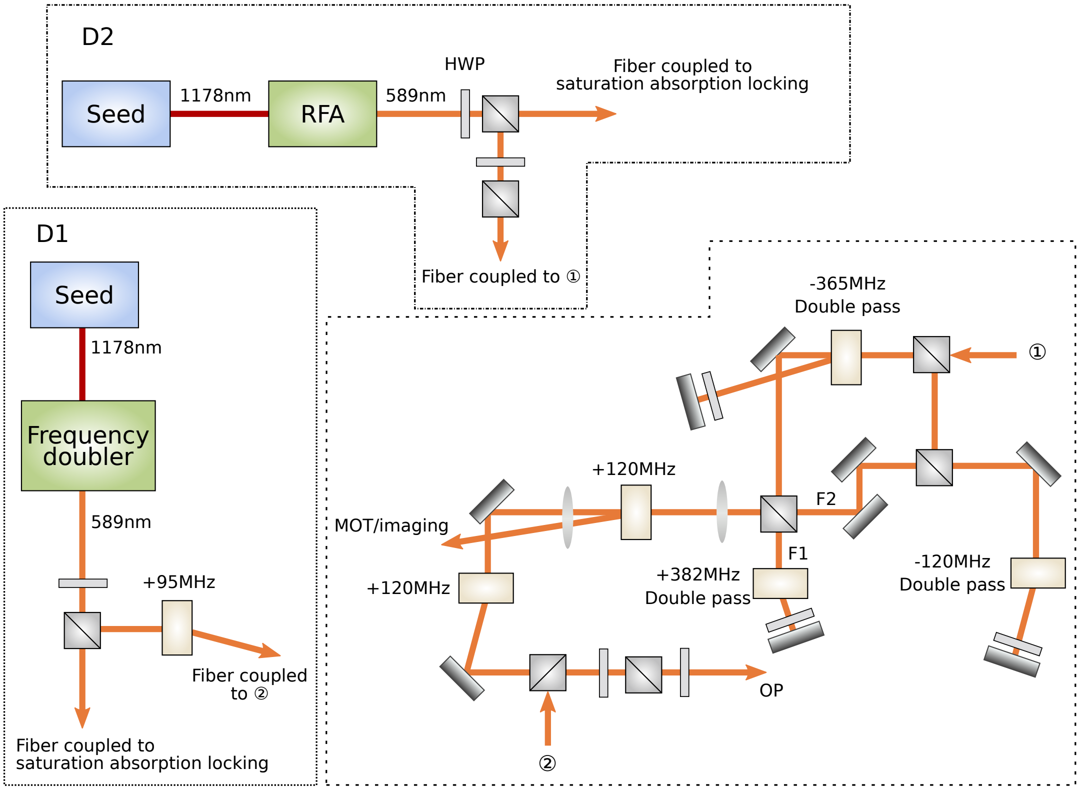

(b) Raman

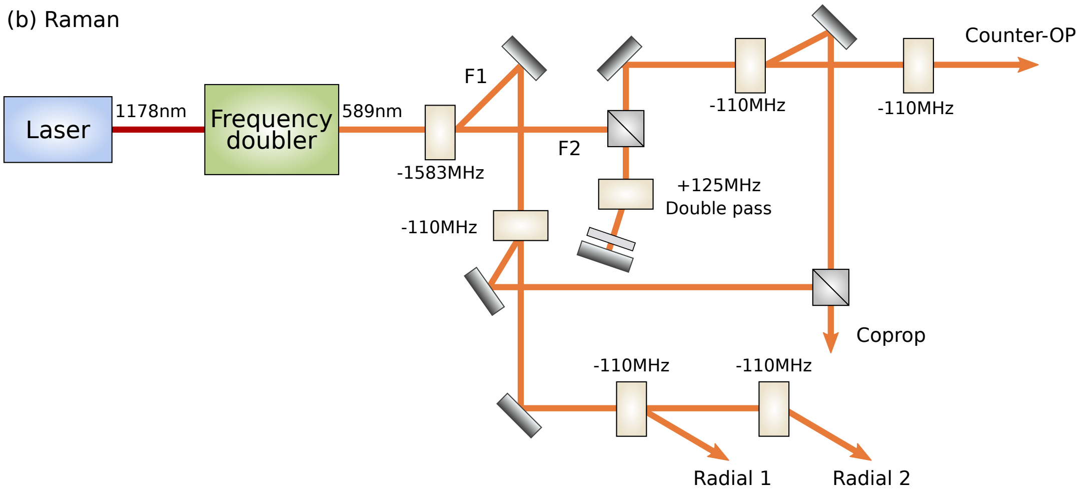

Figure 2.10: Na laser systems schematic.

Raman sideband cooling

The Raman sideband cooling laser system consists of F1 and F2 light with single-photon detuning ~20 GHz, and two-photon detuning on resonance with the Raman transition at the particular fields. To produce the required frequencies, a commercial 1178nm external-cavity quantum dot laser (Time-base, ECQDL-200F) is frequency doubled using a second-harmonic generation crystal (NTT electronics, WH-0589-000-A-B-C 589NM SHG). This produces light at the desired 589 nm, single-photon detuning 20 GHz. An AOM (Brimrose, TEF-1583-100-589-OW) is used to shift one beam by ~1.7 GHz provide the hyperfine splitting. To achieve maximal efficiency on the AOM, the beam is focused into the aperture to the recommended size, and steered as close as possible to the transducer. An additional double-pass in the F1 beam path provided tunability in the two-photon detuning. F1 was used for radial 1 and radial 2, F2 was used for counter-OP, and F1/F2 were combined on a PBS to provide the co-propagating beam.

Tweezer

The laser source for the Na tweezer was a Ti:Sapph (M2, SolsTiS-SRX-XF), pumped by a 532nm seed (Lighthouse, 10W Sprout). The Ti:Sapph was tuned to the lowest possible wavelength 700nm to be as close as possible to the Na D2 line for higher trap depths. The trapping light needed to be modulated with a square pulse with duty cycle ~30% at 2.5MHz and out-of-phase with the D2 MOT/imaging light to eliminate light shifts which caused it to be off-resonant. To achieve the fast rise times necessary for the switching, the laser beam was focused into an AOM. We picked off the 0-th order light from the AOM that the 1.0 apparatus was using, and used the down-time of the switching signal by synchronizing our respective switching signals. This allowed us to effectively recycle unused light in their switching cycle.

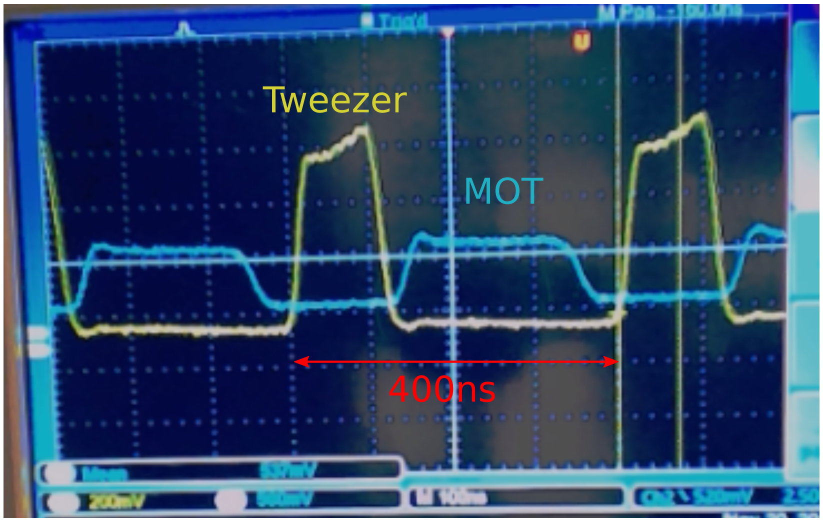

Figure 2.11: AC switching of Na MOT/imaging light and tweezer light. The optical tweezer light and MOT/imaging light for Na are switched in square pulses at 2.5 MHz to eliminate light shifts from the optical tweezer during loading and imaging. The duty cycle for the tweezer (MOT/imaging) is ~30% (~50%).

A scope trace of the AC switching is shown in Fig. 2.11. The power at the experiment was stabilized by a PID servo by feeding back on a low pass filtered photodiode signal picked off in the beam path on the table.

2.3.2 Cs

MOT/imaging and optical pumping lasers

The MOT/imaging lasers and optical pumping (OP) laser for Cs are derived from the same set of distributed Bragg reflection (DBR) diodes (Photodigm, PH852DBR240TS). The master laser is saturation-absorption locked to the $F = 3 \to F' = 3/F' = 4$ crossover peak with a Cs vapor cell and shifted blue in frequency with further AOM's to produce the repump transition light (F3) on resonant with $F = 3 \to F' = 4$. The minion laser was beat locked around

(a) MOT/imaging

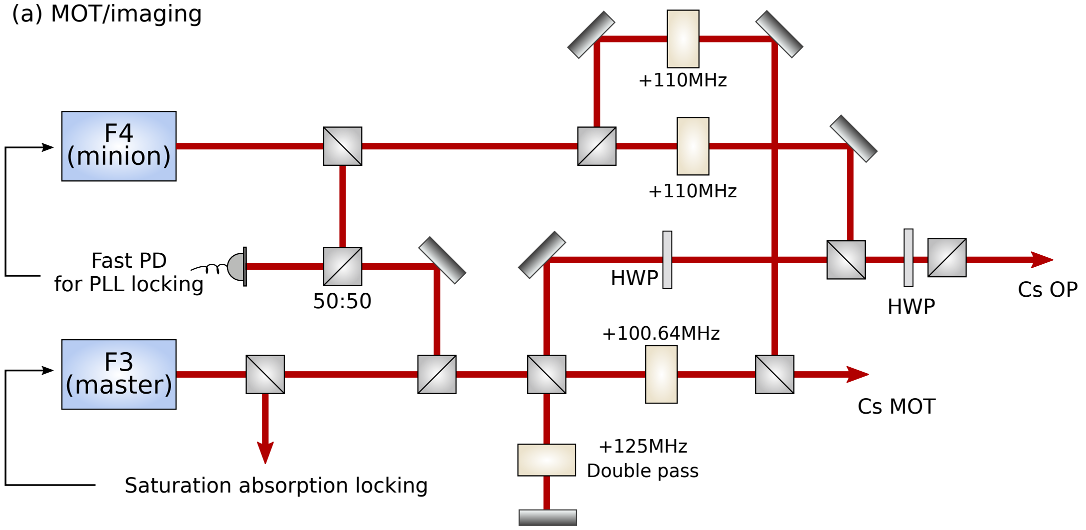

(b) Raman

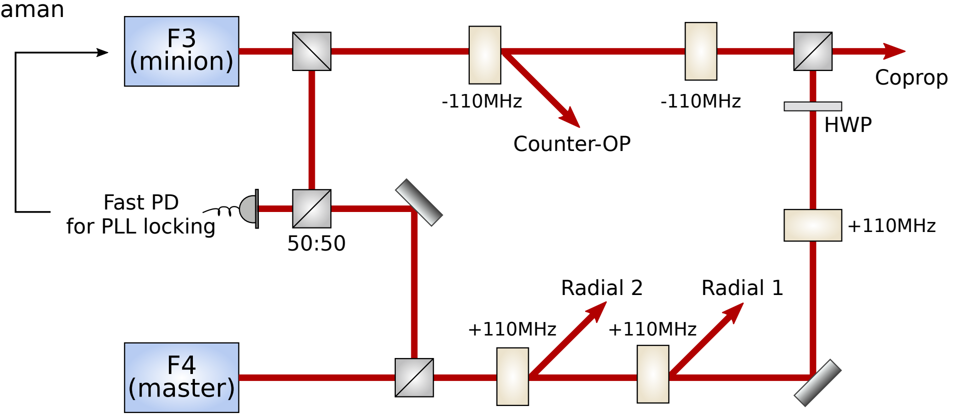

Figure 2.12: Cs laser systems schematic.

8.9 GHz to the master using a fast photodiode (Electro-optics technology, ET-4000) and PLL board (Analog Devices, ADF4159). The exact frequency of the beat lock could be modified in the sequence by changing the reference frequence of the PLL board with a DDS channel, which allowed tuning of F4 frequency.

A small amount of power was picked off from the F3 and F4 light with PBS's for the optical pumping beam path. The frequencies for the optical pumping beam needed to be further shifted with a double-passed AOM to account for the trap depth and magnetic field at which OP is performed.

Raman sideband cooling

The Cs Raman sideband cooling laser system consists of two lasers addressing the F3 and F4 transitions respectively, with a single-photon detuning of ~40 GHz. Compared to the MOT/imaging light, the phase locking requirements for the Raman beams are more stringent, so we opted for external-cavity diode lasers. The master laser (F4) is a home-built cat-eye design with a diode (Eagleyard, EYP-RWE-0860-06010-1500-SOT02-0000) that is detuned ~40 GHz and left free-running. While this design provides good free-running stability, the mode-hop free tuning range is only ~200 MHz, which is not enough for locking as a minion laser. We therefore use a home-built ECDL laser in the Litthrow configuration for the minion laser (F3). The optical signal is beat with the F4 laser on a fast photodiode (Electro-optics technology ET-4000). The phase-lock loop (PLL) board (Analog Devices, ADF4159) provides an error signal, which is then used to lock the laser with a home-built PID servo board for slow integral locking, and a variable gain amplifier (VGA) circuit for direct fast proportional gain. Fig. 2.13(a) shows a schematic of the locking circuit and (b) shows a specturm analyzer trace of the coherence peak with the lock on. The peak is signal ~50-60 dB above background. In practice we found that eliminating undesired optical feedback to the diode was

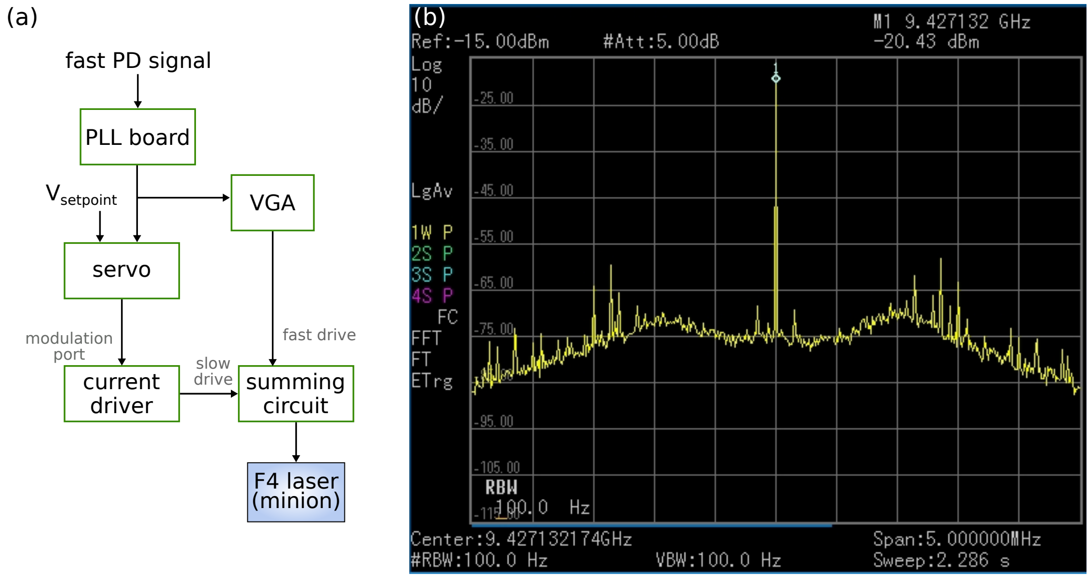

Figure 2.13: Cs Raman laser. (a) Schematic of locking circuit. The signal from the fast photodiode is input to the phase-lock loop board which provides an error signal that fluctuates between 0 and 15 V and is nominally 7.5 V when locked. The error signal is split and sent to a PID servo for slow locking and a variable gain amplifier for fast locking. The setpoint for the PID servo is fixed at the locked voltage, which happens to be 1.5 V. The output of the servo is sent to the moldulation port of the current driver. The fast and slow locking signals are combined and sent to the laser diode. (b) Coherence peak of the lasers. The beat note signal is picked off from the fast photodiode signal that also provides the input to the PLL board. The coherence peak signal is ~50 dB above background.

crucial to obtaining a stable lock. Similar to the MOT/imaging lasers, the exact two-photon detuning was set in the computer control sequence which changes the reference frequency for the PLL locking. F4 light provides the radial 1 and radial 2 beams, while F3 provides the counter-OP beam, and F3/F4 are combined in one fiber for the co-propagating Raman beam.

Tweezer

The laser used to trap Cs single atoms is at 1064 nm, a wavelength for which convenient high power sources are widely available (Coherent, Mephisto 50W laser). This laser is also used for the trapping of atom pairs and molecules. We coupled up to ~3 W output power with ~5 W input using a single-mode patch cable (Thorlabs, P3-1064PM-FC-10), beyond which the coupling efficiency saturated due to spontaneous Brillouin scattering. The power is stabilized by a home built servo by picking off the beam in the tweezer beam path on the apparatus side (see section 2.5.1).

2.3.3 Molecule Raman transfer lasers

The molecule Raman transfer lasers (see Chapter 5) are at 922nm and 635nm for the pump and Stokes transitions respectively. The 635nm light is produced by a commercial ECDL unit (Toptica Photonics DL Pro). The 922nm was a home built external-cavity laser with diode (Eagleyard, EYP-RWE-0920-04010-1500-SOT02-0000). This was injected into a tapered amplifier (Moglabs, 920TA2000) to achieve higher power for the up-leg transition. These were individually frequency locked to a ultra-low-expansion cavity (Stable Laser Systems) by the Pound-Drever-Hall (PDH) technique[91]. The optical cavity has a finesse of ~5×104 at 922 nm, inferred from the cavity ring-down time. By selectively integrating the power spectral density of the error signal of the locked lasers[92], we estimate that the linewidths of the locked pump and Stokes lasers are approximately 2 and 4 kHz, respectively. A schematic of the laser setup is shown in Fig. 2.14. The locking frequency of the lasers is changed by tuning the PDH locking frequency. For the Stokes beam, we also use the switching AOM to scan the frequency in the experiment over a ~1MHz range.

2.4 Microwave systems

For various diagnostic purposes in the experiment, microwave systems were also set up for Na and Cs.

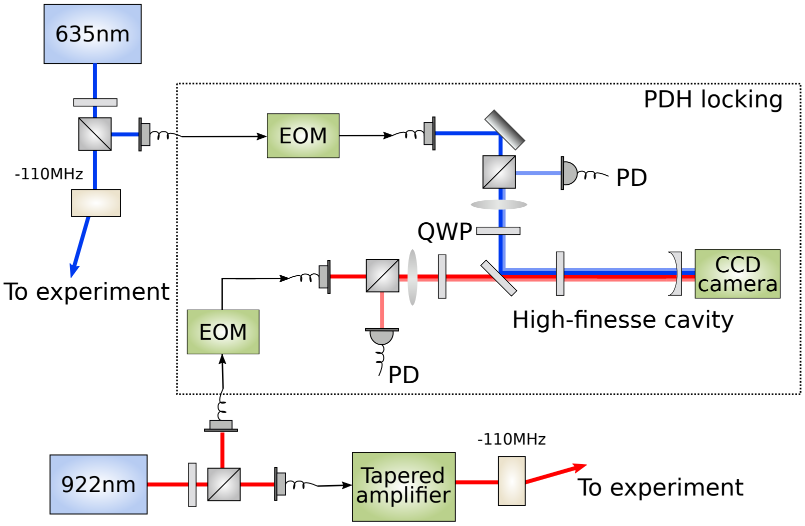

Figure 2.14: Molecule Raman transfer lasers schematic.

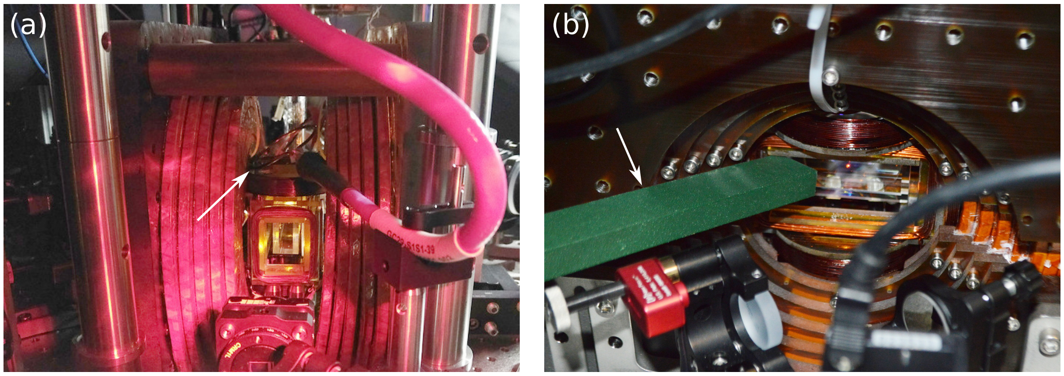

Figure 2.15: Atom hyperfine transition microwave antennae in the apparatus. (a) Loop antenna for Na. Polarization is nominally linear in the vertical direction. (b) Waveguide for Cs. The dominant polarization for H is linear in the horizontal direction.

Na

The hyperfine transition for Na is ~1.771 GHz. The signal was generated by mixing a DDS signal controlled by the FPGA control system at 400 MHz with an RF synthesizer (Valon Technology 5009) at 1.37GHz, and amplified with an amplifier from RF Lambda (RFLUPA0830GK). We tested both a horn and a homemade loop antenna to send the signal to the atoms. Ultimately, for optical access constraints, we opted for a homemade loop antenna made from magnetic wire placed close to the cell. The circumference of the loop antenna was chosen to be the wavelength of the desired microwave signal, which corresponded to a diameter of 5.4cm. In addition, the angle of the loop was oriented to minimize the impedance at the desired frequency due to coupling with the environment. We noticed however, that there were issues putting π-polarization with the magnetic field in the x-direction into the chamber. We attributed this to shielding effects from coils around the chamber.

Cs

The hyperfine transition for Cs is ~9.192 GHz. This was generated by frequency doubling a DDS signal at ~300MHz three times. The signal was amplified using (Xorvo QPA1011 evaluation board). We placed a waveguide with an adapter to coaxial connector (RFWA90A9COAL) that pointed towards the atoms. With this, we achieved Rabi frequencies of up to 200 MHz, which we used for various magnetic field calibration purposes, among others.

2.5 Optical layout

The optical layout on the apparatus side went through many iterations. Here we show the beampath that was used for the majority of results in the first half of the present thesis, which allowed for a single Na atom and an array of Cs atoms. In Chapter 6 we show upgrades to this beampath to expand the capability to optical tweezers arrays of dual species atoms and rovibrational ground state molecules.

The main beams we send into the chamber are shown schematically in Fig. 2.16 and consist of

- *Na/Cs MOT/imaging beams.* The two wavelengths (including Na F1/F2 and Cs F3/F4 light) are combined by a dichroic. Two pairs of counter-propagating beams form the horizontal trapping beams, while a single beam is retro-reflected to produce the vertical beam. See section 3.1.
- *Raman sideband cooling beams.* There are four beams in total that allow us to address the 3 motional axes (two radial and one axial) of the atoms in the optical tweezers, as well as a motion-insensitive carrier transition. The beams for Na and Cs are combined by dichroics in each path and focused down to ~100s of μm at the location of the atoms. See section 3.3.1.
- *Na/Cs optical pumping beams.* These are sent in with circular polarization and colinear with the OP magnetic field to provide $\sigma\pm$ polarization. Glan-Taylor polarizers were used to produce clean polarizations. See section 3.3.1.
- *Molecular Raman transfer beam.* This is sent counter-propagating with the tweezer from the other side of the chamber. The two wavelengths (922 nm and 635 nm) are combined with a dichroic. The beam is focused to a spot size of ~10 μm at the location of the atoms. See section 5.2.
- *Optical tweezer beams.* See next section (2.5.1).

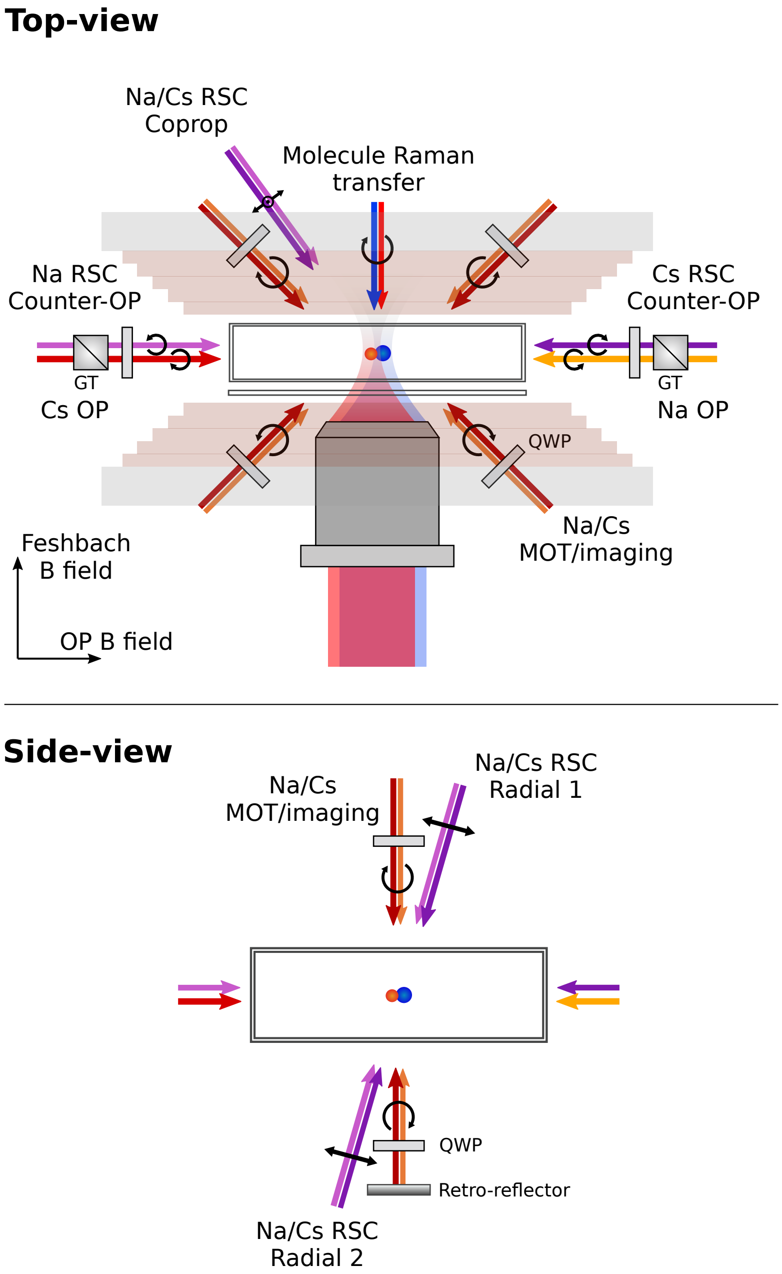

Figure 2.16: Apparatus side beam path schematic.

2.5.1 Optical tweezers

The optical tweezer beams on the apparatus side are formed by focusing large beams through a high-NA microscope objective. The two beams (700 nm and 1064 nm, see section 2.3) are launched independently with triplet collimators (Thorlabs TC12APC-633 and TC12APC-1064 respectively) that give Gaussian beams 2.2 mm and 2.7 mm in diameter. For both 700nm and 1064nm beam paths, the telescopes lens focal lengths were chosen to be $f_1 = 75$mm and $f_2 = 500$mm. These telescope magnifications gave beam diameters measured by a knife-edge of 16.5 mm and 16.8 mm going into the objective respectively, which nominally give diffraction limited spot sizes.

We use an acoustic-optical beam-deflector (AOBD) in the 1064 nm beam path to steer the optical tweezers, and to generate arrays of multiple tweezer beams. The range of deflection for AOBD's is larger in AOBD's compared to typical AOM's and the beams can be steered by changing the RF frequency input to the AOBD. Furthermore, by sending in multiple RF tones at once, multiple deflections can be created simultaneously to produce an array of beams. For the inelastic Feshbach spectroscopy shown in this thesis the AOBD was a 2-axis AOBD from IntraAction (A2D-603AHF3.900), using only a single axis operating between 64-106 MHz. In the later work presented in this thesis the AOBD was a single axis water-cooled AOBD (IntraAction ATD-1403DA2W) operating between 105-175 MHz, which we found to be advantageous for its thermal stability. In addition, RF beating problems rendered using the two axes of the 2-axis AOBD simultaneously impractical.

The AOBD beam path is aligned in a 4f-configuration – the AOBD lies at the focus of the first lens of the telescope (f_1), while the distance from the second lens to the objective is $f_2 + f_{\mathrm{obj}}$. This ensures that angular deflection from the AOBD corresponds to translational movement of the optical tweezer beam at the atoms. The AOBD alters the polarization of the

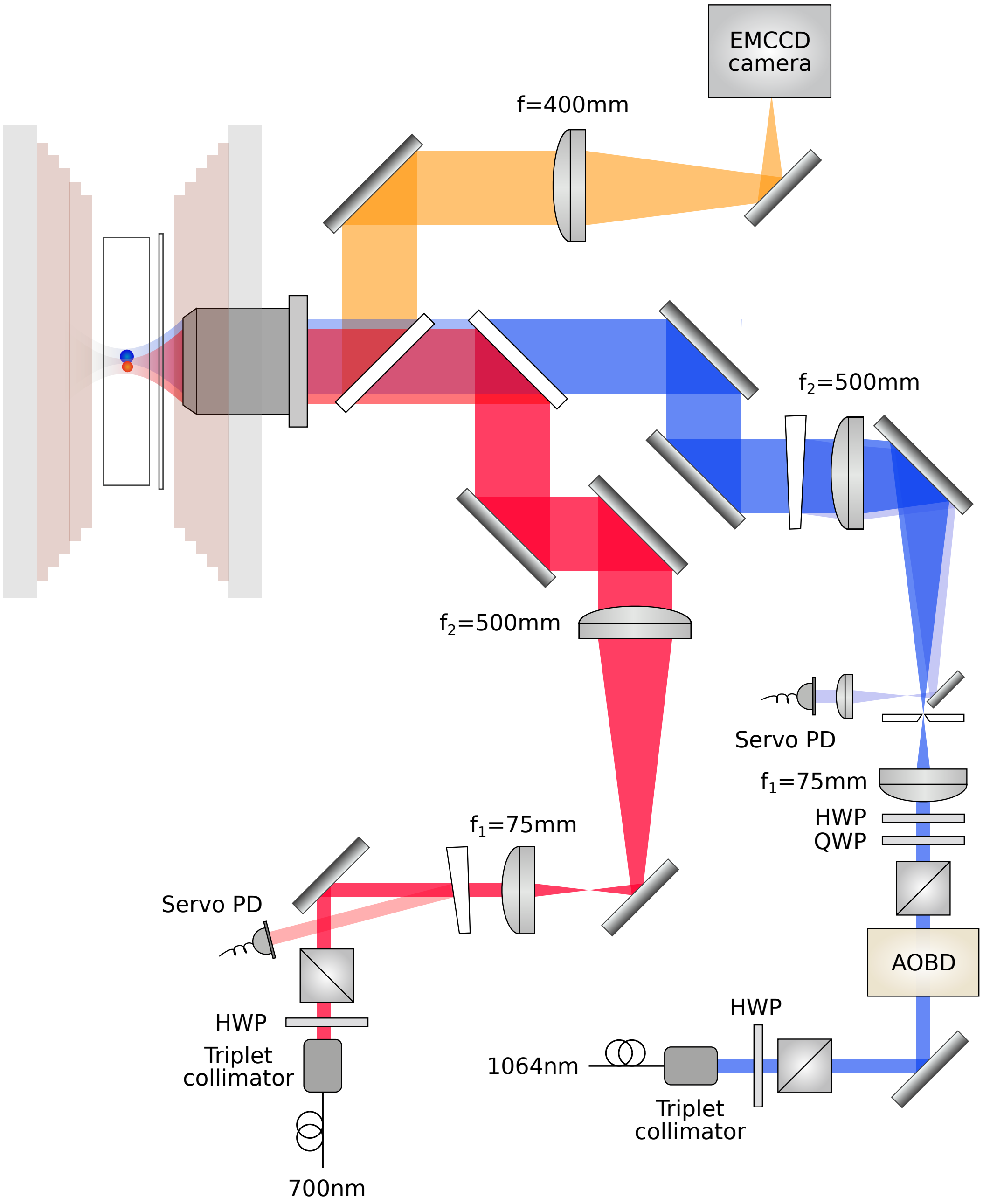

Figure 2.17: Tweezer beam path schematic. Red (blue) beam in the figure corresponds to the Na (Cs) tweezer beams at 700nm (1064nm). Orange is fluorescence from the atoms that is imaged on the EMCCD camera.

beam. Therefore after the AOBD, the polarization is cleaned up with a polarizing beam splitter. In addition, to account for the difference in effective magnetic field of Cs with respect to Na, we placed a quarter waveplate and a half waveplate to allow for polarization control before the tweezer (see section 3.3.1).

To servo after the AOBD, a wedge was placed after the telescope, the reflection of which focuses back through the second telescope lens and gets picked off for monitoring and feedback purposes. This allows us to servo the total power of the AOBD, even in the case of multiple tones, as will be relevant for arrays. This also provided a beam path to image and characterize beams in an array. For the 700 nm beam path, the beam is simply picked-off before the first lens of the telescope.

The separate beams tweezer beams were combined with a dichroic before the objective. We found that the combining dichroic, when poor in flatness quality or fastened too tightly in its mount, caused significant aberrations in the tweezer beam. The one used in the majority of this thesis was from Semrock (Di03-R785-t3-25x36) and performed well.

For imaging, fluorescence from the atoms is collected back through the objective, which is reflected by the imaging dichroic (CVI optics, DS 852/589-T650) and imaged on an EMCCD camera (Andor iXon Ultra 897) by an imaging lens. The EMCCD camera has the ability to collect single photons which we can use to resolve single atoms.

Microscope objective

The microscope objective is custom designed from JenOptiks. The objective corrects for 6 mm of glass and has an effective focal length of 18 mm and working distance of 16 mm. The design was intended to correct for 4 mm of the glass chamber and 2 mm ITO coated glass plates for producing electric fields. In the present apparatus however, we opted not to install electric field plates, so we placed a single 2 mm thick glass plate (Edmund optics #36-946, 400-1000 nm AR-coated, $\lambda/10$ flatness) on the objective side to account for the correction for the objective.

We characterizied the objective using a white light interferometer[83]. In this setup, a collimated white light source is sent through the objective and retro-reflected off a metallic ball bearing and interfered with a beam retro-reflected off a reference flat. By measuring the interference pattern on a beam profiler, we can obtain information on the variation of phase across the wavefront of the beam. A white light source with a short coherence length is neccessary to not have interference with other surfaces in the beam path as well. To characterize the aberrations present which lead to non-uniform wavefronts, we fit the wavefront to a combination of Zernike polynomials[93]. This allowed us to calibrate the tilt of the objective as shown in Fig. 2.18. This was later fine-tuned on the atoms again by maximizing the trapping frequencies (which also tended to lower the ratio between radial and axial directions closer to the theoretical value).

The alignment of the tweezer beampath is highly sensitive to aberrations. Therefore in the alignment process, care was taken to center the beam and pointing perpendicular to all the optical elements. All beams were referenced to the glass chamber. The glass plate and objective were then aligned to the glass chamber by overlapping the retro-reflection off the respective surfaces to ensure they are perpendicular to the input beam as well.

Characterizing tweezer beam shape

As another check for aberrations, the tweezer beam before the objective is picked off and focused down with a long focal length lens ($f = 1000$ mm) and imaged along z near the focus. A long focal length lens ensures minimal aberrations from the alignment of the imaging beam path itself. In the 1.0 generation apparatus, a cylindrical lens was required to correct for astigmatism at the location of the atoms[83]. In the present apparatus, a careful selection of dichroics

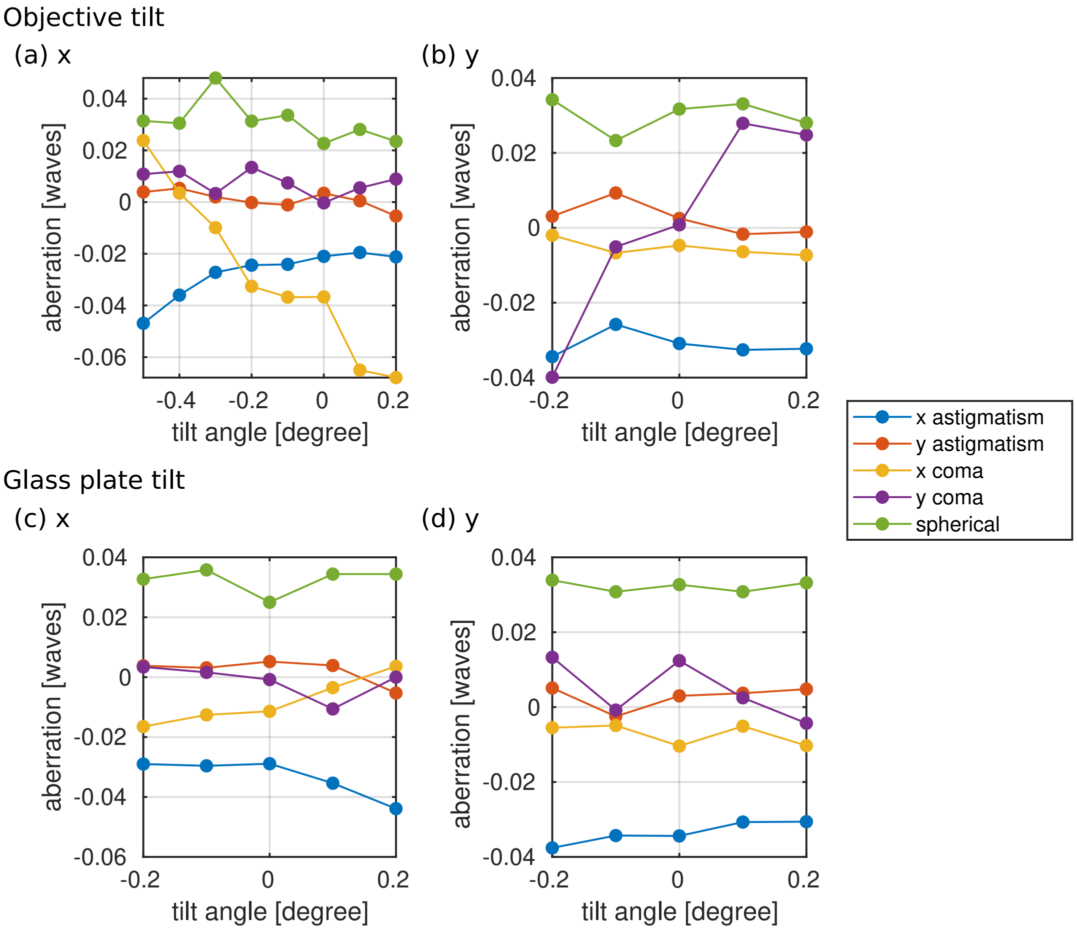

Figure 2.18: Aberration characterization of microscope objective using white light interferometer. Aberration dependence on the (a-b) objective and (c-d) glass plate x and y-tilt angles respectively. Aberrations are characterized by the Zernike polynomial coefficient and expressed in units of waves. We observe a large effect on the coma when the objective tilt is mis-aligned.

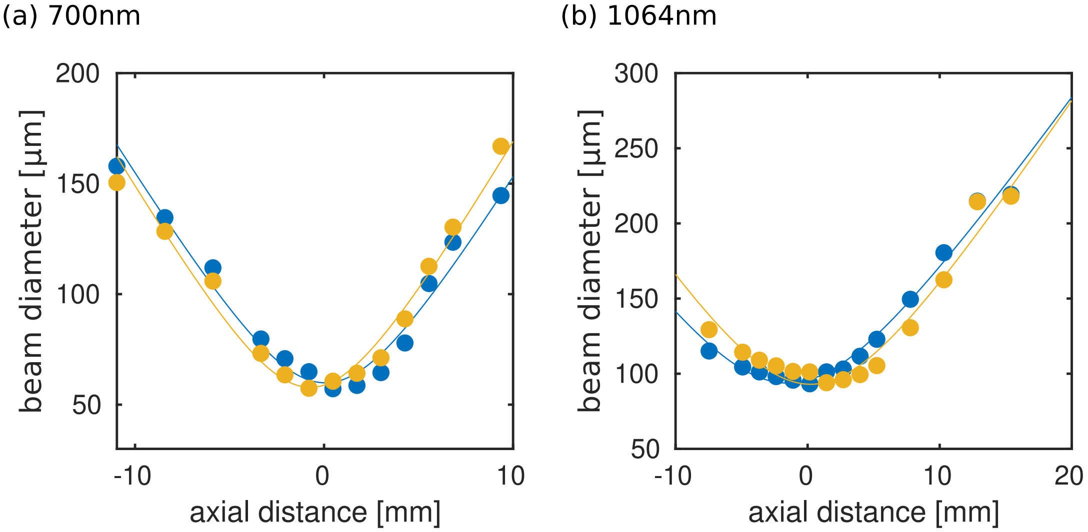

Figure 2.19: Tweezer beam shape characterization. The tweezer beams are focused down by a lens with $f = 1000$ mm and imaged at various locations near the focal point on a beam profiler. The difference in axial direction of the focii position give an indication of astigmatism, which can affect the single atom trapping and cooling performance.

and alignment of optical elements was sufficient to produce a non-astigmatic beam for both wavelengths.

Calibrating pixel size

The pixel size on the EMCCD camera relative to the actual distance at the location of the atoms in the optical tweezers was calibrated using the AOBD deflection angle and the known magnifications of the telescope and imaging systems. In particular, the angular deviation of the AOBD is given by[94]

$$\Delta\theta = \lambda \Delta f / v_{\text{acoustic}} \tag{2.3}$$

where λ is the wavelength of the laser, Δf is the input frequency shift, and v_{acoustic} is the acoustic velocity of the crystal (4.26mm/µs in this case). This angular deviation corresponds to a translational distance of

$$d = \Delta\theta \times \frac{f_2}{f_1} \times f_{\text{objective}} \tag{2.4}$$

at the focus of the objective. By comparing the pixel difference on the camera, we find a distance conversion of 0.712 µm/pixel.

3

Preparing single Na+Cs atoms

The coherent creation of a rovibrational NaCs molecule in optical tweezers requires a single pair of Na and Cs atoms, each in specific states, co-trapped in the same optical tweezer. In particular, as we will see, much of our control over the resulting molecules we create relies on our fine control over the constituent atoms before molecule formation. As such, our ability to control all the internal and external states of the atoms is crucial.

This chapter describes the main steps in the experimental sequence prior to molecule formation, including dual species MOT loading, single atom loading, motional and hyperfine state preparation, and adiabatic merging of traps. These are steps #1-3 in Fig. 1.1. Much of this work was built upon previous work completed in our lab on the 1.0 version of the apparatus[83,84]. Here we will mainly focus on the lessons learned and improvements along the way in the present apparatus. This chapter focuses on a single pair of atoms, which enabled the experiments in Chapters 4-5 of this thesis. Chapter 6 will discuss how this was scaled up to incorporate multiple atoms to form arrays of molecules and additional problems we encountered on the way.

3.1 Dual-species magneto-optical trap

The starting point of our experiment is a dual species – Na and Cs – magneto-optical trap (MOT). Due to the compact size of the glass chamber and optical clearance constraints, we were limited to small MOT beams (diameters for Na 5mm and Cs 5.5mm). This placed challenges on aligning the beams to the center of the MOT coils and center of objective, especially for Na due to its lighter mass. In addition, to clear the sides of the objective, the incidence angle of the MOT beams need to be larger than 45 degrees (see Fig. 2.16), close to the Brewster's angle. This causes significant power loss on transmission, and affects the polarization purity of the beam at the location of the atoms. This effect is further enhanced by the cell being non-AR coated, compared with the previous generation apparatus. As we will discuss in the next section, the loading of single atoms was highly sensitive to the performance of polarization gradient cooling, which is in turn highly sensitive to the alignment polarization purity. We found the following were crucial to obtaining stable MOT's and good polarization gradient cooling for both species:

- In the previous generation, 3 beams were retro-reflected to produce the 6-beam MOT configuration. In the horizontal direction, to account for the power loss on transmission through the glass cell, a cat-eye was placed in the retro-reflected beam to slightly focus the retro-reflected beam to balance the beam intensities. In the present apparatus however, we found it better to send separate beams and not retro-reflect the beams in the horizontal direction. With the same amount of total power (a couple of mW each for Na and Cs respectively), this gives less power in each beam, but resulted in a more stable MOT. The beam path is shown in Fig. 2.16. The beam power ratios are 1:2 for the vertical vs. horizontal beams to account for the stronger confinement from the magnetic field gradient in the vertical direction.

- The relative alignment of the beams for the three axes at the location of the trap is important to creating a stable MOT. As discussed in section 2.5.1, there is a glass plate on the objective side of the chamber. This causes asymmetric refraction on the two sides of the chamber. To align the beams, jigs were 3D-printed that account for this uneven refraction of the beam through the glass cell and additional glass plate on the objective side.

- As mentioned above, the glass chamber is non-AR coated. While this typically leads to less phase retardation, the difference in transmission for s- and p-polarization components causes changes to the polarization of the MOT/imaging beams. This is exacerbated by the incidence angle being close to the Brewster's angle. To account for this, the effects of the glass chamber and glass plate on the polarization were characterized using a polarimeter, by sending in linear polarized light and measuring the polarization after the elements. The change in polarization was compensated for by a combination of quarter and half-wave plates before the glass chamber to produce good circular polarization for each of the beams at the location of the atoms.

- It was found that the choice of glass plate was crucial for the quality of polarization gradient cooling. In particular, a good AR-coating was necessary. In addition, there are requirements on surface flatness to minimize aberrations on the tweezer beams. The glass plate that was ultimately used is from Edmund optics part #36-946, which is 2” in diameter and AR-coated over 400-1000 nm, with a surface flatness of $\lambda/10$.

- As in the previous 1.0 generation, we dithered the beams using piezos (Thorlabs AE0203D04F) wedged in the mirror mounts (Newport Suprema SU100-F2K) at an amplitude of ~2 µm at ~1 kHz, which dithers the beam on the order of a wavelength at the atoms. This reduces interference effects causing nodes in the MOT .

- Overlapping the dual species MOT’s – typically, Na is more sensitive to beam alignment for its lighter mass, while Cs is relatively more sensitive to the shim field * Therefore, the MOT’s were overlapped by an iterative procedure of beam alignment to shift the Na MOT and magnetic field shimming to shift the Cs MOT. Ultimately, the two MOT’s were able to be overlapped to achieve simultaneous loading of Na and Cs single atoms.

---

*The force from the MOT beams on the atoms is given by $\mathbf{F} = \mathbf{F}_+ + \mathbf{F}_-$, where[95]

$$\mathbf{F}_\pm = \pm\frac{\hbar\mathbf{k}\gamma}{2}\frac{s_0}{1+s_0+(2\delta_\pm/\gamma)^2} \tag{3.1}$$

where $\mathbf{k}$ is the k-vector of the beam, γ is the transition linewidth, and s_0 is the saturation parameter. The detuning term $\delta_\pm$ is

$$\delta_\pm = \delta \mp \mathbf{k}\cdot\mathbf{v} \pm \mu' B/\hbar \tag{3.2}$$

where δ is the bare laser detuning, and the second and third terms are the Doppler and Zeeman shifts respectively. In particular, due to the higher velocity of Na, the Doppler term dominates, compared with the larger effect of Zeeman term for Cs.

MOT number and temperature

We optimized the MOT temperature and performance of PGC in free-space using time-of-flight thermometry[96]. This proved crucial to being able to image the single atoms in the trap without introducing significant heating. The Na and Cs MOT each have a diameter of ~0.25 mm and ~0.1 mm, and contain ~10^5 atoms each. Their temperatures are at ~200 μK and ~80 μK respectively before PGC and ~80 μK and ~10 μK respectively after PGC.

3.2 Single atom loading

Loading single atoms into an optical tweezer works by a stochastic process where pairs of atoms are excited by the cooling lasers to a repulsive potential that give the atom pairs sufficient energy to leave the trap[65]. Due to the tight volume of the trap, this parity selection process ensures that either one or no atoms remain.

The tweezer light is red-detuned from the atomic cooling transitions. As discussed in section 2.3, we trap Na with 700 nm light produced from a M2 Ti:Sapph laser, and Cs with 1064 nm light from a Mephisto laser. In addition, the 700 nm light that traps Na is switched at the MHz-level to be out of phase with the Na MOT/imaging light to avoid light shifts[78]. As will be apparent in section 3.4, to have independent control of the atoms and prevent excessive heating during the merging of the two traps to a single tweezer, the trapping wavelength for Na needs to lie between the Na and Cs D1/D2 lines ($589 - 852$ nm)[83]. Due to the lack of high power diodes and amplifiers in this range, this limits the high-power options for Na. In Chapter 6 we will discuss how this is scaled up. On the other hand, Cs trapping light only needs to be red of the D1/D2 lines of Cs (> 890 nm). Therefore, we chose 1064 nm for its convenience of high powers.

A schematic for the single atom loading sequence is shown in Fig. 3.1. A typical sequence

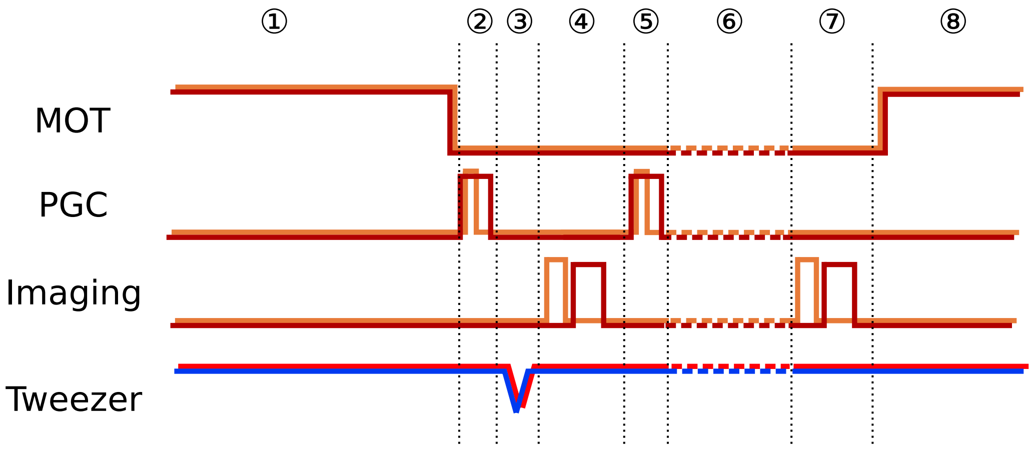

Figure 3.1: Single atom loading sequence schematic.

consists of the following steps.

1. *MOT loading.* The MOT's for both species are loaded simultaneously for ~0.3s. During this time, the tweezer beam powers are also set to their respective loading values, which is ~3 mK for Na and ~0.5 mK for Cs.

2. *PGC.* After the MOT loading step, the MOTs are dropped by setting the magnetic field to zero. The detunings and beam powers of the Na and Cs MOT/imaging beams are set to their respective PGC values for a cooling step. This step starts simultaneously for both species and takes 4 ms for Na and 20 ms for Cs.

3. *Trap lowering.* The tweezer beam powers are lowered adiabatically to ~20% their respective loading depths to let hot atoms spill out of the traps. Without this step, hot atoms appear in the first image as reduced photon counts, and subsequently appear as apparent loss during the imaging process.

4. *Pre-experimental run single atom imaging.* The Na and Cs atoms are imaged in turn by

setting the MOT/imaging beam parameters to their respective imaging values. These values are based off the corresponding PGC values and provides some cooling during the imaging process, which would otherwise heat the atoms out of the trap due to scattering. Due to differences in imaging times and photon collection efficiency, the two species are imaged individually. The imaging time is 3 ms and 10 ms for Na and Cs respectively. This first image can be used to post-select on those experimental runs where either of the atoms or both atoms have been loaded depending on the experimental needs.

5. *Post-imaging PGC.* Another PGC step is performed after imaging for additional cooling prior to the experimental run.
6. *Experimental run.* This varies depending on the sequence.
7. *Post-experimental run single atom imaging.* After the experimental run, another image of each of the two species is taken to measure survival of the two species. The survival is conditioned on the loading to provide the atom survival data we show.
8. *Post-sequence MOT loading.* The MOT light and magnetic field is turned on at the end of the sequence again so that the MOT starts loading during the overhead time between sequences.

The parameters for the MOT, PGC and imaging steps are listed in table 3.1. They all use the same beam path (MOT/imaging in Fig. 2.16) on the apparatus side. For the MOT step, a magnetic field gradient in the z-direction is turned on, and the shim fields are set such that the MOT's are centered with respect to the objective. For PGC and imaging steps, the magnetic field is set to zero, which is calibrated based on optimizing PGC performance.

Table 3.1: Single atom loading parameters. All steps use the same lasers and MOT/imaging beam path. Beam power corresponds to total power that gets split into 5 individual paths in the beam path.

Step		Beam power [mW]	Detuning [MHz]	Time [ms]
MOT	Na	F1: 0.5, F2: 5.0	-8	~300
	Cs	F3: 0.02, F4: 3.0	-13	~300
PGC	Na	F1: 0.5, F2: 5.0	-15	4
	Cs	F3: 0.02, F4: 1.5	-47	20
Imaging	Na	F1:0.5, F2: 2	-11	3
	Cs	F3: 0.02, F4: 3.0	-11	10

We can determine the number of atoms trapped in the tweezer by taking multiple images and looking at the histogram of photon counts within an area of interest. This follows a Poisson distribution for zero or one atom[65]. In daily data-taking, Otsu's method is used for quick threshold determination[97]. This method determines the threshold value between two classes for a grayscale image by minimizing the variance within each class and does not rely on fit parameters. For more detailed analysis, we fit the distributions to determine the uncertainty arising from false positive and false negative signals. We find typical fidelities of 99.96(1)% and 99.83(1)% for Na and Cs respectively. Loading rates – the probability of loading a single atom in each experimental run – under normal experimental conditions are ~50% and ~60% for Na and Cs respectively. An example of a histogram and average atom image for each of the two species is shown in Fig. 3.2. For data analysis, the atom survival probabilities are found by post-processing on the data and taking the ratio of survivals over total loads. The errors for these probabilities are calculated using the Wilson score interval, which computes the error for a Bernoulli process[98].

In the present apparatus, we were able to see a live single atom fluorescence signal that flickered in and out of the optical tweezers on the EMCCD camera when the MOT was simultaneously turned on. This was helpful in optimizing the single atom signals and later aligning

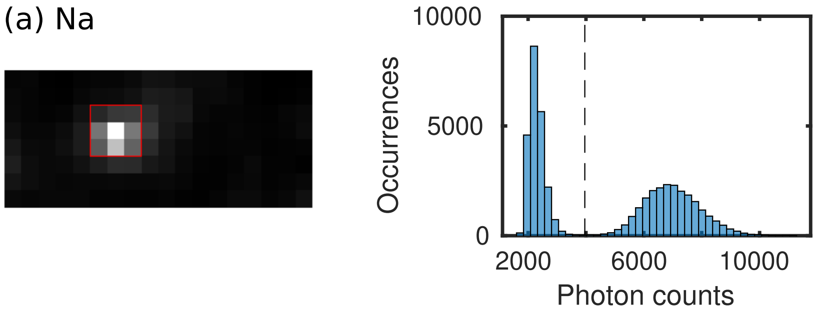

(a) Na

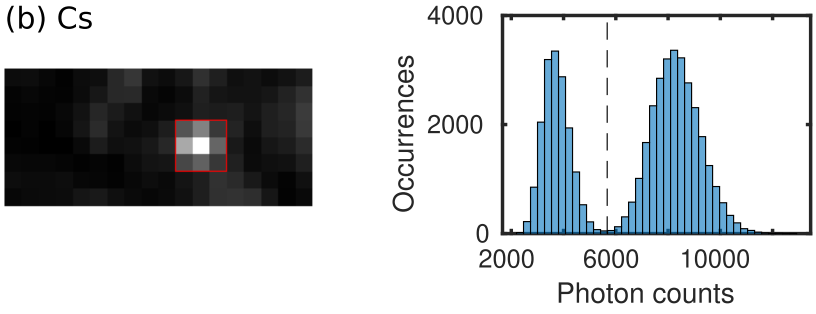

(b) Cs

Figure 3.2: Single atom image and photon count histogram.

beams to the single atoms. However, we found that the presence of a live signal was not indicative of the ability to load and trap the single atoms in a sequence, where the MOT's would be dropped and the atoms imaged using imaging parameters similar to PGC parameters. We attributed this to heating processes during the imaging step. This occurred in two different cases. In one, if the PGC parameters, which also provides cooling during the imaging process of the single atoms, are not optimized, PGC performance during the imaging step is poor or in fact can cause heating of the atoms. This can arise for example, from bad MOT/imaging beam alignment on the atoms, or imbalanced circular polarization for the counter-propagating beams; these can all lead to imbalanced forces which kicks the atom out of the trap during the PGC and imaging processes. In another case, we are also able to see a live signal but no trapped single atoms in a sequence when the intensity noise on the tweezer light causes parametric heating of the atoms out of the trap before we are able to efficiently image them (see also section 3.2.1). We encountered such cases when testing various laser sources, some of which had intensity noise at high frequencies[99], for the Na tweezer beam.

3.2.1 Single atom lifetime

We can characterize the lifetime of the single atoms in their respective traps by measuring the survival after holding the atoms for varying times. For Cs, we initially measured a $1/e$ lifetime of ~80 s independent of trap depth, as shown in Fig. 3.3(a). The heating rate we expect from photon scattering of the tweezer light can be approximated by[100]

$$\Gamma_{\mathrm{sc}} = \frac{\pi c^2 \Gamma^2}{2\hbar\omega_0^3}\left(\frac{2}{\Delta_{3/2}^2} + \frac{1}{\Delta_{1/2}^2}\right) I \tag{3.3}$$

where Γ is the natural linewidth of the atomic transition, $\Delta_{1/2}, \Delta_{3/2}$ are the detunings of the tweezer light from the D1/D2 lines, ω_0 is the transition frequency, and I is the peak intensity

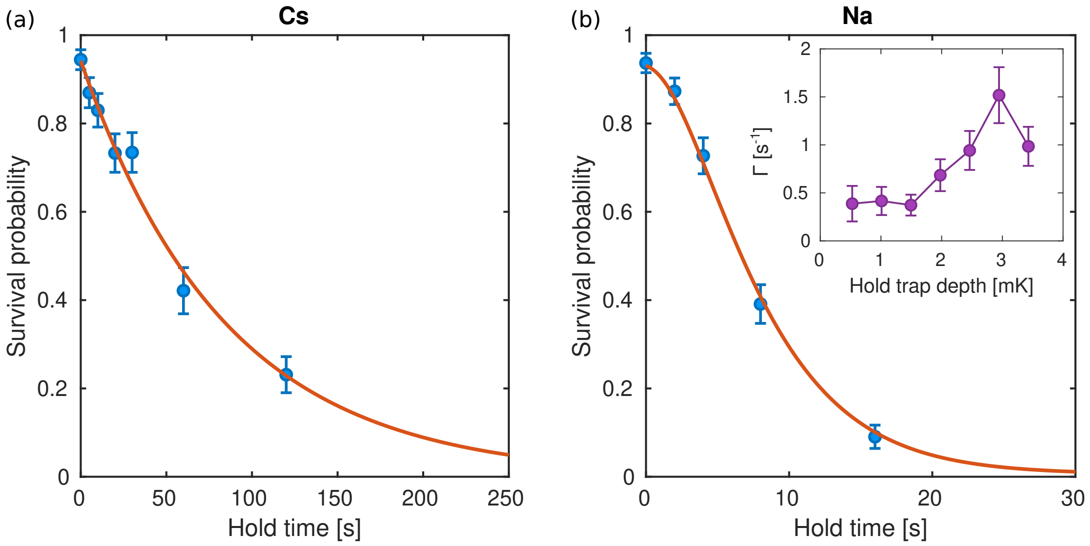

Figure 3.3: Singe Na and Cs atom lifetimes. (a) Single Cs atom lifetime curve. The exponential decay and $1/e$-time independent of trap depth suggests a background collision limited lifetime. (b) Single Na atom lifetime. The non-exponential curve and trap depth dependent rate constant suggests a parametric heating limited lifetime.

of the tweezer. This gives ~1.57 Hz, or ~500 nK/s per mK trap depth, which would give a lifetime two orders of magnitude larger than what we observe. The exponential lifetime curve we observe therefore suggests a background collision limited lifetime. The lifetime decreased to 20 s in the long term after turning up to higher dispenser currents. Nevertheless, as mentioned in section 2.1.5, this is an order of magnitude longer than the lifetime measured in the previous generation apparatus, which we attribute to better vacuum conditions.

On the other hand, for Na we find a non-exponential lifetime curve that is characteristic of heating in the trap, as shown in Fig. 3.3(b). For Na in a 700 nm trap the expected scattering rate is ~2.34 Hz, or ~11 μK/s per mK trap depth, which would also give a lifetime longer than is observed. To check for parametric heating, we measure the lifetime at varying trap depths and extract the rate constant at each trap depth. This can be modelled by the Fokker-Planck equation[101,102]

$$\frac{\partial n(E,t)}{\partial t} = \frac{\Gamma}{4} E^2 \frac{\partial^2 n(E,t)}{\partial E^2} - \frac{\Gamma}{2} n(E,t) \tag{3.4}$$

where $n(E,t)$ is the time evolution of the energy distribution in the trap, and Γ is the rate constant. The probability of the atom surviving in the trap $p(t)$ at time t is then given by the population remaining below the trap depth energy value,

$$p(t) = \frac{\int_0^{E_{\max}} n(E,t) dE}{\int_0^{E_{\max}} n(E,0) dE} \tag{3.5}$$

The best fit parameters can be found by minimizing the χ^2 value of the simulated curves compared to the data.

In particular, we find that the scattering rate is dependent on the trap depth in a non-monotonic manner, indicative of parametric heating, whereby peaks in the intensity noise spectrum can lead to parametric heating resonances coinciding with the specific trapping frequencies at different trap depths. The large trapping frequencies of Na render servo-ing at these frequencies challenging, though can be achieved with a combination of electric-optical modulator and acoustic-optical modulator servoing for different frequency ranges[99]. While this parametric heating is undesirable, we can avoid the resonances and this did not pose a large issue for Raman sideband cooling purposes.

3.3 Atom state preparation

After a single Na and Cs atom have been loaded, we need to prepare the atoms in their motional ground states and specific internal states for the next step of molecule formation.

3.3.1 Motional ground state cooling

To efficiently and coherently form molecules, the atoms need to be in their motional ground states. We cool the atoms to their 3D motional ground states in individual traps using Raman sideband cooling. This technique was developed for Na and Cs in optical tweezers in previous theses[83,84]. Here I will highlight the main points, and refer the reader to those theses for details.

Raman sideband cooling works by iteratively driving a motional sideband of an internal state changing Raman transition on the atom[103]. When the two lasers driving the Raman transition have wavevectors $\mathbf{k}_1, \mathbf{k}_2$ pointing in different directions, their wavevector difference $\Delta\mathbf{k} = \mathbf{k}_1 - \mathbf{k}_2$ imparts a momentum kick on the atom. Using this, it is possible to resolve motional sidebands on the internal state changing transition corresponding to the quantized levels of the harmonic trap. In particular, driving π-pulses on the $\Delta n < 0$ sidebands (red sidebands) lowers the energy of the atom. To initialize the internal state before the cooling pulses, and to reset the internal state between each cooling pulse, an optical pumping pulse relying on spontaneous emission is applied to reset the internal state which also acts to lower the entropy of the system. The ultimate temperature is determined by the equilibrium of the cooling rate from the Raman pulses, and the heating rates in the optical pumping process and other heating mechanisms such as the tweezers.

We drive the internal state transition starting from the stretched states $|F = 2, m_F = 2\rangle_{\mathrm{Na}} \rightarrow |F = 1, m_F = 1\rangle_{\mathrm{Na}}$ and $|F = 4, m_F = 4\rangle_{\mathrm{Cs}} \rightarrow |F = 3, m_F = 3\rangle_{\mathrm{Cs}}$ for Na and Cs respectively. A schematic of this is shown in Fig. 3.4(a). The laser systems are described in section 2.3. The Raman sideband cooling is performed at a bias field of 5.5 G and trap depths of ~3 mK (~4.5 mK) for Na (Cs). We measure trapping frequencies of $\omega_{\mathrm{Na}} = 2\pi \times (445,\ 445,\ 80)$ kHz and $\omega_{\mathrm{Cs}} = 2\pi \times (152,\ 163,\ 30)$ kHz for the radial 1/2 and axial directions respectively. The

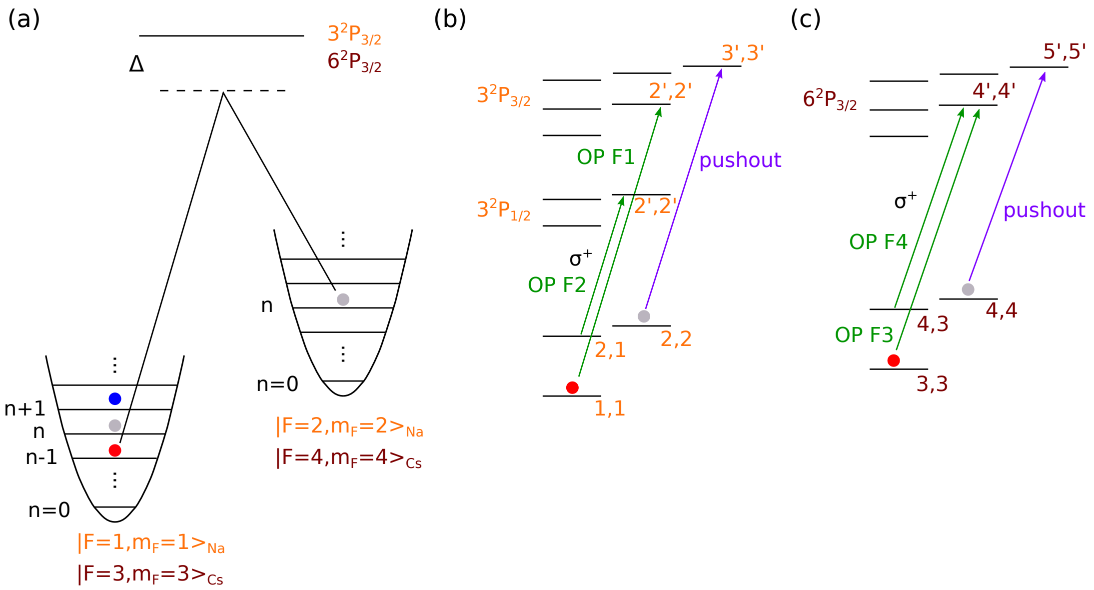

Figure 3.4: Raman sideband cooling and optical pumping/pushout schematic. (a) Raman sideband cooling schematic. The laser is tuned to drive $\Delta n < 0$ transitions to lower the energy of the atom. (b-c) Optical pumping and pushout scheme for (b) Na and (c) Cs. Green (purple) arrows indicate optical pumping (pushout) light. The D1 transition is used for Na to avoid depumping due to the nearby states in the D2 excited state manifold.

counter-OP (σ^-, Na F2, Cs F3) and radial 1/2 (π, Na F1, Cs F4) beams together address the two radial axes, which lie along the diagonal directions in real space, while the counter-OP (σ^-, Na F2, Cs F3) and coprop (π, Na F1, Cs F4) beams together address the axial axis (see Fig. 2.16). The Raman laser beams are focused to ~2-300μm at the atoms, and are aligned by sending in resonant light and pushing the live single atom signal out of the tweezer. The Raman pulses are driven with a Blackman profile[104], which suppresses higher order frequency components compared to a square pulse. This helps to resolve the motional sidebands better, which is especially important for the axial direction of Cs due to its low trapping frequency. We impose the Blackman profile on one of the beams in each pulse, choosing the one that gives less difference in light shift over the course of the ramp[105].

The π-times of the sideband transitions depend on the motional state of the atom. Therefore, to address all the population, the π-times in the cooling sequence are swept through the various π-times given the thermal initial temperature (post-PGC temperature, ~10 μK for Cs). For Na, additional complications arise due to its lighter mass and higher initial temperature (~80 μK)[84]. In particular, the Lamb-Dicke parameter[106]

$$\eta^R = \Delta\mathbf{k} \cdot \mathbf{x}_0 \tag{3.6}$$

where $\mathbf{x}_0$ is along the axis to be addressed, and $x_0 = \sqrt{\hbar/2m\omega}$, characterizes the extent to which the Raman transition causes coupling between higher Δn transitions. In particular, the Lamb-Dicke regime refers to the case where $\eta^R \ll 1$ and coupling between higher Δn is small, and is the typical regime in which most atoms are Raman sideband cooled. For Na, however, the cooling process starts outside of the Lamb-Dicke regime with the trap depths we can achieve. To achieve efficient cooling, higher order sidebands are driven to cool the atoms, starting from $\Delta n = -2$ for the radial directions and $\Delta n = -6$ for the axial direction. Moreover, the order of the pulses and their pulse times are optimized based on numerical simulations detailed in Ref.[84,80]. In total, the Na (Cs) cooling sequence has 920 (600) individual pulses interleaved with optical pumping pulses.

Ultimately, we achieve average motional quantum numbers $\bar{n}_{\text{Na}} = (0.049(20),\ 0.056(19),\ 0.094(32))$ for Na and $\bar{n}_{\text{Cs}} = (0.039(14),\ 0.029(13),\ 0.068(24))$ for Cs. These correspond to 3D motional ground state populations of 81% and 86% respectively. The full cooling step for Na (Cs) takes ~80 ms (~20 ms). The pulse sequences for the two species are set such that the end time of the respective cooling step are aligned to not incur additional heating during the wait time. The method and data for thermometry are shown in section 3.5.1.

Optical pumping

For Raman sideband cooling, σ^+-polarized light copropagating along the bias field direction is used to pump the atoms to the stretched state. A schematic of the optical pumping transitions are shown in green in Fig. 3.4(b-c) for Na and Cs respectively for the states we use for molecule formation. For Cs, the repump is resonant with $|F = 3, m_F = 3\rangle_{\mathrm{Cs}} \to |F' = 4, m_F' = 4\rangle_{\mathrm{Cs}}$ transition, while the F4 light is resonant with the $|F = 4, m_F = 3\rangle_{\mathrm{Cs}} \to |F' = 4, m_F' = 4\rangle_{\mathrm{Cs}}$ transition, all on the D2 line. For Na, since the excited state splitting on the D2 line is only ~10s of MHz, which is on the order of the excited state linewidth, the coupling to $F' = 3$ leads to depumping out of the dark state. Therefore, we optically pump using the $|F = 2, m_F = 1\rangle_{\mathrm{Na}} \to |F' = 2, m_F' = 2\rangle_{\mathrm{Na}}$ transition on the D1 line. The repump light is still on the D2 line, resonant with $|F = 1, m_F = 1\rangle \to |F' = 2, m_F' = 2\rangle$. For work presented in section 4.2, σ^--polarized light is used to optically pump the atoms to the opposite stretched state, and works similarly otherwise.

Ideally, once the atom is pumped to the stretched state, it is dark to the optical pumping light by selection rules. However, in realistic experimental conditions, polarization impurities can lead to population leakage out of the dark state. This depumping out of the stretched state from the optical pumping laser causes undesired heating that affects cooling performance. To achieve the cleanest polarization possible, a Glan-Taylor polarizer is used to produce linear polarization with high extinction ratio before using a quarter-waveplate to produce circularly polarized light propagating along the magnetic field direction (see Fig. 2.16). The quarter-waveplate angle is aligned by reducing the depumping rate on the atoms, and the magnetic field direction is scanned to find the optimal direction in alignment with the optical pumping beam.

We initially found different optimal directions for the Na and Cs optical pumping magnetic fields, despite the beams being well overlapped in direction. This arises from an effective magnetic field created by a vector Stark shift from the optical tweezers themselves. In particular, an atom experiences an effective magnetic field[107,108]

$$\mathbf{B}_{\text{eff}} = -U_0 \frac{\delta_2 - \delta_1}{\delta_2 + 2\delta_1} \mathbf{C} \tag{3.7}$$

where U_0 is the trap depth, δ_1, δ_2 are the detunings from the D1 and D2 lines respectively, and $\mathbf{C}$ is defined by

$$\mathbf{C} = \operatorname{Im}\left(\varepsilon(\mathbf{r}) \times \varepsilon^*(\mathbf{r})\right) \tag{3.8}$$

where $\varepsilon(\mathbf{r})$ is the polarization vector. $\mathbf{C}$ characterizes the ellipticity of the beam, where $|\mathbf{C}| = 1$ ($|\mathbf{C}| = 0$) for circular (linear) polarized light. Due to the tight focus of the tweezers, the paraxial approximation breaks down near the focus, leading to effectively circular polarization near the focus. This produces an effective magnetic field gradient near the center of traps that is perpendicular to both the *k*-vector of the tweezer beam and the linear polarization direction[109,110]. This effect is larger for Cs due to the larger splitting in the D1 and D2 lines.

This effective magnetic field gradient creates an offset in trap centers for the different m_F states. In particular, for the two states we drive between for Raman sideband cooling, the centers of the traps are displaced by ~150 nm, which is large compared to the harmonic oscillator length $\sqrt{\hbar/2m\omega} = 15$ nm in the radial direction. This offset can lead to decoherence and heating during the Raman pulses and optical pumping pulses[110]. To reduce this effect, the effective magnetic field is set to be perpendicular to the bias magnetic field such that the fields add in quadrature, as shown in Fig. 3.5. The π-polarization of the optical tweezers is aligned along the optical pumping bias field direction (horizontal in lab frame) so that the effective magnetic field that is in the physical vertical direction and perpendicular to the optical pumping magnetic field. This however causes a position dependent direction in the total effective

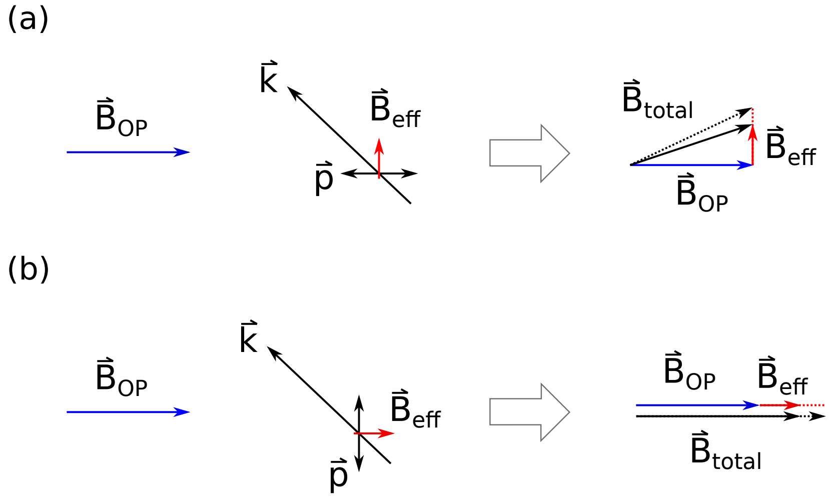

Figure 3.5: Effects of effective magnetic field. The tweezer beam creates a spatially varying effective magnetic field (B_{eff}, red) perpendicular to both the k-vector of the tweezer beam and linear polarization vector. This sums with the optical pumping magnetic field (B_{OP}, blue) to form the total magnetic field experienced by the atoms. (a) When $B_{\text{eff}} \perp B_{\text{OP}}$, the two vectors sum in quadrature, leading to a total magnetic field whose direction varies spatially away from the center of the trap (shown as dashed lines), but whose gradient value is reduced compared to case (b) when $|B_{\text{OP}}| \gg B_{\text{eff}}$. (b) When $B_{\text{eff}} \parallel B_{\text{OP}}$, the two vectors sum linearly, leading to a total magnetic field whose direction is constant away from the center from the trap, but whose gradient follows that of B_{eff}.

magnetic field the atoms experience, which in turn affects the polarization purity of the optical pumping beam that the atoms see.

Therefore, in order to align the optimal magnetic field directions of Na and Cs, it was necessary to adjust both the polarization purity and polarization direction of the tweezer beams. In particular, we found that it was necessary to clean up the polarization after the AOBD. In addition, we used a combination of a quarter- and half-waveplate after the cleanup cube to allow for polarization control. We used this to match the polarization of the 1064 nm beam with that of the 700 nm beam before the objective. We found an improved coincidence of optimal magnetic field pointing to minimize depumping simultaneously for the two species.

State detection

We use a pushout pulse to blast atoms in the stretched state out for state detection. This uses the same lasers and beampath as the optical pumping beams and is tuned to be on resonance with the cycling transitions $|F = 2, m_F = 2\rangle_{\mathrm{Na}} \rightarrow |F' = 3, m_F' = 3\rangle_{\mathrm{Na}}$ and $|F = 4, m_F = 4\rangle_{\mathrm{Cs}} \rightarrow |F' = 5, m_F' = 5\rangle_{\mathrm{Cs}}$ respectively. These are shown in purple in Fig. 3.4(b-c). There is no repump light for the pushout step. The traps are lowered to 10% of the loading trap depths during this step to efficiently push out the atoms. The atom population that remains after the pushout pulse is nominally in the states $|F = 1, m_F = 1\rangle_{\mathrm{Na}}$ and $|F = 3, m_F = 3\rangle_{\mathrm{Cs}}$.

In reality, this pushout state detection is for the most part only F-state sensitive and not m_F-state sensitive. For diagnostic purposes, we can additionally measure the population in specific m_F states by driving a Raman transition then applying a pushout pulse. For example, to measure the population in the stretched m_F state $|F = 4, m_F = 4\rangle_{\mathrm{Cs}}$, we can apply a π-pulse driving the atom to $|F = 3, m_F = 3\rangle_{\mathrm{Cs}}$ (section 3.3.2). Since this is the only m_F transition that is on resonance with this frequency, the measured population that ends up in $|F = 3, m_F = 3\rangle_{\mathrm{Cs}}$, together with information that the atom starts out in the $F = 4$ manifold, would tell us the exact population initially in the stretched state. This is used in next section when we investigate depumping effects.

Depumping

In the experiment, we initially observed an excessive amount of depumping from the stretched state of Cs during the cooling step. This was traced down to Raman scattering arising from intensity noise on the tweezer light. When the trapping light is far-detuned, Rayleigh scattering, where the atoms ends up in the same m_F state, is expected to dominate over m_F state-changing Raman scattering[111]. In particular, the scattering rate from a specific $|FM\rangle$ state to another

$|F''M''\rangle$ state in the ground state is given by[111]

$$\Gamma_{FM\to F''M''} \propto \left| \frac{\alpha^{(1/2)}_{FM\to F''M''}}{\Delta_{1/2}} + \frac{\alpha^{(3/2)}_{FM\to F''M''}}{\Delta_{3/2}} \right|^2 \tag{3.9}$$

where $\Delta_{1/2}$, $\Delta_{3/2}$ are the detunings from the D1 and D2 lines respectively and

$$\alpha^{(J')}_{FM\to F''M''} = \frac{\Gamma_{J'}}{\omega^3_{J'}} \sum_{q,F',M'} \langle F''M''|\mu_q|F'M'\rangle\langle F'M'|\mu_0|FM\rangle \tag{3.10}$$

where $\Gamma_{J'}$ and $\omega_{J'}$ are the linewidths and transition frequencies of the respective excited states. The two terms in the sum give the dipole matrix elements between the initial state $|FM\rangle$ (excited state $|F'M'\rangle$) and excited state $|F'M'\rangle$ (final state $|F''M''\rangle$) with linear (q) polarization and respectively. The sum is over all excited states and scattering polarizations q. Based on this, the ratio of Raman scattering to Rayleigh scattering rate we expect for Cs in the 1064 nm tweezer is ~1:35, and we expect a rate of ~0.32 Hz at the trap depth we perform Raman sideband cooling.

At the magnetic field we perform Raman sideband cooling (5.5G), the neighboring m_F levels of Cs are spaced by ~2 MHz. In the presence of polarization impurity in the optical tweezer, any noise on the optical tweezer beam in the vicinity of this frequency causes m_F state scrambling. This can be interpreted as an optical Raman scattering process, whereby the noise appears as frequency sidebands of the laser, and together with the combination of linear and circular polarization cause Raman scattering on the atoms.

We observed this effect in two separate cases. In one case, we found electronic noise on the PID servo we use to stabilize the intensity of the tweezer light. In another more subtle case, the source of noise was from the RF signal we use to control the AOBD in the 1064 nm beam path. For preliminary work in this thesis, we used a software-defined radio system, the

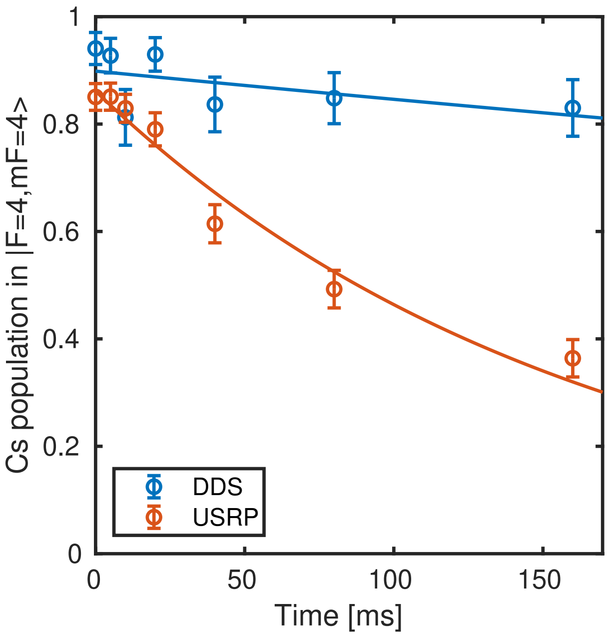

Figure 3.6: Depumping from stretched Cs hyperfine state. The population of Cs in the stretch hyperfine state $|F = 4, m_F = 4\rangle_{\text{Cs}}$ is measured by driving a Raman transition from $|F = 4, m_F = 4\rangle_{\text{Cs}} \rightarrow |F = 3, m_F = 3\rangle_{\text{Cs}}$, then performing pushout. The blue (red) data points correspond to the RF control signal for the AOBD being generated by the DDS (USRP) system. The $1/e$ time for the USRP controlled signal is 161(19) ms, an order of magnitude larger than is expected.

universal software radio peripheral (USRP) system[84] designed by Ettus, and consisted of a motherboard (Ettus N200) and daughterboard (UBX160) to generate the frequency tones for the AOBD. While we could detect no apparent noise of the RF signal on a spectrum analyzer, we observed increased depumping on the Cs atoms when the AOBD's were controlled using the USRP system. This is shown in red in Fig. 3.6, where we observe a depumping time constant out of $|F = 4, m_F = 4\rangle_{\mathrm{Cs}}$ of ~161(19) ms. This is compared with the depumping rate measured when the RF signal is generated by our home-built FPGA-controlled DDS system[84] shown in blue. In the previous generation of the experiment, a different motherboard (X310) and daughterboard (BasicTX) were used and did not have such drastic effects on depumping. For the work presented in Chapters 4, 5 of this thesis, we opted to use RF signals generated from the DDS system[84]. This issue will be re-visited in Chapter 6 when we scale to larger arrays.

3.3.2 Hyperfine state preparation

After optical pumping, the Na and Cs atoms are in either of the stretched states $|F = 2, m_F = \pm 2\rangle_{\mathrm{Na}}$ and $|F = 4, m_F = \pm 4\rangle_{\mathrm{Cs}}$ respectively. To drive the atoms to other hyperfine states, we can either use the Raman lasers to drive an optical Raman transition or the microwave antenna to drive a microwave transition.

Raman transition

By using the Raman beams in copropagating configuration, we can drive a Raman transition without incurring a momentum transfer[105] (see Fig. 2.16). This allows us to drive transitions between the two F levels of the ground atomic states with $\Delta m_F = 0, \pm 1$. For the transitions relevant to coherent molecule formation $|F = 2, m_F = 2\rangle_{\mathrm{Na}} \to |F = 1, m_F = 1\rangle_{\mathrm{Na}}$ and $|F =$

$4, m_F = 4\rangle_{\text{Cs}} \rightarrow |F = 3, m_F = 3\rangle_{\text{Cs}}$ we drive a square pulse with 5 mW (F1) and 2.5 mW (F2) for Na and 15 mW (each of F3/F4) for Cs and achieve π-times of ~5-10 µs for both species. Typical fidelities are 88(2)% and 95(1)% for Na and Cs respectively. While Blackman pulses allow us to better resolve motional sidebands due to suppressed higher-frequency components, they require ~2 times the pulse time. For state preparation, we opted to use square pulses for their shorter times to minimize decoherence issues limiting the fidelity.

In certain experiments, we also want to intentionally excite the motional state of an atom (see section 4.3.8). We can prepare these states by driving a heating sideband in one of the motional directions. This simultaneously prepares the atom in the desired hyperfine state. In particular, the transition of interest is $|F = 2, m_F = 2, n_{\text{radial2}} = 0\rangle_{\text{Na}} \rightarrow |F = 1, m_F = 1, n_{\text{radial2}} = 1\rangle_{\text{Na}}$. We achieve a fidelity of ~84(3)% in the experiment, limited by motional decoherence.

Microwave transition

For the experiments in section 4.2, the atomic hyperfine states were prepared using the microwave systems. In particular, we drive $|F = 2, m_F = -2\rangle_{\text{Na}} \rightarrow |F = 1, m_F = -1\rangle_{\text{Na}}$ and $|F = 4, m_F = -4\rangle_{\text{Cs}} \rightarrow |F = 3, m_F = -3\rangle_{\text{Cs}}$ using Adiabatic Rapid Passage (ARP)[83], whereby the population of the atom is transferred adiabatically as the frequency of the microwave signal is ramped 2 MHz and 3 MHz centered across the resonance at rates of 0.2 MHz/ms and 1 MHz/ms for Na and Cs respectively. We achieve fidelities of ~90% for both species.

3.4 Merging

After the atoms have been individually prepared in their desired internal and external states, the optical tweezers need to be merged so that a single pair of atoms occupies a single trap. Since atomic state preparation is challenging after the atoms are in the same trap, the merging process needs to be adiabatic such that the state preparation initially performed is maintained in the process. This requires a careful selection of merging pulse and parameters.

In our setup, there is an acoustic-optical beam deflector (AOBD) in the 1064 nm tweezer beampath (see section 2.5.1) which can be used to steer the Cs atom in the 1064 nm tweezer to merge with the stationary 700 nm trap containing Na. The AOBD is steered by ramping the RF tone that produces the diffraction. In the previous generation experiment, fringes were observed in the diffraction efficiency during the RF ramp, which placed limitations on the ramp due to parametric heating effects. The fringes were attributed to reflections of the RF signal inside the crystal that acted as a cavity which created standing waves[83]. For the AOBD we use in the present work (IntraAction ATD-1403DA2W), the crystal was angle-cut on one side to reduce the standing waves formed by RF reflections. We measure the diffraction power over a frequency sweep of the input RF tone as in Fig. 3.7. We find an oscillation amplitude of ~0.2-0.4%, and fringe period of ~55 kHz in RF frequency, corresponding to a crystal length of 3.8 cm in agreement with what we expect. This oscillation level is much reduced from the few percent level in the previous generation.

Apart from technical limitations, there are several other fundamental factors that need to be considered in the merge process as discussed in previous work[81,83]:

- Since the 700 nm trap is anti-trapping for Cs, the 1064 nm trap needs to be sufficiently deep so that Cs is not kicked out from the trap during the merge process.

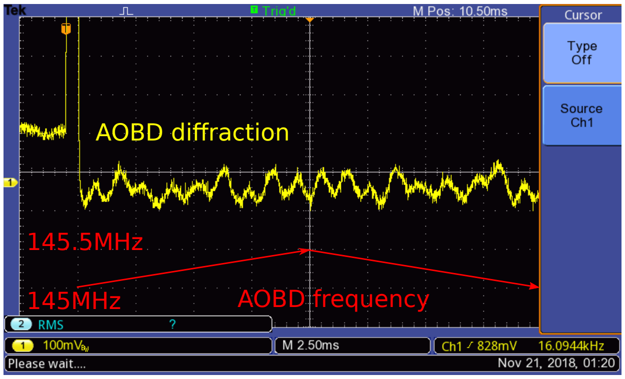

Figure 3.7: Fringes of AOBD RF sweep. The RF input to the AOBD is swept linearly from 145MHz to 145.5MHz and back (schematically shown in red). The yellow scope trace shows the photodiode signal amplified by an SRS pre-amplifier with 100x gain. The DC level of the photodiode signal is ~240mV. The oscillation amplitude of ~50-100mV corresponds to ~0.2-0.4% diffraction efficiency oscillation. The oscillation frequency of ~55kHz corresponds to a crystal length of ~3.8cm, which is in agreement with the crystal size.

- On the other hand, both 700 nm and 1064 nm are trapping for Na. Therefore, there is a maximum limit for 1064 nm beyond which the 1064 nm trap to be merged to would be deeper for Na, which could lead to tunneling and heating during the merge.
- The motion of the tweezers themselves may also cause heating on the atom being moved due to jerking. A minimum-jerk trajectory can be implemented to minimize these effects.

In principle larger polarizability differences between the two wavelengths leads to better separation between the different parameter regimes affecting the first two points. For trapping wavelengths 700 nm and 1064 nm, we compute that a power ratio of $P_{1064\mathrm{nm}}/P_{700\mathrm{nm}}$ in the range $1.5-5.3$ suffices[49]. In the experiment, we use $P_{700\mathrm{nm}} \approx 4$ mW and $P_{1064\mathrm{nm}} \approx 8$ mW respectively, and move the trap over ~3.5 μm in 1 ms by using a linear ramp in RF frequency (we found no significant improvement from a minimum-jerk trajectory).

Since we typically cannot image both atoms in a single trap simultaneously, in most experiments we also separate the traps by performing the merging sequence in reverse in order to image the individual atoms afterwards. This process can be susceptible to servo integrator wind-ups, which notably affects the survival of Na upon turning on the trap again. To reduce these effects, we turn the integrator off when the trap is off.

The performance of the merging process can be measured by comparing the Raman sideband thermometry before and after a merge. This is shown in Fig. 3.9. The difference in temperature between the two corresponds to a two-way sequence. We can take the average temperature to find the one-way performance. Overall, we find that Na is heated by $\Delta(\bar{n}_{\mathrm{r1}}, \bar{n}_{\mathrm{r2}}, \bar{n}_{\mathrm{ax}}) = (0.048(34), 0.020(29), 0.21(7))$, and Cs is heated by $\Delta(\bar{n}_{\mathrm{r1}}, \bar{n}_{\mathrm{r2}}, \bar{n}_{\mathrm{ax}}) = (0.01(2), 0.053(23), 0.036(38))$. The movement of the Cs atom during the merge sequence is diagonally along the two radial axes. The apparent excessive heating of the Na axial direction is likely due to remnant oscillations from the integrator wind-up of the Na servo.

Merging 2 Cs atoms

For experiments in section 4.2 of this thesis, two Cs atoms were also loaded and merged into a single trap. Two traps are generated by sending two RF tones simultaneously into the AOBD in the 1064 nm beam path. One trap is then moved by controlling the RF tone frequency to merge with the other trap. Since both atoms are loaded with 1064 nm light in this way, the lack of wavelength selectivity renders heating due to double well tunneling inevitable in the merge process. In particular, we expect $\Delta\bar{n} = 0.5$ on average in the movement direction based on numerical simulations[81]. Moreover, the lack of wavelength selectivity in the separation process also means the signal is cut in half – half the time both atoms end up in the same trap and appear as loss upon imaging. To ensure the two atoms have equally likely chance of ending up in either trap, the two traps need to have the same amplitude during the separation process, as shown in Fig. 3.8(a).

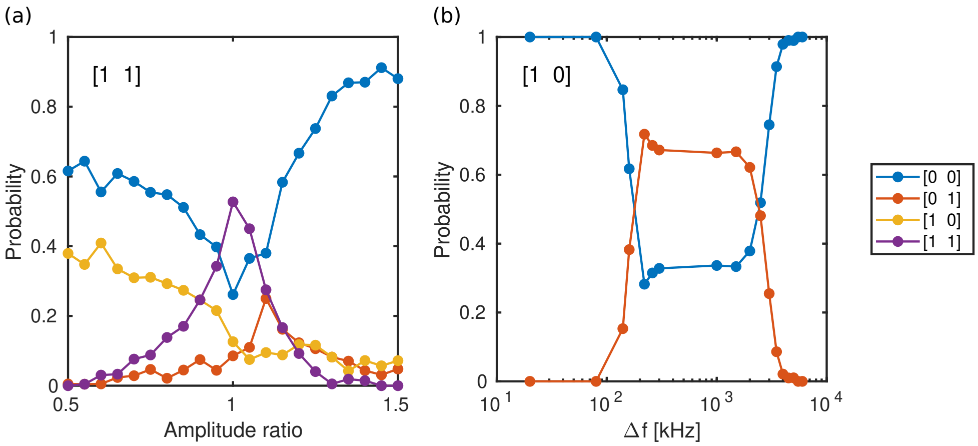

Figure 3.8: Merging of two Cs atoms. (a) A single Cs atom is loaded in each of the two traps (labelled by [1 1]). The resulting configuration after merging and re-separating the two traps is measured as a function of amplitude ratio of the two traps. Recovery into [1 1] occurs maximally when the amplitude ratio is 1. (b) A single Cs atom is loaded in the left trap ([1 0]). Transfer into the right trap is measured as a function of the frequency difference at which the traps merge Δf. Transfer occurs only between ~200 kHz–2.5 MHz.

Furthermore, and perhaps most detrimentally, since the two traps correspond to deflections of the AOBD driven by different RF frequencies f_1, f_2, when the two traps overlap, they optically beat with each other at the frequency difference of the RF tones $\Delta f = f_1 - f_2$. This in turn shows up as intensity noise, which heats up the atoms due to parametric heating processes (see section 3.2.1). This is shown in Fig. 3.8(b), where we see complete atom loss if the frequency difference at which the traps merge cross below Δf~200 kHz, corresponding to 2 times the trapping frequency; this corresponds to 150 nm in distance between the center of the traps. This problem will be revisited and discussed in more detail in Chapter 6. Nevertheless, despite these heating mechanisms, by using this merge procedure we were able to merge two Cs atoms to perform Feshbach resonance spectroscopy of two Cs atoms, and also investigate (lack of) 3-body effects in a single optical tweezer.

3.5 Thermometry

We use a combination of Raman sideband thermometry and interaction shift spectroscopy to characterize the motional state of the atom pair. As we will see in Chapter 4-5, this in turn is critical in allowing us to know the external state of the molecules we form, thereby achieving full quantum-state control.

3.5.1 Raman sideband thermometry

We use Raman sideband thermometry to measure the 3D motional ground state of the individual atoms. This uses a similar setup as that for Raman sideband cooling. In particular, π-pulses for the $\Delta n = -1$ and $\Delta n = +1$ motional sidebands are applied in individual experimental runs. After the spectroscopy pulse, a pushout pulse is applied for state detection. The ratio of the peak heights of the cooling and heating sidebands gives an estimate for $\bar{n}$[83,84]

$$\frac{A_{\text{cooling}}}{A_{\text{heating}}} = \frac{\bar{n}}{\bar{n}+1} \tag{3.11}$$

The thermometry pulse times are chosen to be the π-times of the respective heating sidebands, which are also the pulse times for the last cooling pulses.

In Fig. 3.9 we show Raman sideband thermometry spectra for the individual atoms before and after a round-trip merge sequence. The peaks on the left (right) correspond to the $\Delta n = +1$ ($\Delta n = -1$) sidebands. For this data set, before merging, $\bar{n}_{\text{Na}} = (0.049(20),\ 0.056(19),\ 0.094(32))$ and $\bar{n}_{\text{Cs}} = (0.039(14),\ 0.029(13),\ 0.068(24))$. We can take the average with the values after a round-trip merge sequence to find the ground state population after a one-way merge, giving $\bar{n}_{\text{Na}} = (0.074(26), 0.066(29), 0.20(6))$ and $\bar{n}_{\text{Cs}} = (0.043(28), 0.056(29), 0.087(39))$.

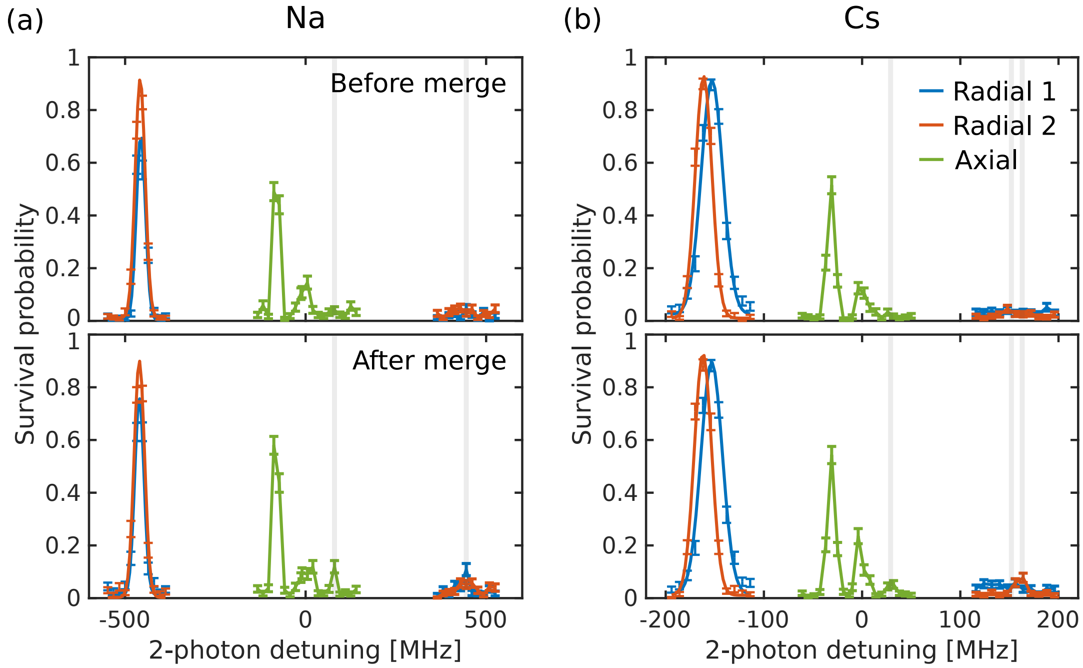

Figure 3.9: 3D thermometry before and after round-trip merge sequence. The top (bottom) panels correspond to the Raman sideband thermometry spectra before (after) merge for (a) Na and (b) Cs.

3.5.2 Interaction shift spectroscopy

After the two atoms have been merged, we are interested in directly measuring the relative motional ground state population of the atom pair. This is relevant for the molecule formation process, whereby only those in the relative motional ground state are most easily converted to the weakly-bound molecular state. We can measure this population by interaction shift spectroscopy[84,82]. When two atoms occupy the same trap, their interactions will incur an energy shift in the states of the two atoms. Depending on the relative motional state, the shift in energy will be different due to differences in their relative motional wavefunction. For the ground relative motional state, this can be approximated by

$$\Delta_{n_{\mathrm{rel}}=0} = a\frac{2\hbar^2}{\mu\sqrt{\pi}}\prod_{i=x,y,z}\frac{1}{\beta_{\mathrm{rel},i}} \tag{3.12}$$

where a is the scattering length, μ is the reduced mass, and $\beta_{\mathrm{rel},i} \equiv \sqrt{\hbar/\mu\omega_{\mathrm{rel},i}}$ is the relative motion oscillator length along the i-th axis. We can compare the amplitude of the energy shifted peak with that of the non-shifted carrier to obtain an estimate of the relative motional ground state population of the atom pair.

In the experiment, we drive a narrow copropagating Raman transition on Cs in the presence of Na atoms as shown in Fig. 3.10. The Na and Cs atoms are Raman sideband cooled and prepared in the states $|F = 2, m_F = 2\rangle_{\mathrm{Na}}$ and $|F = 4, m_F = 4\rangle_{\mathrm{Cs}}$ individually before being merged to a single trap. Then, Cs is driven from $|F = 4, m_F = 4\rangle_{\mathrm{Cs}} \to |F = 3, m_F = 3\rangle_{\mathrm{Cs}}$ using a Blackman pulse. The pulse is parked on the π-time of the carrier at 100 µs such that the energy shifted peaks can be resolved. The data is post-processed to be conditioned on two different atom loading scenarios. With a single Cs atom only, only the carrier transition is visible as shown in blue. In the presence of an Na atom, two additional peaks corresponding

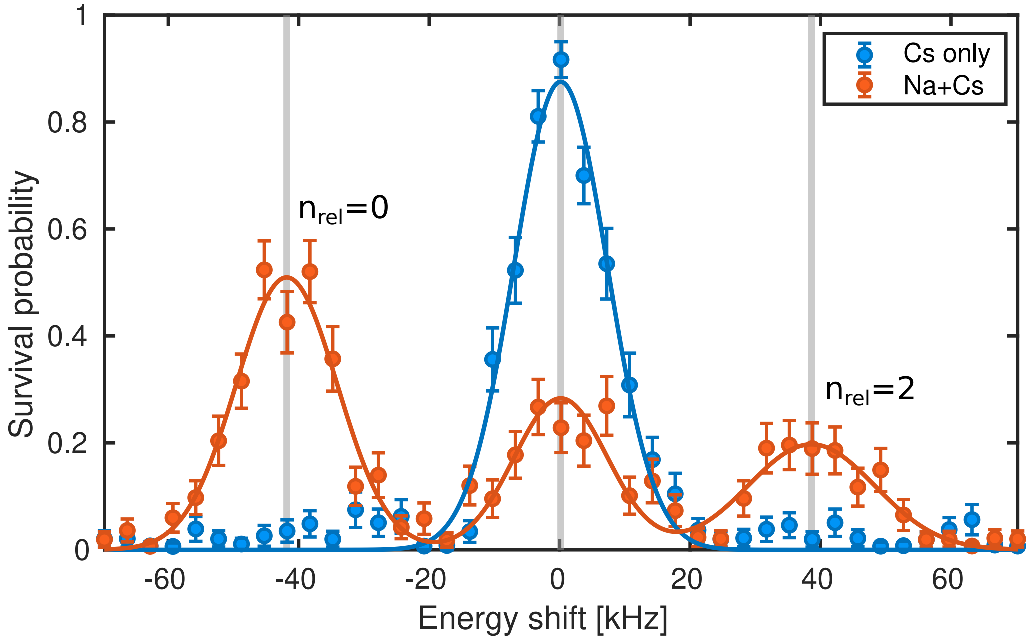

Figure 3.10: Thermometry by interaction shift spectroscopy. Blue (red) correspond to Cs atom only (both Na+Cs atoms) in the trap during the spin flip transition of Cs from $|F=4, m_F=4\rangle_{\text{Cs}} \rightarrow |F=3, m_F=3\rangle_{\text{Cs}}$. The interaction between the atom pair causes the energy of the spin flip transition to be shifted. The magnitude and sign of the shift is dependent on the relative motional state of the atom pair. The $n_{\text{rel}}=0$ peak is compared with the carrier transition without a Na atom to obtain an estimate of the relative motional ground state population.

to $n_{\mathrm{rel}} = 0, 2$ respectively appear. This is shown in red in the figure. For this data set, we find a relative motional ground state population of

$$P(n_{\mathrm{rel}} = 0) \approx \frac{P_{\mathrm{n_{rel}=0}}}{P_{\mathrm{carrier}}} \approx 58.2(6)\%. \tag{3.13}$$

The observed energy shift -41.8(9) kHz agrees well with estimates based on equation 3.12 and known parameters $a_{|F=2,m_F=2\rangle_{\mathrm{Na}}|F=4,m_F=4\rangle_{\mathrm{Cs}}} = 30.4a_0$, $a_{|F=2,m_F=2\rangle_{\mathrm{Na}}|F=3,m_F=3\rangle_{\mathrm{Cs}}} = -693.8{a_0}^{84}$, $\mu = 3.2561 \times 10^{-26}$ kg, and measured trapping frequencies $\omega = 2\pi \times (130, 130, 26)$ kHz, which gives $\Delta_{n_{\mathrm{rel}}=0,|F=2,m_F=2\rangle_{\mathrm{Na}}|F=3,m_F=3\rangle_{\mathrm{Cs}}} - \Delta_{n_{\mathrm{rel}}=0,|F=2,m_F=2\rangle_{\mathrm{Na}}|F=4,m_F=4\rangle_{\mathrm{Cs}}} = -40.1$ kHz.

4

Feshbach resonance spectroscopy and magnetoassociation

Having discussed the loading and preparation of single Na and Cs atoms in the previous chapter, we now turn to molecule creation. As mentioned in Chapter 1, we take a two-step approach to forming rovibrational ground state molecules. The first step is to create a weakly-bound molecule to bridge the size mismatch between the unbound atom pair state in the optical tweezer and the rovibrational ground state. In the present thesis, the approach we take is by magnetoassociation using a magnetic Feshbach resonance. This has been demonstrated in various bi-alkali molecules previously and has proved to be a robust approach to forming weakly-bound molecules. Prior to the present work, however, Feshbach resonances had been predicted but never observed in the bi-alkali Na+Cs system. This necessitated first measuring suitable Feshbach resonances for magnetoassociation. We performed both inelastic and elastic Feshbach resonance spectroscopy, and utilized a particular s-wave resonance in the lowest Zeeman level that is favorable for magnetoassociation.

In section 4.1, we first provide some background on Feshbach resonances and magnetoassociation that will be relevant for the work presented later in the thesis. Then in section 4.2, we present inelastic Feshbach resonance spectroscopy on Cs+Cs and Na+Cs atom pairs in our optical tweezer system. In section 4.3, we measure an elastic Feshbach resonance suitable for molecule formation and use it to form a single fully quantum-state-controlled weakly-bound molecule in the optical tweezer. We characterize its properties and discuss technical room for improvement in the conversion efficiencies. We conclude with an outlook on future work in section 4.4.

4.1 Background

Quantum scattering resonances between particles can occur when the energy of the incoming particles coincide with a bound state[112]. These can typically be categorized into shape resonances, where the bound state is supported by a potential barrier in the near range, and Fano-Feshbach resonances, where the bound state is supported by other channels. These Feshbach resonances are the main subject of the this chapter. In the case of atomic systems, magnetically tunable Feshbach resonances can occur due to the presence of multiple hyperfine

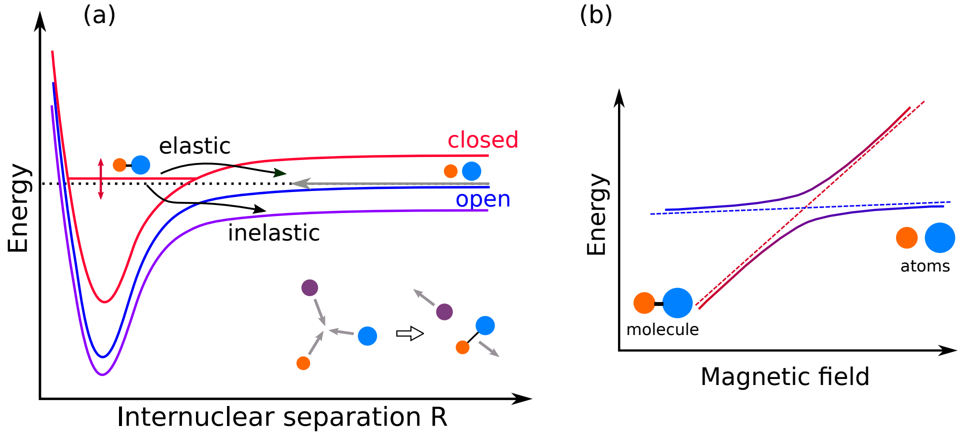

Figure 4.1: Feshbach resonance schematic. (a) A Feshbach resonance can occur when the energy of the incoming atom pair in a open channel (blue potential curve) coincides with a bound molecular state in a closed channel (red potential curve) and the states are coupled. The bound molecular state supporting an elastic resonance is not coupled to any other, whereas an inelastic resonance may decay to other channels lower in energy. Inset: for an elastic collision, atom loss from trap can occur only through (at least) 3-body processes due to conservation of energy and momentum. (b) Magnetoassociation is possible by the adiabatic crossing that forms between the free atom pair state and the bound molecular state. In particular, atom pairs can be converted adiabatically to a molecular state by ramping the magnetic field across the resonance.

channels that are coupled to each other by spin-spin interactions. These hyperfine channels typically have different magnetic moments, so that the relative energies between different channels can be tuned with an external magnetic field. As with general resonances, Feshbach resonances can lead to an adiabatic crossing, whereby ramping the magnetic field across the resonance leads to an adiabatic transfer between the free atoms and weakly-bound molecular states. This is the process we use in the first step to form a weakly-bound molecule, and the molecules formed in this manner are termed Feshbach molecules. Schematics of Feshbach resonances and magnetoassociation are shown in Fig. 4.1.

As with general collisional phenomena, Feshbach resonances can be split into elastic and inelastic resonances, as shown schematically in Fig. 4.1(a). In the elastic case, the outgoing pair has the same energy as the incoming atoms, whereas in the inelastic case the outgoing atoms relax into a different channel lower in energy, whether as an atom pair or other molecular state. Energy is released in such an inelastic process. For high fidelity coherent molecule formation, elastic resonances are desirable. Toward this end, Feshbach resonances in the hyperfine channel with the lowest energy are desired to suppress the possibility of relaxing to other states.

Prior to the present work, Feshbach resonances between Na and Cs atoms had been predicted[113] but never experimentally observed. We performed Feshbach resonance spectroscopy with atom pairs in our optical tweezer system to map out various Feshbach resonances, both inelastic and elastic. This required different measurement techniques due to the nature of the resonances. In typical bulk gas experiments, Feshbach resonances can be observed by measuring atom loss – the scattering length and thus collision cross section between two particles near a Feshbach resonance varies drastically and can lead to enhanced or suppressed atom loss[114]. Of note is that in the case of elastic resonances, it is necessarily at least a 3-body loss process due to conservation of energy and momentum. This is shown schematically in the inset of Fig. 4.1(a). For an inelastic resonance, 2-body loss is possible as energy is released in the process. In our experiment, we have only a single pair of atoms in an optical tweezer and therefore while we can expect to measure inelastic resonances by atom pair loss, we cannot rely on 3-body loss for elastic Feshbach resonance detection[115]. In section 4.3 we discuss how we get around this to measure elastic Feshbach resonances by direct molecule formation.

In our initial search for Feshbach resonances, we were guided by multichannel quantum defect theory and coupled channel calculations by theory collaborators Bo Gao and Jeremy Hutson[116,117]. These also benefited from early experimental work probing the near threshold states of the $a^3\Sigma$ and $X^1\Sigma$ potentials[113]. Because Feshbach resonances arise from interactions between hyperfine channels near threshold, they can be crucial to enhancing our understanding of interaction potentials in these bi-alkali systems[82] and in turn refine the parameters that feed into the theoretical models.

4.1.1 Theory

In this section we provide a brief theoretical background on Feshbach resonances. This is helpful to understanding the coupled-channel picture of Feshbach resonances, and is also relevant to finding the wavefunctions of the Feshbach molecules we create. This will be relevant in Chapter 5, where we use these to find the optical coupling strengths for the internal state transfer to the rovibrational ground state.

The Hamiltonian of the interaction between two atoms can be written as[118]

$$H = \frac{\hbar^2}{2\mu}\left[-R^{-1}\frac{d^2}{dR^2}R + \frac{\hat{L}^2}{R^2}\right] + H_1 + H_2 + V_{\text{int}}(R) \tag{4.1}$$

where $H_{1,2}$ are the internal parts of the Hamiltonian of each of the constituent atoms including electron and nuclear spin $\mathbf{S}_i, \mathbf{I}_i$ in the presence of an external magnetic field $\mathbf{B}$

$$H_i = \alpha_i \mathbf{S}_i \cdot \mathbf{I}_i + g_e \mu_B \mathbf{B} \cdot \mathbf{S}_i + g_n \mu_B \mathbf{B} \cdot \mathbf{I}_i \tag{4.2}$$

where α_i is the hyperfine constant of the respective atom, g_e, g_n are the electron and nuclear g-factors, and μ_B is the Bohr magneton.

$V_{\text{int}}(R)$ is the interaction between the two atoms and consists of two parts

$$V_{\text{int}}(R) = V_{\text{el}}(R) + V_{\text{ss}}(R) \tag{4.3}$$

The first is the electronic part of the interaction energy, and depends on the spin state of the atom pair, which arise from the singlet ($X^1\Sigma$) and triplet ($a^3\Sigma$) potential energy curves

$$V_{\mathrm{el}}(R) = V_S(R)\mathcal{P}^S + V_T(R)\mathcal{P}^T \tag{4.4}$$

where $\mathcal{P}^S, \mathcal{P}^T$ are the projection operators into the spin singlet and triplet subspaces. The second term is the dipole-dipole interaction between two electron spins

$$V_{\mathrm{ss}}(R) = \frac{g_e^2\mu_B^2\mu_0}{4\pi}\frac{1}{R^3}\left(\mathbf{S}_1 \cdot \mathbf{S}_2 - 3(\mathbf{S}_1 \cdot \hat{\mathbf{r}})(\mathbf{S}_2 \cdot \hat{\mathbf{r}})\right) \tag{4.5}$$

This term couples different partial waves and is off-diagonal in partial waves[119]. Without this dipole-dipole interaction term, Feshbach resonances can still arise from the channels being mixed near threshold, which is the case for the *s*-wave resonance relevant for our molecule formation. Of note is that a purely singlet or triplet state (such as the stretched hyperfine states $|F = 2, m_F = 2\rangle_{\mathrm{Na}}|F = 4, m_F = 4\rangle_{\mathrm{Cs}}$ and $|F = 2, m_F = -2\rangle_{\mathrm{Na}}|F = 4, m_F = -4\rangle_{\mathrm{Cs}}$ which are pure spin triplet for Na+Cs) cannot support Feshbach resonances of this nature.

This Hamiltonian is inherently a multichannel one, and therefore the solution to equation 4.1 requires a multichannel wavefunction to fully describe. This can be expressed as[119]

$$\psi(R,E) = \sum_{\beta} \psi_\beta(R,E)|\beta\rangle \tag{4.6}$$

where the $|\beta\rangle$ encode the channel information, typically consisting of angular momentum numbers, and forms a complete basis. The $\psi_\beta(R,E)$ can be thought of as spatially varying coefficients for the angular momenta basis components. For the Na+Cs system, there are in total 128 hyperfine spin states and one would naively expect correspondingly 128 states to describe the wavefunction. Within the Hamiltonian (equation 4.1) however, the total projection of angular momentum $m_{F,\mathrm{tot}}$ is conserved, which means the number of states required to describe

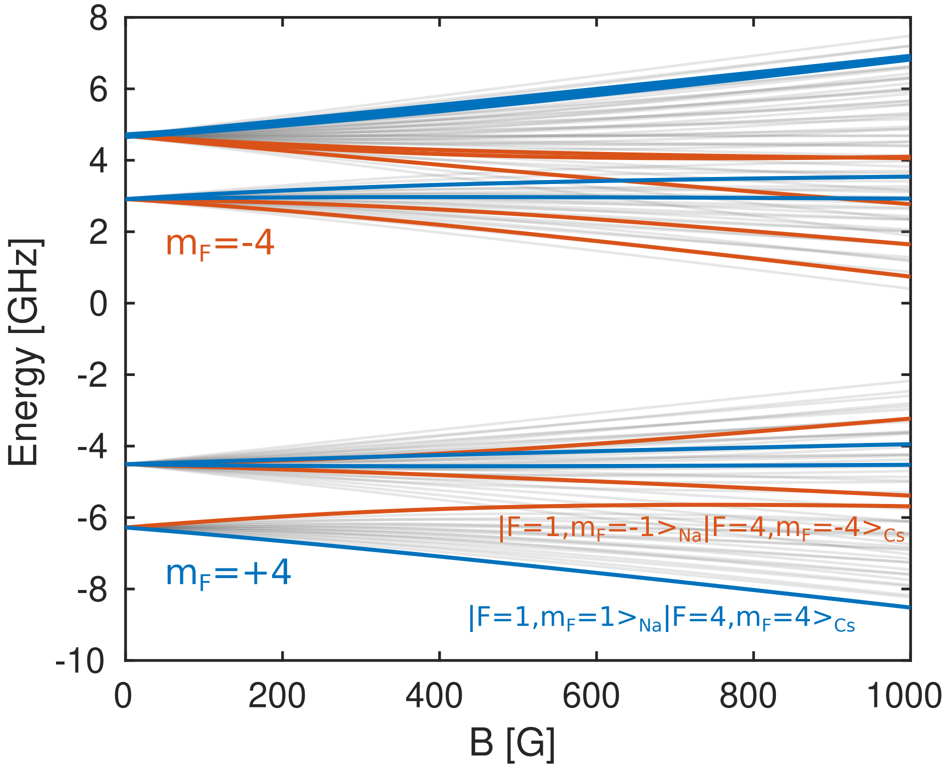

Figure 4.2: Hyperfine energy levels of Na+Cs atom pair. Gray lines show all the 128 hyperfine energy levels as a function of external magnetic field. Blue (red) highlighted curves are the states with total $m_F = +4$ ($m_F = -4$). The two states within these two manifolds that we search for Feshbach resonances in this work are $|F = 1, m_F = -1\rangle_{\text{Na}}, |F = 3, m_F = -3\rangle_{\text{Cs}}$ and $|F = 1, m_F = 1\rangle_{\text{Na}}, |F = 3, m_F = 3\rangle_{\text{Cs}}$ and have been labelled.

the state in well-chosen basis sets can typically be greatly reduced. The channels relevant for the results presented in this chapter are shown in Fig. 4.2.

Bases

For two atoms each having nuclear and electron spin I_i, S_i $(i = 1, 2)$ respectively, their combined angular momentum state can be expressed in terms of different bases. At long range, where the atoms do not interact strongly, this can be typically described by the uncoupled basis, $|S_1, m_{S_1}; I_1, m_{I_1}; S_2, m_{S_2}; I_2, m_{I_2}\rangle$. In the short range, where the atoms are close and the electrons are coupled, it may be convenient to work in coupled bases. A useful choice is that a coupled basis such as the electron spin-coupled basis $|S_1, S_2, S, m_S; I_1, m_{I_1}; I_2, m_{I_2}\rangle$ which can correspond to the projections onto the singlet and triplet potentials (see section 4.3.7). In addition, in certain cases, it may be convenient to work in the fully-coupled basis $|S_1, S_2, I_1, I_2; F, m_F\rangle$. These bases can be straightforwardly converted to each other by the Wigner 3-j symbols[120]. In the case where the angular momentum of the atom pair $L \neq 0$, then $|L, m_L\rangle$ is also included in the basis states, and total m_F includes the rotational part m_L as well.

Feshbach resonance properties

Near a Feshbach resonance B_0, the scattering length diverges following[119]

$$a(B) = a_{\text{bg}} \left(1 - \frac{\Delta}{B - B_0}\right) \tag{4.7}$$

where a_{bg} is the background scattering length. The width of the Feshbach resonance is defined as Δ, which is the zero-crossing of the scattering length. By ramping adiabatically over the resonance towards large negative scattering lengths, the atom pair can be converted to a bound Feshbach molecular state. The nature of the resonance sets the required magnetic field ramp direction. The Feshbach molecule state can be expressed as a linear combination of open channel and closed channel components (see section 4.3.3).

4.2 Inelastic Feshbach resonance spectroscopy

In this section we present results of inelastic Feshbach resonance spectroscopy performed on single pairs of Cs+Cs and Na+Cs atoms in optical tweezers. Since atom pair loss arising from inelastic resonances do not require the atom pair to be in the absolute relative motional

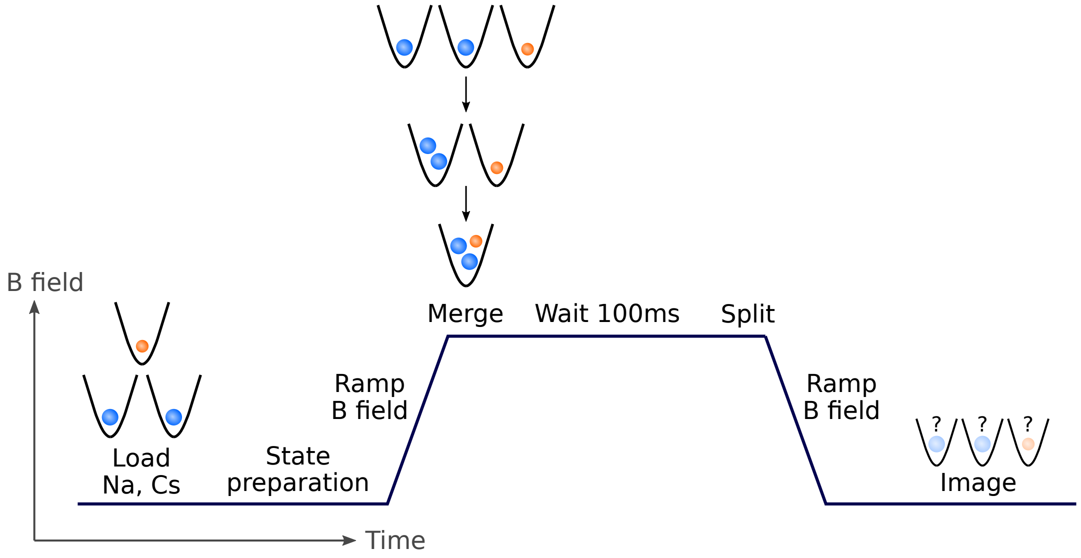

Figure 4.3: Inelastic Feshbach resonance spectroscopy experimental sequence timing schematic. For the inelastic spectroscopy experiments presented in this section, two Cs atoms and one Na atom are loaded into separate individual optical tweezers. The magnetic field is ramped up before merging the three atoms into a single trap by first merging the two Cs then combing them with Na. The atoms are held at high field for 100 ms before being separated into individual traps again. The trap separation process is the same sequence in reverse. The magnetic field is ramped back down for atom detection in their individual tweezers.

ground state*, this relaxes conditions on the motional state cooling of the atom pair. In these experiments, the atoms were polarization gradient cooled but not motional ground-state cooled by Raman sideband cooling, and were therefore in a thermal distribution.

4.2.1 Cs+Cs spectroscopy

We first measured Cs+Cs Feshbach resonances between a single pair of Cs atoms in our system and compared the results to the measurement of these resonances performed in bulk gases. The experimental sequence is shown in Fig. 4.3. Two Cs atoms and one Na atom are

---

*For spectroscopy using atom loss, higher atom temperatures may broaden the resonances but still lead them to be observable. This is in contrast to the case of finding elastic resonances by magnetoassociation in section 4.3, where the requirements on atom pair temperature is much more stringent.

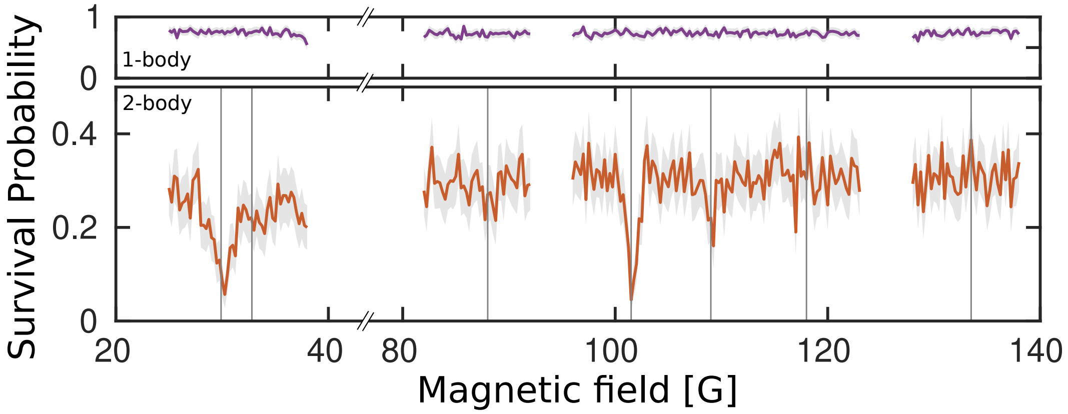

Figure 4.4: Inelastic Cs+Cs Feshbach resonance atom-loss spectrum. Upper (lower) panel show data conditioned on a single Cs atom (a single pair of Cs atoms) loaded. The overall signal for the 2-body case is cut in half due to the trap separation process (see section 3.4). The correlated 2-body loss at specific magnetic field values is indicative of Feshbach resonances. Gray lines are comparisons with previous results from Ref.[121].

loaded and polarization gradient cooled in individual optical tweezers and optically pumped to the stretched states. The hyperfine states of the atoms are prepared by microwave adiabatic rapid passage (section 3.3.2) to $|F=1,m_F=-1\rangle_{\text{Na}}$ and Cs $|F=3,m_F=-3\rangle_{\text{Cs}}$ respectively. A magnetic field produced by the Feshbach coils is ramped up in 40 ms along the axial direction of the optical tweezers to various values and held for 100 ms. The three traps are then merged, first by merging the two Cs atoms, then merging Cs and Na, so that all the atoms are held in a single optical tweezer. The merging procedures are discussed in section 3.4. We loaded three atoms with the intent of investigating 3-body processes as well. However, we found no significant signal compared to 2-body processes, and therefore post-selected only on those with two Cs atoms loaded. We note that the magnetic field is ramped up before merging the traps to avoid hitting other Feshbach resonances during the ramp up. This is in contrast to typical bulk gas experiments, whereby a common workaround is to implement high field imaging to circumvent running into Feshbach resonances at low field[121].

The atom loss spectrum is shown in Fig. 4.4. The bottom (upper) panel shows the data post-processed to be conditioned on having loaded exactly two Cs (one Cs) atoms. We find a correlated loss in the 2-body case at various magnetic field locations. We compare these to known resonances from the literature[121], and find good agreement. Some narrower resonances are not observed, which is likely due to the higher atom temperatures. Nevertheless, the observation of Feshbach resonances in our system establishes the validity of our approach of using atom pairs in optical tweezers for Feshbach resonance detection.

4.2.2 Na+Cs spectroscopy

Having demonstrated the ability to detect inelastic Feshbach resonances in the optical tweezers, we next turn to Feshbach spectroscopy of the heteronuclear pair Na+Cs, which had previously not been done in any platform. The experiment proceeds similar to that in the case of Cs spectroscopy in the previous section as shown in Fig. 4.3, where two Cs atoms and one Na atom are loaded into optical tweezers. In this case, we post-process to condition on those experimental runs where exactly a single Na and single Cs have been loaded. The Na+Cs pair Zeeman level of interest is labelled in red in Fig. 4.2. This is not the lowest Zeeman level, and therefore can relax to other spin states causing inelastic loss from the trap. Since this is the lowest energy level within the same m_F manifold, these processes arise from the electron spin-spin interaction term as in equation 4.5. Initial predictions were performed by Bo Gao using a multichannel quantum defect theory model[82].

Fig. 4.5 shows atom loss spectra obtained around two different magnetic field locations. In particular, Fig. 4.5(a) shows an s-wave resonance located at 652.1(4) G, and Fig. 4.5(b) shows a p-wave resonance located at 791.10(5) G. The latter also shows possible additional features in the spectrum as indicated by the arrow. These resonances agree with initial theory predictions to within 2%.

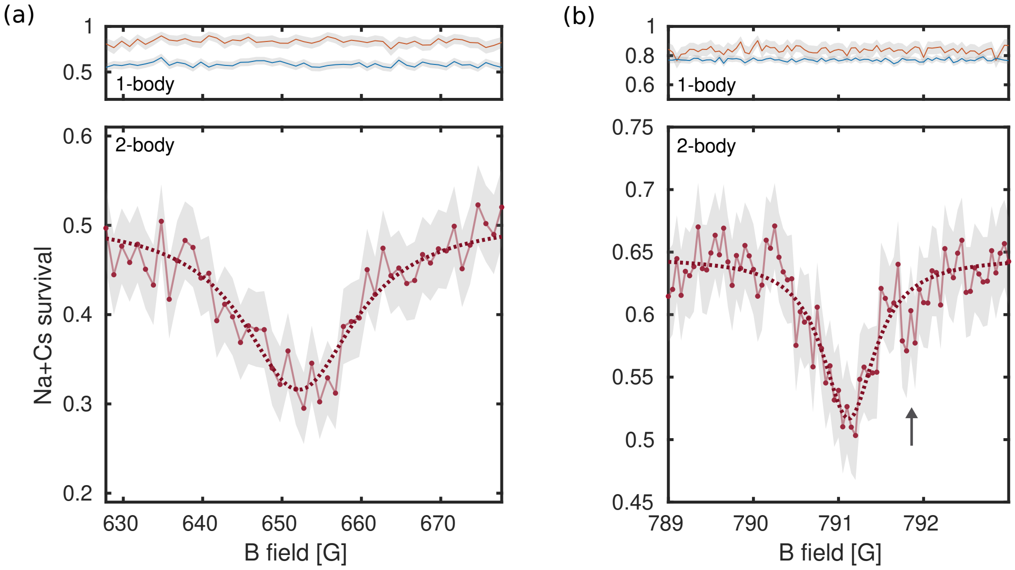

Figure 4.5: Inelastic Na+Cs Feshbach resonance atom-loss spectrum. Upper panel shows data conditioned on a single Na (red) or Cs (blue) atom being loaded, while lower panel shows that of exactly a single Na and Cs atom being loaded. We observe an (a) *s*-wave at 652.1(4) G and (b) *p*-wave resonance at 791.10(5) G respectively. Arrow in (b) marks a possible feature within the resonance. Shaded area indicates errorbar on data.

4.3 Elastic resonances

In this section, we turn to our search for elastic Feshbach resonances that enable magnetoassociation without incurring atom loss from inelastic collisions. In order to avoid spin relaxation to other states lower in energy, this necessitates being in the lowest Zeeman energy level of the atom pair. For Na+Cs, this is the state labelled at low field by $|F = 1, m_F = 1\rangle_{\mathrm{Na}}|F = 3, m_F = 3\rangle$, with total $m_{\mathrm{F}} = +4$. This state is labelled in blue in Fig. 4.2. For further transport down to the rovibrational ground state in our transfer scheme, apart from being in the lowest Zeeman energy level, the Feshbach resonance also needs to be an s-wave resonance due to parity selection rules[34].

While in the case of inelastic resonances direct correlated atom loss could be used to measure resonances, this is not possible for elastic resonances for a system with only two atoms in their lowest energy states due to conservation of energy and momentum. Therefore we directly utilize molecule formation by magnetoassociation for the Feshbach resonance search[115]. Somewhat unexpectedly, we also observed Feshbach resonance-enhanced photoassociation from the tweezer beam itself despite there being no photoassociation resonances in the vicinity of the tweezer beam wavelength. We used this to search for and locate p-wave resonances.

4.3.1 s-wave resonance detection

The experimental sequence for magnetoassociation, which we also use to detect the Feshbach resonance, is shown schematically in Fig. 4.6. After single atom trapping, ground-state cooling and hyperfine state preparation to $|F = 1, m_F = 1\rangle_{\mathrm{Na}}$ and $|F = 3, m_F = 3\rangle_{\mathrm{Cs}}$ (see section 3.3), a magnetic field produced by the Feshbach coils is ramped up in 40 ms along the axial direction of the optical tweezers to 866.5 G. The two traps are then merged, so that the Na and Cs atoms are held in a single optical tweezer at 1064 nm and a peak intensity of 81 kW/cm^2,

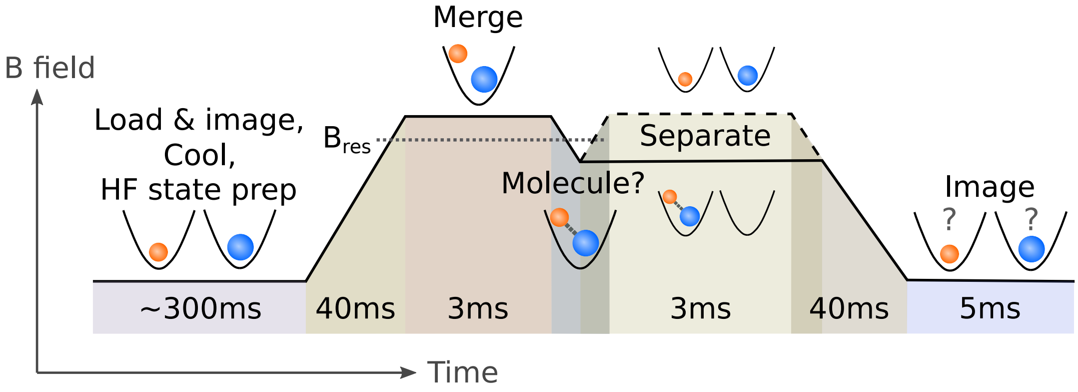

Figure 4.6: Magnetoassociation experimental sequence timing schematic. Schematic of magnetic field ramp and trap merge and separation sequence as a function of time. Solid (dashed) line indicates one-way molecule conversion (conversion back to atoms for molecule survival detection). Time spent for magnetoassociation is varied for different experiments.

giving trapping frequencies $\omega_{\text{Cs}} = 2\pi \times (30, 30, 5)$ kHz and $\omega_{\text{Na}} \simeq 1.07\ \omega_{\text{Cs}}$[81]. As in the case of inelastic resonance spectroscopy, the magnetic field is ramped up before merging the traps to avoid crossing other Feshbach resonances during the ramp up.

From the high magnetic field, the magnetic field is then ramped linearly down to various values at a rate of 1 G/ms (see section 4.3.2 for a discussion on the choice of ramp rate). If the magnetic field ramp crosses a Feshbach resonance then magnetoassociation is possible. For detection, the tweezer is separated back into their species-specific tweezers before ramping the magnetic field down to zero for imaging the surviving atoms, as shown by the solid line in Fig. 4.6. Because the imaging detects only the atoms, magnetoassociation to form Feshbach molecules is manifest as a two-body loss.

We locate an s-wave Feshbach resonance at $864.11(5)$ G, as shown in the lower panel of Fig. 4.7; the position is determined by a fit to an error function. An additional loss feature is detected at 864.5 G, which we attribute to photoassociation enhanced by a narrow resonance

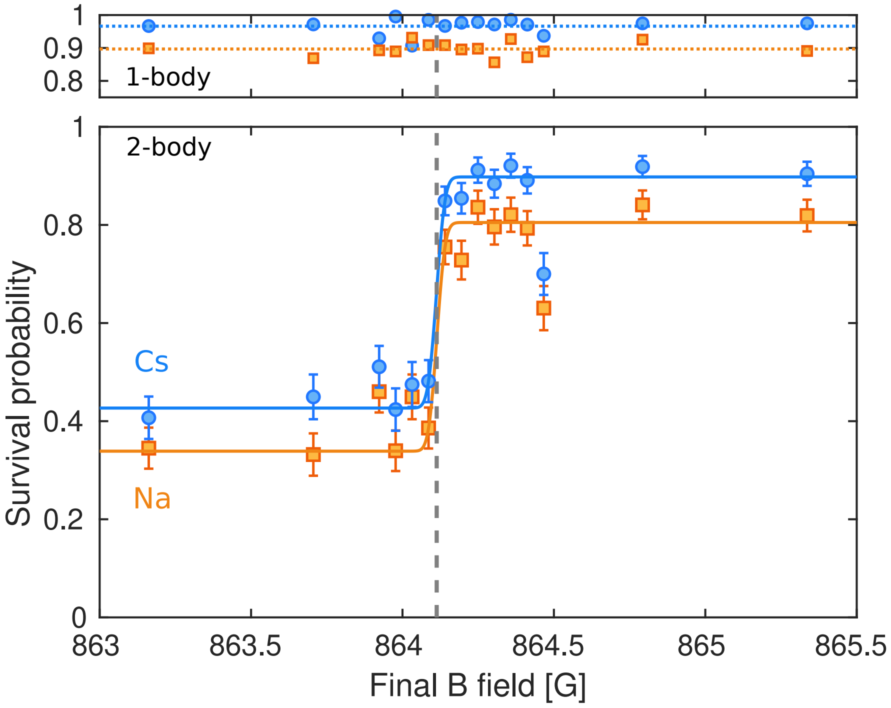

Figure 4.7: *s*-wave Feshbach resonance detection by magnetoassociation. The magnetic field is ramped linearly from 866.5 G to the various magnetic fields at 1 G/ms. Lower panel: survival probabilities of Na (orange squares) and Cs (blue circles) when both species are loaded. The solid lines are fits to an error function, from which we extract the left and right asymptote values and resonance location. Vertical dashed line indicates resonance location determined from the fit. Upper panel: same experimental run with initial one-body loading. Horizontal dotted lines are the mean values for each species.

nearby [†]. As confirmation of the two-body nature of the processes, we also measure the survival rates of the single atoms when loaded without the presence of the other species; these are shown in the upper panel of Fig. 4.7, and show no features. The contrast between the left and right asymptotes in the two-body loss data gives a molecule conversion efficiency of $47(1)\%$.

Proof of molecule formation

We note that mere correlated atom pair loss after the magnetic field is ramped down is necessary but not sufficient to prove coherent molecule formation. In particular, in our system we also observe incoherent Feshbach resonance-enhanced photoassociation of the atom pair in the presence of the intense tweezer beam (see section 4.3.4). Thus, during the ramp down of the magnetic field, it is possible that the time spent during the ramp over the Feshbach resonance field leads to correlated atom pair loss that colludes with the ramp direction to give an appearance of magnetoassociation. We can use one of two different approaches to verify that we are indeed coherently forming Feshbach molecules:

- *Demonstrate coherent disaasociation*. In this direct approach we can use coherent disassociation of the Feshbach molecules to verify the existence of molecules. In our case, we measure a lifetime curve of the molecules. In addition, we observe a Landau-Zener type dependence for the molecule formation efficiency, which is also a telltale sign of adiabaticity and thus coherent molecule formation. These are discussed in the next two sections.

- *Inverse ramp*. An alternative approach is to contrast the case of ramping the magnetic field in the opposite direction across the same range of magnetic fields. Since the direc-

---

[†] A d-wave resonance in the s-wave scaterring channel is predicted at 866 G[117]. The tweezer power is ramped up to 400 kW/cm^2 during separation back to individual traps that could lead to Feshbach resonance-enhanced photoassociation.

tion of the magnetic field ramp matters in magnetoassociation, a reverse ramp would show no apparent molecule formation. We use this approach in section 4.3.8 for the verification of magnetoassociation with a *p*-wave Feshbach resonance.

4.3.2 Adiabaticity characterization

We first characterize the adiabaticity of the magnetoassociation process. The atom-to-molecule conversion process can be described by a Landau-Zener (LZ) type avoided crossing with an efficiency that depends on the ramp rate of the magnetic field and characteristic parameters intrinsic to the Feshbach resonance[122,123,115]. To investigate molecule formation, we vary the rate of a linear magnetic field ramp from 866 G to 863.9 G. The resulting joint Na and Cs survival probabilities are shown as the purple circles in Fig. 4.8(a). A lower two-body survival probability indicates a higher molecule conversion probability. The one-way molecule conversion efficiency follows the LZ formula[112]

$$p_{\mathrm{mol}} = 1 - e^{-2\pi\delta_{\mathrm{LZ}}} \tag{4.8}$$

where

$$\delta_{\mathrm{LZ}} = \frac{2\pi n_2}{\mu} \left| \frac{a_{\mathrm{bg}}\Delta}{\dot{B}} \right| \tag{4.9}$$

Here $\Delta = 1.29$ G and $a_{\mathrm{bg}} = 30.7\ a_0$ are the width and background scattering length of the Feshbach resonances, obtained from coupled-channel calculations using the method of Ref.[124], $\mu = \frac{m_{\mathrm{Na}} m_{\mathrm{Cs}}}{m_{\mathrm{Na}} + m_{\mathrm{Cs}}} = 19.60$ amu is the reduced mass, $n_2 = \int\int n_{\mathrm{Na}}(\mathbf{r})\, n_{\mathrm{Cs}}(\mathbf{r})\, d\mathbf{r}$ is the density of a single pair of Na and Cs atoms in the optical tweezer, and $\dot{B}$ is the magnetic field ramp rate, which is varied experimentally. The purple curve in Fig. 4.8 is the best fit to the LZ formula. The fit value of the pair density based on this is $n_2 = 2.5(9) \times 10^{13}$ cm^{-3}.

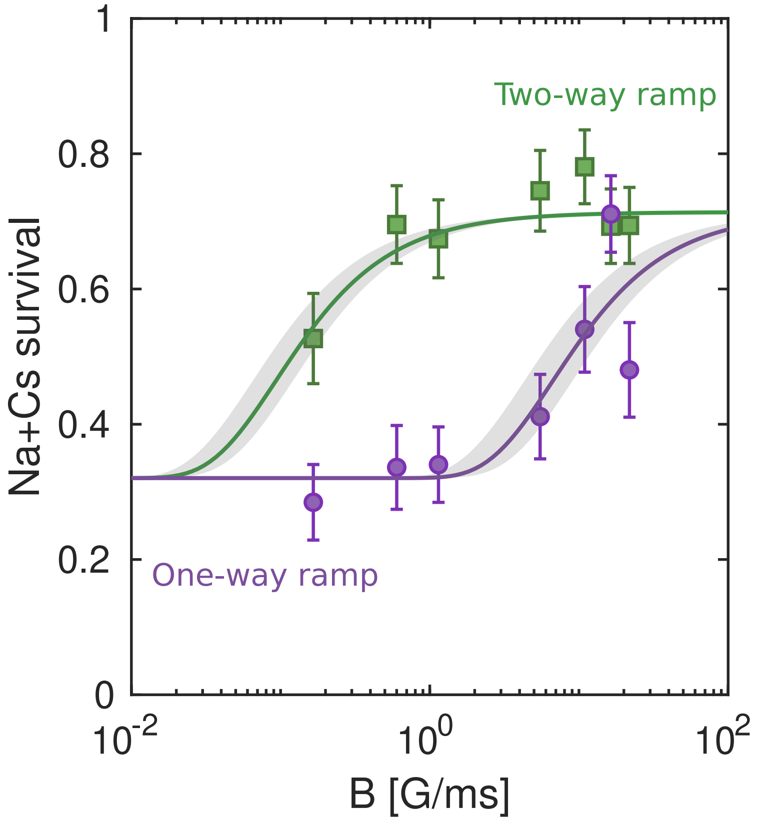

Figure 4.8: Feshbach molecule formation and dissociation efficiencies. Purple circles indicate Na+Cs joint survival probability after magnetoassociation. The magnetic field is ramped linearly from 866 G to 863.9 G at different rates. Green squares indicate Na+Cs joint survival probability with an additional reverse magnetic field ramp at the same rate after molecule formation. The solid lines are best-fit curves to the Landau-Zener model and the gray shaded areas indicate the errors on the fit.

We can estimate the pair density directly by[79]

$$n_2 = \int\int n_{\text{Na}}(x, y, z) n_{\text{Cs}}(x, y, z) dxdydz \tag{4.10}$$

where $n_{\text{Na}}, n_{\text{Cs}}$ are the probability densities of Na and Cs respectively. For atoms in the motional ground state of the optical tweezer, this can be approximately separated into components in the three dimensions

$$n(x, y, z) = \prod_{u=x,y,z} |\psi_0(u)|^2 \tag{4.11}$$

where $\psi_0(u) = \left(\frac{m\omega}{\pi\hbar}\right)^{1/4} \exp\left(\frac{-m\omega u^2}{2\hbar}\right)$ is the wavefunction of the ground state of a harmonic trap with trapping frequency ω. For the trap powers we operate at for magnetoassociation, $(\omega_x, \omega_y, \omega_z) = (25, 25, 5)$ kHz and $1.07 \times (25, 25, 5)$ kHz for Na and Cs respectively. From this we can estimate $n_2 \approx 2.9 \times 10^{13}$ cm^{-3}, in agreement with the fit values from the Landau-Zener sweeps.

4.3.3 Feshbach molecule detection and lifetime

To detect the survival of the Feshbach molecules in the optical tweezer, we dissociate the molecules back into atoms by performing a reverse magnetic field ramp, as shown by the dashed line in Fig. 4.6. We assume the Feshbach molecule dissociates with certainty since no molecular state exists above resonance[125]. The two-way conversion efficiency back to atoms is limited by the time the Feshbach molecules spend in the optical tweezer. This can be expressed as

$$p_{\text{atom}} \approx e^{-t_{\text{mol}}/\bar{\tau}} \tag{4.12}$$

where

$$t_{\text{mol}} = \frac{2|B - B_{\text{res}}|}{\dot{B}} \tag{4.13}$$

is the time spent below the Feshbach resonance, and $\bar{\tau}$ is the molecular lifetime, averaged over the ramped magnetic field. The green curve in Fig. 4.8 is a best fit to the two-way ramp that yields $\tau = 6(2)$ ms.

We can also directly measure the lifetime of the molecules at a particular magnetic field in a separate experiment by holding the molecules for varying times before dissociating and detecting atom survival. At $B - B_{\text{res}} = -0.3$ G and a trap peak intensity of 81 kW/cm^2, we observe a lifetime of $\tau = 4.7(7)$ ms as shown in Fig. 4.9. In particular, we note that this loss rate is much faster than the bare atom pair loss rate at the same magnetic field. We can measure the latter by simply holding the atom pairs at the magnetic field value without performing a sweep to form molecules – the atom pair survival remains flat within the same time range as shown in the inset of Fig. 4.9. This rules out the apparent loss in the lifetime curve coming from the atom pairs in the trap that are not converted to molecules. Therefore, such a lifetime curve is a sign of molecule formation. In addition, the lifetimes we find from two different methods above agree well, which corroborates the lifetime-limited conversion efficiency for the disassociation process.

In order to characterize the factors limiting the lifetime of the Feshbach molecules in the optical tweezers, we measure the lifetimes under various hold conditions. In one case, we vary the power of the trap used to hold the molecules after formation. The Feshbach molecules are formed and dissociated with a ramp rate of 3 G/ms and are held at $B - B_{\text{res}} = -0.3$ G. We find that the lifetime of the molecules is inversely proportional to trap intensity, as shown in Fig. 4.11(a), suggesting that the lifetime is limited by scattering from the trap light. This observation agrees with lifetimes previously reported for Feshbach molecules in optical lattices[123]. However, we note that, given similar trapping frequencies, optical lattices typically require an order of magnitude less intensity compared to that required for optical tweezers, and therefore give rise to much less scattering. This is discussed in Appendix A.

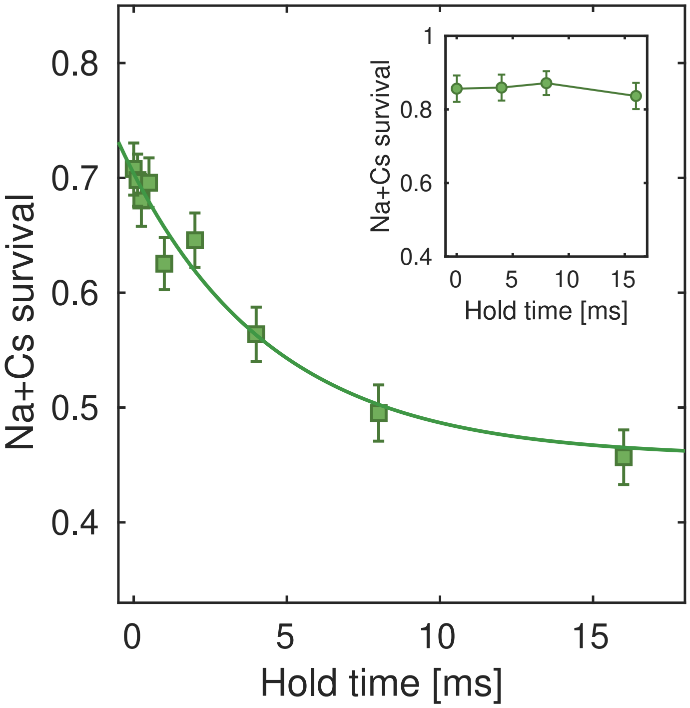

Figure 4.9: Lifetime of Feshbach molecule. After Feshbach molecule formation, the molecule is held at $B - B_{\text{res}} = -0.3$ G and trap intensity 81 kW/cm^2 for varying times. Solid line is best fit to an exponential decay. Inset: Bare atom pair survival. The magnetic field is held at the same value $B - B_{\text{res}} = -0.3$ G without forming molecules. The data was taken in a different experimental run and therefore has a slightly different baseline survival with the main figure.

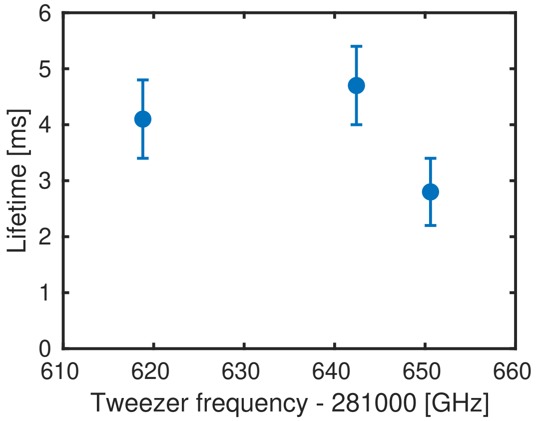

Figure 4.10: Feshbach molecule lifetime dependence on tweezer wavelength. The Feshbach molecule lifetime is measured at various frequencies of the 1064 nm tweezer, which holds the Feshbach molecules. In all cases, the molecule is held at $B - B_{\text{res}} = -0.3$ G and trap intensity 81 kW/cm^2. No clear dependence is observed.

While no molecular lines are predicted between the Feshbach molecule and any of the excited molecular states, as a check, we tune the 1064 nm laser frequency to rule out accidental coincidence with unknown lines. We find no clear variation in lifetime over ~50 GHz, the largest range that the laser could be tuned. This is shown in Fig. 4.10.

From these scattering rates, we can determine the imaginary part of the polarizability at 1064 nm to be 2.8(3)Hz/(kW/cm^2); this is $\sim$ 100 times higher than expected from theoretical predictions[126]. A similar excessive scattering is also observed in various excited NaCs molecular states, both in the 1.0 generation of our experiment, as well as in Chapter 5 of the present thesis. There is not yet any clear theoretical explanations for these observations. Perhaps relatedly, we also observe Feshbach resonance-enhanced photoassociation from the tweezer light, which is unexpected as well (see next section). While the lifetime is much shorter than expected, it is fortunately for us long enough for the further transfer down to the rovibrational ground state (Chapter 5).

We also vary the magnetic field at which the Feshbach molecules are held, over fields that correspond to binding energies up to $E_{\mathrm{b}} = 3$ MHz. The trap peak intensity is fixed at 81 kW/cm^2. As shown in Fig. 4.11(b), we observe no significant variation of the lifetime in this range. The scattering rate of the trapping light depends on the Franck-Condon overlap between the Feshbach molecular state and excited molecular states in the vicinity of the tweezer wavelength; under some circumstances this is proportional to the closed-channel fraction $Z(B)$ of the wavefunction for the Feshbach molecule[123]. Based on coupled-channel bound-state calculations, we can evaluate $Z(B)$ from the expression

$$Z(B) = \frac{\mu_{\mathrm{b}} - \mu_{\mathrm{a}}}{\mu_{\mathrm{bare}} - \mu_{\mathrm{a}}} \tag{4.14}$$

where μ_{b} (μ_{bare}) is the magnetic moment of the Feshbach molecular state (the bare molecular state well below threshold), and μ_{a} is that of the separated atoms[112]. Intuitively, this gives a measure of how similar the Feshbach molecule state is compared to the bare molecular state well below threshold. Z and $-E_{\mathrm{b}}$ are shown as functions of magnetic field in Fig. 4.11(c). From these we find that this resonance has only a small region of universality – the region of magnetic field such that the binding energy scales quadratically, as opposed to linearly, with scattering length. At the magnetic fields we use, $B - B_{\mathrm{res}}$ between -1 G and -0.15 G, Z is close to 1 and varies slowly with magnetic field.

4.3.4 Feshbach resonance-enhanced photoassociation from tweezer light

Despite not being near any molecular lines, either known or predicted, the 1064 nm tweezer light is also observed to cause Feshbach resonance-enhanced photoassociation of atom pairs. An example of this is shown in Fig. 4.12. The atom pair is held at various magnetic fields for 30 ms in traps with an intensity of 1500 kW/cm^2. We see an enhanced loss that depends on the magnetic field. We can perform such a measurement at various trap intensities and fit to a

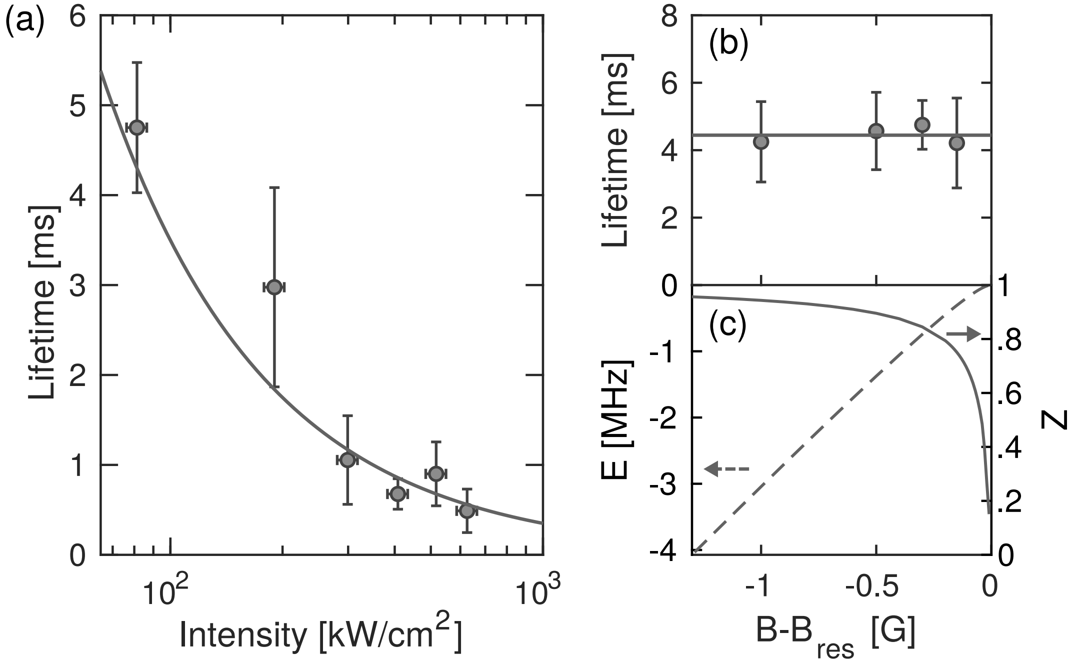

Figure 4.11: Characterization of *s*-wave Feshbach molecule lifetime. (a) Dependence on trap intensity. The trap is adiabatically ramped to and held at different intensities after magnetoassociation at $B - B_{\text{res}} = -0.3$ G. The line is a best fit to inverse scaling. (b) Dependence on magnetic field. The field is ramped to different values during magnetoassociation while the trap intensity is fixed at 81 kW/cm^2. The solid line is the mean value. (c) The negative binding energy $-E_{\text{b}}$ (dashed line, left axis) and closed-channel fraction Z (solid line, right axis) from coupled-channel bound-state calculations as a function of magnetic field.

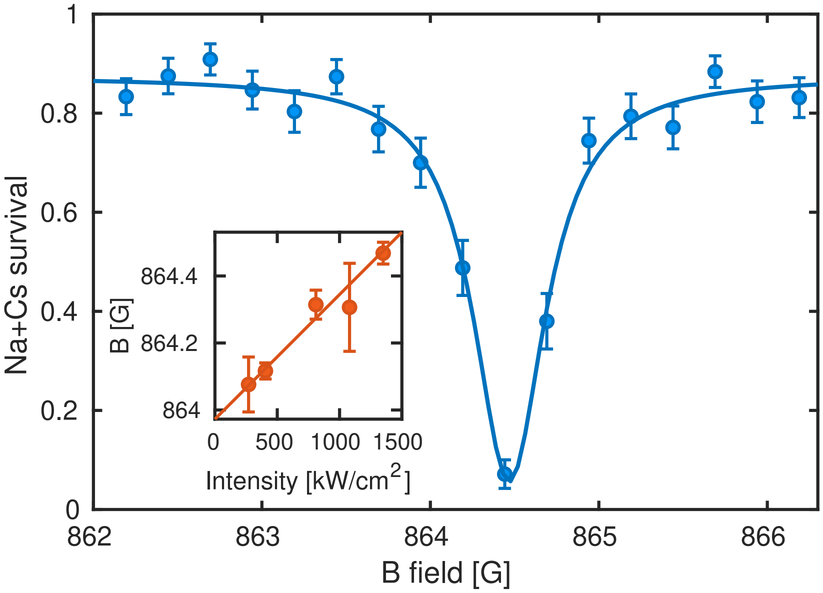

Figure 4.12: Feshbach resonance-enhanced photoassociation by optical tweezer light. Enhanced photoassociation from tweezer light at 1064nm. The atom pair is held at an intensity of 1500 kW/cm^2 for 30 ms at each magnetic field. The solid line is a fit to a Lorentzian lineshape to extract the resonance location. Inset: Resonance location at varying trap intensities. Solid line is a fit to a line. The extrapolated value at zero intensity gives the unshifted resonance location, which agrees with that obtained through magnetoassociation spectroscopy, while the slope gives the AC Stark shift of the resonance location.

Lorentzian profile to extract their respective resonance locations. These are shown in the inset of Fig. 4.12. The linear dependence suggests an AC Stark shift from the tweezer light. In particular, the extrapolation value of the intercept $B = 863.97(3)$ G gives the unshifted resonance location, which agrees well with our magnetoassociation measurements. Meanwhile the slope 0.37(8) mG/(kW/cm^2) gives the Stark shift dependence on intensity. From this, we can estimate the light shift on the Feshbach molecule state. Since the molecule is very weakly-bound, we expect it to be similar to that of the pair of free atoms. The magnetic moment of the Na+Cs atom pair is -2.41 MHz/G, while that of the Feshbach molecule is found to be ~0.83 MHz/G based on coupled-channel calculations. Furthermore, the expected light shift of the atom pair from the 1064 nm tweezer beam is ~0.065 MHz/(kW/cm^2). This gives a light shift on the Feshbach molecule of ~0.066 MHz/(kW/cm^2), which is similar to the atom pair as expected.

4.3.5 Conversion efficiency

The successful conversion of an atom pair to a single molecule in an optical tweezer relies on several conditions to be simultaneously satisfied. Here we list the various steps involved and their respective fidelities, which are also summarized in Table 4.1, and discuss potential room for improvement in future work.

- *Loading of single atoms.*

  In the work presented in this section, we post-process on the experimental runs where exactly a single Na and single Cs have been trapped. The atom pair probability is therefore assumed to be limited only by the imaging fidelities, which are Na $0.9996(1)$ and Cs $0.9983(1)$ respectively (see section 3.2). When scaling up to multiple tweezers, the tweezer array can be rearranged *in situ* to obtain near-unity atom filling[68,69] so that the initial atom loading probability does not factor into the final molecule filling fraction of array.

- *Population in relative motional ground state.*

  The motional state of an atom pair can be described in terms of the relative and center-of-mass motions. In a separable trap, these motional states are decoupled and can be individually quantized in the number basis of a harmonic trap. A derivation of this is given in Appendix B. Fig. 4.13 shows a schematic of the energies of the atom pair motional states in the optical tweezer. In the presence of a Feshbach resonance, the relative motional ground states adiabatically cross over to the molecular bound state[127]. These are shown as the black and purple curves; the black curve corresponds to $n_{\text{com}} = 0$, while the purple curves are center-of-mass motional excited states. The higher relative motional states adiabatically cross over to the corresponding motional state with $\Delta n_{\text{rel}} = -1$, which are shown as the blue curves. In cases where the relative and center-of-mass motions are coupled, which could arise when the trap is not perfectly separable or harmonic, some of the crossings between the purple and blue curves may be an adiabatic crossing as well[128,129,130]. These effects are expected to give only a small difference in conversion population, and we omit these for the present discussion.

  In particular, based on this picture, atom pairs can be most efficiently converted to molecules when they are in the ground state of relative motion. Based on interaction shift spectroscopy as discussed in section 3.5.2, we can directly measure the population of the relative motional ground state, which we find to be $\sim$58% under these experimental conditions. This is the population we expect to be converted into a Feshbach molecule given that all other conditions are met as well.

- *Atom hyperfine state preparation.*

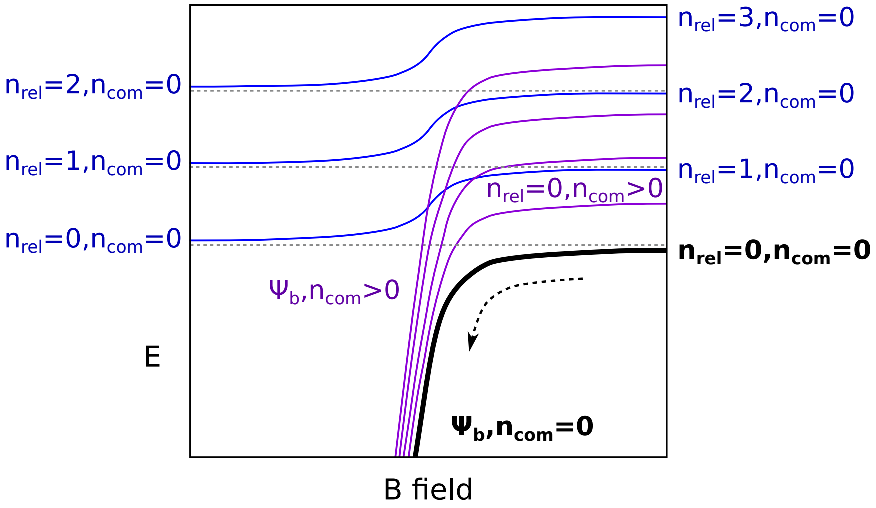

Figure 4.13: Schematic energy diagram of two atoms in a trap near a Feshbach resonance. Energy as a function of magnetic field. Bound molecular state is shown as the asymptote downwards. Bold black line corresponds to the 6D motional ground state of the atom pair $|n_{\text{rel}} = 0, n_{\text{com}} = 0\rangle$, and is capable of creating a Feshbach molecule in its center-of-mass motional ground state. Each relative motional state has multiple higher lying bands corresponding to excited center-of-mass motion, which are shown in purple for the $|n_{\text{rel}} = 0\rangle$ state. States with excited relative motion, shown in blue, cannot form molecules in the center-of-mass motional ground state. Adapted from Ref.[127].

As mentioned in section 3.3, after the atoms are cooled to their ground states and before merging the two traps, the atoms are optically pumped to the stretched state $|F = 2, m_F = 2\rangle_{\text{Na}}$, $|F = 4, m_F = 4\rangle_{\text{Cs}}$, then driven individually by Raman π-pulses to the $|F = 1, m_F = 1\rangle_{\text{Na}}$, $|F = 3, m_F = 3\rangle_{\text{Cs}}$ state. The fidelities of these are Na 0.882(24) and Cs 0.956(13), which is limited by purity of optical pumping and dephasing and decoherence during the π-pulse. This can also be seen in the difference in survival probabilities between the 1-body case and 2-body case above resonance in Figure 4.7 – any atom pair not in the desired hyperfine state or stretched state is subject to spin-changing collisions that expel both atoms from the trap[79].

- *Adiabaticity of magnetic field ramp.*

  As discussed in section 4.3.2, this is dependent on magnetic field ramp rate and follows the Landau-Zener formula. At rates below 1 G/ms in a trap with trapping frequencies $\omega_{\text{Cs}} = 2\pi \times (30, 30, 5)$ kHz and $\omega_{\text{Na}} \simeq 1.07\omega_{\text{Cs}}$, we expect the fidelity to be larger than $0.993(6)$.

Table 4.1: Step-by-step fidelities in molecule conversion

Experimental condition	Fidelity
Loading of single atoms (post-selected)	
Na	0.9996(1)
Cs	0.9983(1)
Population in relative motional ground state	0.584(44)
Atom hyperfine state preparation	
Na $\lvert F = 1, m_F = 1\rangle$	0.882(24)
Cs $\lvert F = 3, m_F = 3\rangle$	0.956(13)
Adiabaticity of magnetic field ramp	0.993(6)
Overall expected efficiency	0.48(6)

While there is much room for technical improvements to improve the conversion efficiency, we believe it is not fundamentally limited. Moreover, this is, to the best of our knowledge, to date the best conversion efficiency directly from trapped atom pairs to Feshbach molecules. Typical bulk gas experiments suffer from 3-body loss processes which cause loss of Feshbach molecules in the conversion process, leading to conversion efficiencies around ~10%[41]. In the meantime, loading single pairs of dual species atoms into individual sites of an optical lattice is also limited by the overlap and interparticle collisions in the loading process. The best efforts of heteronuclear molecules in optical lattices have been around ~30% filling fraction[52,131]. By using optical tweezers and starting with individually trapped single atoms, we mitigate the need for avoiding three-body losses, thereby increasing the conversion efficiency. Furthermore, this technique of loading heteronuclear atom pairs into the same trap is generally applicable to a wide variety of species-pairs.

4.3.6 External state of Feshbach molecule

Based on the physical picture presented in our discussion of the relative motional states above, the center-of-mass motional state of the Feshbach molecule is inherited from that of the constituent atoms, as shown by the black and purple lines in Fig. 4.13. We can therefore estimate the ground-state population by estimating the center-of-mass ground-state population of the constituent atoms. While pairs of atoms must be in the relative motional ground state to be most efficiently magnetoassociated to form molecules, they may be in an arbitrary center-of-mass motional state. We use Raman sideband thermometry on the Na and Cs single atoms (section 3.5.1) to infer the portion of the atom pairs capable of forming molecules ($|n_{\mathrm{rel}} = 0\rangle$) that are also in the center-of-mass motional ground state ($|n_{\mathrm{com}} = 0, n_{\mathrm{rel}} = 0\rangle$).

Using Raman sideband thermometry, we can obtain the mean occupation number $\bar{n}_{\mathrm{Na}},\ \bar{n}_{\mathrm{Cs}}$ of each atom along each axis individually. The relative motional ground state population $P(n_{\mathrm{rel}} = 0)$ can be expressed analytically in terms of the $\bar{n}_{\mathrm{Na}},\ \bar{n}_{\mathrm{Cs}}$ values that are measured. In particular, based on the discussion of center-of-mass and relative motional coordinates presented in Appendix B, we are interested in finding

$$
\begin{aligned}
P(n_{\text{rel}} = 0) &= \sum_{n=0}^{\infty} P(n_{\text{rel}} = 0, n_{\text{com}} = n) && (4.15)\\
&= \sum_{n_1,n_2=0}^{\infty} P(n_{\text{Na}} = n_1, n_{\text{Cs}} = n_2)\times \\
&\qquad |\langle n_{\text{rel}} = 0, n_{\text{com}} = n_1 + n_2 | n_{\text{Na}} = n_1, n_{\text{Cs}} = n_2\rangle|^2 && (4.16)\\
&= \sum_{n_1,n_2=0}^{\infty} P(n_{\text{Na}} = n_1, n_{\text{Cs}} = n_2)\times \\
&\qquad |\langle n_{\text{rel}} = 0, n_{\text{com}} = n_1 + n_2 | \frac{(a^{\dagger}_{\text{Na}})^{n_1}(a^{\dagger}_{\text{Cs}})^{n_2}}{\sqrt{n_1!n_2!}} | n_{\text{Na}} = 0, n_{\text{Cs}} = 0\rangle|^2. && (4.17)
\end{aligned}
$$

Equation 4.16 follows from equation B.7 since conservation of energy ensures the total excitation numbers in the atomic harmonic modes and center-of-mass and relative motional modes must be the same. The matrix elements in equation 4.17 can be found readily using the relations B.10 and noting that we need to consider only terms with $(n_1 + n_2)$ center-of-mass modal excitations.

$$
\begin{aligned}
&|\langle n_{\text{rel}} = 0, n_{\text{com}} = n_1 + n_2 | \frac{(a^{\dagger}_{\text{Na}})^{n_1}(a^{\dagger}_{\text{Cs}})^{n_2}}{\sqrt{n_1!n_2!}} | n_{\text{Na}} = 0, n_{\text{Cs}} = 0\rangle|^2 && (4.18)\\
&= \frac{1}{n_1!n_2!}\left|\langle n_{\text{rel}} = 0, n_{\text{com}} = n_1 + n_2 | \left(\sqrt{\frac{m_{\text{Na}}}{M}}a^{\dagger}_{\text{com}}\right)^{n_1}\left(\sqrt{\frac{m_{\text{Cs}}}{M}}a^{\dagger}_{\text{com}}\right)^{n_2} | n_{\text{rel}} = 0, n_{\text{com}} = 0\rangle\right|^2 && (4.19)\\
&= \frac{m_{\text{Na}}^{n_1} m_{\text{Cs}}^{n_2}}{M^{n_1+n_2} n_1!n_2!}\left|\langle n_{\text{rel}} = 0, n_{\text{com}} = n_1 + n_2 | \left(a^{\dagger}_{\text{com}}\right)^{n_1}\left(a^{\dagger}_{\text{com}}\right)^{n_2} | n_{\text{rel}} = 0, n_{\text{com}} = 0\rangle\right|^2 && (4.20)\\
&= \left(\frac{m_{\text{Na}}}{M}\right)^{n_1}\left(\frac{m_{\text{Cs}}}{M}\right)^{n_2}\frac{(n_1 + n_2)!}{n_1!n_2!}. && (4.21)
\end{aligned}
$$

With the assumption that the atoms take on a thermal distribution, we have

$$P(n) = \frac{1}{Z} e^{-\beta\hbar\omega(n+1/2)} \tag{4.22}$$

and

$$\bar{n} = \frac{1}{e^{\beta\hbar\omega} - 1} \tag{4.23}$$

where $\beta = 1/k_B T$ and $Z = \frac{e^{-\beta\hbar\omega/2}}{1-e^{-\beta\hbar\omega}}$ is the partition function. Let $\alpha = e^{-\beta\hbar\omega} = \frac{\bar{n}}{\bar{n}+1}$, then $P(n) = P(0)\alpha^n$. Using this, we can perform the sum in equation 4.17,

$$\begin{aligned}
P(n_{\text{rel}} = 0) &= \sum_{n_1,n_2=0}^{\infty} P(n_{\text{Na}} = n_1, n_{\text{Cs}} = n_2) \left(\frac{m_{\text{Na}}}{M}\right)^{n_1} \left(\frac{m_{\text{Cs}}}{M}\right)^{n_2} \frac{(n_1+n_2)!}{n_1! n_2!} && (4.24)\\
&= P(n_{\text{Na}} = 0) P(n_{\text{Cs}} = 0) \sum_{n_1,n_2=0}^{\infty} \left(\frac{m_{\text{Na}}\alpha_{\text{Na}}}{M}\right)^{n_1} \left(\frac{m_{\text{Cs}}\alpha_{\text{Cs}}}{M}\right)^{n_2} \frac{(n_1+n_2)!}{n_1! n_2!} && (4.25)\\
&= P(n_{\text{Na}} = 0) P(n_{\text{Cs}} = 0) \sum_{n=0}^{\infty} \left(\frac{m_{\text{Na}}\alpha_{\text{Na}}}{M} + \frac{m_{\text{Cs}}\alpha_{\text{Cs}}}{M}\right)^{n}. && (4.26)
\end{aligned}$$

Since we necessarily have $(\frac{m_{\text{Na}}\alpha_{\text{Na}}}{M} + \frac{m_{\text{Cs}}\alpha_{\text{Cs}}}{M}) < 1$, the last expression can be summed up to yield

$$P(n_{\text{rel}} = 0) = \frac{P(n_{\text{Na}} = 0) P(n_{\text{Cs}} = 0)}{1 - \frac{m_{\text{Na}}}{M}\frac{\bar{n}_{\text{Na}}}{\bar{n}_{\text{Na}}+1} - \frac{m_{\text{Cs}}}{M}\frac{\bar{n}_{\text{Cs}}}{\bar{n}_{\text{Cs}}+1}}. \tag{4.27}$$

This is the population of atom pairs that can be magnetoassociated to form molecules. On the other hand, the population of the atom pair in the absolute motional ground state is simply given by the joint probability of the two atoms being in their individual ground states,

$$P(n_{\text{rel}} = 0, n_{\text{com}} = 0) = P(n_{\text{Na}} = 0) P(n_{\text{Cs}} = 0). \tag{4.28}$$

Combining equation 4.27 and equation 4.28, we can find the molecular center-of-mass ground state fraction

$$P(n_{\text{mol-com}} = 0) = \frac{P(n_{\text{rel}} = 0, n_{\text{com}} = 0)}{P(n_{\text{rel}} = 0)} \tag{4.29}$$

$$= 1 - \frac{m_{\text{Na}}}{M} \frac{\bar{n}_{\text{Na}}}{\bar{n}_{\text{Na}} + 1} - \frac{m_{\text{Cs}}}{M} \frac{\bar{n}_{\text{Cs}}}{\bar{n}_{\text{Cs}} + 1}. \tag{4.30}$$

From Raman sideband thermometry measurements for atom conditions during these magnetoassociation experimental runs, we find the occupation numbers of the single Na, Cs atoms along each of the 3 axes (2 radial + axial) to be $\bar{n}_{\text{Na}} = \{0.09(3), 0.07(2), 0.30(6)\}$ and $\bar{n}_{\text{Cs}} = \{0.04(2), 0.08(2), 0.10(3)\}$. By applying equation 4.30 to each axis individually and taking the product, we find the molecular center-of-mass ground state population to be $P(n_{\text{mol-com}} = 0) = 77(5)\%$ as stated in the main text.

4.3.7 Feshbach molecule wavefunction

The wavefunction of the Feshbach molecular state we drive to is shown in 4.14. As discussed in section 4.1, the wavefunction is a multichannel one, and includes 8 channels with total $m_F = 4$ (Fig. 4.2). The wavefunction is computed using a coupled-channel model[132,133,117]. This is shown in the spin-coupled basis labelled by $|S, m_S; m_{I_{Na}}, m_{I_{Cs}}\rangle$ in Fig. 4.14. The admixtures of each component are tabulated in Table 4.2. The admixture is found by integrating the probability amplitude of each component in spatial coordinates. In particular, we find that the Feshbach molecule is predominantly spin-triplet in character. This has consequences for the internal state transfer to the rovibrational ground state, which is spin-singlet. This will be discussed in Chapter 5.

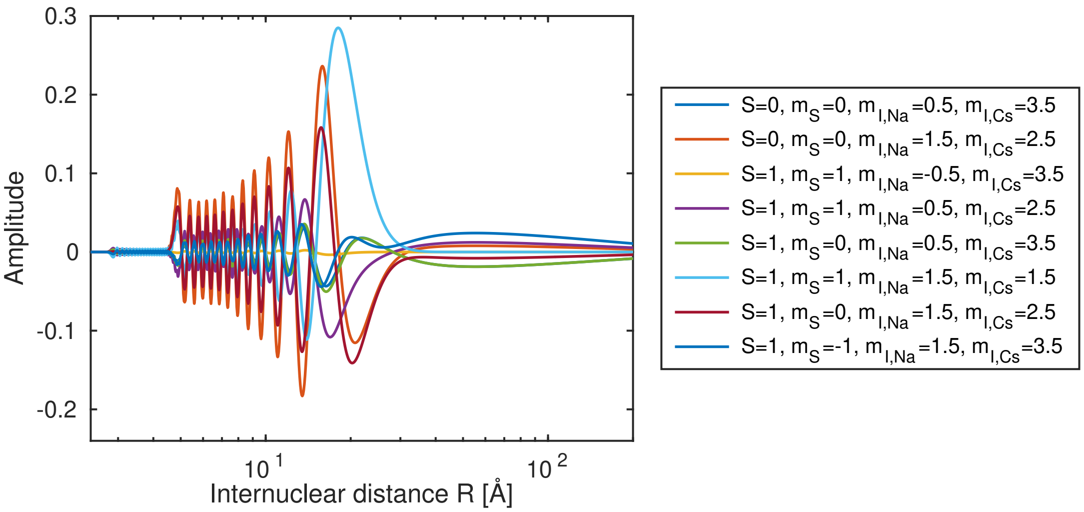

Figure 4.14: *s*-wave Feshbach molecule multichannel wavefunction. The spatially varying wavefunction amplitudes of the 8 hyperfine channels with total $m_F = +4$ at $B - B_{\text{res}} = -0.4$ G, where the binding energy of the Feshbach molecule $E_{\text{B}} \approx 1$ MHz. The wavefunctions are shown in the spin-coupled basis. The predominant admixture comes from $|S = 1, m_S = 1; m_{I_{Na}} = 1.5, m_{I_{Cs}} = 1.5\rangle$ [117].

S	M_S	$M_{I_{\text{Na}}}$	$M_{I_{\text{Cs}}}$	Admixture
0	0	$1/2$	$7/2$	0.0405
0	0	$3/2$	$5/2$	0.2336
1	1	$-1/2$	$7/2$	4.8×10^{-5}
1	1	$1/2$	$5/2$	0.0634
1	0	$1/2$	$7/2$	0.0425
1	1	$3/2$	$3/2$	0.3905
1	0	$3/2$	$5/2$	0.1663
1	-1	$3/2$	$7/2$	0.0632

Table 4.2: Theoretical electron and nuclear spin composition of the Feshbach molecule state at a magnetic field of $B - B_{\text{res}} = -0.4$ G, where experimentally $B_{\text{res}} = 864.11(5)$ G.

4.3.8 *p*-wave molecule formation

In addition to controlling the motional state of the Feshbach molecule, we can control the internal state through choice of the atomic motional states. In particular, we can use a *p*-wave resonance to form a rotationally excited molecule. A *p*-wave resonance can occur when the incoming atom pair is in an excited rotational state with $L = 1$, or when off-diagonal components in L couple by the electron spin dipole-dipole interaction term in equation 4.5[119].

While atoms in their motional ground states have no relative angular momentum, we can controllably excite the radial motional state of the Na atom by one motional quantum. In particular, starting from atoms cooled to their motional ground states, $|n_{\text{Na}} = 0, n_{\text{Cs}} = 0\rangle = |n_{\text{rel}} = 0, n_{\text{com}} = 0\rangle$, we prepare the atoms in $|n_{\text{rel}} = 1, n_{\text{com}} = 0\rangle$ by exciting one quantum of motion of Na along the radial direction. We perform the excitation using the heating motional sideband, which simultaneously prepares the hyperfine state of the atom as discussed in section 3.3.2. We can find the population in the relative-motion excited state after a single excitation of the Na atom using equations B.10. In particular, we have

$$\left|\langle n_{\text{rel}} = 1, n_{\text{com}} = 0|a^{\dagger}_{\text{Na}}|n_{\text{rel}} = 0, n_{\text{com}} = 0\rangle\right|^2 = \frac{m_{\text{Cs}}}{M} \approx 0.85 \tag{4.31}$$

Of note is that exciting the lighter (heavier) atom would give a larger excitation in the relative (center-of-mass) motion. Taking into account the fidelity of the Na motional excitation (75%), Cs hyperfine state preparation (95%), and initial relative ground-state population (40% for the p-wave molecule experiment), we expect $\sim$ 24% of the pairs to be excited in relative motion along one of the radial directions. Since the excitation is in the plane perpendicular to the magnetic field axis, the resulting state has relative angular momentum $m_L = \pm 1$.

Coupled-channel calculations predict two p-wave bound states that cross threshold near 807 G, with total molecular spin angular momentum $M_{F,\text{b}} = 4$ and 5[117]. Each of these splits into components with total angular momentum $M_{\text{tot}} = M_{F,\text{b}}$ and $M_{F,\text{b}} \pm 1$. The colliding atoms have $m_{F,\text{Na}} + m_{F,\text{Cs}} = 4$ and $M_{\text{tot}} = 3$ or 5 in the radially excited motional state. We thus expect 3 resonant features for such atoms. We detect these features by Feshbach resonance-enhanced photoassociation, similar to the case of the s-wave resonance in section 4.3.4, as shown in Fig. 4.15. The two atoms are held for 20 ms in a tweezer with peak inten-

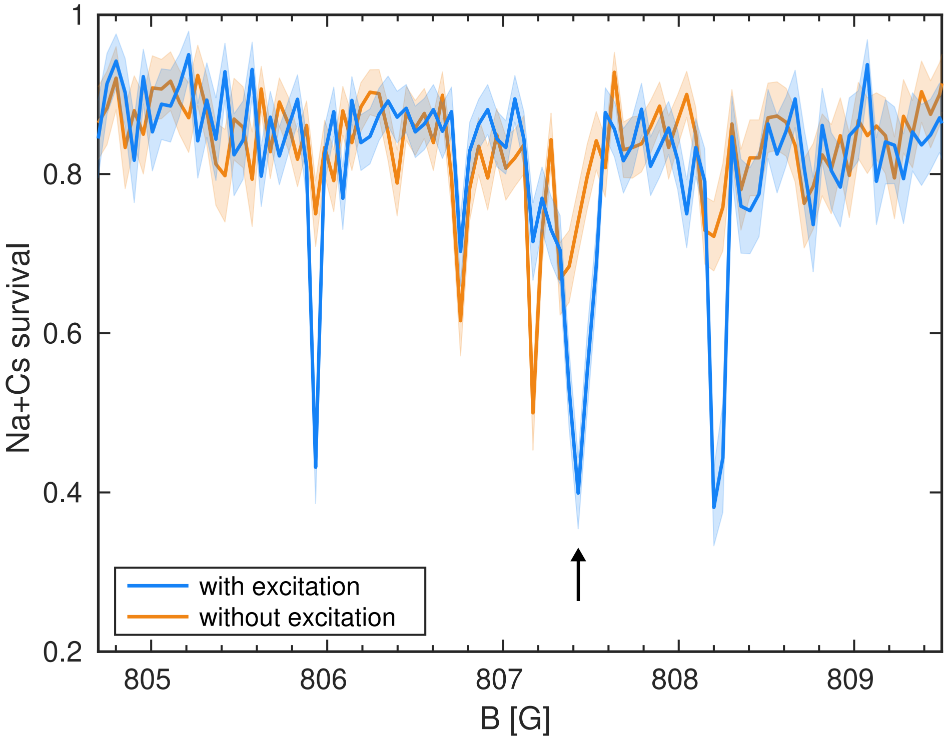

Figure 4.15: *p*-wave Feshbach resonance spectroscopy by Feshbach resonance-enhanced photoassociation. The atoms are held at fixed magnetic fields in an intense tweezer, which provides the photoassociation light. Blue (orange) line shows the spectrum with (without) relative motional excitation of $\Delta n = +1$ of Na. Shaded areas indicate error bars. We find various features that are enhanced with the motional excitation, suggesting the *p*-wave character. The arrow indicates the resonance used for magnetoassociation in Fig. 4.16.

sity 1350 kW/cm^2 after merging the traps at a magnetic field value that is scanned. We detect simultaneous two-body loss when the atoms are photoassociated via the excited electronic states by the tweezer light. For comparison, we also show the same scan without the motional excitation on Na.

As for the *s*-wave Feshbach molecules, we can ramp the magnetic field across a *p*-wave Feshbach resonance to transfer the atoms into a *p*-wave molecule. Fig. 4.16(a) shows the survival probability when the magnetic field is ramped linearly down from 807.6 G to various fields at a rate of 0.02 G/ms in the tweezer held at 81 $\mathrm{kW/cm^2}$ peak intensity. We observe a clear 2-body loss feature when we perform the motional excitation, in contrast to the case of no motional excitation. We attribute this to *p*-wave molecule formation and find a conversion efficiency of 16(2)%.

As discussed in section 4.3.1, in order to demonstrate that the apparent loss upon ramping over the Feshbach resonance does not arise from incoherent photoassociation during the ramp, we perform a separate experiment that ramps the magnetic field upwards instead and contrast it to the case of ramping the magnetic field downwards. The orange points in Fig. 4.16(b) shows the survival probability when the magnetic field is ramped linearly upwards from 807 G to various fields at a rate of 0.02 G/ms in the tweezer held at 81 $\mathrm{kW/cm^2}$ peak intensity. In both the upward and downward ramp cases, the radial motion of Na is excited by $\Delta n = +1$. We see that in the upward ramp case, there is loss near the Feshbach resonance location which may be due to Feshbach resonance-enhanced photoassociation during the trap separation process. However, the 2-body survival revives after ramping across the resonance and the trap separation is completed off-resonance.

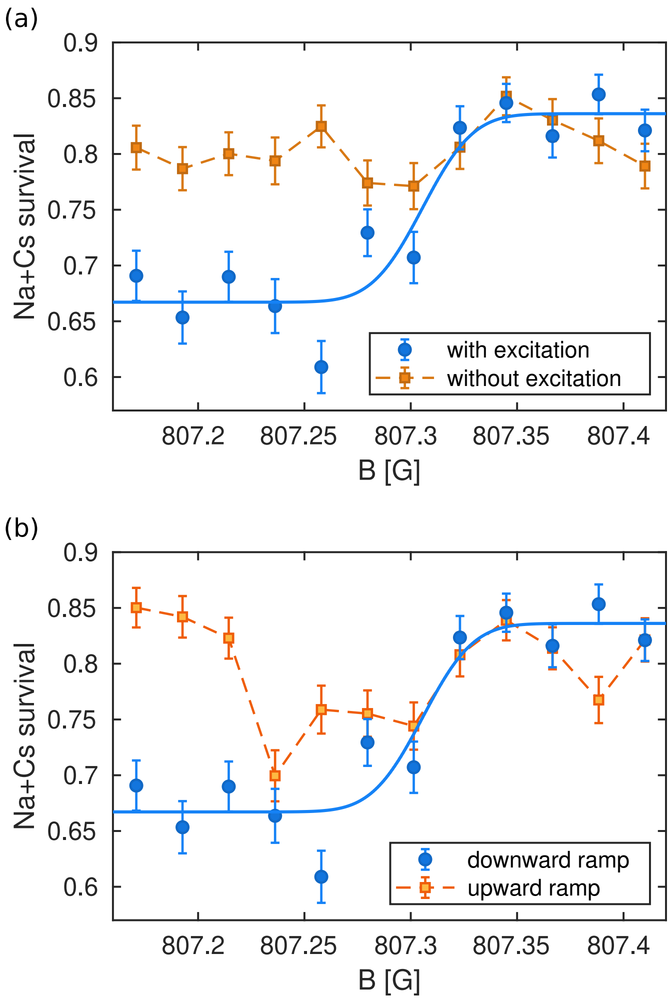

Figure 4.16: *p*-wave Feshbach molecule formation. By exciting the atom pair to a relative motional excited state and using a *p*-wave Feshbach resonance, we can magnetoassociate to a *p*-wave Feshbach molecule. The magnetic field is ramped linearly from 807.6 G downwards to the various magnetic fields at 0.02 G/ms. Blue (orange) points shows results with (without) radial motional excitation of $\Delta n = +1$ of Na. We fit the blue (orange) data points to an error function (mean value across the range), and find a magnetoassociation signal with motional excitation.

4.4 Summary and outlook

In this chapter, we presented results on the first Feshbach resonance spectroscopy studies of the heteronuclear Na+Cs system, including both inelastic and elastic resonances. This was achieved by a combination of atom-loss spectroscopy, magnetoassociation spectroscopy and Feshbach resonance-enhanced photoassociation spectroscopy.

By using a suitable *s*-wave resonance in the lowest Zeeman energy level, we were able to magnetoassociate a single pair of Na and Cs atoms to form a single weakly-bound *s*-wave Feshbach molecule. Crucially, this process is fully coherent, as evidenced by the Landau-Zener type dependence of adiabaticity, as well as the ability to measure a lifetime curve. We achieve up to ~50% conversion efficiencies, and there is still room to improve the efficiency, which we believe is not fundamentally limited. Since the process is fully coherent, the resulting molecule is in a fully defined internal and external state, governed by the internal and external states of the atom pair. Such a fully-controlled molecule in an optical tweezer provides the first step to create a fully quantum state controlled molecule in its rovibrational ground state, which will be the subject of the next chapter. The ability to detect and utilize Feshbach resonances in optical tweezers also establishes the platform as a viable candidate for the investigation of few-body physics, such as Efimov physics and other collisional studies[134,135].

5

Coherent transfer to rovibrational ground state molecule

In the previous chapter we presented results on magnetoassociating a single NaCs Feshbach molecule using an s-wave Feshbach resonance. While this is a bound molecule we form with full quantum state control, this molecule has only a small dipole moment due to the large bond length (the dipole moment of a diatomic molecule scales with internuclear separation as R^{-7} asymptotically[136]), and has a short lifetime in the optical tweezers. This makes them unsuitable for most applications requiring stable molecules with a large dipole moment. In this chapter, we will present results on transferring the molecule from the Feshbach molecular state to the rovibrational (meaning both rotational and vibrational) ground state of NaCs. The resulting state is the most stable against relaxations, and has a large dipole moment of 4.6 D[76,77].

As in the step of magnetoassociation, the transfer process needs to be coherent to populate a single final state while also preserving the external state of the molecule. The standard approach for transferring to the rovibrational ground state of bi-alkali molecules has been to use STimulated Adiabatic RAman Passage (STIRAP) via an intermediate state[41,137,138,123,46,139,43,44]. This process transfers population between two ground states adiabatically by ramping the amplitudes of two Raman beams in a two-photon process[140]. In the present work however, we found it more straightforward to perform a direct detuned Raman π-pulse transfer. A schematic of the transfer process is shown in Fig. 5.1.

In section 5.1, we provide the background for the Raman transfer process presented in this chapter, including the idealized three-level system, Raman transfer, STIRAP and dark resonance. In section 5.2 we provide a description of the laser set up that enabled the studies in this chapter. In section 5.3, we present spectroscopy results for a specific vibrational state in the $c^3\Sigma_1$ excited state manifold. We discuss a model that we use to assign the states and find a suitable intermediate state for transfer. In section 5.4, we discuss dark resonance spectroscopy that we used to locate the rovibrational ground state in the $X^1\Sigma$ potential. These together lead to the results in section 5.5, where we show the first coherent creation of a ground state NaCs molecule by use of a detuned π-pulse transfer. In section 5.6, we characterize some of the properties of the rovibrational ground state molecule that we form in the optical tweezers. Before concluding, we briefly discuss our initial attempts at STIRAP transfer and discuss its

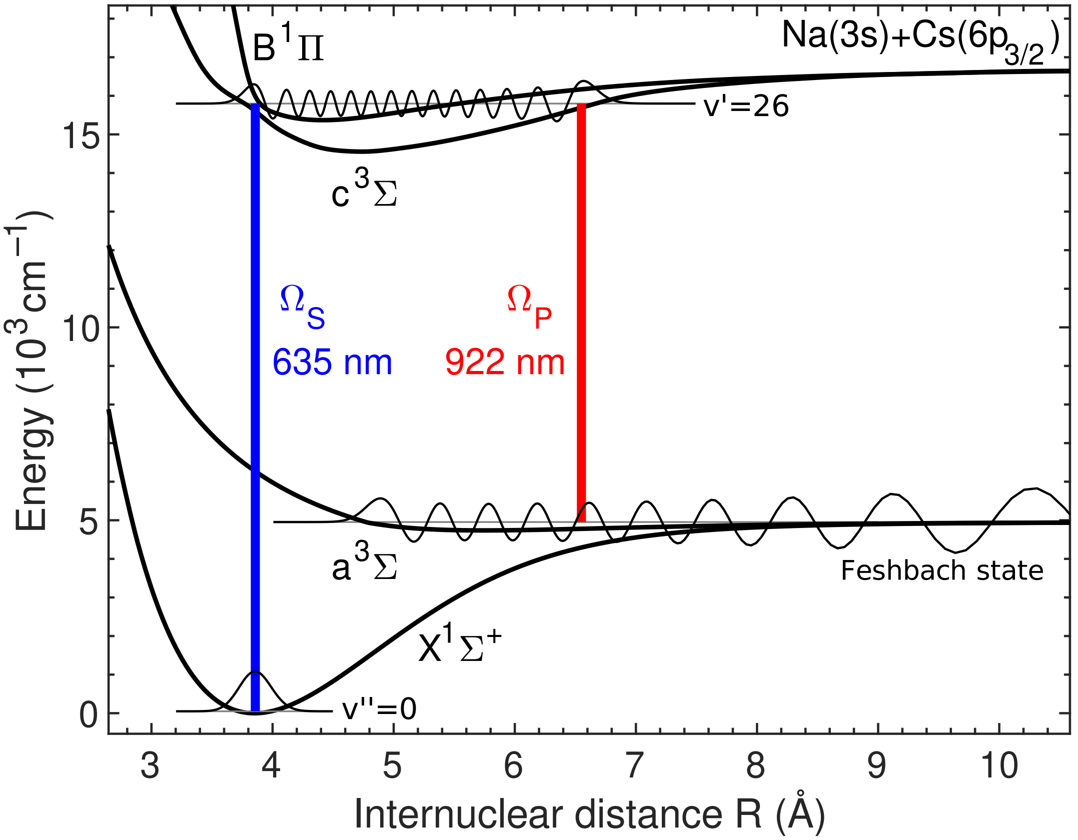

Figure 5.1: NaCs molecular potentials and states relevant for coherent transfer. We transfer from the Feshbach state to the rovibrational ground state in the $X^1\Sigma$ potential using a two-photon process through a specific intermediate state in the $c^3\Sigma_1$ excited state potential, which asymptotes to Na(3s)+Cs(6p$_{3/2}$). $c^3\Sigma_1$ is mixed by spin-orbit coupling with $B^1\Pi$, which provides the necessary bridge to convert from a predominantly spin-triplet state to a pure spin-singlet state. The wavelengths of the pump and Stokes beams are 922 nm and 635 nm respectively.

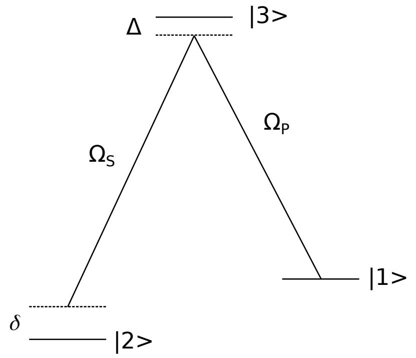

Figure 5.2: Schematic of three level system. States $|1\rangle, |2\rangle$ are coupled to an intermediate state $|3\rangle$ with Rabi frequencies Ω_P, Ω_S and single- and two-photon detunings Δ, δ respectively. The intermediate state suffers scattering at a rate Γ.

limitations in the present system in section 5.7.

5.1 Background

The Hamiltonian for an atom with three levels $|1\rangle, |2\rangle, |3\rangle$ addressed with two lasers with single- and two-photon detunings δ and Δ respectively, and coupling the respective transitions with Rabi frequencies Ω_P and Ω_S (corresponding to pump and Stokes respectively) can be written in the rotating wave approximation as[140]

$$H = \hbar \begin{pmatrix} 0 & 0 & \Omega_P \\ 0 & -\delta & \Omega_S \\ \Omega_P & \Omega_S & -\Delta - i\Gamma/2 \end{pmatrix} \tag{5.1}$$

Here, an imaginary $i\Gamma/2$ term is included to account for scattering from the intermediate excited state. A schematic of the energy levels is shown in Fig. 5.2.

As we will see below, there are in fact multiple levels in the excited state molecular structure. In addition, in our system we find a large scattering rate from the excited states Γ that is comparable to the inter-level spacing in the excited state. Therefore, in certain cases it is also necessary to include additional states to account for these effects. For the present discussion however, we focus on an ideal three-level system. This will be discussed in section 5.7.

STIRAP

In previous bi-alkali molecule coherent association work, the technique used was STIRAP. In this process, the lasers are tuned to be on two-photon resonance, such that $\delta = 0$. With this, one of the energy eigenstates of the Hamiltonain can be written as

$$|\Phi_0\rangle = \cos\theta|1\rangle - \sin\theta|2\rangle \tag{5.2}$$

where $\tan\theta = \frac{\Omega_P}{\Omega_S}$. For $\tan\theta \to 0$, $|\Phi_0\rangle \to |1\rangle$, whereas for $\tan\theta \to +\infty$, $|\Phi_0\rangle \to |2\rangle$. Therefore, by ramping Ω_P and Ω_S such that the eigenstates asymtotically start as $|1\rangle$ and $|1\rangle$, one can obtain adiabatic transfer of population from $|1\rangle$ to $|2\rangle$ without populating the excited state $|3\rangle$ significantly. This requires ramping Ω_S up before ramping Ω_S down and Ω_P down, what is known as a counter-intuitive fashion.

Complications to STIRAP arise, however, when we consider multiple excited levels. The ramp in amplitudes cause light shifts from the detuned transitions that shift the two-photon resonance. In addition, this causes the eigenstates to have components in the excited states, leading to scattering from the other excited levels.

Detuned Raman π-pulse transfer

An alternate approach to driving the population from $|1\rangle$ to $|2\rangle$ with minimal population in state $|3\rangle$ is to use a large single-photon detuning Δ. In this case, the excited state can be eliminated, and one obtains an effective transition between states $|1\rangle$ and $|2\rangle$. The effective two-photon Rabi rate is given by[140]

$$\Omega_R = \frac{\Omega_P \Omega_S}{\Delta} \tag{5.3}$$

In addition, the lasers induce a differential light shift on the transition, given by

$$\Delta E = \frac{\Omega_P^2}{\Delta} - \frac{\Omega_S^2}{\Delta} \tag{5.4}$$

In principle, both lasers can couple to both transitions which give rise to light shifts. For the 3-level system of interest here however, the laser is far off detuned when addressing the alternate transition, and one only needs to consider the terms from direct coupling of the dominant transition. The lasers also incur scattering, whose rate is given by

$$R_{\text{sc}} = \frac{\Gamma \Omega_P^2}{\Delta^2} + \frac{\Gamma \Omega_S^2}{\Delta^2} \tag{5.5}$$

In the case of multiple excited levels, the Rabi frequencies and light shifts sum over all the excited states. However, the system is conceptually more simple compared to STIRAP, as the single-photon detuning Δ is large and the laser beam is far-detuned from all excited states.

5.2 Experimental setup

For the results presented in this chapter of the thesis, the relative orientation of the laser beams used for spectroscopy and Raman transfer on the apparatus side is shown in Fig. 2.16. The 922 nm and 635 nm beams are launched from separate fibers and combined with a dichroic. The combined beam is sent through a telescope to expand the beam size before being focused down to the atoms with an achromat with $f = 50$mm. This gives a spot size of ~10 μm for both beams at the location of the atoms. Since the beam is counter-propagating with the tweezer beampath, the beams are first rough-aligned using the Andor EMCCD camera that

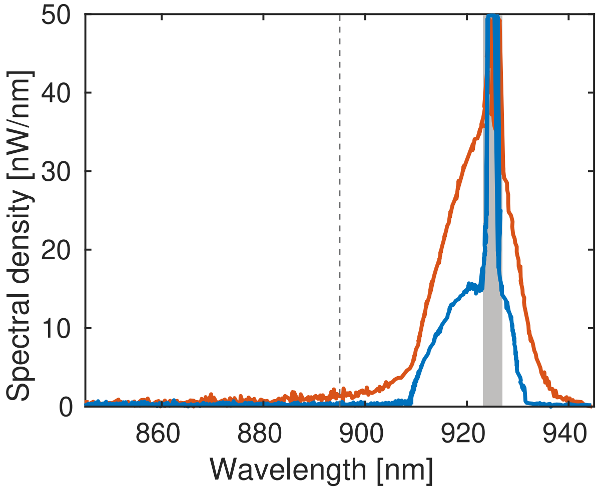

Figure 5.3: Comparison of 922 nm laser with and without ASE filter. Optical spectrum measured after tapered amplifier. The ASE filter is placed after the tapered amplifier. Gray shaded area indicates central frequency. Dashed line corresponds to Cs D2 line near 894.5 nm.

we use to image single atoms. The beam is then fine-aligned to the atoms using a vector light shift measurement. As discussed in section 3.3.1, the hyperfine levels of the Cs atoms experience a vector light shift in the presence of circular polarized light, the magnitude of which is proportional to beam intensity. We use this to optimize the beam pointing of the 922 nm beam. We measure a 500 kHz light shift with 20 mW power, which allows us to obtain the corresponding intensity value at the atoms. Since 635 nm does not induce significant light shift on either of the atoms, we rely on aligning the 635 nm beam to the 922 nm beam on the camera.

The setup for the lasers including locking schematic is shown in Fig. 2.14. Of particular note is that we found it necessary to filter the laser beams. The broad pedestal in the light as shown in Fig. 5.3 was sufficient to depump the atoms. We use amplified spontaneous emission (ASE) filters before the fibers for both beams (Coherent/Ondax 118-ER315-004 and 114-ER464-001 for 635 nm and 922 nm respectively). These have a bandwidth of ~100s of GHz.

Fig. 5.3 shows a comparison of the optical spectrum for the 922 nm laser with and without an ASE filter after the tapered amplifier.

5.3 Excited state spectroscopy

A two-photon transfer to the ground state had not been previously performed in NaCs, necessitating first a search for and characterization of a suitable intermediate state as well as locating the ground state resonance. In this section we discuss the excited state spectroscopy performed to identify an appropriate intermediate state.

Based on predictions based on the potentials in Ref.[141], we choose $|c^3\Sigma_1, v' = 26\rangle$ as an intermediate state due to several factors:

- It has relatively high Franck-Condon overlap with the Feshbach molecule state.
- It is expected to have strong transition dipole moments to both the Feshbach molecule and rovibrational ground states due to the large spin-orbit coupling constant of the Cs atom. The Feshbach molecular state is predominantly spin-triplet in character, while the rovibrational ground state is purely spin-singlet.
- It is accessible from the Feshbach molecule and rovibrational ground states with convenient laser wavelengths of 922 nm and 635 nm, respectively (see Fig. 5.1).

5.3.1 Spectroscopy

We used a prediction based on the potential curves of Ref.[141], and located $|c^3\Sigma_1, v' = 26\rangle$ using photoassociation spectroscopy[142], as shown in Fig. 5.4. The atom pairs are Raman sideband cooled and merged into a single trap at different magnetic fields. The 922 nm beam is turned on for 20 ms. We post-process on experimental runs with pairs of Na+Cs loaded, and

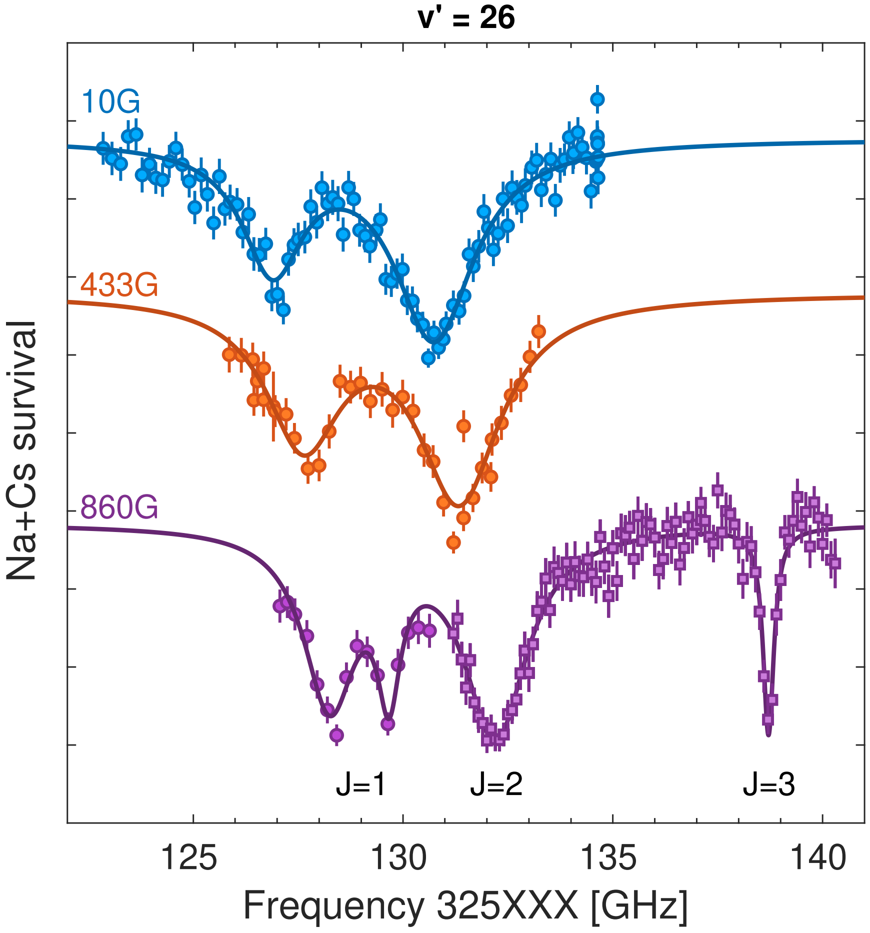

Figure 5.4: Photoassociation spectroscopoy of $|c^3\Sigma_1, v = 26\rangle$. A single pair of Na+Cs atoms is excited with the 922 nm laser at various magnetic fields. Circle (square) points correspond to data taken with $\sigma^+ + \sigma^-$ (pure σ^+) polarization. The photoassociation pulse is applied for 20ms. The peaks are fit to Lorentzian lineshapes to serve as a guide to the eye.

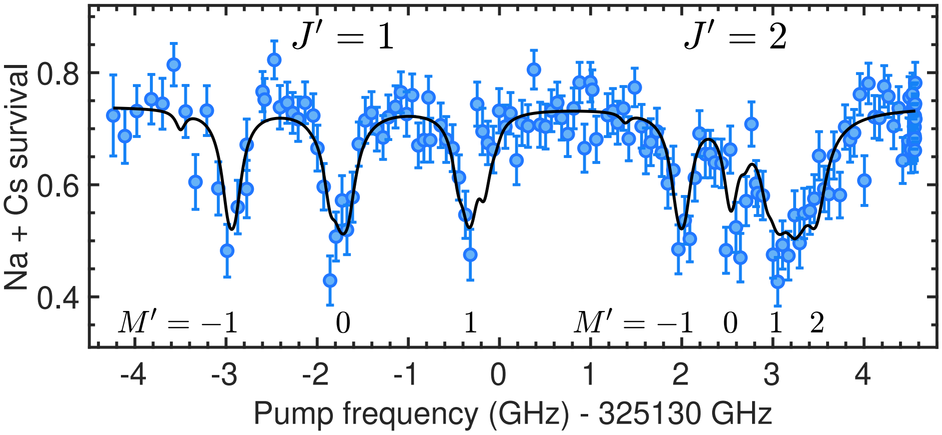

Figure 5.5: Hyperfine-resolved depletion spectroscopy of $|c^3\Sigma_1, v' = 26, J = 1, m_J = 1\rangle$. Feshbach molecules are excited with the 922 nm laser with $\sigma^+ + \sigma^-$ polarization for 20 µs. The magnetic field is set at -0.3 G below the Feshbach resonance.

look for correlated Na+Cs atom loss. Measuring the photoassociation spectra as a function of various magnetic fields allows us to identify the J components and rotational splitting of the excited state[34]. In particular, we find features near 325130 GHz that we identify as the $J = 1, 2, 3$ components of $|c^3\Sigma_1, v' = 26\rangle$.

To further resolve the hyperfine structure of the excited state, we perform depletion spectroscopy on the Feshbach molecules, which have better Frank-Condon overlap with the excited states. Fig. 5.5 shows a high-resolution spectrum of the transition from the Feshbach state to the $J' = 1$ and $J' = 2$ manifolds, where J' is the rotational plus electronic angular momentum in the $c^3\Sigma_1$ state, along with a model that incorporates the excited state structure that will be discussed in section 5.3.2.

5.3.2 $c^3\Sigma_1$ model

In order to to identify the various lines we observe in the depletion spectroscopy in Fig. 5.5, we model the hyperfine structure of the lowest few rotational levels of the excited state and coupling matrix elements with the Feshbach molecular state.

Excited state Hamiltonian

The Hamiltonian for the lowest few rotational levels of the $c^3\Sigma_1$ excited state can be written as

$$H_{c^3\Sigma_1} = H_{\text{rot}} + H_{\text{hf}} + H_Z + H_\Omega \tag{5.6}$$

where the rotational, hyperfine and Zeeman parts are

$$H_{\text{rot}} = B\mathbf{J}^2 \tag{5.7}$$

$$H_{\text{hf}} = \alpha_{\text{Na}}\mathbf{I}_{\text{Na}} \cdot \mathbf{S} + \alpha_{\text{Cs}}\mathbf{I}_{\text{Cs}} \cdot \mathbf{S} \tag{5.8}$$

$$H_Z = g_S\mu_B\mathbf{B} \cdot \mathbf{S} \tag{5.9}$$

The Ω-doubling Hamiltonian matrix elements,

$$\langle\Omega'|H_\Omega|\Omega\rangle = \frac{\omega_{ef}}{2}\delta_{\Omega',-\Omega}, \tag{5.10}$$

cause the eigenstates of effective Hamiltonian $H_{c^3\Sigma_1}$ to be states of good parity $|P = \pm\rangle \sim |\Omega\rangle \pm |-\Omega\rangle$. We access only one of these parity states in the experiment, so the value of ω_{ef} cannot be determined.

To compute the Franck-Condon coupling to the Feshbach molecular state, we model the vibrational structure of the $c^3\Sigma_1$ state using the experimental potential given in Ref.[141]. We note that this assumes the same vibrational wavefunction for both the spin-singlet and spin-triplet components.

Coupling matrix elements

The laser couples the ground and excited states by the term[34]

$$H_{\text{laser}} = -\mathbf{d} \cdot \mathcal{E}_{\text{laser}} = \sum_{p=-1}^{1} (-1)^p T_{-p}(\mathbf{d}) T_p(\varepsilon_{\text{laser}}) \tag{5.11}$$

and the matrix element between an initial state *i* and final state *f*, *k*, where *f* indicates final and *k* is the label of the specific state is

$$\langle \psi_i | H_{\text{laser}} | \psi_{f,k} \rangle \tag{5.12}$$

In the present case, $|\psi_i\rangle$ corresponds to either the Feshbach molecule state wavefunctions we find in section 4.3.7 or free atoms pairs that are bound by the harmonic trapping potential. The wavefunctions for the latter can be found by solving for bound states of the multichannel Hamiltonian in equation 4.1 along with a harmonic confinement potential. The individual states $|\psi_{f,k}\rangle$ correspond to the eigenstates of the Hamiltonian in equation 5.6. For this, we choose to work in the Hund's case (b) basis[34].

The resulting scattering rate during a photoassociation pulse can be expressed as

$$R_{\text{sc}}(\nu_{\text{laser}}) = \text{Im} \sum_k \frac{|\langle \psi_i | H_{\text{laser}} | \psi_{f,k} \rangle|^2}{(E_{f,k} - E_i)/h - \nu_{\text{laser}} + i\Gamma} \tag{5.13}$$

Fitting

Using equation 5.13, we can model the photoassociation spectrum by

$$P_{\text{surv}} = P_{\text{mol}} e^{-R_{\text{sc,mol}} t} + P_{\text{offset}} e^{-R_{\text{sc,atom}} t} \tag{5.14}$$

where P_{mol} is the Feshbach molecule population, and P_{offset} accounts for the atom population not converted to Feshbach molecules which is still susceptible to photoassociation albeit at a much slower rate.

The rotational constant is fixed by our photoassociation measurement in Fig. 5.4 giving B=0.962 GHz, and we take the value of ω_{ef} to be 1 MHz. The free parameters in the model are $\alpha_{\text{Na}}, \alpha_{\text{Cs}}$ and $P_{\text{mol}}, P_{\text{atom}}$. From this, we find $\alpha_{\text{Na}} = -0.57(4)$ GHz and $\alpha_{\text{Cs}} = 0.37(1)$ GHz. The fit is shown as the solid line in Fig. 5.5. In particular, this allows us to identify the various lines, and provides a model for the states involved in the Raman transfer process discussed later in this chapter.

5.3.3 Linewidth characterization of $|c^3\Sigma_1, v' = 26, J' = 1, M_J' = 1\rangle$

The linewidth of the intermediate state has a significant influence on our state transfer scheme as we will see in section 5.5 and 5.7. In earlier molecular association experiments, the molecular excited state used as an intermediate had a width comparable to that of the atomic transition to which it is asymptotically connected. In our system, that would be the Cs 6s → 6p transition, with a natural linewidth of order $\Gamma_{\text{atom}}/2\pi \approx 5$ MHz. However, we measure the linewidth for $|c^3\Sigma_1, v' = 26, J' = 1, M_J' = 1\rangle$ to be $\Gamma/2\pi = 120(30)$ MHz as shown in Fig. 5.6, where M_J' is the projection of J' onto the laboratory magnetic field. This is more than an order of magnitude larger than the atomic linewidth.

In previous experiments of photoassociation to other excited states in the 1.0 generation apparatus, a dependence of the linewidth on the tweezer was observed[84]. To eliminate the possibility of two-photon effects, whether coupling to excited states or to the motional continuum of the ground state, we also measured the linewidth with the tweezer dropped over the duration of the depletion pulse (2 µs). In particular, we jump the AOBD frequency controlling the 1064 nm tweezer beam 10 MHz away during the course of the 10 µs depletion pulse.

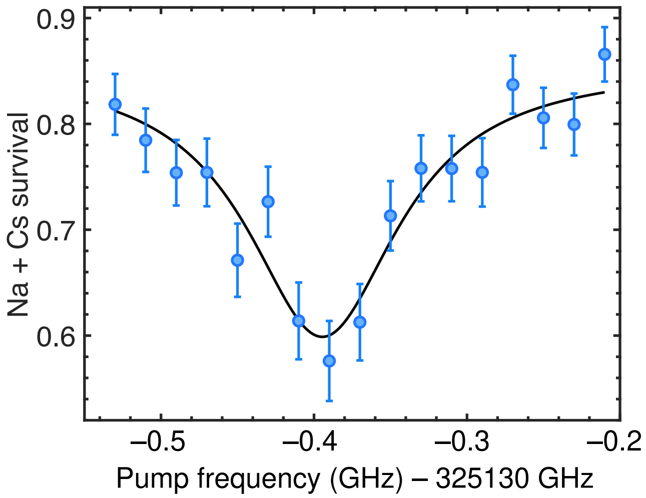

Figure 5.6: Linewidth measurement of $|c^3\Sigma_1, v' = 26, J' = 1, m_J' = 1\rangle$. The line is probed with σ^+ polarization. The curve is a fit to a Lorentzian lineshape, with fit linewidth $\Gamma = 2\pi \times 120(30)\,\mathrm{MHz}$.

Since the beam is intensity stabilized after the AOBD, this results in the beam power maintaining the same over the course of the drop and avoids integrator wind-up issues of the servo. Using this method, we find no significant change in excited state linewidth, which eliminates the possibility of two-photon transitions broadening the apparent linewidth.

We also characterized the scattering arising from all $|c^3\Sigma_1, v' = 26\rangle$ lines when red-detuned from resonance, as shown in Fig. 5.7. We find scattering rates consistent with our independent measurements of the $|c^3\Sigma_1, v' = 26\rangle$ linewidth and transition strength, with the addition of a background scattering rate of $[200(100)\,\mu\mathrm{s}]^{-1}$ that may arise from further-detuned states.

5.4 Ground state spectroscopy

Having identified $|c^3\Sigma_1, v' = 26\rangle$, we next set out to locate the rovibrational ground state in the $X^1\Sigma$ potential using dark resonance spectroscopy. In this section, we will first discuss a model to describe the structure of the rovibrational ground state, which aided in our spectroscopy, then show the experimental results.

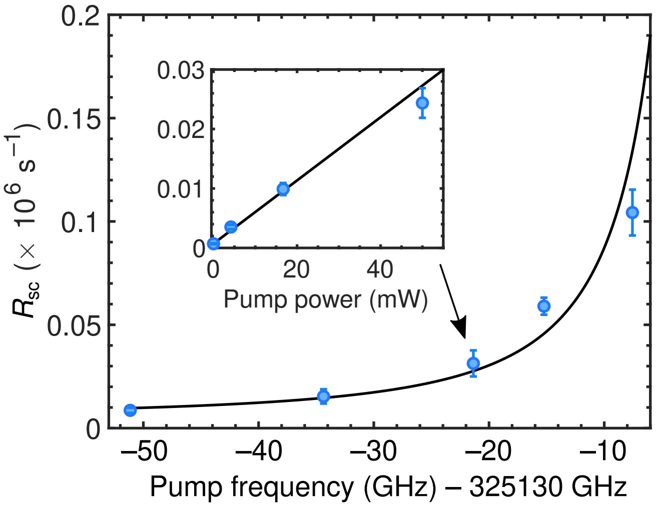

Figure 5.7: Scattering rate from $|c^3\Sigma_1, v' = 26\rangle$. The single-photon scattering rate $R_{\rm sc}$ due to the pump laser when red-detuned from $|c^3\Sigma_1, v' = 26\rangle$ is characterized. The curve is a fit to the scattering rate derived from the same model discussed in section 5.3.2. Inset: the linear dependence of the scattering rate on the pump laser power at the -21 GHz detuning is consistent with single-photon scattering.

5.4.1 $X^1\Sigma$ model

In the $X^1\Sigma$ ground state, there is no electron spin, and the relevant quantum numbers are N, I_1, I_2. In particular, the Hamiltonian for the molecule in the $X^1\Sigma$ state can be expressed as[143]

$$H_{X^1\Sigma} = H_{\rm rot} + H_{\rm hf} + H_{\rm Z} \tag{5.15}$$

The rotational part

$$H_{\rm rot} = B_v \mathbf{N}^2 \tag{5.16}$$

The centrifugal distortion is typically very small and is omitted. The hyperfine component

$$H_{\rm hf} = \sum_{i=1,2} \mathbf{V}_i : \mathbf{Q}_i + \sum_{i=1,2} c_i \mathbf{N}\cdot\mathbf{I}_i + c_3 \mathbf{I}_1 \cdot \mathbf{T} \cdot \mathbf{I}_2 + c_4 \mathbf{I}_1 \cdot \mathbf{I}_2 \tag{5.17}$$

Here, the first term is the interaction between the the nuclear electric quadrople tensor $\mathbf{Q}_i$ and the electric field gradient produced by the electrons experienced by the respective nucleus $\mathbf{Q}_i$. The second term is the interaction of the nuclear magnetic moments and the rotation of the molecule. The third and fourth terms are the tensor and scalar nuclear-nuclear interaction terms respectively.

Finally the Zeeman term is

$$H_Z = -g_r \mu_N \mathbf{B} \cdot \mathbf{N} - \sum_{i=1,2} g_i \mu_N \mathbf{I}_i \cdot \mathbf{B}(1 - \sigma_i) \tag{5.18}$$

where the first term is from a magnetic moment that arises from the molecular rotation, and the second describes the interaction of the nuclear magnetic moments with the magnetic field.

We use hyperfine constants from Ref.[143], and for the vibrational wavefunction we use the $X^1\Sigma$ potential from Ref.[113].

Couplings

A diagonalization of $H_{X^1\Sigma}$, together with the wavefunctions for the Feshbach molecular state and diagonalization of $c^3\Sigma_1$ above, gives us a complete picture of the initial, intermediate, and final states that the lasers can drive between.

As discussed in section 5.3.2, we can find the coupling matrix elements between the intermediate state and the components in the $X^1\Sigma$ ground state using equation 5.11. Due to the multi-level structure of the excited state and strong scattering from neighboring states, we need to consider the additional excited states for dark resonance spectroscopy as well as Raman transfer.

For dark resonance spectroscopy, the intermediate state on single-photon resonance provides the strongest coupling. However, other states may still contribute to scattering. To opti-

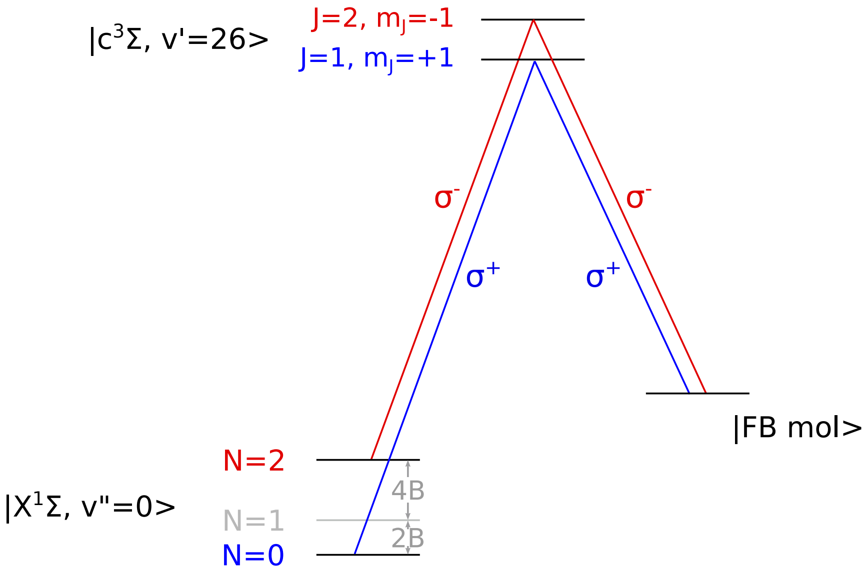

Figure 5.8: Transition schematic for $|X^1\Sigma, v = 0, N = 0\rangle$ and $|X^1\Sigma, v = 0, N = 2\rangle$ search using dark resonance spectroscopy.

mize for coherent coupling, we compare $\Omega_P\Omega_S$, where Ω_P, Ω_S are the pump and Stokes Rabi frequencies respectively, with the sum of off resonant scattering rates through all the other excited states. Given the geometric constraints of the pump and Stokes laser beams addressing the atoms in our systems, we find that σ^+ for both pump and Stokes beams coupled through the intermediate state $|c^3\Sigma_1, v' = 26, J = 1, m_J = +1\rangle$ provides the best coupling. This couples the Feshbach molecular state to predominantly the $|M''_{I_{\mathrm{Na}}} = 3/2, M''_{I_{\mathrm{Cs}}} = 5/2\rangle$ hyperfine component in the ground state. This pathway is shown in blue in Fig. 5.8.

5.4.2 Dark resonance spectroscopy

$|X^1\Sigma, v = 0, N = 0\rangle$

Having understood the relevant states, we perform dark resonance spectroscopy to locate the rovibrational ground state. We set the pump beam on resonance with the transition to the

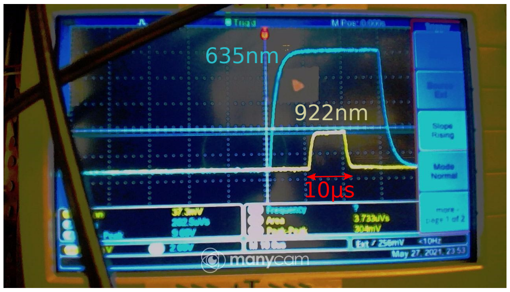

Figure 5.9: Pulse timing for dark resonance spectroscopy. The pump beam is turned on for 10 µs, while the Stokes beam is turned on for 30 µs to ensure the dark resonance condition.

$|c^3\Sigma_1, v' = 26, J = 1, m_J = +1\rangle$ line, and scan the frequency of the Stokes laser. When the two lasers are not on two-photon resonance, the pump beam depletes the Feshbach molecule population, which results in correlated Na+Cs atom pair loss. On the other hand, when the two lasers are on two-photon resonance, we observe a suppressed depletion of Feshbach molecules due to a dark resonance in the presence of the lasers. The timing of the pulses is shown in Fig. 5.9. The length of the pump beam pulse 10 µs is chosen to be just long enough to deplete the molecules. The Stokes beam pulse is set to be wider than the pump beam pulse before and after by 10 µs each to ensure the state is dark when the pump beam is on.

Fig. 5.10 shows the dark resonance spectra obtained with different Stokes beam intensities. Based on this, we narrow down the Stokes transition to be 472166.16(9) GHz, dominated by the uncertainty in wavemeter reading. This measurement provides a value of the NaCs binding energy $D_0 = 147044.86(11)$ GHz of the $v = 0$ state with respect to the degeneracy-weighted atomic hyperfine centroid at zero magnetic field.

$|X^1\Sigma, v = 0, N = 2\rangle$

To unambiguously identify this as the rovibrational ground state, we also performed additional dark resonance spectroscopy to locate the $|X^1\Sigma, v = 0, N = 2\rangle$ state. Due to parity selection

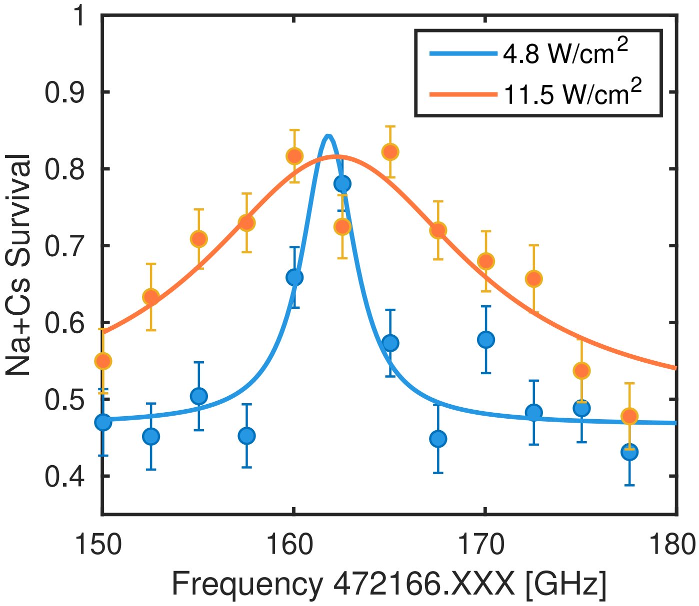

Figure 5.10: Dark resonance spectroscopy to locate $|X^1\Sigma, v = 0, N = 0\rangle$. The pump beam is set on resonance with the $|c^3\Sigma_1, v' = 26, J = 1, m_J = +1\rangle$ transition. σ^+ polarization is used for both pump and Stokes beams. The Stokes beam frequency is scanned at two different beam intensities. The features are fit to Lorentzian lineshapes to extract the resonance location.

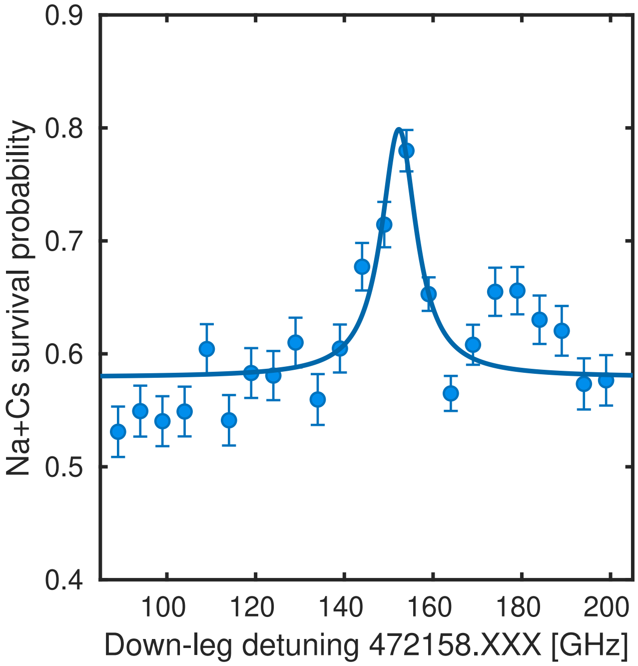

Figure 5.11: Dark resonance spectroscopy locating $|X^1\Sigma, v = 0, N = 2\rangle$. The pump beam is set on resonance with the $|c^3\Sigma_1, v' = 26, J = 2, m_J = -1\rangle$ line. σ^- polarization is used for both pump and Stokes beams.

rules, we cannot use a two-photon Raman transition to drive to $N = 1$ from the Feshbach molecular state, and $N = 2$ is the next nearest state we can observe.

We found that due to different coupling strengths and the presence of strong scattering in the excited state mentioned above, this required a different intermediate state and polarization combination to couple most favorably to the $|X^1\Sigma, v = 0, N = 2\rangle$ state. Whereas when driving to the $N = 0$ state we use the intermediate state $|c^3\Sigma_1, v' = 26, J = 1, m_J = +1\rangle$ and σ^+ polarization for both beams, to couple to the $N = 2$ state, we use the intermediate state $|c^3\Sigma_1, v' = 26, J = 2, m_J = -1\rangle$ and σ^- polarization for both beams. This is shown in red in Fig. 5.8.

In Fig. 5.11 we show the results of dark resonance spectroscopy in this configuration. We find a resonance in the Stokes frequency at 472158.158(5) GHz. From this, we can obtain a rotational constant using[34]

$$E(N) = BN(N+1) \tag{5.19}$$

In particular, we find $B = 1.744(80)$ GHz. This is in agreement with previous *ab initio* predictions[76,143].

5.5 Raman transfer

Having identified a suitable transfer pathway down to the rovibrational ground state, we next proceed to coherently transfer the molecular state. This requires first calibrating the Rabi frequencies of the pump and Stokes beams. We then discuss the Raman transfer process we use to transfer the population.

5.5.1 Rabi frequency calibrations

Pump beam

We calibrate the pump Rabi frequency by measuring the Feshbach molecules loss rate as a function of laser power when the laser is resonant with the $|J' = 1, M'_J = 1\rangle$ state. In the regime where $\Omega_P \ll \Gamma$, the depletion rate is $1/\tau \approx \Omega_P^2/\Gamma$. We fit the inverse Feshbach molecule lifetime versus pump power as shown in Fig. 5.12, and extract a Rabi frequency of $\Omega_P/2\pi = 6.2(8)\ \text{MHz} \times \sqrt{\frac{P_P}{1\ \text{mW}}}$.

Stokes beam

We calibrate the Stokes laser Rabi frequency using Autler-Townes spectroscopy[144]. After locating the rovibrational ground state, we tune the Stokes laser onto resonance with the $|J' =$

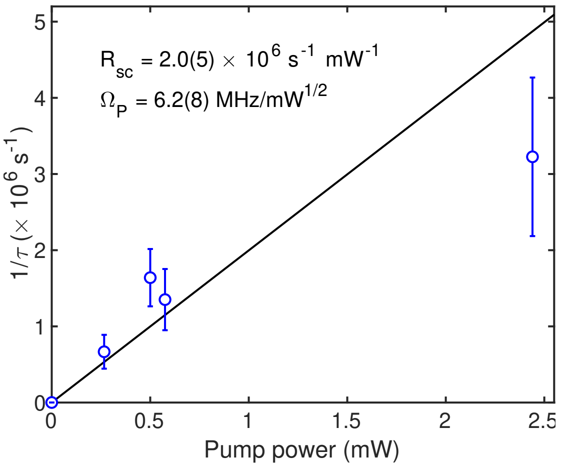

Figure 5.12: Pump laser Rabi frequency calibration. The depletion rate of Feshbach molecules is measured as a function of pump laser power.

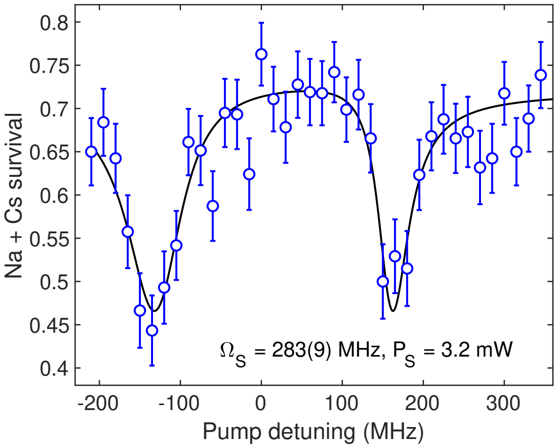

Figure 5.13: Stokes laser Rabi frequency calibration. The Stokes laser is calibrated using Autler-Townes spectroscopy. The Stokes laser is parked on resonance, and the pump detuning is scanned. The doublet feature is fit to give the Stokes Rabi frequency.

$1, M' = 1\rangle$ state, and measure the depletion of Feshbach molecules as a function of pump laser frequency. We observe an Autler-Townes doublet feature as shown in Fig. 5.13, and fit it to a model function for the 2-body survival probability $P_{\mathrm{Na+Cs}}$ after a pulse duration t[144]

$$P_{\mathrm{Na+Cs}}(t) = P_{\mathrm{atom}} + P_{\mathrm{mol}} \exp\left(-\Omega_P^2 t \frac{4\Gamma\delta}{|\Omega_S^2 + 2i\delta(\Gamma + 2i\Delta)|^2}\right), \tag{5.20}$$

where P_{atom} is an atomic background population, P_{mol} is the Feshbach molecule creation fidelity, and $\Delta_{P,S}$ are the one-photon detunings of pump and Stokes lasers, respectively. We obtain a value of $\Omega_S/2\pi = 283(9)$ MHz at $P_S = 3.2$ mW, or $\Omega_S/2\pi = 158(8)\text{ MHz} \times \sqrt{P_S/(1\text{ mW})}$ for the Stokes laser Rabi frequency.

5.5.2 Coherent transfer process

For a coherent Raman π-pulse transfer, a large ratio between the coherent effective 2-photon Raman coupling (Ω_R in equation 5.3) and the incoherent scattering (R_{sc} in equation 5.5) is crucial[84]. We calculate this based on our achievable Rabi frequencies as measured above, and include all the neighboring excited states. A plot of the coherence ratio as a function of single-photon detuning is shown in Fig. 5.14.

We find that σ^+ polarization for both beams gives the best ratios out of the achievable polarization configurations in our system. This configuration couples the Feshbach molecular state predominantly to the $|M''_{I_{\mathrm{Na}}} = 3/2, M''_{I_{\mathrm{Cs}}} = 5/2\rangle$ hyperfine component in the $|X^1\Sigma, v = 0, N = 0\rangle$ state. With a σ^-/π combination for the pump/Stokes beams, a larger ratio is achievable, which couples to the $|M''_{I_{\mathrm{Na}}} = 3/2, M''_{I_{\mathrm{Cs}}} = 3/2\rangle$ hyperfine component in the ground state. In the present experimental configuration however, we are unable to address the atoms with π polarization.

Generally, larger detuning is strictly better in terms of incoherent scattering (due to the $1/\Delta$

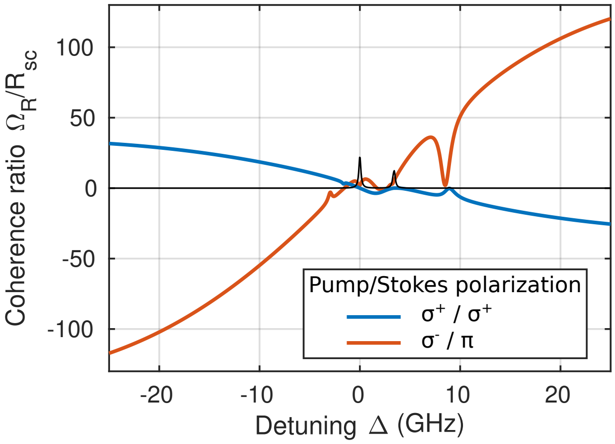

Figure 5.14: Raman transfer coherence ratio. The best scenario with the achievable polarizations in the present experimental configuration is shown in blue (σ^+/σ^+). With a σ^-/π (pump/Stokes) combination, a better ratio can be achieved by coupling to a different hyperfine component in the rovibrational ground state.

scaling of effective Rabi rate compared to the $1/\Delta^2$ scaling of scattering rate); the limitation lies in decoherence factors that may come into play with slower effective Rabi rates given a finite amount of laser power. We note that in this regard, the optical tweezer platform we use has the advantage that we can afford larger beam intensities due to the small volumes of the traps.

In our case, we choose to detune both pump and Stokes lasers by 21 GHz to the red of the $|c^3\Sigma_1, v' = 26\rangle$ manifold, which gives a coherence ratio of ~30. With a 3 μs pulse, we locate the Raman resonance as shown in Fig. 5.15 by scanning the Stokes laser detuning. We observe only a single resonance, consistent with our expectation from that we populate predominantly the $|M''_{I_{\text{Na}}} = 3/2, M''_{I_{\text{Cs}}} = 5/2\rangle$ hyperfine component of the rovibrational ground state for our choice of laser polarizations.

Fixing the Stokes laser frequency on resonance and varying the pulse duration, we observe coherent Rabi oscillations as shown in Fig. 5.16. We measure a Raman Rabi frequency of

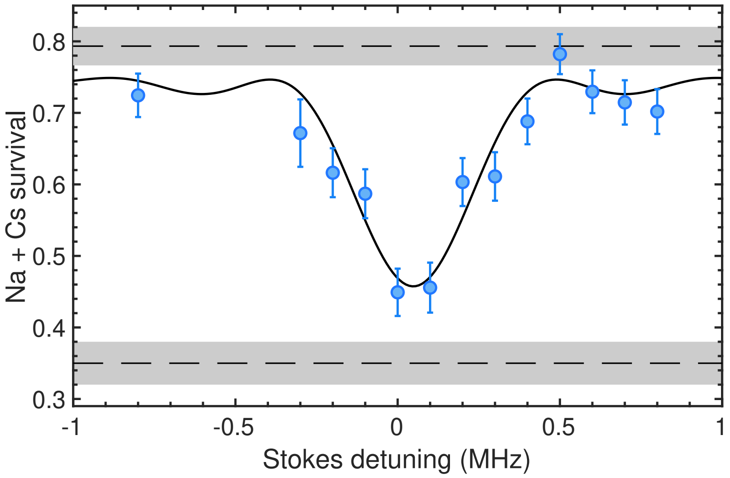

Figure 5.15: Two-photon Raman resonance between Feshbach molecular state and $|X^1\Sigma, v = 0, N = 0\rangle$**.** The pump and Stokes lasers are detuned by $21\,\mathrm{GHz}$ to the red of the $|c^3\Sigma_1, v' = 26\rangle$ manifold. Both lasers are pulsed on for 3 µs. The Stokes laser detuning is scanned, giving a Rabi lineshape. Dashed lines and grey area show the Feshbach molecule contrast and errorbars. The data shown here and in Fig. 5.16 are fit simultaneously to a Rabi lineshape including loss and decoherence.

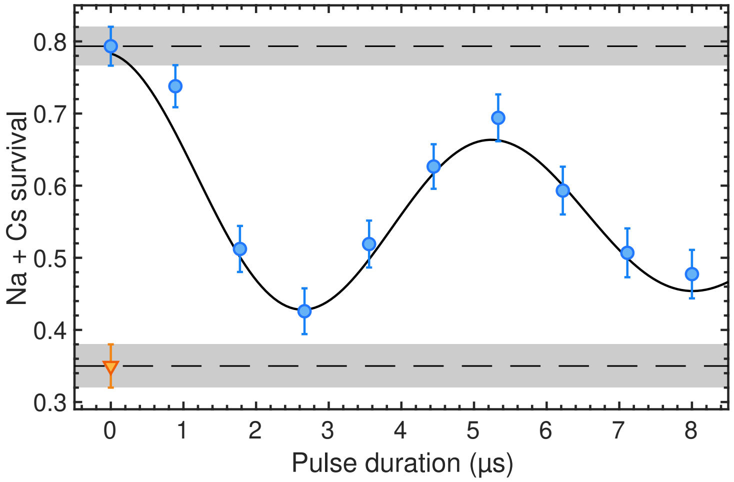

Figure 5.16: Coherent transfer from Feshbach molecular state to $|X^1\Sigma, v = 0, N = 0\rangle$. The Stokes laser is fixed on two-photon resonance based on the Rabi lineshape scan. Dashed lines and grey area show the Feshbach molecule contrast and errorbars which was collected simultaneously with the data. The data point is shown by the first blue circle and orange triangle. The data shown here and in Fig. 5.15 are fit simultaneously to a Rabi lineshape including loss and decoherence.

$\Omega_R/2\pi = 187(2)$ kHz, consistent with the theoretical value of 210(30) kHz with pump Rabi frequency $\Omega_P/2\pi \approx 44(6)$ MHz at $P_P = 50$ mW, and Stokes Rabi frequency $\Omega_S/2\pi \approx 230(10)$ MHz at $P_S = 2.1$ mW. We find a ratio $\Omega_R/R_{\text{sc}} = 27(7)$, similar to our expectation from calculations above, indicating that coherent transfer dominates over loss.

We find a one-way transfer efficiency of 82(10)% from Feshbach molecules to rovibrational ground state molecules. Incorporating the present Feshbach molecule creation fidelity of 38(1)%, the overall efficiency for creation of ground-state molecules from individual atoms is $31(4)\%$, and the round-trip efficiency from atoms to ground state molecules and back is $26(6)\%$. The dominant factor limiting the overall molecule creation fidelity from atoms is that of Feshbach molecule creation, which have been detailed in Chapter 4. In the experimental runs here, additional heating during the trap merge was present which led to slightly lower Feshbach molecule formation efficiency.

Another significant factor limiting ground-state molecule formation is decoherence. We fit a dephasing time in Fig. 5.16 of $\gamma^{-1} = 17(5)$ µs, while the scattering time is $R_{\text{sc}}^{-1} = 23(6)$ µs. The observed decoherence can be accounted for by fluctuating AC Stark shifts arising from drifts in the pump and Stokes laser intensities. For the data presented here, the optical power in each of these beams drifted by $\sim 5\%$ due to thermal variation in the laboratory environment and were not actively stabilized. By stabilizing the Raman laser powers it is possible for the transfer efficiency to be limited by off-resonant scattering from $c^3\Sigma_1$.

5.6 Rovibrational ground state characterization

5.6.1 Lifetime

We characterize the lifetime of the rovibrational ground state by varying the hold times of the molecule in the optical tweezer before applying an addition π-pulse to transfer the molecules back to Feshbach molecules, then back to atoms. Since our experiment involves only a single molecule in a deep optical trap, we expect the ground state lifetime to be primarily limited by scattering of the trap light or collisions with background gas. At our typical trap intensity of $80\,\mathrm{kW/cm^2}$, we find a ground-state lifetime of 3.4 ± 1.6 s. In order to investigate possible limits to the molecule lifetime, we increased the tweezer intensity to $10\times$ and $27\times$ the typical trap intensity. These are shown in Fig. 5.17. We find that the rovibrational ground state lifetime can be reduced to 0.5(1) s and 130(40) ms at trap intensities of 0.8 MW/cm^2 and 2.2 MW/cm^2, respectively, consistent with a linear scaling.

Assuming a linear dependence on trap intensity, we find a loss rate for ground state molecules of $2.3(5)\ \mathrm{s^{-1}(MW/cm^2)^{-1}}$, as shown in the inset of Fig. 5.17. The precision of our measurement is limited by a maximum cycle time of 1.5 s due to thermal fluctuations of the apparatus. Using the theoretical ground state polarizability of NaCs from Ref.[145], we expect a scattering rate of $54\,\mathrm{s^{-1}(MW/cm^2)^{-1}}$, suggesting either an overestimate of the theoretical polarizability or a high proportion of Rayleigh over Raman scattering at this wavelength. Nevertheless, we believe the second-scale lifetime we observe at the normal operating intensities is sufficient for most future applications.

5.6.2 External state

As in the case of the Feshbach molecules, we are interested in the external state of the rovibrational molecule that we transfer to. Being in the lowest motional state is crucial for longer coherence times for the dipolar interactions between the molecules in future applications[36]. The rovibrational ground state molecule primarily inherits the motional quantum state of the Feshbach molecule, which arises from the individually laser cooled atoms.

In Chapter 4, we estimated that the center of mass (COM) ground state fraction of Feshbach molecules we formed was 77(5)% using Raman sideband thermometry. We also observed a

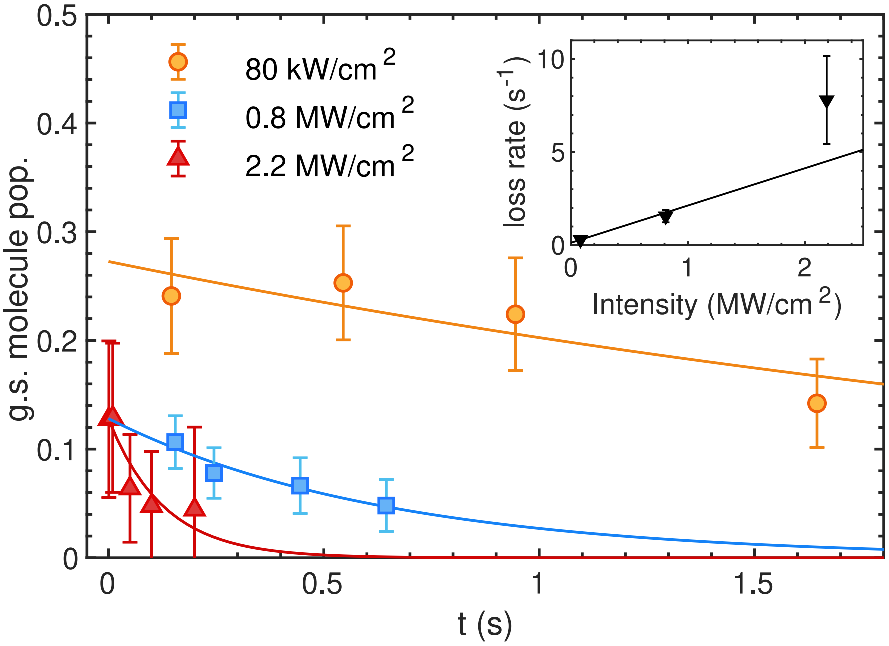

Figure 5.17: Characterization of rovibrational ground state molecule lifetime in optical tweezer. The rovibrational ground state molecule is held in the optical tweezer for varying times at different intensities before being transferred back to Feshbach molecules then atoms for detection. Atomic background has been subtracted. Inset: the increase in molecule loss rate with laser intensity is consistent with a linear trend corresponding to one-photon scattering.

Feshbach molecule creation fidelity of 47(1)%, consistent with a relative motional ground state population of 58(4)%. In the data presented in this chapter, we observe a slightly reduced Feshbach molecule creation fidelity of 38(3)%, while the atomic ground state cooling conditions have not changed from. The reduced fidelity of Feshbach molecule creation arises from an axial misalignment of the dual species optical tweezers, which primarily leads to heating of the Na atom during the merge process. Because Na is much lighter than Cs, heating of the Na atom primarily contributes to excitation of the relative motional degree of freedom, as opposed to the COM. Using the Feshbach molecule creation fidelity as a proxy for thermometry, we estimate that the COM ground state fraction of Feshbach molecules under present experimental conditions is 75(5)%.

Two main effects cause COM motional excitation of the molecule during Raman transfer. First arises from the differential wavenumber of the pump and Stokes lasers, Δk. In the Raman transfer process, motional sidebands of the COM degree of freedom are not resolved: The Raman Rabi frequency is of order $\Omega_R \approx 2\pi \times 200$ kHz, while the axial trap frequency during transfer is $\omega_z \approx 2\pi \times 3$ kHz. Coherent absorption of a pump photon and emission of a Stokes photon during Raman transfer thus creates a coherent state of the molecule's COM motion with momentum $\hbar\Delta k$. The mean occupation number resulting from this kick is $\bar{n} \approx 0.085$, giving a 92% probability to remain in the ground motional state.

A second source of motional excitation during Raman transfer is the mismatch of initial and final state trap frequencies, due to a difference in polarizability of each state to the trapping laser. The Feshbach state polarizability is estimated as $\mathrm{Re}[\alpha_{\mathrm{Na+Cs}}(1064\text{ nm})] = 1397\ a_0^3$ from the sum of atomic polarizabilities, while the $X^1\Sigma$ polarizability is $\mathrm{Re}[\alpha_{X^1\Sigma}(1064\text{ nm})] = 936\ a_0^3$ from[145]. The ratio of trap depths is then $1397/936 \approx 1.5$, so that ratio of trap frequencies is $\sqrt{1.5}$ which we call f below, and the ratio of harmonic oscillator lengths is $(1.5)^{1/4}$. The probability of remaining in the motional ground state is

$$P_{0\leftarrow 0} = |\langle n'_x = 0, n'_y = 0, n'_z = 0|e^{i\Delta kz}|n_x = 0, n_y = 0, n_z = 0\rangle|^2. \tag{5.21}$$

The initial Feshbach molecule COM spatial wavefunction is essentially projected onto the rovibrational ground state COM wavefunction. Because the Raman transfer lasers propagate along the z axis, we can separate the integrals and evaluate them straightforwardly, finding

$$P_{0\leftarrow 0} = \frac{8f^{3/2}}{(f+1)^3} \exp\left(-\frac{f\eta^2}{2f+2}\right), \tag{5.22}$$

where $\eta = \Delta k\, z_{\text{ho}} \approx 0.413$ is the Lamb-Dicke parameter. We find $P_{0\leftarrow 0} \approx 0.94$.

In the worst case, in which these two motional excitation effects add up, we would expect a reduction of the motional ground state population by a factor 0.862. We estimate the overall COM ground state fraction of the rovibrational ground state to be 75(5)% × 0.862 = 65(5)%. Both excitation effects can be mitigated by performing the Raman transfer more slowly with a larger detuning and at a higher trap frequency. However, loss of Feshbach molecules and finite laser coherence will limit the maximum transfer time. In the limit of resolved motional sidebands during Raman transfer, both effects can be eliminated. It is also possible to apply the Raman lasers perpendicular to the tweezer axis in order to take advantage of the higher trap frequencies in the radial direction. Nevertheless, these results present the first time a polar molecule has been created with full quantum-state control in its rovibrational ground state, and provides a starting point for many exciting applications.

5.7 STIRAP

In this section we briefly discuss our initial attempts at coherent transfer using STIRAP. As discussed in section 5.1, this process uses a counter-intuitive pulse sequence to achieve adiabatic transfer of population[140]. Due to its relative relaxed requirements on laser power stability and less intensity required, this has been the established approach in the literature to transferring to the rovibrational ground state in bi-alkali's. Typically, STIRAP is performed with pump and Stokes lasers on both single- and two-photon resonance. This ensures no light shifts from the lasers, so that the excited state remains dark over the course of the ramp (equation 5.2). In our initial attempt we performed detuned-STIRAP, which detunes both beams off of single-photon resonance[146]. Detuned-STIRAP has the advantage that a loss feature when scanning the two-photon detuning can be more apparent and indicative of a resonance. A molecule formation signal after performing a one-way STIRAP pulse is detected by simultaneous loss of Na+Cs atoms. Due to the large excited state linewidth, performing STIRAP on single-photon resonance leads to atom pair loss from the pump beam and may occlude any additional loss that would indicate a STIRAP transfer. On the other hand, with detuned-STIRAP, loss from the pump beam is reduced, and any molecule formation signal when on two-photon resonance can be clearer. In this configuration, however, light shifts arise from the SITRAP beams themselves and the single-photon detuning needs to be scanned. In addition, light shifts cause the STIRAP beams to not be entirely on two-photon resonance over the course of the entire pulse, causing additional coupling to the intermediate state, which can affect the transfer efficiencies.

In the experiment, we use linear ramps as shown in Fig. 5.18. These pulses were programmed using a function generator and triggered by the experiment control system. We use $\Omega_P = 2\pi \times 4.7$ MHz and $\Omega_S = 2\pi \times 20$ MHz, with rise times of 5 μs. We expect this to

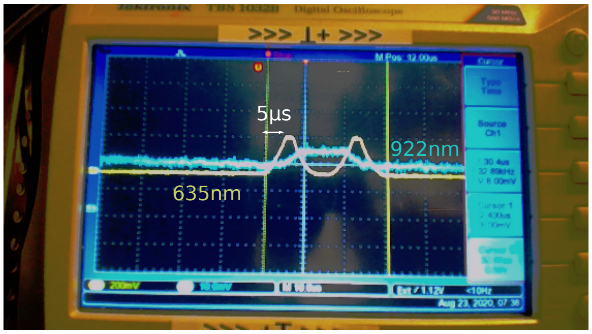

Figure 5.18: STIRAP laser pulse sequence. The Stokes laser is ramped on first before ramping up the pump laser and ramping down the Stokes laser. In the two-way scenario shown, an additional Stokes laser pulse is applied in the time the pump laser is ramped down.

be in the adiabatic regime as the ramp rates are an order of magnitude slower than the single-photon Rabi rates leading to a large pulse area[140]. We blue-detune 900 MHz away from the $|c^3\Sigma_1, v' = 26, J = 1, m_J = +1\rangle$ line; the next nearest state is ~1.5 GHz further blue-detuned with weaker couplings.

In Fig. 5.19 we show the results of scanning the two-photon detuning. We compare between a one-way pulse, which would nominally convert Feshbach molecules to the rovibrational ground state on resonance, and a two-way pulse, which would nominally bring the population back. We observe a resonance feature for the one-way pulse, indicating a transfer to the rovibrational ground state. Moreover, we observe a contrast between the one-way and two-way signal at particular detunings where there is also one-way molecule formation, indicating a revival of Feshbach molecules. We find a one-way transfer efficiency of ~47%. Shown in dotted lines are numerical simulations with parameters similar to the the experiment incorporating all the coupled excited states. We find that our experimental results qualitatively agree with theory. In the simulations, oscillations in the revival signal appear due to interference between the two ground state populations.

While we were able to observe a transfer signal using detuned-STIRAP, we found that the

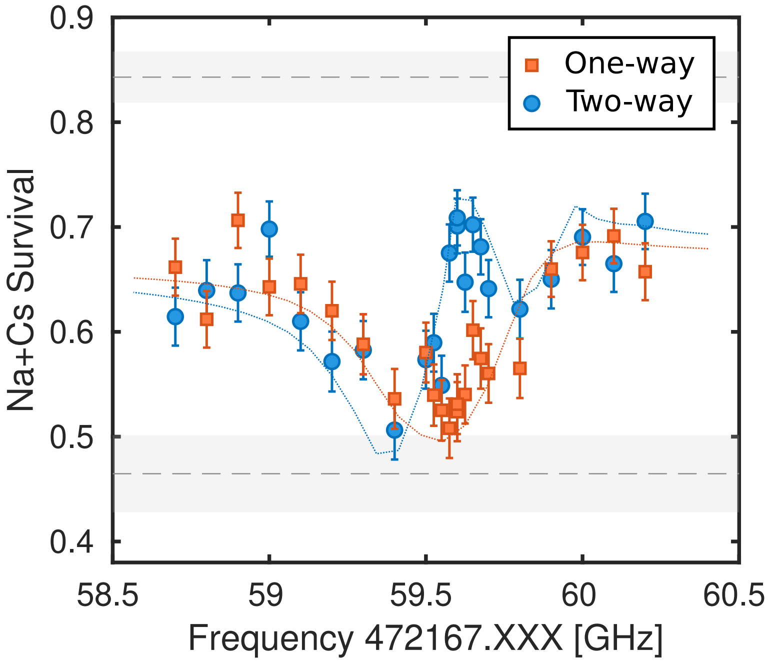

Figure 5.19: Detuned-STIRAP to rovibrational ground state. The pump and Stokes beams are blue-detuned 900 MHz from the $|c^3\Sigma_1, v' = 26, J = 1, m_J = +1\rangle$ line. The pump laser frequency is fixed, while the Stokes laser frequency is scanned. A one-way STIRAP pulse (orange square) and two-way STIRAP pulse (blue circle) is compared. We find a dip in the one-way signal, indicating a transfer to the rovibrational ground state. Moreover, we find a parameter regime where there is revival of Feshbach molecule population upon a two-way pulse, indicating a coherent transfer process. Dotted lines are numerical simulations using parameters similar to the experiment. We find a qualitative agreement. Dashed grey lines correspond to baseline Feshbach molecule production efficiency.

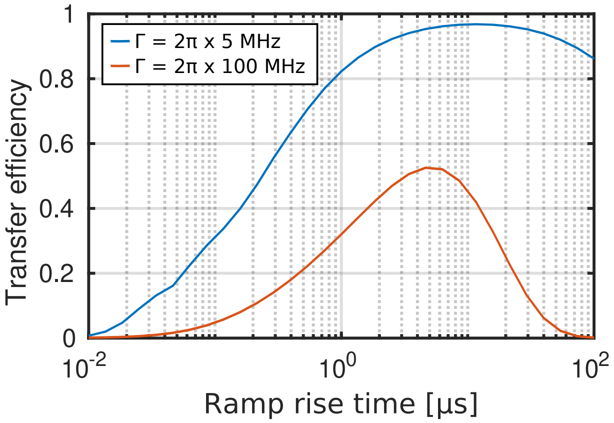

Figure 5.20: Numerical simulation of detuned-STIRAP as function of ramp rate. We find that for the large scattering rate in our system, there is only a small parameter regime where the transfer efficiency is optimal.

signal was susceptible to drifts of unknown origin. One possibility is that due to the oscillations in the round-trip transfer, which we typically use to verify coherent molecule formation, the signal can be rather narrow, which caused day-to-day fluctuations in the signal. In addition, the dependence of light shifts on laser intensities also cause the transfer efficiency to vary. In principle, effects of lights shifts are eliminated when both lasers are on single-photon resonance. However, we were unable to observe signal on resonance, despite theoretical calculations suggesting it to be possible.

Moreover, we found that the optimization of the pulses were counter-intuitive. This can in part be explained by the large excited state scattering rate. For example, in Fig. 5.20 we show numerical simulations of a one-way detuned-STIRAP transfer assuming different excited state scattering rates. This incorporates all the nearby excited states that are coupled to the initial and final states by the lasers. In particular, for a small excited state scattering rate, we expect that the transfer efficiency to improve as the ramp rate is decreased, due to increased adiabaticity, so long as it remains within the decoherence time of the lasers. However, in the presence of strong scattering from the intermediate state, we find that the transfer efficiency can decrease significantly when the pulse times are increased, leaving only a small window for optimization.

These complications ultimately convinced us to turn to a detuned π-pulse Raman transfer for coherent transfer to the rovibrational ground state.

5.8 Summary and outlook

In this chapter we presented a coherent approach to transferring the internal state of a single NaCs Feshbach molecule to the rovibrational ground state. This involved performing excited state spectroscopy to identify a suitable intermediate state for transfer, as well as locating the rovibrational ground state. We used theoretical models of the ground and excited states to guide the transfer. In particular, with a large observed excited state linewidth, we found that a detuned Raman transfer was relatively more straightforward compared to a STIRAP approach. This constitutes the first time NaCs rovibrational ground state molecules have been coherently formed. Moreover, this constitutes the first fully quantum-state-controlled single neutral molecule in an optical tweezer. This serves as a starting point to scale the system up to larger arrays, which will be the subject of the next chapter.

As we will see in the next chapter as well, the large excited state linewidth presents challenges in obtaining high fidelity transfer. Therefore, a search for alternative pathways to the ground state is underway that could help improve the fidelity and relax intensity stability requirements.

6

Scaling to an array of rovibrational ground state molecules

After having created a single rovibrational ground state molecule in an optical tweezer, we set out to scale the system up to multiple tweezers and molecules. This involved overcoming a series of technical hurdles which will be described in this chapter. In the present work, we opted to use acoustic optical beam deflectors (AOBD) to generate arrays of optical tweezers. Using this, we successfully trapped and cooled individual 1D arrays of 10 Na and Cs atoms simultaneously, and successfully assembled an array of 4 NaCs rovibrational ground state molecules by performing the process detailed in the previous chapters of this thesis on an array in parallel.

6.1 Optical upgrades

6.1.1 High power source for Na optical tweezer

As discussed in section 3.2, the trapping of Na requires a wavelength lying in the range 590 nm to 852 nm. The lack of high power diodes or amplifiers in this wavelength range render this challenging to obtain directly. Previously, using a Ti:Sapph laser tuned to 700 nm, we were able to trap and cool* a single Na atom in an optical tweezer. To achieve the trap depths necessary, we produce light at 623 nm using a sum-frequency generation system. This wavelength is closer to resonance, which, although leading to higher rates of scattering, requires ~5 times less power per trap depth.

We use a MgO:PPLN sum-frequency generation crystal (Covesion MSFG626-0.5-40) to produce 623 nm from 1038 nm and 1550 nm sources. The 1038 nm light is produced by an Innolume Butterfly seed that is amplified by an ALS fiber amplifier. The 1550 nm light is produced by a distributed feedback laser (DFB-1555-NL-PM-FCA) and amplified by an NKT photonics fiber amplifier.

PPLN sum-frequency generation involves a non-linear process that generates photons at their combined energy. The generated photons need to be in phase with that of the input beam to not cause destructive interference on the output beam. In PPLN this is achieved by a peri-

---

*Efficient cooling requires a higher trap depth than merely loading a single atom. For Na we cool at ~3× the minimal loading trap depth.

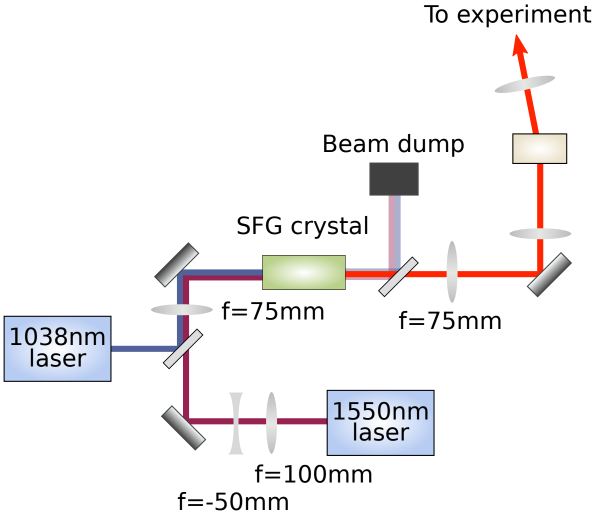

Figure 6.1: Schematic of sum-frequency generation beampath. The 1038 nm and 1550 nm beams are combined on a dichroic before being focused into the SFG crystal. The beam diameters out of the lasers are ~2 mm and ~5 mm respectively. An additional dichroic after the crystal filters out unconverted IR light. The beam is recollimated before being focused into the switching AOM and coupled to the experiment.

odically poled crystal, such that each period flips the phase of the generated photon[147]. The temperature of the crystal needs to be adjusted such that the phase-matching condition is met. For the particular crystal we use, we find a temperature dependence of ~50 GHz/°C. In addition, the temperature condition for phase matching depends on the specific frequencies of the seeds, therefore the frequencies of the seeds are actively servo-ed by a slow wavemeter lock that feeds back on the laser frequency by controlling a piezo voltage.

In addition to tuning the temperature for phase matching, the beam size and intensity are important to achieving good conversion efficiency. In particular, since the Rayleigh length is constrained by the spot size of the beam, there is a compromise between a stronger intensity over a smaller range, or lower peak intensity but over a larger range. The Boyd-Kleimann focusing condition states that the ratio of the crystal length to Rayleigh length be 2.84 for optimal photon generation[148]. The length of the crystal in our system is 40 mm. In our system we use spot sizes of 52 µm and 57 µm for the 1038 nm and 1550 nm beams respectively. A schematic of the beampath is shown in Fig. 6.1. With 9.1 W and 8.6 W input of 1038 nm and 1550 nm respectively we obtain ~5 W of 623 nm light after the crystal.

At this wavelength it is still necessary to switch between the tweezer light and MOT/imaging light, which we do in a similar manner as before (see section 2.3.1)[78]. The need for switching unfortunately cuts down the available power due to the ~30% duty cycle. Recently, it has been demonstrated that magic trapping is possible on the D1 line at 619 nm[149]. A magic trapping condition occurs when the polarizabilities of the ground and excited states are the same, leading to no AC Stark shift on the atom from the trapping light. This would eliminate the need for switching between the MOT/imaging light and tweezer light, and would allow for more power. Nevertheless, with the present setup, after the switching AOM and fiber coupling, we obtain ~400 mW at the experiment. The fiber is coupled by a single-mode patch cable (Thorlabs, P3-488PM-FC-10), where we get an efficiency of ~75%, which does not saturate at the powers at which we operate. In planned upgrades we plan to use photonic crystal fibers for higher power transmission and stability[150].

6.1.2 Optical tweezer beampath

Previously, the optical tweezer beampath shown in Fig. 2.17, with a single AOBD (IntraAction ATD-1403DA2W) in the 1064 nm tweezer beampath, allowed for an array of Cs atoms as well as steering of Cs in one dimension along the array direction (horizontal). To accommodate arrays for both species, we add two AOBD's (IntraAction, ATD-1403DA2W[†]) in the 623 nm tweezer beampath. One (horizontal direction) generates the array of tweezer beams, while another (vertical direction) steers the entire array to be merged with the 1064 nm

---

[†] These were originally designed and specified for 1064 nm, but we found them to work well for 623 nm too. We achieved ~80% efficiency over a 70 MHz sweep range for 623 nm, whereas the efficiency was ~50% for 1064 nm.

tweezer array. Notably, this setup would allow for *in situ* rearrangement in the future.[‡]

A schematic of the upgraded beampath is shown in Fig. 6.2. Each AOBD (vertical then horizontal) is followed by a telescope, before the beam is sent into the objective. The combination of AOBD and telescopes form an optical relay system[151]. Specifically, the first vertical AOBD lies at the focal point of the $f_1 = 100$ mm lens, while the second horizontal AOBD lies at the focal points of both the $f_2 = 150$ mm and $f_3 = 100$ mm lens. Finally, the distance from the $f_4 = 500$ mm lens to the objective is $f_4 + f_{\text{obj}}$. These together ensure that (1) the diffracted beams entering the second horizontal AOBD is at the same point regardless of diffraction angle of the first AOBD for optimal efficiency and (2) the diffracted beams correspond to parallel translation of the optical tweezers at the focus of the objective.

The angular magnification of the second telescope consisting of lenses f_3 and f_4 is

$$|M_{\text{ang}}| = \frac{f_3}{f_4} \tag{6.1}$$

To achieve maximal separation of the traps given the limited bandwidth of the AOBD's, we ideally want f_3 as large as possible given a fixed f_4. Therefore, the beam size at the input of the horizontal AOBD is chosen to be maximally large ~2.3 mm, limited by the aperture size of the AOBD.

In comparison with the previous beampath, we also substituted a new imaging dichroic (custom ordered from LayerTec) to accommodate the new wavelength at 623 nm.

[‡] The alternative is to use a single AOBD for each species and interleave the two arrays. This would preclude the possibility of *in situ* rearrangement.

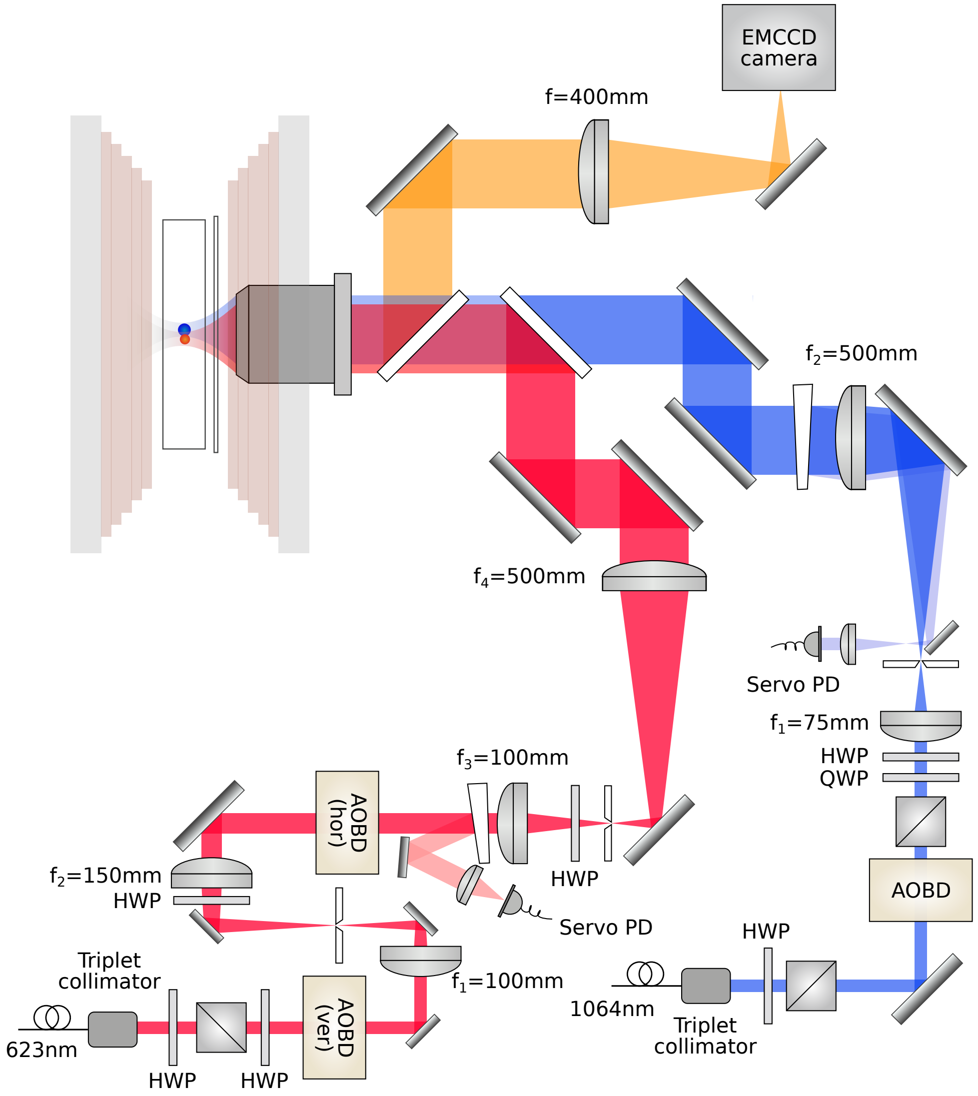

Figure 6.2: Schematic of tweezer beampath. (Not drawn to scale).

6.2 Dual species array

6.2.1 AOBD RF control

We use an arbitrary waveform generator (AWG, Spectrum Instruments M4i.6622-x8) to simultaneously generate multiple RF tones for the AOBD's in the horizontal direction for the 623 nm and 1064 nm beampaths. These use two separate channels on the AWG board. The amplitude and phase for each tone can be individually modified.

The sampling rate of the AWG is at 625 MHz. As a result, we observe peaks in the spectrum corresponding to the aliased signals along with the desired tones. The RF signals are high-passed and low-passed to filter extraneous frequencies. While we found that lowering the output amplitude of the AWG output helped to suppress the extraneous peaks in the signal, we found that m_F depumping of the atoms was significantly worse at lower amplitudes. This is reminiscent of the depumping observed in section 3.3.1, where noise on the RF signal generated by the USRP system caused rapid depumping as well. This suggests that the source of the noise of the AWG is constant in the background and is amplified more downstream when operating at lower amplitudes. Due to this, we opted to use the maximal output power from the AWG.

The RF signals are then amplified by an RF amplifier (Mini-Circuits ZHL-20W-13+). While the maximum output power we require is $<$ 5 W (limited by the AOBD), the high power specification of this amplifier allows us to operate well below the saturation regime (the relevant specification being the third-order intercept point). This reduces intermodulation causing beating effects downstream.

For the vertical AOBD in the 623 nm beampath used for merging, only a single tone is necessary, so we use a DDS channel controlled by our FPGA-control system and amplified with an RF amplifier (Mini-Circuits ZHL-03-5WF+).

6.2.2 Trap normalization

The RF signal output from the AWG is nominally of the form

$$\sum_i \cos\left(2\pi f_i t + \varphi_i\right) \tag{6.2}$$

However, due to non-linearities in the system, whether from the AWG and amplifier, or the AOBD, terms in this sum can mix and result in terms

$$\cos(2\pi f_i t + \varphi_i)\cos(2\pi f_j t + \varphi_j) \propto \cos\Big(2\pi(f_i - f_j) + (\varphi_i - \varphi_j)\Big) + \cos\Big(2\pi(f_i + f_j) + (\varphi_i + \varphi_j)\Big) \tag{6.3}$$

The terms involving $f_i - f_j$ can then mix again with the original signal and result in terms near the original desired tones $f_k + (f_i - f_j)$. For a uniformly spaced array, where the neighboring f_i are equally spaced, these terms can collude with the original signal and destructively or constructively interfere leading to unequal amplitudes in the desired tones. There are methods to optimize this to avoid interference effects[68]. In practice, we found that by starting from a uniformly distributed random set of phases for each of the tones, destructive interference was minimal, and we could optimize homogeneity by adjusting amplitudes only.

The RF amplitudes are first adjusted by normalizing the beam intensity of the array focused onto a beam profiler. We then normalize the 1064 nm array on the atoms by matching the light shift on Cs atoms at individual sites. Due to lack of light shifts on Na with the switching trap for 623 nm, we crudely normalize the array by matching the minimal single atom loading powers at each site. After initial normalization of the arrays using these methods, we optimize more finely on the uniformity of the trapping frequencies using parametric heating spectroscopy[83] or Raman sideband spectroscopy.

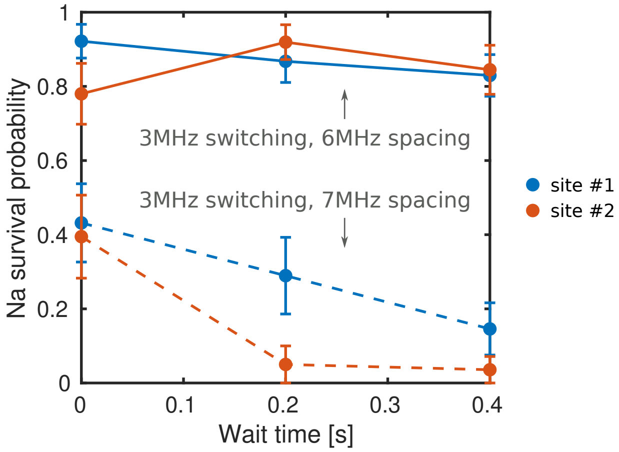

Figure 6.3: Heating of Na atoms in array. The tweezer and MOT/imaging light is pulsed out of phase at 3 MHz. Solid (dashed) line shows survival of two Na atoms spaced 6 MHz (7 MHz) apart. In both cases, both atoms are held at the same trap depth (~3mK). In particular, we see significant heating and loss when the AOBD frequency spacing is not a multiple of the switching frequency.

6.2.3 Heating problems

As discussed in section 2.3.1, we modulate our Na trap at 2.5 MHz out of phase with the MOT/imaging light to eliminate light shifts from the tweezer light that inhibits loading and imaging. In the array, we found that when the array spacing frequency difference is a non-integer multiple of the modulation frequency, heating would occur. An example of this is shown in Fig. 6.3 where we load and measure the lifetime of the Na atoms in two traps only. In particular, when the switching frequency is at 3 MHz, and two traps are spaced 7 MHz away, rapid loss was seen from the trap. However, with a spacing of 6 MHz (an integer multiple of 3 MHz), no significant heating was observed.

The switching of the laser frequency f_L at f_S with a 30% duty cycle square pulse leads to frequency sidebands on the laser at frequencies $f_L + n \cdot f_S$, where n is any integer (the amplitudes are lower for larger n). In the simple case of two tones f_1 and f_2 driving the AOBD, the laser beam is deflected and generates two beams containing frequency components

$$f_L + n \cdot f_S + f_1 \text{ and} f_L + m \cdot f_S + f_2 \tag{6.4}$$

If the two beams overlap in space at the location of the atoms, this can lead to beating at frequencies

$$(f_1 - f_2) - n \cdot f_S \tag{6.5}$$

When $\Delta f = f_1 - f_2$ is not an integer multiple of f_S, this difference can lead to frequencies near two times the trapping frequency, causing parametric heating on the atoms. Therefore, we found it necessary to find frequencies that avoid this situation.

Our choice of switching frequency f_S is limited by various considerations[78]

- (1) The switching frequency needs to be less than the excited state linewidth ($2\pi \times$ 10 MHz) so that the atom has sufficient time to scatter light.
- (2) The switching frequency needs to be larger than the trapping frequency (~500 kHz) so that the atom motion is unaffected by the switching.

This constrains our choice of frequency spacing for the AOBD array. We choose a switching frequency f_S of 3.5 MHz and AOBD frequency spacing Δf of 7 MHz or 14 MHz for the Na array. To align the Na and Cs traps, this corresponds to an AOBD frequency spacing of 5.28 MHz or 10.57 MHz for Cs.

In Fig. 6.4 we show a dual species array consisting of 10 Na and Cs atoms each. The atoms within each row are spaced by 3.6 µm, and the two rows are spaced by 3.3 µm. These correspond to 7 MHz and 5.28 MHz spacing for the 623 nm and 1064 nm horizontal AOBD's respectively.

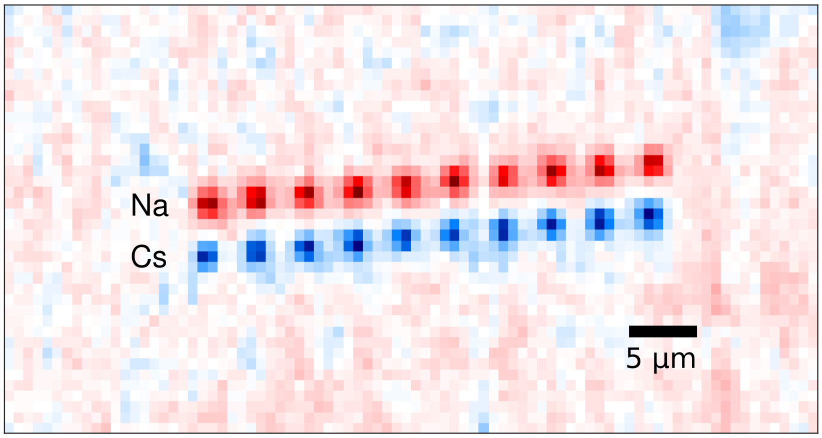

Figure 6.4: Dual species array of single atoms. Na and Cs arrays are generate individually by AOBD's in the horizontal direction. Na and Cs atoms are imaged separately and overlaid to produce the image, which is averaged over 132 experimental runs. Red (blue) corresponds to trapped single Na (Cs) atoms. The atoms are spaced ~3.7 µm in their individual arrays, while the spacing between the Na and Cs arrays is ~3 µm. A separate AOBD in the vertical direction for the 623 nm tweezer steers the Na array to merge with 1064 nm Cs tweezer beams.

6.3 Raman sideband cooling

After we have trapped a dual species array, we Raman sideband cool the array of atoms to their motional ground states. The cooling sequence is the same as discussed in 3.3.1. Since the Raman beams are ~200-300 μm in diameter, this is sufficient to address the entire array homogeneously with proper centering of the beams on the array.

In Fig. 6.5 we show Raman sideband thermometry spectra obtained after Raman sideband cooling of an array of 10 Na (a) and Cs (b) atoms. In Fig. 6.6 we show the $\bar{n}$ for each of the 3 axes for each species at each individual site. On average, we achieve $\bar{n}_{\mathrm{Na}} = (0.15(5), 0.13(5), 0.18(4))$ and $\bar{n}_{\mathrm{Cs}} = (0.056(22), 0.068(23), 0.054(25))$ over all sites. In particular, these results demonstrate that, since the atoms are neutral and do not interact with each other strongly in an array, scaling up this platform to include multiple atoms for Raman sideband cooling does not come at the expense of compromised performance.

6.4 Merging arrays

After Raman sideband cooling, the Na and Cs arrays are merged together in parallel such that a single pair of Na and Cs atoms occupies each site of the 1064 nm tweezer array. The motion is controlled by ramping the frequency of the vertical AOBD in the 623 nm tweezer beampath, similar to the case of merging a single pair of atoms (section 3.4). In addition to aligning the final AOBD frequency to ramp to, there are additional degrees of freedom we need to account for in the merge alignment process:

- The horizontal shift between the two arrays is controlled by a motorized mirror mount in the 623 nm beampath. In principle this could also be completed by introducing an overall frequency shift in one of the horizontal AOBD's. The alignment of this is op-

(a) Na

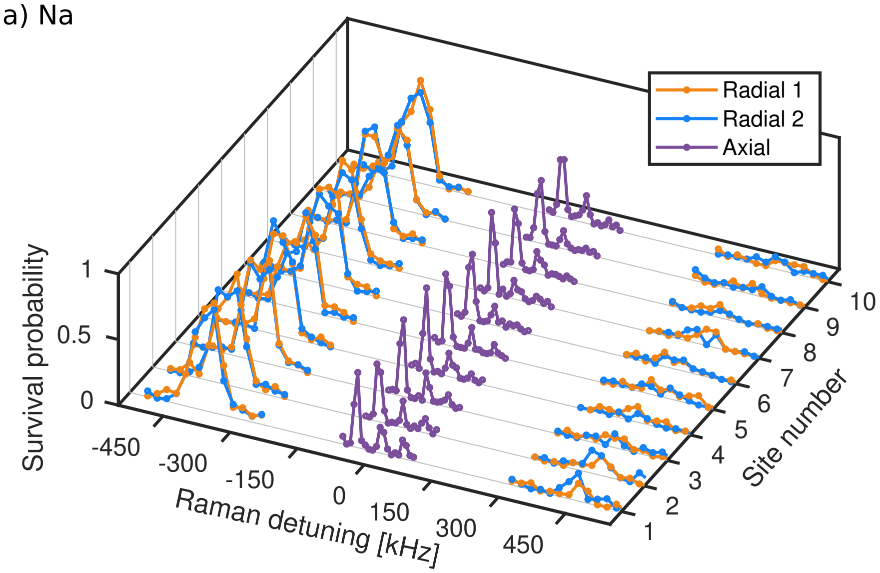

(b) Cs

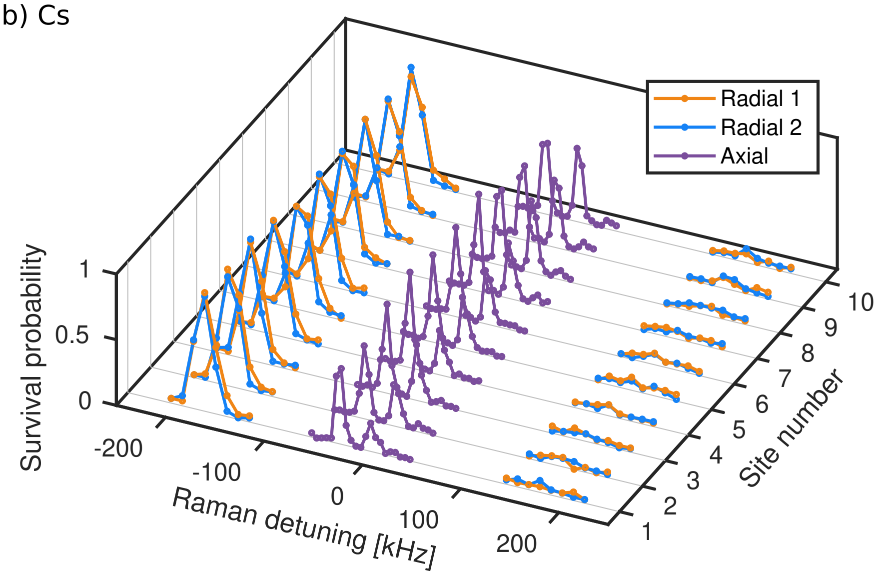

Figure 6.5: Raman sideband thermometry in an array after cooling. 10 atoms of each species are loaded simultaneously and Raman sideband cooled. Raman sideband thermometry is performed after the cooling sequence, and is shown for (a) Na and (b) Cs individually.

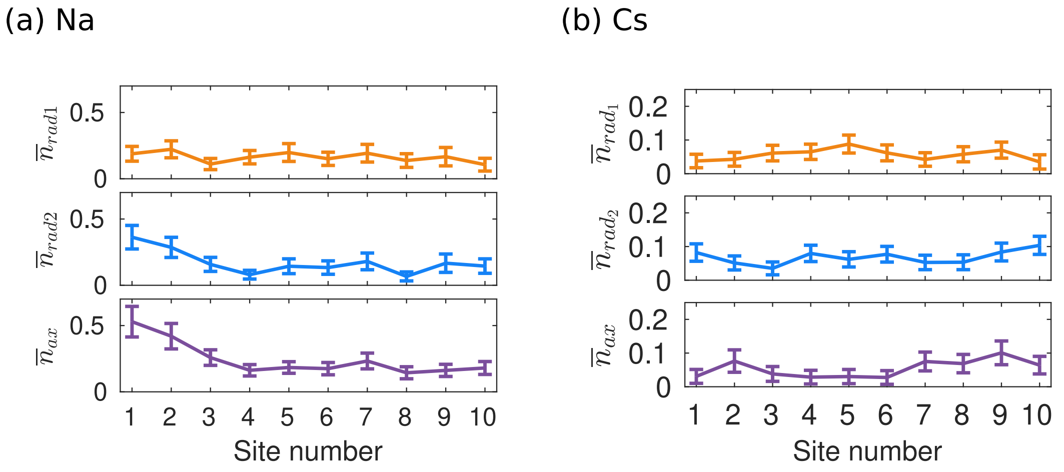

Figure 6.6: $\bar{n}$ after Raman sideband cooling in an array. The $\bar{n}$ values of each axis for each site is shown for (a) Na and (b) Cs. To extract the $\bar{n}$ values, the heating and cooling sidebands in Fig. 6.5 are fit to a Lorentzian lineshape to obtain the respective sideband amplitudes. The worse cooling performance in sites 1-2 of Na is due to inhomogeneities in the trapping frequency.

timized by maximizing the pushout of Cs atoms from the 623 nm light, which is anti-trapping for Cs, at the merge location.

- The relative tilt between the two arrays is aligned by manually adjusting the tilt of the horizontal AOBD in the 623 nm beampath, which lies on a 5-axis mount. The alignment is optimized by comparing the tilts of the atom arrays on the camera, which is found by fitting each of the atom arrays to linear arrays of Gaussian profiles that are equally spaced apart.
- The spacing between atoms in each of the individual arrays also need to be the same to ensure optimal merging. Due to the constraints on the frequency spacing of the Na array as discussed in section 6.2.3, the spacing of the Cs array is adjusted to match that of the Na array. This too is optimized by comparing the atom arrays on the camera.

6.5 Forming Feshbach molecules

With the atoms Raman sideband cooled, we proceed to form Feshbach molecules using the procedure described in Chapter 4. In particular, in the experiment we ramp the magnetic field from zero to 867 G before merging the traps and forming molecules by magnetoassociation. We initially however, found no Feshbach molecule creation, and traced this to loss of m_F population during the magnetic field ramp up to high fields. Specifically, we found, for example, that the population for Cs would be lost in an array spaced by 5.28 MHz for the 1064 nm array upon going above ~15 G. At ~15 G, the neighboring m_F level energy spacing 5.25 MHz coincides with the neighboring trap frequency difference Δf.

In section 3.3.1, we discussed how the presence of noise in the RF signal driving the AOBD causes depumping of the m_F state for Cs. We note that for an AOBD, noise on the input RF signal in fact shows up as frequency sidebands in the RF signal, and therefore leads to additional deflected beams in the AOBD output. Therefore the noise causing depumping is ultimately a beating or combined Raman scattering effect between the extra deflected beams. In the present case, for an AOBD being driven by equally spaced tones f_i, where $f_{i+1} - f_i = \Delta f$ is constant, neighboring tones, if they overlap optically, will also cause beating. The overlap is exacerbated by clipping in the beampath, which causes Airy disk patterns in the images of the individual trap beams (see Fig. 6.8). In the presence of circular polarization component at the location of the atoms, this will cause m_F state scrambling similar to the mechanism aforementioned in section 3.3.1.

In Fig. 6.7(a) we show the depumping of a single Cs atom from the stretched state $|F = 4, m_F = 4\rangle_{\mathrm{Cs}}$ as a function of neighboring trap frequency. The blue data points show the case of bad depumping, whereby traps spaced closer than 15 MHz causes depumping. In Fig. 6.7(b) we measure the intensity spectrum of a single trap clipped off at the focus. In particular,

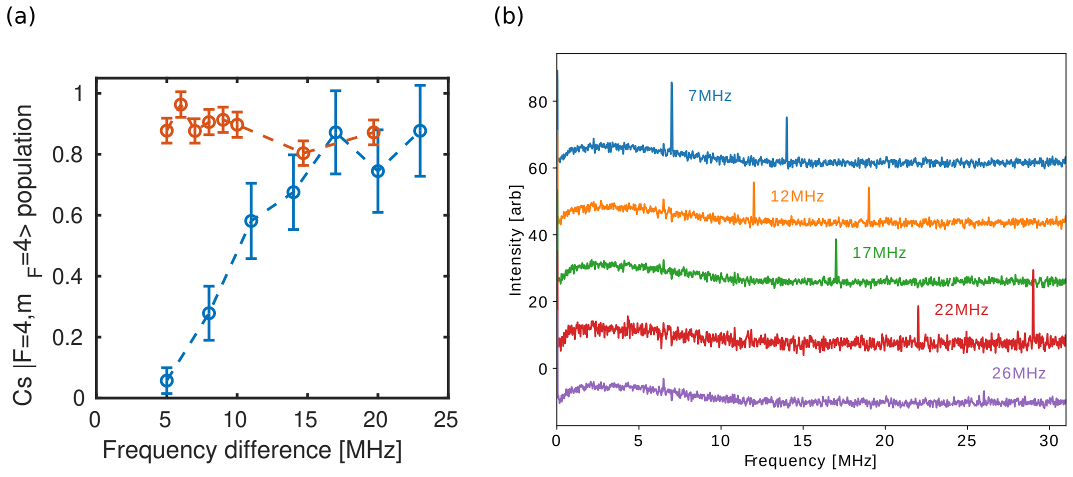

Figure 6.7: m_F **depumping of Cs atom in an array.** (a) Depumping of a single Cs atom out of the stretched state $|F=4, m_F=4\rangle_{\mathrm{Cs}}$ with varying neighboring AOBD trap frequency difference. Blue (red) points indicate the depumping before (after) implementing the changes discussed in the text. (b) Optical intensity noise spectrum of a single trap measured with varying neighboring trap frequency. The tweezer beam is clipped at the focus to pick out a single trap.

We find a decreasing beatnote as the neighboring trap frequency is increased.

To mitigate these effects, we jump the magnetic field from 0 to 30 G using the shim field coils in the x-direction before ramping the Feshbach coil up to the desired field. The jump causes oscillations due to Eddy currents and servo responses, sowe wait an additional 20 ms for the magnetic field to settle. Finally, we ramp the trap intensities down during the magnetic field ramp, which also lowers the Raman scattering rate. The depumping after these implementations are shown in red in Fig. 6.7(a). While this effectively eliminates the depumping effects, we still opt to separate the traps to double the spacing, so that the frequency is 14 MHz and 10.57 MHz for Na and Cs respectively, corresponding to a distance of 7.4 µm, to preempt further problems during molecule formation (Fig. 6.8).

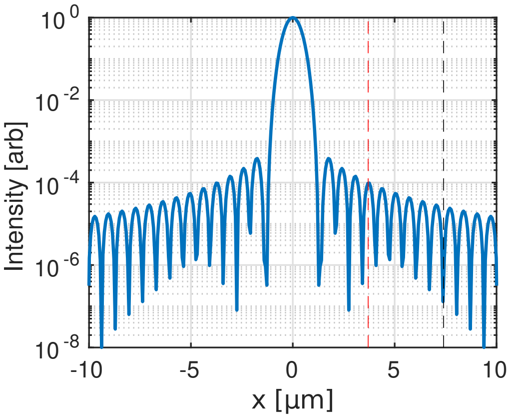

Figure 6.8: Simulation of clipped Gaussian beam. A Gaussian beam 16mm in diameter is clipped by the objective aperture 25.4mm and imaged by the objective with focal length 16mm. The Airy patterns arising from the clipping are suppressed by an order magnitude between ~3.7µm and double that (comparing nearest peaks from those distances).

6.6 Array of rovibrational ground state molecules

6.6.1 Addressing arrays

As discussed in Chapter 5, the method we use to transfer the molecule from the Feshbach molecular state to the rovibrational ground state relies on a driving a π-pulse with a two-photon Raman transition. Compared with STIRAP, this approach is more susceptible to beam intensity fluctuations. Therefore, to uniformly drive the array to rovibrational ground state molecules, the Raman transfer beams need to uniformly address the array over ~30 µm.

While the two-photon Rabi frequency is given by $\frac{\Omega_1\Omega_2}{4\Delta} \propto \sqrt{I_1 I_2}$ and scales to the square root of intensity of the Raman transfer beams, we also need to consider the differential light shift $\frac{\Omega_1^2}{4\Delta} - \frac{\Omega_2^2}{4\Delta}$ that would shift the transition out of resonance. A numerical simulation of the dependence of transfer efficiency on the pump and Stokes beam Rabi frequencies is shown Fig. 6.9(a). Based on this, we estimate that with our Rabi frequencies, the transfer fidelity can be above 95% across the array, if the intensity variation over the array is less than 16% for

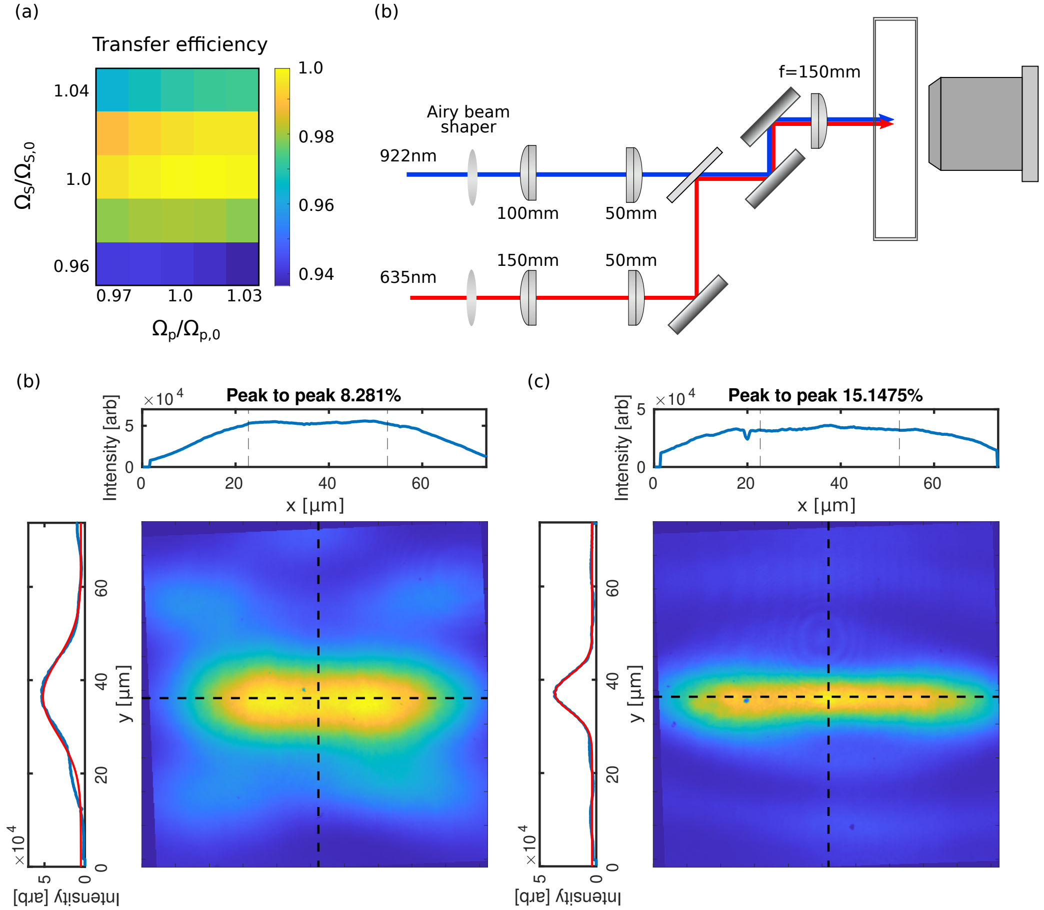

Figure 6.9: Tophat beam shaping. (a) Molecule Raman state transfer efficiency as a function of pump and Stokes Rabi frequencies relative to center frequencies based on numerical simulations. $\Omega_{p,0}$ and $\Omega_{S,0}$ are taken to be $2\pi \times 40$ MHz and $2\pi \times 200$ MHz respectively. (b) Schematic of beampath. The 635 nm and 922 nm beams are launched individually using fiber launchers (Schafter+Kirchhoff 60FC-L-4-M60L-02) such that the beam sizes match that required by the Airy beam shaper. The cylindrical telescope shrinks the horizontal beam size to give the cylindrical beam shape at the atoms. The two beams are combined by a dichroic before being focused into the chamber with a spherical lens. The beams are sent counter-propagating with the tweezer beams. (c-d) The intensity profiles of the (c) 922 nm and (d) 635 nm beams are imaged on a beam profiler at the focus of the beam. The vertical direction is a Gaussian profile. The tophat profile is in the horizontal direction to address the array. The peak-to-peak variation is taken over 30 µm, which is the array size to address.

635 nm and 8% for 922 nm[§].

For a typical Gaussian beam with a waist of w_0, the region where the intensity is within 15% of peak intensity has a radius of only ~$0.6w_0$. Therefore, instead, we opt to create a tophat shape at the location of the atoms.

Tophat beam shaping

We use an Airy beam shaper (Asphericon ASM25-10-D-B-780 and ASM25-10-D-B-632 for 922 nm and 635 nm respectively) to create an Airy disk phase pattern in the Fourier plane, which then gets imaged by a lens to form a tophat beam shape at the location of the atoms. We use a cylindrical shaped beam to address the 1D array for higher intensities. A schematic of the beam path is shown in Fig. 6.9(b). The beam shape is sensitive to the alignment along the z-direction, as the beam profile varies drastically around the focal plane. Since the beam is counter-propagating to the optical tweezer beam path, we image the beam on the Andor CCD camera we normally use to image the single atoms for alignment in z, and alignment in x-y to the atoms. We are able to achieve an intensity uniformity of 8% and 15% over the peak of the 922 nm and 635 nm beam respectively on a beam profiler as shown in Fig. 6.9(c-d).

We use a vector light shift measurement to fine align the 922 nm beam to the atoms as shown in Fig. 6.10(a-b). In particular, the light shift is proportional to beam intensity, and we find a uniformity of 6(2)%. To check the uniformity of the 635 nm beam, we use an Aulter-Townes spectroscopy measurement as discussed in section 5.5.1. This is shown in Fig. 6.10(c-d). We find that the uniformity of the 635 nm Rabi frequency is 14(10)%,

---

[§] These numbers are chosen based on the achieved intensity uniformity below. In principle, the requirement for either beam can be relaxed by compensating with tighter constraints on the other beam.

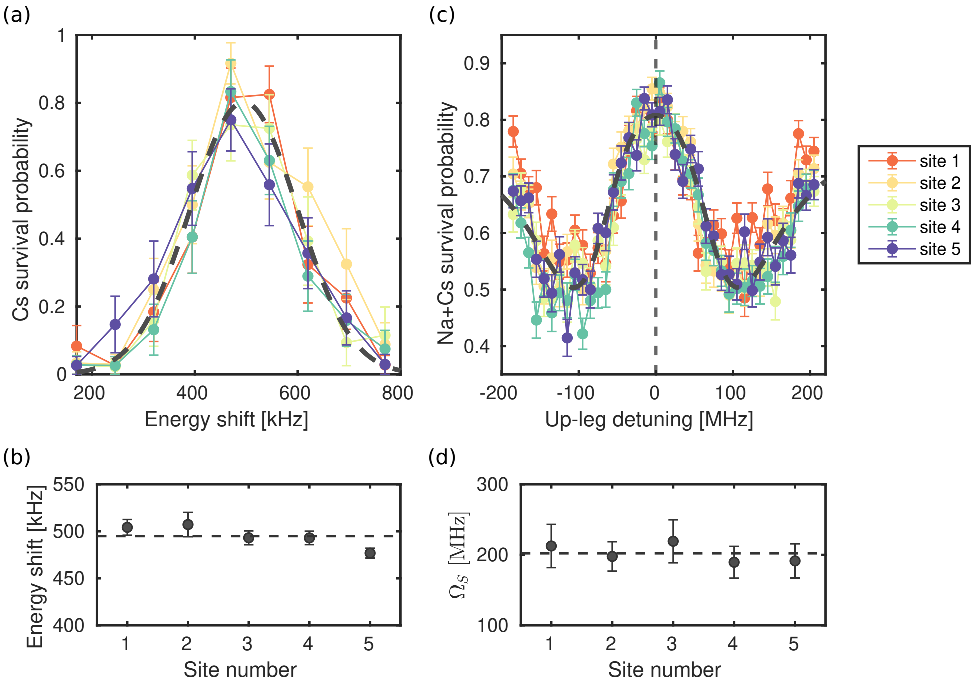

Figure 6.10: Raman transfer beam uniformity calibration. (a-b) The uniformity of the 922 nm beam is measured by the vector light shift induced on Cs atoms by the beam. The absolute energy shift is proportional to intensity, and we find a site-to-site variation of 6(2)%. (c-d) the uniformity of the 635 nm is measured by Autler-Townes spectroscopy. The down-leg laser frequency is parked on single-photon resonance, and the up-leg frequency is scanned. The spacing roughly corresponds to the down-leg Rabi frequency. The exact fitting procedure is discussed in section 5.5.1. We find a site-to-site variation in Rabi frequency of 14(10)%.

6.6.2 Coherent molecule formation

At long last, we drive the Feshbach molecules to the rovibrational state using the same Raman transfer process as discussed in Chapter 5. We create an array of 4 rovibrational ground state molecules, shown in Fig. 6.11. We use 50 mW for the up-leg 922 nm, and 6 mW power for the down-leg 635 nm out of the fiber and achieve a π-pulse time of 5.7(6) µs. The Rabi flopping from Feshbach molecules to rovibrational ground state $|X^1\Sigma, v = 0, N = 0\rangle$ for each individual site is shown in (a), and the π-times for each individual site are plotted in (b). The one-way efficiency averaged over all sites is 69(5)%.

6.7 Outlook

In this chapter, we have presented our initial attempts in scaling the single molecule assembly process up to arrays of molecules. In the present approach, we used an AOBD to create a dual species array of up to 10 Na+Cs atom pairs, and achieved an array of 4 rovibrational ground state NaCs molecules. In the process, we have also learned the challenges in scaling up the platform which helps to guide further work. In planned upgrades, the following are considered:

- *Spatial light modulators for tweezer array generation.* As we have seen in the present chapter, many problems arise from using AOBD's to generate an array of optical tweezers. In particular, beating phenomena due to non-linear effects, both optical and RF, cause issues in bringing the traps close together. On the other hand, spatial light modulators (SLM) have been demonstrated to be a flexible and robust approach to generating large arrays of optical tweezers[69,152]. SLM's can impose a phase pattern on an input beam in the Fourier plane that can be tailored to correspond to arbitrary tweezer array patterns in the imaging plane. They function by driving liquid crystals at the mi-

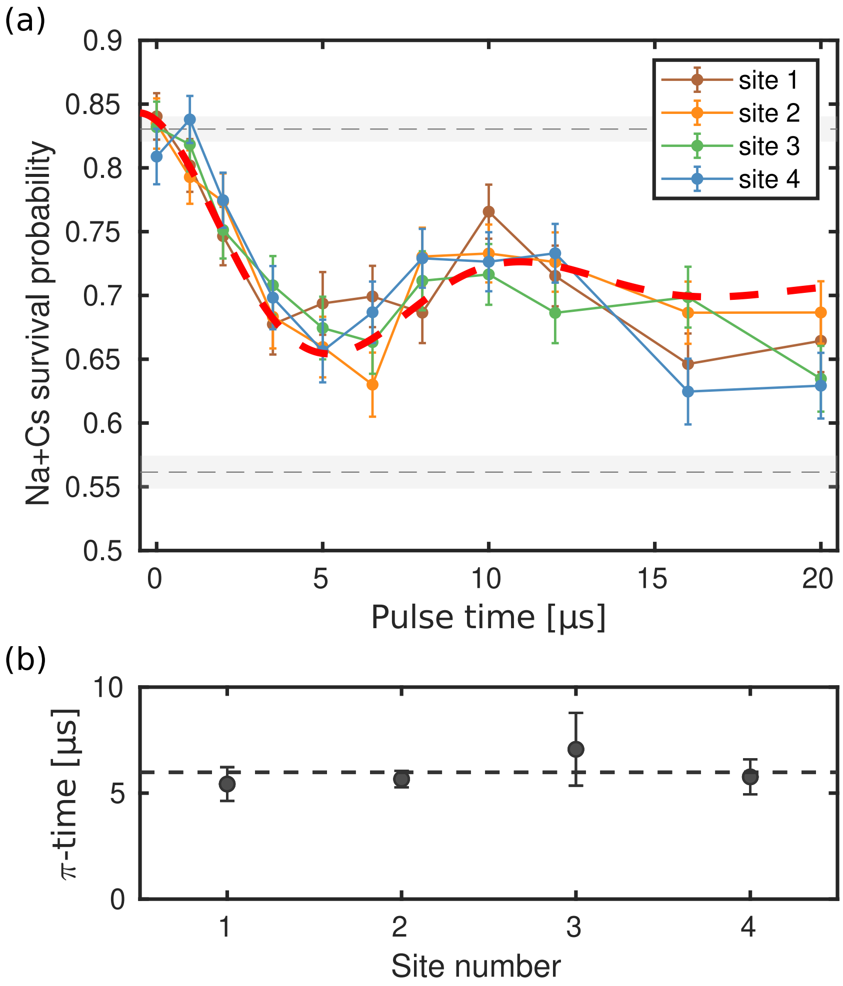

Figure 6.11: Coherent transfer of an array of Feshbach molecules to the rovibrational ground state. (a) An array of four Feshbach molecules is coherently transferred to the rovibrational ground state using the method discussed in Chapter 5. The data from each site is overlaid. Dashed red line is a fit to the average of all sites. Dashed grey lines and shaded grey area indicate Feshbach molecule formation contrast and errorbars. (b) The π-pulse time obtained from fitting the data to an exponentially decaying sinusoidal function for each site.

cron scale, and are not susceptible to RF beating problems as AOBD's are. Therefore, we expect that using SLM's should help improve the molecule formation fidelity and allow for traps closer in distance, which would be advantageous for larger dipole-dipole interactions between molecules.

- *In situ rearrangement of single atoms. In situ* rearrangement has previously been demonstrated in 1D and 2D arrays of atom arrays. This would allow for higher filling fraction of the resulting molecular arrays. In addition, this would allow for higher data taking rates and better statistics overall. With rearrangement, we can ensure that a single Na and Cs atom are present with certainty before molecule formation and would enable schemes to post-select on data with molecules. Better yet, the possibility of non-destructive direct molecule detection[153], or indirect detection of atom pairs left behind[¶], would allow for rearranging based on the existence of molecules at each site.
- *Larger and higher dimensional arrays.* In the present work we assembled a 1D array of single molecules. In the future this can be expanded to higher dimensions, by use of SLM's or additional AOBD's. In addition, to achieve larger arrays, more optical power will be needed.

  - At present Thorlabs patch cable fibers are used to couple the tweezer light from the lasers to the experiment, which work well at the powers we operate at. However, to go to higher powers, photonic crystal fibers will be needed to achieve higher coupling efficiency and higher saturation powers.

  - For both species, the implementation of *in situ* rearrangement also relaxes power

---

[¶] When atom-to-rovibrational-ground-state-molecule conversion is unsuccessful, which is predominantly due to the atoms not being in the relative motional ground state of the trap, the atoms are left behind in the trap. One possibility is to image the atoms without addressing the molecules, and any sites without atoms would indicate the presence of a molecule. This requires high field imaging or ramping the magnetic field to low fields for imaging.

requirements, since higher powers are necessary for Raman sideband cooling. By turning off traps with no atoms, more power can be used for the traps to cool the atoms in.

- For Na, the current limitation is in the 623 nm power. Recent work has shown magic trapping on the D1 line is possible for Na[149], opening an avenue to create larger arrays of Na atoms. In particular, assuming similar achievable powers in the sum frequency generation process, we expect a factor of ~3.5 more power due to the increased power from no switching and less power required per trap depth by being closer to resonance.

- *Improved molecule formation.* In the molecule assembly process, the Raman transfer process is susceptible to intensity variations over the array. In the present work we used an Airy beam shaper to create a tophat beam shape to uniformly address the arrays.

  - Alternate Raman transfer schemes. One possibility is to chirp the frequency of the Raman transfer beams to achieve adiabatic transfer by ARP[154]. This would relax intensity stability and uniformity requirements for the transfer process.

  - Raman transfer beam addressing. Alternate approaches include using an SLM or AOM to generate individual addressing beams that can then be aligned to the individual atoms. This would allow for smaller beam waists and thus higher intensities, as well as better individual control.

  - Alternate transfer pathways. As discussed in Chapter 5, the molecule formation fidelity is limited by the excited state scattering. This leads to decoherence after 1-2 Rabi cycles. Work is under progress to identify transfer pathways with less scattering. This could enable, for example, (a) STIRAP transfer, which is less susceptible to non-uniform intensities across the array, or (b) with longer coherence times, dynamic decoupling pulse sequences[155,156], which typically require 10s of π-pulses, may be possible for creating uniform transfer across the array despite non-uniform beam intensities across the array.

7

Outlook

In this thesis, we presented results on creating an array of fully quantum-state controlled rovibrational ground state polar NaCs molecules in optical tweezers. With their large dipole moments (4.6 D), NaCs molecules are promising candidates to generate strong dipole-dipole interactions. With the fine control over individual molecules in this platform, this opens exciting new opportunities in quantum science applications harnessing the rich properties of molecules.

7.1 Looking forward

- *Microwave and electric field control*

  In order to entangle multiple molecules, the molecules need to be driven to internal states that can interact with each other. Convenient options are the lowest excited rotational levels[157,158,159]. These can be accessed by microwave or two-photon Raman transitions. In addition to microwave control, electric fields would enable polarizing the molecules in the lab frame[160], and would allow for a wide range Hamiltonians to be simulated[161,162].

- *Entanglement*

  Even without external eletric fields, it is possible to entangle two polar molecules by virtue of their dipolar exchange interaction, as detailed in Ref.[36]. With an array of molecules under control, this can soon be a reality.

- *Scaling ever up*

  In this thesis we demonstrated scaling up to a 1D array of molecules. As discussed in Chapter 6, plans are under way to scale the system to even larger systems consisting of more molecules and higher dimensions[152,68].

- *Quantum simulation and quantum computation*

  Many quantum simulation and quantum computation applications rely on the ability to address and control individual molecules[163,40,164,165]. The platform presented in this thesis is a starting point for many of these applications.

- *Other directions*

As demonstrated in Chapter 4, optical tweezers also provide a good platform to study well-controlled few-body physics. This can be expanded to molecules to study atom+molecule or even molecule+molecule collisions, Feshbach resonances, and even coherent formation of larger molecules using similar approaches[166,135,134]. Opportunities abound.

A

Tweezer vs. lattice confinement

The potential experienced by an atom in a laser field with spatial intensity distribution $I(\mathbf{r})$ is[100]

$$U_{\text{dip}} = -\frac{\text{Re}(\alpha)}{2\varepsilon_0 c} I(\mathbf{r}) \tag{A.1}$$

where α is the polarizability at the laser wavelength. The scattering rate is given by

$$\Gamma_{\text{sc,tweezer}} = \frac{\text{Im}(\alpha)}{\hbar \varepsilon_0 c} I(\mathbf{r}) \tag{A.2}$$

Optical tweezer

The intensity profile of a Gaussian beam with power P and wavelength λ focused to a beam waist of w_0 can be expressed as

$$I_{\text{tweezer}}(r, z) = I_{0,\text{tweezer}} \left(\frac{w(z)}{w_0} \right)^2 \exp\left(-\frac{2r^2}{w(z)^2} \right) \tag{A.3}$$

where $z_R = \pi w_0^2/\lambda$ is the Rayleigh range, $w(z) = w_0\sqrt{1 + (z/z_R)^2}$, and the peak intensity $I_{0,\text{tweezer}} = P/2\pi w_0^2$. The resulting dipole potential near the focus can be approximated as

$$\begin{aligned} U(r, z) &= -U_{0,\text{tweezer}} \left(\frac{w(z)}{w_0} \right)^2 \exp\left(-\frac{2r^2}{w(z)^2} \right) \\ &\simeq -U_{0,\text{tweezer}} \left(1 - 2\left(\frac{r}{w_0} \right)^2 - \left(\frac{z}{z_R} \right)^2 \right) \end{aligned} \tag{A.4}$$

where $U_{0,\text{tweezer}} = \frac{\text{Re}(\alpha)}{2\varepsilon_0 c} I_{0,\text{tweezer}}$.

Near the bottom of the potential, the trapping frequencies in the radial and axial directions are given by

$$\omega_{R,\text{tweezer}} = \sqrt{\frac{4U_0}{m w_0^2}}, \quad \omega_{z,\text{tweezer}} = \sqrt{\frac{2U_0}{m z_R^2}} \tag{A.5}$$

respectively. In particular, the ratio of the axial and radial trapping frequency is fixed by the geometry

$$\omega_{z,\text{tweezer}}/\omega_{R,\text{tweezer}} = \frac{\sqrt{2}\pi w_0^2}{\lambda^2} \approx 4.45 \tag{A.6}$$

where we can approximate $w_0 \approx \lambda$ in the diffraction-limited scenario.

The scattering rate at the center of the trap is

$$\hbar\Gamma_{\text{sc,tweezer}} = \frac{1}{\varepsilon_0 c}\text{Im}(\alpha) I_{0,\text{tweezer}} \tag{A.7}$$

1D lattice

The intensity profile of two counter-propagating beams in the z-direction can be expressed as

$$I(z) = I_1(z) + I_2(z) + 2\sqrt{I_1(z)I_2(z)}\cos(\delta\varphi) = I_0(1+\cos(kz)) \tag{A.8}$$

The corresponding potential experienced by an atom in the presence of such a profile can be expressed as

$$U(r,z) = -U_{0,\text{lattice}}\sin^2(kz) \simeq -U_{0,\text{lattice}}\left(1-k^2z^2\right) \tag{A.9}$$

where we have let $U_{0,\text{lattice}} = \frac{\text{Re}(\alpha)}{2\varepsilon_0 c} I_{0,\text{lattice}}$. Note that for the same amount of power, the peak intensity $I_{0,\text{lattice}} = 4I_{0,\text{tweezer}}$ due to interference effects. However, we are interested in comparing the intensity values.

The trapping frequency in this case is

$$\omega_{\text{lattice}} = \sqrt{\frac{2U_{0,\text{lattice}}k^2}{m}} = \sqrt{\frac{8\pi^2 U_{0,\text{lattice}}}{m\lambda^2}} \tag{A.10}$$

The scattering rate follows from equation

$$\Gamma_{\text{sc,lattice}} = \frac{1}{\hbar\varepsilon_0 c}\text{Im}(\alpha) I_{0,\text{lattice}} \tag{A.11}$$

Comparison

With the same peak intensity, i.e. $U_{0,\text{tweezer}} = U_{0,\text{lattice}}$, the ratio between the trapping frequencies arising from a lattice and optical tweezer potential are

$$\frac{\omega_{\text{lattice}}}{\omega_{R,\text{tweezer}}} = \frac{\sqrt{2}\pi w_0}{\lambda} \tag{A.12}$$

$$\frac{\omega_{\text{lattice}}}{\omega_{z,\text{tweezer}}} = \frac{2\pi^2 w_0^2}{\lambda^2} \tag{A.13}$$

On the other hand, to produce the same trapping frequency in the radial direction, the peak intensity values are

$$\frac{I_{0,\text{R lattice}}}{I_{0,\text{tweezer}}} = \frac{\lambda^2}{2\pi^2 w_0^2} = \frac{D^2}{2\pi^2} \tag{A.14}$$

while to produce the same trapping frequencies as the axial direction, this is

$$\frac{I_{0,\text{z lattice}}}{I_{0,\text{tweezer}}} = \frac{\lambda^4}{4\pi^4 w_0^4} = \frac{D^4}{4\pi^4} \tag{A.15}$$

where we have defined $D = \lambda/w_0 \approx 1$.

Thus, for a 3D lattice formed with the same trapping frequencies as an optical tweezer, assuming no interference between the three axes, the total peak intensity is

$$I_{0,\text{3D lattice}} = 2I_{0,\text{R lattice}} + I_{0,\text{z lattice}} = \left(\frac{2D^2}{2\pi^2} + \frac{D^4}{4\pi^4}\right) I_{0,\text{tweezer}} \approx \frac{I_{0,\text{tweezer}}}{\pi^2} \tag{A.16}$$

And thus the scattering rate

$$\Gamma_{\text{sc,tweezer}} \approx \pi^2 \times \Gamma_{\text{sc, 3D lattice}} \tag{A.17}$$

This means the scattering rate of an optical tweezer is an order of magnitude larger than that of an optical lattice given the same trapping frequencies.

The confinement in an optical lattice potential comes from the interference of laser beams, and the length scale is on the order of the wavelength. The confinement from optical tweezers on the other hand, arises from the focusing of the beam.

One method to improve the axial confinement is to superimpose a lattice in the axial direction. In this case, to achieve the same radial trapping frequency, the total intensity is

$$I_{0,\text{3D lattice}} = I_{0,\text{tweezer}} + I_{0,\text{R lattice}} = \left(1 + \frac{D^2}{2\pi^2}\right) I_{0,\text{tweezer}} \approx \left(1 + \frac{1}{2\pi^2}\right) I_{0,\text{tweezer}} \tag{A.18}$$

which incurs ~5% extra scattering on the atoms.

B

Relative and COM motional states

The Hamiltonian for a pair of Na and Cs atoms in a 1D harmonic trap, neglecting interactions, can be expressed in the atomic position coordinates as

$$H = \sum_{i=\mathrm{Na,Cs}} \frac{p_i^2}{2m_i} + \frac{1}{2} m_i \omega_i^2 x_i^2 = \sum_{i=\mathrm{Na,Cs}} \hbar\omega_i \left(a_i^\dagger a_i + \frac{1}{2} \right). \tag{B.1}$$

In particular, $a_i(a_i^\dagger)$ are the annihilation and creation operators for the harmonic modes of the individual atoms in the harmonic trap, which gives rise to a number basis $|n_{\mathrm{Na}}, n_{\mathrm{Cs}}\rangle$ for the motional states. When forming molecules from atom pairs, however, it is more natural to work in terms of the center-of-mass (COM) and relative coordinates, which casts the two-body problem in the lab frame into a one-body problem in the molecular frame of reference. The coordinate transformation is given by

$$x_{\mathrm{com}} = \frac{m_{\mathrm{Na}} x_{\mathrm{Na}} + m_{\mathrm{Cs}} x_{\mathrm{Cs}}}{M} \tag{B.2}$$

$$x_{\mathrm{rel}} = x_{\mathrm{Na}} - x_{\mathrm{Cs}} \tag{B.3}$$

and

$$p_{\mathrm{com}} = M\dot{x}_{\mathrm{com}} = p_{\mathrm{Na}} + p_{\mathrm{Cs}} \tag{B.4}$$

$$p_{\mathrm{rel}} = \mu \dot{x}_{\mathrm{rel}} = \frac{m_{\mathrm{Cs}} p_{\mathrm{Na}} - m_{\mathrm{Na}} p_{\mathrm{Cs}}}{M}, \tag{B.5}$$

where $M = m_{\mathrm{Na}} + m_{\mathrm{Cs}}$ and $\mu = \frac{m_{\mathrm{Na}} m_{\mathrm{Cs}}}{M}$. Then the Hamiltonian in eq. B.1 can be equivalently expressed as

$$\begin{aligned} H = & \frac{p_{\mathrm{com}}^2}{2M} + \frac{1}{2} M \frac{m_{\mathrm{Na}} \omega_{\mathrm{Na}}^2 + m_{\mathrm{Cs}} \omega_{\mathrm{Cs}}^2}{M} x_{\mathrm{com}}^2 \\ & + \frac{p_{\mathrm{rel}}^2}{2\mu} + \frac{1}{2} \mu \frac{m_{\mathrm{Cs}} \omega_{\mathrm{Na}}^2 + m_{\mathrm{Na}} \omega_{\mathrm{Cs}}^2}{M} x_{\mathrm{rel}}^2 + \mu(\omega_{\mathrm{Na}}^2 - \omega_{\mathrm{Cs}}^2) x_{\mathrm{com}} x_{\mathrm{rel}}. \end{aligned} \tag{B.6}$$

The trapping frequencies for the Na and Cs atoms in the optical tweezers $\omega_{\mathrm{Na}} \approx 1.07\omega_{\mathrm{Cs}}$ are approximately equal, so we omit the coupling term and take $\omega = \omega_{\mathrm{Na}} = \omega_{\mathrm{Cs}}$ to simplify eq. B.6 to

$$H = \frac{p_{\text{com}}^2}{2M} + \frac{1}{2}M\omega^2 x_{\text{com}}^2 + \frac{p_{\text{rel}}^2}{2\mu} + \frac{1}{2}\mu\omega^2 x_{\text{rel}}^2 = \hbar\omega\left(a_{\text{com}}^\dagger a_{\text{com}} + \frac{1}{2}\right) + \hbar\omega\left(a_{\text{rel}}^\dagger a_{\text{rel}} + \frac{1}{2}\right), \tag{B.7}$$

where

$$a_{\text{com}}^\dagger = \sqrt{\frac{M\omega}{2\hbar}}\hat{x}_{\text{com}} - \frac{i}{\sqrt{2M\omega\hbar}}\hat{p}_{\text{com}} \tag{B.8}$$

$$a_{\text{rel}}^\dagger = \sqrt{\frac{\mu\omega}{2\hbar}}\hat{x}_{\text{rel}} - \frac{i}{\sqrt{2\mu\omega\hbar}}\hat{p}_{\text{rel}} \tag{B.9}$$

are defined similarly to the atomic case and are related to $a_{\text{Na}}^\dagger, a_{\text{Cs}}^\dagger$ by

$$a_{\text{Na}}^\dagger = \sqrt{\frac{m_{\text{Cs}}}{M}}a_{\text{rel}}^\dagger + \sqrt{\frac{m_{\text{Na}}}{M}}a_{\text{com}}^\dagger, \quad a_{\text{Cs}}^\dagger = -\sqrt{\frac{m_{\text{Na}}}{M}}a_{\text{rel}}^\dagger + \sqrt{\frac{m_{\text{Cs}}}{M}}a_{\text{com}}^\dagger. \tag{B.10}$$

The motional states can then be expressed in terms of a number basis in the COM and relative motional modes $|n_{\text{com}}, n_{\text{rel}}\rangle$. Our discussion of motional state population pertaining to molecule formation is in terms of this basis.

C

Table of Feshbach resonances observed

Table C.1: Table of all Feshbach resonances observed in the present work.

Channel	Total m_F	Method	B [G]	Character
$\lvert F=1, m_F=1\rangle_\mathrm{Na}\lvert F=3, m_F=3\rangle_\mathrm{Cs}$	+4	magnetoassociation	864.11(5)	s-wave
$\lvert F=1, m_F=1\rangle_\mathrm{Na}\lvert F=3, m_F=3\rangle_\mathrm{Cs}$	+4	FR-enhanced PA	807	p-wave
$\lvert F=1, m_F=-1\rangle_\mathrm{Na}\lvert F=3, m_F=-3\rangle_\mathrm{Cs}$	-4	inelastic	652.1(4)	s-wave
$\lvert F=1, m_F=-1\rangle_\mathrm{Na}\lvert F=3, m_F=-3\rangle_\mathrm{Cs}$	-4	inelastic	791.10(5)	p-wave

D

Feshbach coil winding

The Feshbach coil was wound with the help of a lathe, as shown in Fig. D.1(a). Jigs as shown in Fig. D.1(b-c) were used to hold the wires in place while the epoxy cured. A particular challenge was forcing the wires to cross over each other to create the pancake structure desired. In an initial attempt, a short developed in the coil resulting from the large stress that builds up where the wires cross over each other. Learning from the failed experience, during the winding process, the wires were wrapped with extra layers of Kapton tape to prevent shorts.

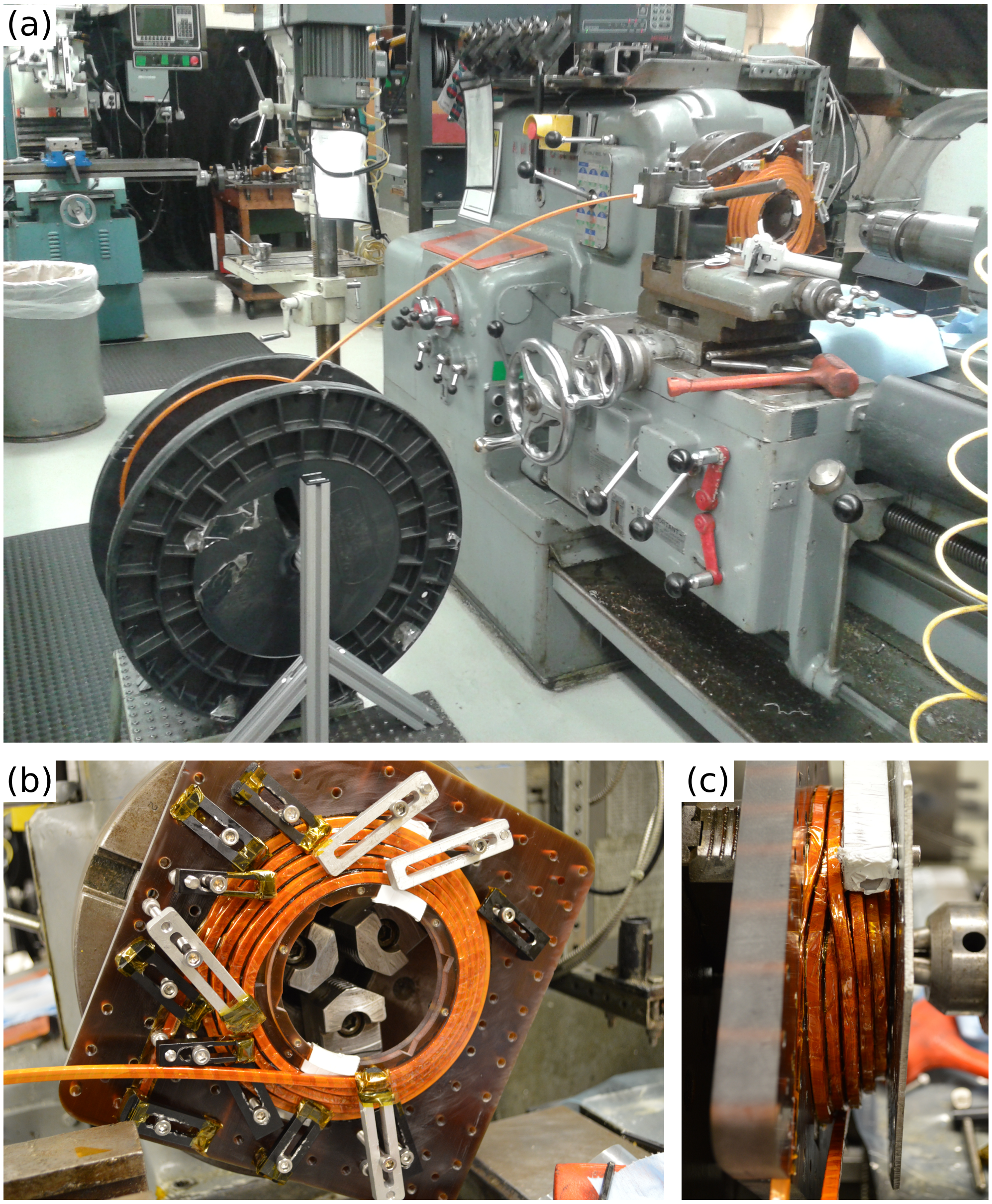

Figure D.1: Feshbach coil winding. (a) The coil is wound with the help of a lathe. (b-c) The coil is wound layer by layer, waiting for the epoxy to cure between each layer. The wire is clamped down to ensure they fall in place following the staggered pancake structure.

References

[1] David P. DiVincenzo. The physical implementation of quantum computation. *Fortschritte der Physik*, 48(9-11):771–783, 2000.

[2] J. W. Britton, B. C. Sawyer, A. C. Keith, C.-C. J. Wang, J. K. Freericks, H. Uys, M. J. Biercuk, and J. J. Bollinger. Engineered two-dimensional Ising interactions in a trapped-ion quantum simulator with hundreds of spins. *Nature*, 484:489–492, April 2012.

[3] J. Zhang, G. Pagano, P. W. Hess, A. Kyprianidis, P. Becker, H. Kaplan, A. V. Gorshkov, Z. X. Gong, and C. Monroe. Observation of a many-body dynamical phase transition with a 53-qubit quantum simulator. *Nature*, 551(7682):601–604, November 2017.

[4] Mari Carmen Banuls, Rainer Blatt, Jacopo Catani, Alessio Celi, Juan Ignacio Cirac, Marcello Dalmonte, Leonardo Fallani, Karl Jansen, Maciej Lewenstein, Simone Montangero, Christine A. Muschik, Benni Reznik, Enrique Rico, Luca Tagliacozzo, Karel Van Acoleyen, Frank Verstraete, Uwe-Jens Wiese, Matthew Wingate, Jakub Zakrzewski, and Peter Zoller. Simulating lattice gauge theories within quantum technologies. *Eur. J. Phys. D*, 74:165, 2020.

[5] D Leibfried, R Blatt, C Monroe, and D Wineland. Quantum dynamics of single trapped ions. *Reviews of Modern Physics*, 75(1):281–324, 2003.

[6] Norbert M. Linke, Dmitri Maslov, Martin Roetteler, Shantanu Debnath, Caroline Figgatt, Kevin A. Landsman, Kenneth Wright, and Christopher Monroe. Experimental comparison of two quantum computing architectures. *Proceedings of the National Academy of Sciences*, 114(13):3305–3310, 2017.

[7] I. M. Georgescu, S. Ashhab, and Franco Nori. Quantum simulation. *Rev. Mod. Phys.*, 86:153–185, Mar 2014.

[8] T. D. Ladd, F. Jelezko, R. Laflamme, Y. Nakamura, C. Monroe, and J. L. O’Brien. Quantum computers. *Nature*, 464(7285):45–53, March 2010.

[9] Karl D. Nelson, Xiao Li, and David S. Weiss. Imaging single atoms in a three-dimensional array. *Nature Physics*, 3(8):556–560, 2007.

[10] Waseem S. Bakr, Jonathon I. Gillen, Amy Peng, Simon Fölling, and Markus Greiner. A quantum gas microscope for detecting single atoms in a Hubbard-regime optical lattice. *Nature*, 462(7269):74–77, 2009.

[11] Christof Weitenberg, Manuel Endres, Jacob F. Sherson, Marc Cheneau, Peter Schauß, Takeshi Fukuhara, Immanuel Bloch, and Stefan Kuhr. Single-spin addressing in an atomic Mott insulator. *Nature*, 471(7338):319–324, March 2011.

[12] Lawrence W. Cheuk, Matthew A. Nichols, Melih Okan, Thomas Gersdorf, Vinay V. Ramasesh, Waseem S. Bakr, Thomas Lompe, and Martin W. Zwierlein. Quantum-gas microscope for fermionic atoms. *Phys. Rev. Lett.*, 114:193001, May 2015.

[13] Peter T. Brown, Debayan Mitra, Elmer Guardado-Sanchez, Peter Schauß, Stanimir S. Kondov, Ehsan Khatami, Thereza Paiva, Nandini Trivedi, David A. Huse, and Waseem S. Bakr. Spin-imbalance in a 2D Fermi-Hubbard system. *Science*, 357(6358):1385–1388, 2017.

[14] Yiheng Lin, David R. Leibrandt, Dietrich Leibfried, and C.-W. Chou. Quantum entanglement between an atom and a molecule. *Nature*, 581:273–277, 2020.

[15] Chin-wen Chou, Christoph Kurz, David B. Hume, Philipp N. Plessow, David R. Leibrandt, and Dietrich Leibfried. Preparation and coherent manipulation of pure quantum states of a single molecular ion. *Nature*, 545(7653):203–207, May 2017.

[16] J. R. Maze, P. L. Stanwix, J. S. Hodges, S. Hong, J. M. Taylor, P. Cappellaro, L. Jiang, M. V. Gurudev Dutt, E. Togan, A. S. Zibrov, A. Yacoby, R. L. Walsworth, and M. D. Lukin. Nanoscale magnetic sensing with an individual electronic spin in diamond. *Nature*, 455(7213):644–647, October 2008.

[17] J. M. Taylor, P. Cappellaro, L. Childress, L. Jiang, D. Budker, P. R. Hemmer, A. Yacoby, R. Walsworth, and M. D. Lukin. High-sensitivity diamond magnetometer with nanoscale resolution. *Nature Physics*, 4(10):810–816, October 2008.

[18] Romana Schirhagl, Kevin Chang, Michael Loretz, and Christian L Degen. Nitrogen-vacancy centers in diamond: nanoscale sensors for physics and biology. *Annual review of physical chemistry*, 65:83–105, 2014.

[19] M. H. Devoret and R. J. Schoelkopf. Superconducting circuits for quantum information: An outlook. *Science*, 339(6124):1169–1174, 2013.

[20] Göran Wendin. Quantum information processing with superconducting circuits: a review. *Reports on Progress in Physics*, 80(10):106001, 2017.

[21] Frank Arute, Kunal Arya, Ryan Babbush, Dave Bacon, Joseph C Bardin, Rami Barends, Rupak Biswas, Sergio Boixo, Fernando GSL Brandao, David A Buell, et al.

Quantum supremacy using a programmable superconducting processor. *Nature*, 574(7779):505–510, 2019.

[22] Jianwei Wang, Fabio Sciarrino, Anthony Laing, and Mark G Thompson. Integrated photonic quantum technologies. *Nature Photonics*, 14(5):273–284, 2020.

[23] Ali W Elshaari, Wolfram Pernice, Kartik Srinivasan, Oliver Benson, and Val Zwiller. Hybrid integrated quantum photonic circuits. *Nature Photonics*, 14(5):285–298, 2020.

[24] Sergei Slussarenko and Geoff J Pryde. Photonic quantum information processing: A concise review. *Applied Physics Reviews*, 6(4):041303, 2019.

[25] Ehud Altman, Kenneth R. Brown, Giuseppe Carleo, Lincoln D. Carr, Eugene Demler, Cheng Chin, Brian DeMarco, Sophia E. Economou, Mark A. Eriksson, Kai-Mei C. Fu, Markus Greiner, Kaden R.A. Hazzard, Randall G. Hulet, Alicia J. Kollár, Benjamin L. Lev, Mikhail D. Lukin, Ruichao Ma, Xiao Mi, Shashank Misra, Christopher Monroe, Kater Murch, Zaira Nazario, Kang-Kuen Ni, Andrew C. Potter, Pedram Roushan, Mark Saffman, Monika Schleier-Smith, Irfan Siddiqi, Raymond Simmonds, Meenakshi Singh, I.B. Spielman, Kristan Temme, David S. Weiss, Jelena Vučković, Vladan Vuletić, Jun Ye, and Martin Zwierlein. Quantum simulators: Architectures and opportunities. *PRX Quantum*, 2:017003, Feb 2021.

[26] William D. Phillips. Nobel lecture: Laser cooling and trapping of neutral atoms. *Rev. Mod. Phys.*, 70(3):721–741, Jul 1998.

[27] V. M. Schäfer, C. J. Ballance, K. Thirumalai, L. J. Stephenson, T. G. Ballance, A. M. Steane, and D. M. Lucas. Fast quantum logic gates with trapped-ion qubits. *Nature*, 555:75 EP –, 02 2018.

[28] C. L. Degen, F. Reinhard, and P. Cappellaro. Quantum sensing. *Rev. Mod. Phys.*, 89:035002, Jul 2017.

[29] Immanuel Bloch, Jean Dalibard, and Wilhelm Zwerger. Many-body physics with ultracold gases. *Rev. Mod. Phys.*, 80:885–964, Jul 2008.

[30] S. M. Brewer, J. S. Chen, A. M. Hankin, E. R. Clements, C. W. Chou, D. J. Wineland, D. B. Hume, and D. R. Leibrandt. Al+ 27 Quantum-Logic Clock with a Systematic Uncertainty below 10-18. *Physical Review Letters*, 123(3):033201, 2019.

[31] Lincoln D Carr, David DeMille, Roman V Krems, and Jun Ye. Cold and ultracold molecules: science, technology and applications. *New J. Phys.*, 11(5):055049, 2009.

[32] Deborah S. Jin and Jun Ye. Introduction to ultracold molecules: New frontiers in quantum and chemical physics. *Chem. Rev.*, 112, 2012.

[33] Bryce Gadway and Bo Yan. Strongly interacting ultracold polar molecules. *Journal of Physics B: Atomic, Molecular and Optical Physics*, 49(15):152002, 2016.

[34] J. M. Brown and A. Carrington. *Rotational spectroscopy of diatomic molecules*, pages 224–230. Cambridge Univ., Cambridge, UK, 2003.

[35] P. Rabl, D. DeMille, J. M. Doyle, M. D. Lukin, R. J. Schoelkopf, and P. Zoller. Hybrid quantum processors: Molecular ensembles as quantum memory for solid state circuits. *Phys. Rev. Lett.*, 97:033003, Jul 2006.

[36] Kang-Kuen Ni, Till Rosenband, and David D. Grimes. Dipolar exchange quantum logic gate with polar molecules. *Chem. Sci.*, 9:6830–6838, 2018.

[37] Ryan Barnett, Dmitry Petrov, Mikhail Lukin, and Eugene Demler. Quantum Magnetism with Multicomponent Dipolar Molecules in an Optical Lattice. *Phys. Rev. Lett.*, 96(19):190401, may 2006.

[38] Alexey V. Gorshkov, Salvatore R. Manmana, Gang Chen, Jun Ye, Eugene Demler, Mikhail D. Lukin, and Ana Maria Rey. Tunable superfluidity and quantum magnetism with ultracold polar molecules. *Phys. Rev. Lett.*, 107:115301, Sep 2011.

[39] Alexey V. Gorshkov, Salvatore R. Manmana, Gang Chen, Eugene Demler, Mikhail D. Lukin, and Ana Maria Rey. Quantum magnetism with polar alkali-metal dimers. *Phys. Rev. A*, 84:033619, Sep 2011.

[40] Bhuvanesh Sundar, Bryce Gadway, and Kaden R. A. Hazzard. Synthetic dimensions in ultracold polar molecules. *Scientific Reports*, 8:3422, 2018.

[41] K.-K. Ni, S. Ospelkaus, M. H. G. de Miranda, A. Pe'er, B. Neyenhuis, J. J. Zirbel, S. Kotochigova, P. S. Julienne, D. S. Jin, and J. Ye. A High Phase-Space-Density Gas of Polar Molecules. *Science*, 322(5899):231–235, 2008.

[42] Kai K. Voges, Philipp Gersema, Mara Meyer zum Alten Borgloh, Torben A. Schulze, Torsten Hartmann, Alessandro Zenesini, and Silke Ospelkaus. Ultracold gas of bosonic ^{23}Na^{39}K ground-state molecules. *Phys. Rev. Lett.*, 125:083401, Aug 2020.

[43] Jee Woo Park, Sebastian A. Will, and Martin W. Zwierlein. Ultracold dipolar gas of fermionic ^{23}Na^{40}K molecules in their absolute ground state. *Phys. Rev. Lett.*, 114:205302, May 2015.

[44] Mingyang Guo, Bing Zhu, Bo Lu, Xin Ye, Fudong Wang, Romain Vexiau, Nadia Bouloufa-Maafa, Goulven Quéméner, Olivier Dulieu, and Dajun Wang. Creation of an ultracold gas of ground-state dipolar ^{23}Na^{87}Rb molecules. *Phys. Rev. Lett.*, 116:205303, May 2016.

[45] A. Yang, S. Botsi, S. Kumar, S. B. Pal, M. M. Lam, I. Čepaitė, A. Laugharn, and K. Dieckmann. Singlet pathway to the ground state of ultracold polar molecules. *Phys. Rev. Lett.*, 124:133203, Apr 2020.

[46] Tetsu Takekoshi, Lukas Reichsöllner, Andreas Schindewolf, Jeremy M. Hutson, C. Ruth Le Sueur, Olivier Dulieu, Francesca Ferlaino, Rudolf Grimm, and Hanns-Christoph Nägerl. Ultracold dense samples of dipolar RbCs molecules in the rovibrational and hyperfine ground state. *Phys. Rev. Lett.*, 113:205301, Nov 2014.

[47] Luigi De Marco, Giacomo Valtolina, Kyle Matsuda, William G Tobias, Jacob P Covey, and Jun Ye. A degenerate fermi gas of polar molecules. *Science*, 363(6429):853–856, 2019.

[48] K.-K. Ni, S Ospelkaus, D Wang, G Quéméner, B Neyenhuis, M H G de Miranda, J L Bohn, J Ye, and D S Jin. Dipolar collisions of polar molecules in the quantum regime. *Nature*, 464(7293):1324–8, Apr 2010.

[49] Yu Liu, Ming-Guang Hu, Matthew A. Nichols, David D. Grimes, Tijs Karman, Hua Guo, and Kang-Kuen Ni. Photo-excitation of long-lived transient intermediates in ultracold reactions. *Nature Physics*, 16(11):1132–1136, November 2020.

[50] M.-G. Hu, Y. Liu, D. D. Grimes, Y.-W. Lin, A. H. Gheorghe, R. Vexiau, N. Bouloufa-Maafa, O. Dulieu, T. Rosenband, and K.-K. Ni. Direct observation of bimolecular reactions of ultracold krb molecules. *Science*, 366:1111, 2019.

[51] Bo Yan, Steven A. Moses, Bryce Gadway, Jacob P. Covey, Kaden R. A. Hazzard, Ana Maria Rey, Deborah S. Jin, and Jun Ye. Observation of dipolar spin-exchange interactions with lattice-confined polar molecules. *Nature*, 501(7468):521–525, 09 2013.

[52] Steven A Moses, Jacob P Covey, Matthew T Miecnikowski, Bo Yan, Bryce Gadway, Jun Ye, and Deborah S Jin. Creation of a low-entropy quantum gas of polar molecules in an optical lattice. *Science*, 350(6261):659–662, 2015.

[53] J. F. Barry, D. J. McCarron, E. B. Norrgard, M. H. Steinecker, and D. DeMille. Magneto-optical trapping of a diatomic molecule. *Nature*, 512(7514):286–289, aug 2014.

[54] Loïc Anderegg, Benjamin L. Augenbraun, Eunmi Chae, Boerge Hemmerling, Nicholas R. Hutzler, Aakash Ravi, Alejandra Collopy, Jun Ye, Wolfgang Ketterle, and John M. Doyle. Radio frequency magneto-optical trapping of caf with high density. *Phys. Rev. Lett.*, 119:103201, Sep 2017.

[55] Louis Baum, Nathaniel B. Vilas, Christian Hallas, Benjamin L. Augenbraun, Shivam Raval, Debayan Mitra, and John M. Doyle. 1d magneto-optical trap of polyatomic molecules. *Phys. Rev. Lett.*, 124:133201, Mar 2020.

[56] Shiqian Ding, Yewei Wu, Ian A. Finneran, Justin J. Burau, and Jun Ye. Sub-doppler cooling and compressed trapping of yo molecules at μK temperatures. *Phys. Rev. X*, 10:021049, Jun 2020.

[57] S. Truppe, H. J. Williams, M. Hambach, L. Caldwell, N. J. Fitch, E. A. Hinds, B. E. Sauer, and M. R. Tarbutt. Molecules cooled below the doppler limit. *Nature Physics*, 13:1173, 08 2017.

[58] Lawrence W. Cheuk, Loïc Anderegg, Benjamin L. Augenbraun, Yicheng Bao, Sean Burchesky, Wolfgang Ketterle, and John M. Doyle. Λ-enhanced imaging of molecules in an optical trap. *Phys. Rev. Lett.*, 121:083201, Aug 2018.

[59] Loïc Anderegg, Lawrence W. Cheuk, Yicheng Bao, Sean Burchesky, Wolfgang Ketterle, Kang-Kuen Ni, and John M. Doyle. An optical tweezer array of ultracold molecules. *Science*, 365:1156–1158, Sep 2019.

[60] Kyle Matsuda, Luigi De Marco, Jun-Ru Li, William G. Tobias, Giacomo Valtolina, Goulven Quéméner, and Jun Ye. Resonant collisional shielding of reactive molecules using electric fields. *Science*, 370(6522):1324–1327, December 2020.

[61] Jee Woo Park, Zoe Z. Yan, Huanqian Loh, Sebastian A. Will, and Martin W. Zwierlein. Second-scale nuclear spin coherence time of ultracold ^{23}Na^{40}K molecules. *Science*, 357(6349):372–375, 2017.

[62] Frauke Seeßelberg, Xin-Yu Luo, Ming Li, Roman Bause, Svetlana Kotochigova, Immanuel Bloch, and Christoph Gohle. Extending rotational coherence of interacting polar molecules in a spin-decoupled magic trap. *Phys. Rev. Lett.*, 121:253401, Dec 2018.

[63] M W Gempel, T Hartmann, T A Schulze, K K Voges, A Zenesini, and S Ospelkaus. Versatile electric fields for the manipulation of ultracold NaK molecules. *New Journal of Physics*, 18(4):045017, Apr 2016.

[64] Wade G Rellergert, Scott T Sullivan, Steven J Schowalter, Svetlana Kotochigova, Kuang Chen, and Eric R Hudson. Evidence for sympathetic vibrational cooling of translationally cold molecules. *Nature*, 495(7442):490–494, 2013.

[65] N Schlosser, G Reymond, I Protsenko, and P Grangier. Sub-poissonian loading of single atoms in a microscopic dipole trap. *Nature*, 411(6841):1024–7, jun 2001.

[66] S. Kuhr, W. Alt, D. Schrader, M. Müller, V. Gomer, and D. Meschede. Deterministic delivery of a single atom. *Science*, 293(5528):278–280, 2001.

[67] A. M. Kaufman, B. J. Lester, M. Foss-Feig, M. L. Wall, A. M. Rey, and C. A. Regal. Entangling two transportable neutral atoms via local spin exchange. *Nature*, 527(7577):208–211, November 2015.

[68] Manuel Endres, Hannes Bernien, Alexander Keesling, Harry Levine, Eric R. Anschuetz, Alexandre Krajenbrink, Crystal Senko, Vladan Vuletic, Markus Greiner, and Mikhail D. Lukin. Atom-by-atom assembly of defect-free one-dimensional cold atom arrays. *Science*, 354(6315):1024–1027, 2016.

[69] Daniel Barredo, Sylvain de Léséleuc, Vincent Lienhard, Thierry Lahaye, and Antoine Browaeys. An atom-by-atom assembler of defect-free arbitrary two-dimensional atomic arrays. *Science*, 354(6315):1021–1023, 2016.

[70] A. M. Kaufman, B. J. Lester, M. Foss-Feig, M. L. Wall, A. M. Rey, and C. A. Regal. Entangling two transportable neutral atoms via local spin exchange. *Nature*, 527(7577):208, 2015.

[71] Harry Levine, Alexander Keesling, Ahmed Omran, Hannes Bernien, Sylvain Schwartz, Alexander S. Zibrov, Manuel Endres, Markus Greiner, Vladan Vuletić, and Mikhail D. Lukin. High-Fidelity Control and Entanglement of Rydberg-Atom Qubits. *Physical Review Letters*, 121(12):123603, September 2018.

[72] Ivaylo S. Madjarov, Jacob P. Covey, Adam L. Shaw, Joonhee Choi, Anant Kale, Alexandre Cooper, Hannes Pichler, Vladimir Schkolnik, Jason R. Williams, and Manuel Endres. High-fidelity entanglement and detection of alkaline-earth Rydberg atoms. *Nature Physics*, 16(8):857–861, August 2020.

[73] Sylvain de Léséleuc, Vincent Lienhard, Pascal Scholl, Daniel Barredo, Sebastian Weber, Nicolai Lang, Hans Peter Büchler, Thierry Lahaye, and Antoine Browaeys. Observation of a symmetry-protected topological phase of interacting bosons with Rydberg atoms. *Science*, 365(6455):775–780, August 2019.

[74] Giulia Semeghini, Harry Levine, Alexander Keesling, Sepehr Ebadi, Tout T. Wang, Dolev Bluvstein, Ruben Verresen, Hannes Pichler, Marcin Kalinowski, Rhine Samajdar, and et al. Probing topological spin liquids on a programmable quantum simulator, Apr 2021.

[75] Hannes Bernien, Sylvain Schwartz, Alexander Keesling, Harry Levine, Ahmed Omran, Hannes Pichler, Soonwon Choi, Alexander S. Zibrov, Manuel Endres, Markus Greiner, Vladan Vuletić, and Mikhail D. Lukin. Probing many-body dynamics on a 51-atom quantum simulator. *Nature*, 551:579, 11 2017.

[76] M. Korek, S. Bleik, and A. R. Allouche. Theoretical calculation of the low laying electronic states of the molecule nacs with spin-orbit effect. *J. Chem. Phys.*, 126(12):124313, 2007.

[77] M. Aymar and O. Dulieu. Calculations of transition and permanent dipole moments of heteronuclear alkali dimers nak, narb and nacs. *Molecular Physics*, 105(11-12):1733–1742, 2007.

[78] Nicholas R Hutzler, Lee R Liu, Yichao Yu, and Kang-Kuen Ni. Eliminating light shifts for single atom trapping. *New J. Phys.*, 19(2):023007, 2017.

[79] L. R. Liu, J. D. Hood, Y. Yu, J. T. Zhang, N. R. Hutzler, T. Rosenband, and K.-K. Ni. Building one molecule from a reservoir of two atoms. *Science*, 360(6391):900–903, 2018.

[80] Y. Yu, N. R. Hutzler, J. T. Zhang, L. R. Liu, J. D. Hood, T. Rosenband, and K.-K. Ni. Motional-ground-state cooling outside the lamb-dicke regime. *Phys. Rev. A*, 97:063423, Jun 2018.

[81] L. R. Liu, J. D. Hood, Y. Yu, J. T. Zhang, K. Wang, Y.-W. Lin, T. Rosenband, and K.-K. Ni. Molecular assembly of ground-state cooled single atoms. *Phys. Rev. X*, 9:021039, May 2019.

[82] Jonathan D. Hood, Yichao Yu, Yen-Wei Lin, Jessie T. Zhang, Kenneth Wang, Lee R. Liu, Bo Gao, and Kang-Kuen Ni. Multichannel interactions of two atoms in an optical tweezer. *Phys. Rev. Research*, 2:023108, 2020.

[83] Lee R. Liu. *Building Single Molecules - Reactions, Collisions, and Spectroscopy of Two Atoms*. PhD thesis, Harvard University, 2019.

[84] Yichao Yu. *Coherent Creation of Single Molecules from Single Atoms*. PhD thesis, Harvard University, 2020.

[85] John Weiner, Vanderlei S. Bagnato, Sergio Zilio, and Paul S. Julienne. Experiments and theory in cold and ultracold collisions. *Rev. Mod. Phys.*, 71:1–85, Jan 1999.

[86] Lara Torralbo-Campo, Graham D. Bruce, Giuseppe Smirne, and Donatella Cassettari. Light-induced atomic desorption in a compact system for ultracold atoms. *Scientific Reports*, 5(1):14729, December 2015.

[87] J. Van Dongen, C. Zhu, D. Clement, G. Dufour, J. L. Booth, and K. W. Madison. Trap-depth determination from residual gas collisions. *Phys. Rev. A*, 84:022708, Aug 2011.

[88] David J. Griffiths. *Quantum Computation and Quantum Information*. Cambridge University Press, 2000.

[89] G. Breit and I. I. Rabi. Measurement of nuclear spin. *Phys. Rev.*, 38:2082–2083, Dec 1931.

[90] Michele Olsen. *Experiments with Feshbach molecules in a Bose-Fermi mixture*. PhD thesis, University of Colorado, 2008.

[91] Eric D. Black. An introduction to Pound–Drever–Hall laser frequency stabilization. *American Journal of Physics*, 69(1):79–87, January 2001.

[92] Gianni Di Domenico, Stéphane Schilt, and Pierre Thomann. Simple approach to the relation between laser frequency noise and laser line shape. *Appl. Opt., AO*, 49(25):4801–4807, September 2010.

[93] James C. Wyant and Katherine Creath. Basic Wavefront Aberration Theory for Optical Metrology. In Robert R. Shannon and James C. Wyant, editors, *Applied Optics and Optical Engineering, Volume XI*, volume 11, page 2, January 1992.

[94] IntraAction Corp. *Acousto-optic Deflector Instruction Manual*.

[95] H. J. Metcalf and P. van der Straten. *Laser Cooling and Trapping*. Spring, New York, 1999.

[96] Paul D. Lett, Richard N. Watts, Christoph I. Westbrook, WilliamD. Phillips, Phillip L. Gould, and Harold J. Metcalf. Observation of atoms laser cooled below the Doppler limit. *Phys. Rev. Lett.*, 61(2):169, July 1988.

[97] Nobuyuki Otsu. A threshold selection method from gray-level histograms. *IEEE Transactions on Systems, Man, and Cybernetics*, 9(1):62–66, 1979.

[98] Edwin B. Wilson. Probable inference, the law of succession, and statistical inference. *Journal of the American Statistical Association*, 22(158):209–212, 1927.

[99] Yu Wang, Kenneth Wang, Eliot F. Fenton, Yen-Wei Lin, Kang-Kuen Ni, and Jonathan D. Hood. Reduction of laser intensity noise over 1 mhz band for single atom trapping. *Opt. Express*, 28(21):31209–31215, Oct 2020.

[100] Rudolf Grimm, Matthias Weidemüller, and Yurii B. Ovchinnikov. Optical dipole traps for neutral atoms. *Advances In Atomic, Molecular, and Optical Physics*, 42:95–170, 2000.

[101] M. E. Gehm, K. M. O'Hara, T. A. Savard, and J. E. Thomas. Dynamics of noise-induced heating in atom traps. *Phys. Rev. A*, 58:3914–3921, Nov 1998.

[102] Charles Tuchendler, Andrew Matheson Lance, A Browaeys, Yvan RP Sortais, and Philippe Grangier. Energy distribution and cooling of a single atom in an optical tweezer. *Physical Review A*, 78(3):033425, 2008.

[103] Mark Kasevich and Steven Chu. Laser cooling below a photon recoil with three-level atoms. *Phys. Rev. Lett.*, 69:1741–1744, Sep 1992.

[104] R. B. Blackman and J. W. Tukey. *The Measurement of Power Spectra*. Dover, 1959.

[105] D. J. Wineland, M. Barrett, J. Britton, J. Chiaverini, B. DeMarco, W. M. Itano, B. Jelenković, C. Langer, D. Leibfried, V. Meyer, T. Rosenband, and T. Schätz. Quantum information processing with trapped ions. *Philosophical Transactions of the Royal Society of London A: Mathematical, Physical and Engineering Sciences*, 361(1808):1349–1361, 2003.

[106] DJ Wineland, C Monroe, WM Itano, D Leibfried, BE King, and DM Meekhof. Experimental issues in coherent quantum-state manipulation of trapped atomic ions. *Journal of Research of the National Institute of Standards and Technology*, 103(3):259, 1998.

[107] K. L. Corwin, S. J. M. Kuppens, D. Cho, and C. E. Wieman. Spin-polarized atoms in a circularly polarized optical dipole trap. *Phys. Rev. Lett.*, 83:1311–1314, Aug 1999.

[108] Ivan H. Deutsch and Poul S. Jessen. Quantum-state control in optical lattices. *Phys. Rev. A*, 57:1972–1986, Mar 1998.

[109] A. M. Kaufman, B. J. Lester, and C. A. Regal. Cooling a Single Atom in an Optical Tweezer to Its Quantum Ground State. *Phys. Rev. X*, 2(4):041014, Nov 2012.

[110] J. D. Thompson, T. G. Tiecke, A. S. Zibrov, V. Vuletić, and M. D. Lukin. Coherence and raman sideband cooling of a single atom in an optical tweezer. *Phys. Rev. Lett.*, 110:133001, Mar 2013.

[111] R. A. Cline, J. D. Miller, M. R. Matthews, and D. J. Heinzen. Spin relaxation of optically trapped atoms by light scattering. *Opt. Lett.*, 19(3):207–209, Feb 1994.

[112] Cheng Chin, Rudolf Grimm, Paul Julienne, and Eite Tiesinga. Feshbach resonances in ultracold gases. *Reviews of Modern Physics*, 82(2):1225, 2010.

[113] O Docenko, M Tamanis, J Zaharova, R Ferber, A Pashov, H Knöckel, and E Tiemann. The coupling of the x 1 Σ + and a 3 Σ + states of the atom pair na + cs and modelling cold collisions. *J. Phys. B*, 39(19):S929, 2006.

[114] S. Inouye, M. R. Andrews, J. Stenger, H.-J. Miesner, D. M. Stamper-Kurn, and W. Ketterle. Observation of Feshbach resonances in a Bose-Einstein condensate. *Nature*, 392(0):151, March 1998.

[115] Manfred J. Mark, Florian Meinert, Katharina Lauber, and Hanns-Christoph Nägerl. Mott-insulator-aided detection of ultra-narrow Feshbach resonances. *SciPost Physics*, 5:055, Nov 2018.

[116] Bo Gao. Private communication.

[117] Jeremy Hutson. Private communication.

[118] Hannah J. Patel, Caroline L. Blackley, Simon L. Cornish, and Jeremy M. Hutson. Feshbach resonances, molecular bound states, and prospects of ultracold-molecule formation in mixtures of ultracold k and cs. *Phys. Rev. A*, 90:032716, Sep 2014.

[119] C. Chin, R. Grimm, P. Julienne, and E. Tiesinga. Feshbach resonances in ultracold gases. *arXiv:0812.1496*, 2008.

[120] R.N. Zare. *Angular momentum: understanding spatial aspects in chemistry and physics*. George Fisher Baker non-resident lectureship in chemistry at Cornell University. Wiley, 1988.

[121] Cheng Chin, Vladan Vuletić, Andrew J. Kerman, Steven Chu, Eite Tiesinga, Paul J. Leo, and Carl J. Williams. Precision Feshbach spectroscopy of ultracold Cs 2. *Physical Review A*, 70(3):032701, September 2004.

[122] G. Thalhammer, K. Winkler, F. Lang, S. Schmid, R. Grimm, and J. Hecker Denschlag. Long-lived Feshbach molecules in a three-dimensional optical lattice. *Phys. Rev. Lett.*, 96(5):050402–4, February 2006.

[123] Amodsen Chotia, Brian Neyenhuis, Steven A. Moses, Bo Yan, Jacob P. Covey, Michael Foss-Feig, Ana Maria Rey, Deborah S. Jin, and Jun Ye. Long-lived dipolar molecules and Feshbach molecules in a 3d optical lattice. *Phys. Rev. Lett.*, 108:080405, Feb 2012.

[124] M. D. Frye and J. M. Hutson. Characterizing Feshbach resonances in ultracold scattering calculations. *Physical Review A*, 96(4):042705, 2017.

[125] Thorsten Kohler, Krzysztof Goral, and Paul S. Julienne. Production of cold molecules via magnetically tunable Feshbach resonances. *Rev. Mod. Phys.*, 78(4):1311, 2006.

[126] Olivier Dulieu. Private communication.

[127] Thomas Busch, Berthold-Georg Englert, Kazimierz Rzażewski, and Martin Wilkens. Two cold atoms in a harmonic trap. *Found. Phys.*, 28(4):549–559, 1998.

[128] J P Kestner and L-M Duan. Anharmonicity-induced resonances for ultracold atoms and their detection. *New Journal of Physics*, 12(5):053016, may 2010.

[129] Simon Sala and Alejandro Saenz. Theory of inelastic confinement-induced resonances due to the coupling of center-of-mass and relative motion. *Phys. Rev. A*, 94:022713, Aug 2016.

[130] Krzysztof Jachymski, Zbigniew Idziaszek, and Tommaso Calarco. Feshbach resonances in a nonseparable trap. *Phys. Rev. A*, 87:042701, Apr 2013.

[131] Lukas Reichsöllner, Andreas Schindewolf, Tetsu Takekoshi, Rudolf Grimm, and Hanns-Christoph Nägerl. Quantum engineering of a low-entropy gas of heteronuclear bosonic molecules in an optical lattice. *Phys. Rev. Lett.*, 118:073201, Feb 2017.

[132] J. M. Hutson and C. R. Le Sueur. MOLSCAT: a program for non-reactive quantum scattering calculations on atomic and molecular collisions. *Comp. Phys. Commun.*, 241:9–18, 2019.

[133] J. M. Hutson and C. R. Le Sueur. BOUND and FIELD: programs for calculating bound states of interacting pairs of atoms and molecules. *Comp. Phys. Commun.*, 241:1–8, 2019.

[134] Pascal Naidon and Shimpei Endo. Efimov physics: a review. *Reports on Progress in Physics*, 80(5):056001, Mar 2017.

[135] Chris H. Greene, P. Giannakeas, and J. Pérez-Ríos. Universal few-body physics and cluster formation. *Rev. Mod. Phys.*, 89:035006, Aug 2017.

[136] T Lahaye, C Menotti, L Santos, M Lewenstein, and T Pfau. The physics of dipolar bosonic quantum gases. *Reports on Progress in Physics*, 72(12):126401, Nov 2009.

[137] Johann G. Danzl, Elmar Haller, Mattias Gustavsson, Manfred J. Mark, Russell Hart, Nadia Bouloufa, Olivier Dulieu, Helmut Ritsch, and Hanns-Christoph Nägerl. Quantum gas of deeply bound ground state molecules. *Science*, 321(5892):1062–1066, 2008.

[138] F. Lang, K. Winkler, C. Strauss, R. Grimm, and J. Hecker Denschlag. Ultracold triplet molecules in the rovibrational ground state. *Phys. Rev. Lett.*, 101:133005, Sep 2008.

[139] Peter K. Molony, Philip D. Gregory, Zhonghua Ji, Bo Lu, Michael P. Köppinger, C. Ruth Le Sueur, Caroline L. Blackley, Jeremy M. Hutson, and Simon L. Cornish. Creation of ultracold ^{87}Rb^{133}Cs molecules in the rovibrational ground state. *Phys. Rev. Lett.*, 113:255301, Dec 2014.

[140] Nikolay V. Vitanov, Andon A. Rangelov, Bruce W. Shore, and Klaas Bergmann. Stimulated raman adiabatic passage in physics, chemistry, and beyond. *Rev. Mod. Phys.*, 89:015006, Mar 2017.

[141] A. Grochola, P. Kowalczyk, J. Szczepkowski, W. Jastrzebski, A. Wakim, P. Zabawa, and N. P. Bigelow. Spin-forbidden $c\,^3\Sigma^+(\Omega = 1) \leftarrow x\,^1\Sigma^+$ transition in nacs: Investigation of the $\Omega = 1$ state in hot and cold environments. *Phys. Rev. A*, 84:012507, Jul 2011.

[142] Kevin M. Jones, Eite Tiesinga, Paul D. Lett, and Paul S. Julienne. Ultracold photoassociation spectroscopy: Long-range molecules and atomic scattering. *Rev. Mod. Phys.*, 78:483–535, May 2006.

[143] Jesus Aldegunde and Jeremy M. Hutson. Hyperfine structure of alkali-metal diatomic molecules. *Phys. Rev. A*, 96:042506, Oct 2017.

[144] Michael Fleischhauer, Atac Imamoglu, and Jonathan P. Marangos. Electromagnetically induced transparency: Optics in coherent media. *Rev. Mod. Phys.*, 77:633, 2005.

[145] R. Vexiau, D. Borsalino, M. Lepers, A. Orban, M. Aymar, O. Dulieu, and N. Bouloufa-Maafa. Dynamic dipole polarizabilities of heteronuclear alkali dimers: optical response, trapping and control of ultracold molecules. *International Reviews in Physical Chemistry*, 36(4):709–750, 2017.

[146] Kang-Kuen Ni. *A Quantum Gas of Polar Molecules*. PhD thesis, University of Colorado Boulder, 2009.

[147] Covesion. *Covesion Guide to PPLN: Introduction*.

[148] G. D. Boyd and D. A. Kleinman. Parametric interaction of focused gaussian light beams. *Journal of Applied Physics*, 39(8):3597–3639, 1968.

[149] Mohammad Mujahid Aliyu, Luheng Zhao, Xiu Quan Quek, Krishna Chaitanya Yellapragada, and Huanqian Loh. D1 magic wavelength tweezers for scaling atom arrays. *arXiv e-prints*, page arXiv:2105.15047, May 2021.

[150] Jonathan C. Knight. Photonic crystal fibres. *Nature*, 424(6950):847–851, 2003.

[151] Eugene Hecht. *Optics*. Pearson, 2013.

[152] Daniel Barredo, Vincent Lienhard, Sylvain de Léséleuc, Thierry Lahaye, and Antoine Browaeys. Synthetic three-dimensional atomic structures assembled atom by atom. *Nature*, Sep 2018.

[153] Qingze Guan, Michael Highman, Eric J. Meier, Garrett R. Williams, Vito Scarola, Brian DeMarco, Svetlana Kotochigova, and Bryce Gadway. Nondestructive dispersive imaging of rotationally excited ultracold molecules. *Phys. Chem. Chem. Phys.*, 22:20531–20544, 2020.

[154] V.S. Malinovsky and J.L. Krause. General theory of population transfer by adiabatic rapid passage with intense, chirped laser pulses. *The European Physical Journal D - Atomic, Molecular, Optical and Plasma Physics*, 14(2):147–155, May 2001.

[155] Lorenza Viola and Seth Lloyd. Dynamical suppression of decoherence in two-state quantum systems. *Phys. Rev. A*, 58:2733–2744, Oct 1998.

[156] Lorenza Viola, Emanuel Knill, and Seth Lloyd. Dynamical decoupling of open quantum systems. *Phys. Rev. Lett.*, 82:2417–2421, Mar 1999.

[157] S Ospelkaus, K-K Ni, G Quéméner, B Neyenhuis, D Wang, MHG De Miranda, JL Bohn, J Ye, and DS Jin. Controlling the hyperfine state of rovibronic ground-state polar molecules. *Physical review letters*, 104(3):030402, 2010.

[158] Sebastian A. Will, Jee Woo Park, Zoe Z. Yan, Huanqian Loh, and Martin W. Zwierlein. Coherent microwave control of ultracold ^{23}Na^{40}K molecules. *Phys. Rev. Lett.*, 116:225306, Jun 2016.

[159] Jacob A Blackmore, Luke Caldwell, Philip D Gregory, Elizabeth M Bridge, Rahul Sawant, Jesús Aldegunde, Jordi Mur-Petit, Dieter Jaksch, Jeremy M Hutson, B E Sauer, M R Tarbutt, and Simon L Cornish. Ultracold molecules for quantum simulation: rotational coherences in CaF and RbCs. *Quantum Science and Technology*, 4(1):014010, dec 2018.

[160] Jacob Covey. *Enhanced optical and electric manipulation of a quantum gas of KRb molecules*. PhD thesis, University of Colorado Boulder, Boulder, 2017-07 2017.

[161] S. F. Yelin, K. Kirby, and Robin Côté. Schemes for robust quantum computation with polar molecules. *Phys. Rev. A*, 74(5):050301, 2006.

[162] Michael L. Wall, Kaden R. A. Hazzard, and Ana Maria Rey. *From atomic to mesoscale: The Role of Quantum Coherence in Systems of Various Complexities*, chapter Quantum magnetism with ultracold molecules. World Scientific, 2015.

[163] Thomas Schuster, Felix Flicker, Ming Li, Svetlana Kotochigova, Joel E Moore, Jun Ye, and Norman Y Yao. Realizing hopf insulators in dipolar spin systems. *Physical Review Letters*, 127(1):015301, 2021.

[164] Norman Y Yao, Michael P Zaletel, Dan M Stamper-Kurn, and Ashvin Vishwanath. A quantum dipolar spin liquid. *Nature Physics*, 14(4):405–410, 2018.

[165] Dries Sels, Hesam Dashti, Samia Mora, Olga Demler, and Eugene Demler. Quantum approximate bayesian computation for nmr model inference. *Nature Machine Intelligence*, 2:396–403, 2020.

[166] Huan Yang, De-Chao Zhang, Lan Liu, Ya-Xiong Liu, Jue Nan, Bo Zhao, and Jian-Wei Pan. Observation of magnetically tunable feshbach resonances in ultracold 23na40k+ 40k collisions. *Science*, 363(6424):261–264, 2019.

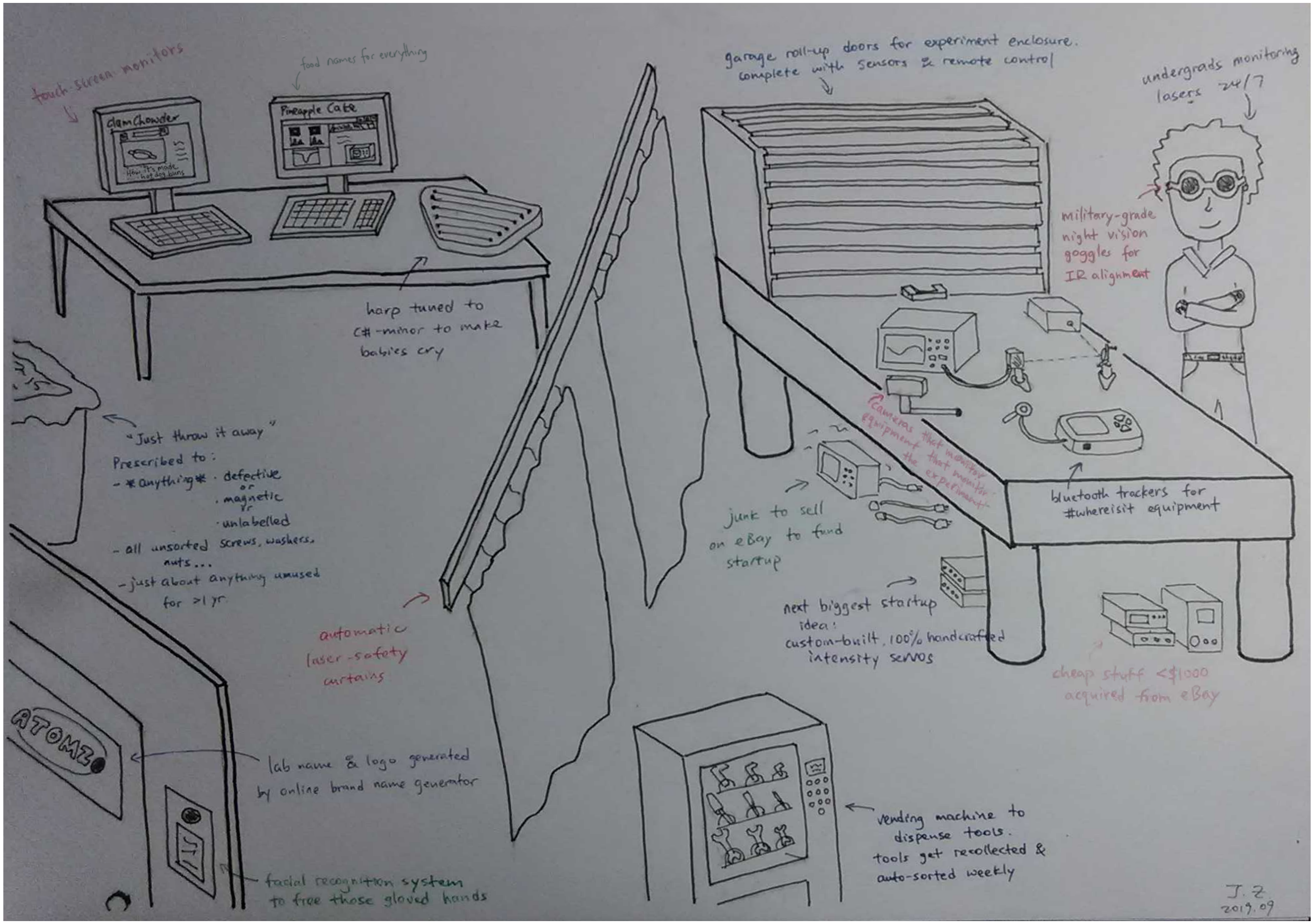touch screen monitors
food names for everything
ClamChowder
How it's made hot dog buns
Pineapple Cake
harp tuned to C#-minor to make babies cry
"Just throw it away"
Prescribed to:
- *anything* · defective or · magnetic or · unlabelled
- all unsorted screws, washers, nuts...
- just about anything unused for >1 yr.
automatic laser-safety curtains
ATOMZ
lab name & logo generated by online brand name generator
facial recognition system to free those gloved hands
garage roll-up doors for experiment enclosure. complete with sensors & remote control
undergrads monitoring lasers 24/7
military-grade night vision goggles for IR alignment
cameras that monitor equipment that monitor the experiment
bluetooth trackers for #whereisit equipment
junk to sell on eBay to fund startup
next biggest startup idea: custom-built, 100% handcrafted intensity servos
cheap stuff <$1000 acquired from eBay
vending machine to dispense tools. tools get recollected & auto-sorted weekly
J. Z
2019.09